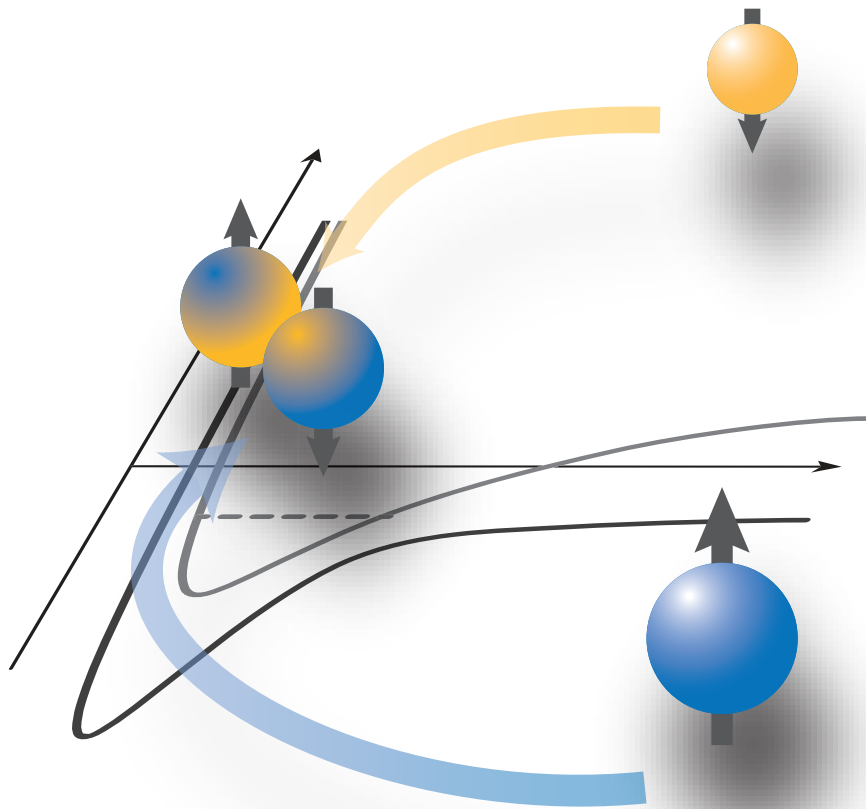

A two-orbital quantum gas with tunable interactions

Moritz Höfer



München 2017

A two-orbital quantum gas with tunable interactions



Dissertation an der Fakultät für Physik
Ludwig-Maximilians-Universität München

vorgelegt von

Moritz Höfer

aus Stade

München, den 02. März 2017

Tag der mündlichen Prüfung: 7. April 2017

Erstgutachter: Prof. Immanuel Bloch

Zweitgutachter: Prof. Wilhelm Zwerger

Weitere Prüfungskommissionsmitglieder: Prof. A. Högele, Prof. M. Punk

Zusammenfassung

Im letzten Jahrzehnt haben sich Quantengasexperimente als gut kontrollierbare Modellsysteme zur Untersuchung komplexer Fragestellungen aus diversen Bereichen der Physik etabliert. Ultrakalte Quantengase zeichnen sich insbesondere dadurch aus, dass sie einen direkten und experimentell einfach realisierbaren Zugang zu ihrer Wechselwirkung bieten. Das gezielte Einstellen der Wechselwirkungsstärke und die Erforschung der daraus resultierenden Aggregatzustände erlaubt es ein tiefes Verständnis der kondensierten Materie zu gewinnen. Insbesondere erdalkaliähnliche Atome wie Ytterbium bieten die Möglichkeit Phänomene der Festkörperphysik zu untersuchen, die durch die Wechselwirkung von Elektronen in verschiedenen Orbitalen oder durch eine größere Rotationssymmetrie des Spins als in gewöhnlichen Spin-1/2 Systemen hervorgerufen werden.

Diese Doktorarbeit präsentiert die experimentelle Charakterisierung der Wechselwirkung ultrakalter, fermionischer Ytterbium-Atome (^{173}Yb) in verschiedenen elektronischen Orbitalen. Dabei wird nachgewiesen, dass sich die Wechselwirkungsstärke mit Hilfe eines externen Magnetfeldes, analog zu einer Feshbach-Resonanz bei Alkali-Atomen, einstellen lässt. Bei Ytterbium wird diese Resonanz durch eine starke Spinaustauschwechselwirkung zwischen den verschiedenen Orbitalen hervorgerufen. Der Nachweis der einstellbaren Wechselwirkung erfolgt über Thermalisierungsexperimente in einer harmonischen Falle und mit Hilfe von hochauflösender Spektroskopie in einem dreidimensionalen Gitter. Des Weiteren wird mit Hilfe der neu entdeckten Resonanz zum ersten Mal experimentell ein stark wechselwirkendes Fermigas in verschiedenen Orbitalen erzeugt und spektroskopisch untersucht. Die Möglichkeit, die interorbitale Wechselwirkung direkt zu manipulieren und somit stark wechselwirkende Quantengase zu erzeugen, ebnet den Weg für die Realisierung und Untersuchung neuartiger Aggregatzustände der kondensierten Materie.

Contents

Introduction	1
1 Interactions in ultracold quantum gases	7
1.1 Elastic scattering of cold atoms	7
1.1.1 Two atoms in a central potential	8
1.1.2 The van der Waals potential	11
1.1.3 Interactions in a harmonic trap	14
1.2 Feshbach resonances	16
1.2.1 Scattering of atoms with spin and hyperfine interaction	17
1.2.2 Coupled channel approach	18
1.2.3 Classification of Feshbach resonances	21
1.2.4 Optical Feshbach resonances	21
1.2.5 Experimental investigation of Feshbach resonances	22
2 Ytterbium – an alkaline-earth-like atom	23
2.1 $SU(N)$ symmetric two-orbital interactions	24
2.1.1 Interactions for high spin fermions	24
2.1.2 Emergence of $SU(N)$ symmetry in AEL atoms	25
2.1.3 Two-orbital $SU(N)$ -symmetric interactions	27
2.2 Electronic structure and optical transitions	28
2.2.1 Level structure of ytterbium	28
2.2.2 Forbidden transitions are not forbidden	30
2.2.3 Differential Zeeman shift of the clock transition	31
2.3 Traps for alkaline-earth-like atoms	33
2.3.1 Optical potentials	33
2.3.2 State-dependent optical potentials	35
2.4 Alkaline-earth-like atoms for quantum simulation	36
2.4.1 $SU(N)$ Fermi liquid	37
2.4.2 The $SU(N)$ -symmetric Fermi Hubbard model	38
2.4.3 Two-orbital $SU(N)$ -symmetric models	40
3 Experimental apparatus and sequence	43
3.1 Experimental apparatus	43
3.1.1 Magnetic field coils	43
3.1.2 Optical setup	45
3.1.3 Laser sources	47

3.2	Experimental sequence	48
3.2.1	Production of a degenerate Fermi gas	48
3.2.2	Manipulation and detection of the nuclear spin	49
3.2.3	Clock-line spectroscopy	50
4	Orbital Feshbach resonance	53
4.1	An interorbital Feshbach resonance	53
4.1.1	Absence of intraorbital Feshbach resonances for AEL atoms	53
4.1.2	Orbital interaction-induced Feshbach resonance	55
4.1.3	A two-channel model for the interorbital interaction	58
4.2	Determination of the scattering amplitude	61
4.2.1	Measurement of the elastic cross section	61
4.2.2	Determination of the inelastic scattering cross section	67
4.2.3	The s -wave scattering length	70
4.3	Interaction spectroscopy in the isotropic magic lattice	72
4.3.1	Two atoms on an isotropic lattice site	73
4.3.2	Spectroscopic determination of the interaction states symmetry	77
4.3.3	Position of the Feshbach resonance in the bulk	79
5	A strongly interacting Fermi gas in two dimensions	81
5.1	Interactions in a quasi-2D geometry	81
5.2	Clock-line spectroscopy of the quasi-2D dimer	84
5.2.1	Magnetic field dependence of the binding energy	85
5.2.2	Confinement dependence of the binding energy	87
5.2.3	Many-body effects on the dimer	88
5.3	Spectroscopy of the quasi-2D many-body system	90
5.3.1	Mean-field interaction shift	91
5.3.2	Repulsive and attractive polarons	94
	Conclusion and Outlook	99
A	Two-body problem in free space	103
B	Two-body problem in a harmonic trap	107
C	Two-body problem in quasi-2D	109
	References	111

Introduction

The most diverse phases of condensed matter emerge from the underlying interactions. Interactions drive phase transitions, induce spontaneous symmetry breaking and lead to the build up of strong correlations. Modelling these fascinating phenomena, requires a fundamental understanding of how quantum many-body systems are shaped by the interactions. The possibility to directly control the interaction strength and to explore the associated states of matter is an intriguing notion. Yet, condensed-matter systems rarely offer such a far-ranging degree of control. Furthermore, in contrast to classical systems, most interacting quantum mechanical many-body systems defy computational approaches [1]. Instead, for the investigation of unresolved problems originating from condensed matter, few- and many-body physics controllable quantum systems are needed [2–5]. Here, ultra-cold atomic quantum gases represent a versatile platform, offering a remarkable degree of control combined with innovative detection methods [5, 6]. In particular, we find the exquisite possibility of tuning the interatomic interaction strength to arbitrary values. This enables the access to repulsive and attractive interactions in the same physical system. Even the continuous crossover between the two contrary regimes can be explored.

Atomic quantum gases are formed from dilute gases at ultra-low temperatures. In this limit, the interatomic interactions can be characterised by a single parameter, the so-called *s*-wave scattering length. Typically, the scattering length is much shorter than the interparticle spacing and the quantum gas is weakly interacting. In this regime, the many-body properties of a bosonic as well as fermionic quantum gas can be described by an effective single-particle theory based on non-interacting quasiparticles [7, 8]. In contrast, for strong interactions, where the interaction energy is on the order of the Fermi energy, analytic and numerical approaches are expensive, since the system is free of small parameters. Therefore creating strong interactions is of particular interest. A quantum gas enters the regime of strong interaction when the scattering length is on the order of the interparticle spacing. In this context, Feshbach resonances have become an indispensable tool as they provide a simple experimental protocol to control the interaction strength over multiple orders of magnitude by means of an external magnetic field [9].

As an example, employing a Feshbach resonance allows to continuously modify the superfluid ground state of a Fermi gas. In the limit of attractive interaction, fermions form Cooper pairs, as described by the Bardeen-Cooper-Schrieffer (BCS) theory [10]. For repulsive interactions, the atoms are strongly bound into molecules, which form a Bose-Einstein-Condensate (BEC), as they are composite bosons. The experimentally observed connection between these two limits, the so-called BEC-BCS crossover [11, 12], is one of the most celebrated successes of interaction tuning via Feshbach resonances [13–15].

Directly on resonance, experiments [16, 17] provide a valuable insight into strongly-interacting states of matter, as they are predicted to exist in the crusts of neutron stars [18].

An alternative route towards strong interactions is offered in optical lattices. In contrast to Feshbach resonances, this technique relies on the limitation of the kinetic energy instead of the direct variation of the scattering length. In addition, ultracold atoms in optical lattices resemble the Hubbard model [19], one of the most prominent and extensively studied models in condensed matter physics. In particular, the fermionic Hubbard model is believed to incorporate the effect of high-temperature superfluidity [20]. Tuning the ratio of kinetic to interaction energy grants access to the strongly interacting regime, as demonstrated by the observation of Mott insulating states with bosons [21] and fermions [22, 23].

By completely suppressing the motion along one or more directions, optical lattices have paved the way towards low-dimensional systems. In lower dimensions, quantum fluctuations become more dominant and can suppress the build up of long-range order [24], as demonstrated by the observation of the Kosterlitz-Thouless crossover in two dimensions [25]. In one dimension, the influence of the interaction becomes completely counter-intuitive. The 1D gas becomes strongly interacting with decreasing density, i.e. increasing particle separation. In this limit, strongly interacting bosons behave as if they are identical fermions [26].

Besides this high degree of control, ultracold atomic gases offer numerous possibilities to probe global as well as local properties. Conventionally, after the atoms have been released from the confining potential, the shadow of the expanded atomic cloud is imaged onto a CCD camera. This technique grants access to global properties such as the inter-atomic interaction strength [27], the dispersion relation [28] or even correlations inside the trap [29]. In recent years, high-resolution *in-situ* imaging techniques have been developed and allow to directly measure the in-trap atomic distribution [30]. In particular, the possibility to resolve and manipulate single atoms on individual lattice sites has to be mentioned [31, 32]. All these techniques go far beyond typical detection methods of condensed matter experiments.

Ultracold atomic gases have proven to exhibit an immense potential for quantum simulations. In particular, alkali atoms are well suited for laser cooling and trapping due to their simple hydrogen-like electronic structure. At the same time, this simplicity poses major limitations to the range of phenomena that can be explored. As an example, electrons in solids often possess an additional orbital degree of freedom besides their spin. The interplay between the spin and orbital degree of freedom gives rise to effects like Kondo screening [33], heavy-Fermi liquids [34] and unconventional superconductivity [35], beyond the single-orbital Hubbard model. Therefore, new experiments based on more complex systems such as magnetic atoms, polar molecules and alkaline-earth atoms have been constructed lately.

In contrast to alkali atoms, alkaline-earth like (AEL) atoms, such as ytterbium, exhibit a helium-like electronic structure, i.e. two valence electrons in addition to a set of completely filled shells. The peculiar electronic structure gives rise to low-lying, long-lived

excited states and a vanishing electronic angular momentum in the atomic ground state, both for the electronic spin singlet 1S_0 and for the triplet 3P_0 . For the fermionic isotopes, the large nuclear spin is strongly decoupled from the orbital degree of freedom, giving rise to an extended $SU(N)$ symmetry in the interaction [36–39]. Therefore, the production of AEL degenerate Fermi gases [40, 41] has paved the way for the implementation of otherwise inaccessible many-body phenomena, such as the realisation of $SU(N)$ Mott insulators [42, 43].

In the case of a $SU(2)$ spin model, naturally realisable with alkali atoms, the ground state always breaks the $SU(2)$ symmetry and possesses magnetic order [44–46]. The enlarged $SU(N > 2)$ spin rotation symmetry of fermionic AEL atoms gives rise to a strong frustration [36, 39]. For example, in a cubic lattice, with increasing number of degrees of freedom (N), magnetic order vanishes and the ground state is expected to preserve the full $SU(N)$ symmetry of the model [47–49].

As already mentioned, in many condensed-matter systems such as transition metal oxides [35] or manganese oxide perovskite [50], electrons have both orbital and spin degree of freedom. Fermionic AEL atoms exhibiting these degrees of freedom have been suggested for the simulation of these materials [38, 51, 52].

Furthermore, the large nuclear spin of AEL atoms can even be employed to go beyond condensed matter and investigate highly symmetric gauge theories from the field of high-energy and particle physics. The interactions within a nucleus are described by a global flavour $SU(3)$ symmetry group within the framework of quantum chromodynamics. The implementation of gauge theories with $SU(N)$ symmetric quantum gases [53–55] would allow to study particle physics with table-top experiments rather than large colliders.

The realisation of the aforementioned models crucially depends on the actual strength of the interorbital interaction. At the time of the construction of our experimental apparatus, the orbital interaction properties were unknown for ^{173}Yb . Therefore, the first experiments addressed the characterisation of these interactions. For the states 1S_0 and 3P_0 , we could prove that the intra- and interorbital interactions are indeed $SU(N)$ symmetric [56]. In particular, the observation of a strong orbital exchange interaction [56, 57], the elementary building block for the aforementioned models, brings the implementation of orbital magnetism within experimental reach.

Previously, we have argued that the ability to tune the interatomic interaction is a desirable ingredient for quantum gas experiments. So far, the regime of strong interactions in AEL atoms could only be reached in an optical lattice. Based on this technique, we were able to study the metal to Mott insulator crossover and reveal the non trivial influence of the $SU(N)$ symmetry [43]. Tuning of the interaction strength outside the lattice or changing the sign of the interaction seems out of reach. The strong suppression of hyperfine interactions for states with vanishing electronic angular momentum implies that no magnetic Feshbach resonances are expected within the 1S_0 and 3P_0 states.

However, the strong orbital exchange interaction in ^{173}Yb [56, 57] is based on two starkly different interaction channels. This peculiar configuration, has led to the prediction of a magnetically accessible interorbital scattering resonance [58].

This thesis provides a detailed investigation of the interorbital interaction between ^{173}Yb atoms in the $^1\text{S}_0$ and $^3\text{P}_0$ state. In order to understand how a Feshbach resonance can arise from the orbital exchange interaction, we start by reviewing the physics of Feshbach resonances in alkali atoms. There, we will identify three major ingredients for the appearance of a Feshbach resonance: (i) two collision channels (ii) a coupling and (iii) a differential magnetic moment between the channels. Afterwards, we turn to ^{173}Yb , where we find that the interorbital interaction fulfils these three requirements. Therefore, we construct a new two-channel model for the interorbital interactions. In the main part of this thesis, we experimentally reveal the existence of this novel orbital Feshbach resonance [59]. We map out the magnetic-field dependence of the interorbital s -wave scattering length in the bulk as well as the pair interaction energy in a deep isotropic lattice. Both experimental results are in excellent agreement with our two-channel model. Although the orbital Feshbach resonance is a so-called narrow resonance, we show that the strongly interacting, degenerate Fermi gas exhibits a long lifetime. In the last part of this thesis, we present preliminary results concerning the strongly interacting two orbital quantum gas in a quasi two-dimensional geometry. There, we quench the system from the weakly into the strongly interacting regime and find evidences of metastable, strongly interacting impurities, i.e. attractive and repulsive polarons. These measurements are a first step towards the realisation of novel Fermi superfluids with an orbital degree of freedom.

Outline

In Chapter 1, the fundamental principle of interactions in ultracold quantum gases are reviewed. Particularly with regard to the emergence of Feshbach resonances, the influence of the underlying molecular potential on the s -wave scattering length is discussed.

Chapter 2 surveys the distinct properties of ytterbium, a member of the alkaline-earth like family. The implication of long-lived excited states and $SU(N)$ symmetry on the inter-atomic interaction are considered.

Chapter 3 introduces the experimental apparatus and sequence. The construction of the experimental apparatus has already been discussed in great detail in previous works [60, 61]. Here, we focus on the recent updates, necessary for the experiments presented in this thesis.

In Chapter 4, we report on the observation of a novel type of Feshbach resonance, arising from the orbital exchange interaction. In the bulk, the magnetic field dependence of the elastic and inelastic scattering cross section are determined by cross-dimensional thermalisation and loss spectroscopy respectively. Additionally, employing high-resolution clock line spectroscopy in an isotropic lattice, we directly probe the pure two-body interaction properties of a two-orbital atom pair. All our experimental results are in good agreement with a two-channel scattering model, incorporating effective ranges and confinement effects.

In Chapter 5, we present the create a strongly interacting two-orbital Fermi gas in quasi two dimensions. The influence of the reduced dimensionality on the interorbital interaction is probed spectroscopically. We demonstrate the existence of a confinement induced dimer and the universal scaling of the binding energy. Furthermore, a regime strongly interacting impurities is investigated. Here, the measured interaction shifts are well described by a polaron theory.

In the final Chapter, the main results of this thesis are summarised. We discuss the feasibility of new experiments based on the novel ability of tuning the two-orbital interaction strength.

Publications

The main results of this thesis have been published in the following journals:

C. Hofrichter, L. Riegger, F. Scazza, M. Höfer, D. R. Fernandes, I. Bloch, and S. Fölling, *Direct Probing of the Mott Crossover in the $SU(N)$ Fermi-Hubbard Model*, Physical Review X 6, 021030 (2016).

M. Höfer, L. Riegger, F. Scazza, C. Hofrichter, D. R. Fernandes, M. M. Parish, J. Levinsen, I. Bloch, and S. Fölling, *Observation of an Orbital Interaction Induced Feshbach Resonance in ^{173}Yb* , Physical Review Letters 115, 265302 (2015)

F. Scazza, C. Hofrichter, M. Höfer, P. C. De Groot, I. Bloch, and S. Fölling, *Observation of two-orbital spin-exchange interactions with ultracold $SU(N)$ -symmetric fermions*, Nature Physics 10, 779–784 (2014)

The following articles have also been published during the course of this thesis:

E. Nicklas, M. Karl, M. Höfer, A. Johnson, W. Muessel, H. Strobel, J. Tomkovič, T. Gasenzer, and M.K. Oberthaler, *Observation of Scaling in the Dynamics of a Strongly Quenched Quantum Gas*, Physical Review Letters 115, 245301 (2015).

Interactions in ultracold quantum gases

The most fundamental process of interaction for two atoms is a binary collision, whether they are bosons or fermions. The process of scattering is common to many different fields of physics, ranging from high energy physics to ultracold quantum gases for charged and neutral particles. Before introducing the central part of this thesis, presenting the observation of a novel interorbital interaction induced Feshbach resonance, we have to shine a light on the way ultracold atoms in a dilute gas interact with each other.

In this chapter, we will first give a brief review of the quantum mechanical treatment of scattering between two neutral atoms in free space. Here, we focus on the introduction of the terminology widely used in scattering theory, especially the interpretation of the *s*-wave scattering length as an effective hard sphere radius. Using the example of the van der Waals potential, we will demonstrate how the scattering length is influenced by the position of the least-bound state in the potential. Subsequently, we investigate the influence of a harmonic confinement on the atomic interactions.

The second major topic of this chapter are Feshbach resonances. For alkali atoms, Feshbach resonances allow for tuning the scattering length via an external magnetic field. We demonstrate how the internal structure of alkali atoms gives rise to multiple coupled scattering channels. Due to a differential magnetic moment, an external magnetic field can tune the energy of the least-bound state and thus the interaction strength between two atoms. Later, in chapter 4, we will compare the novel interorbital Feshbach resonance in AEL atoms to the magnetic Feshbach resonances in alkali atoms.

1.1 Elastic scattering of cold atoms

In the following, we will discuss the elastic scattering of two neutral atoms under typical conditions found in ultracold quantum gases. In most experiments, dilute gases of ultracold atoms are trapped in a harmonic potential. First we will study the implications of this terminology on the way two atoms interact. We present the textbook solution of the scattering problem in free space based on the partial-wave expansion. Thereupon, we demonstrate how the underlying interaction potential influences the scattering properties base on the example of the van der Waals potential. Finally, we present the solution to the scattering problem under the influence of confinement.

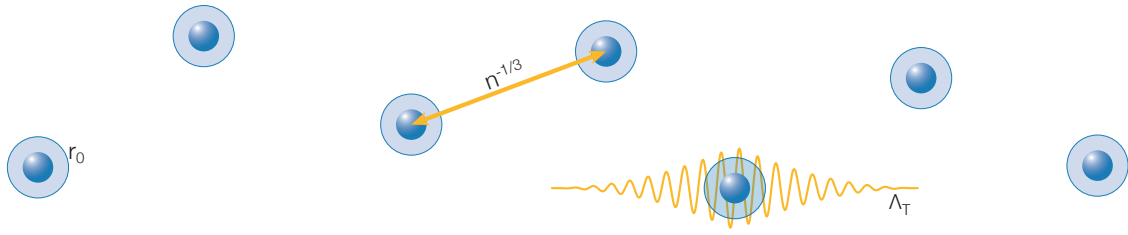


Figure 1.1 – Schematic drawing of an ultracold and dilute gas. The impenetrable, i.e. hard-core atoms (dark blue spheres) are surrounded by a short-range interaction potential (light blue sphere) with a characteristic length r_0 . In an ultracold and dilute gas the inter particle spacing $n^{-1/3}$ and the thermal wavelength Λ_{th} have to be larger than r_0 . Under typical experimental conditions with an atomic density of 10^{13} atoms/cm³ and a temperature around 100 nK we find $n^{-1/3} \approx \Lambda_{\text{th}} \approx 0.5 \mu\text{m}$, whereas r_0 is usually on the order of one to hundred Bohr radii $r_0 \approx 100a_0 \approx 5 \text{ nm}$ and thus $r_0 \ll n^{-1/3}, \Lambda_{\text{th}}$.

1.1.1 Two atoms in a central potential

The interaction of neutral atoms can be modelled by an isotropic and short-range inter-atomic molecular potential. A typical example is the van der Waals type potential which we will study in the next section. Yet, the following consideration holds for any isotropic and short-range potential. Short range implies that the potential falls off quickly to zero beyond a characteristic length scale r_0 . We want to focus on the case of binary collisions. This simplification is justified in a dilute and cold gas, as we will show. Since the typical atomic densities n in quantum gases are very low, the mean particle separation $n^{-1/3}$ is much larger than r_0

$$nr_0^3 \ll 1. \quad (1.1)$$

Here, the probability to find more than two atoms in a sphere with radius r_0 is strongly suppressed and the gas is called dilute. Furthermore, we work at ultra-low temperatures, therefore we can assume that the atoms move slowly through the gas. By this, we mean that the thermal wavelength $\Lambda_{\text{th}} = h/\sqrt{2\pi mk_{\text{B}}T}$ is much larger than r_0 . In terms of the momentum of the free atoms $k \propto 1/\Lambda_{\text{th}}$, we require the atoms to move so slowly that only up to two at a time are found within a sphere of the radius r_0

$$kr_0 \ll 1. \quad (1.2)$$

Only if the gas satisfies (1.1) and (1.2), we can restrict our description to binary collisions and the scattering process is reduced to a two-body problem.

Isotropic interactions are given by a conservative central potential $V(r)$, where $r = |\mathbf{r}_1 - \mathbf{r}_2|$ is the radial distance between the two atoms. Hence, we can separate the relative from the centre-of-mass motion. The relative motion can be reduced to the motion of a single particle with the reduced mass $M = m_1 m_2 / (m_1 + m_2)$ in the same potential. Furthermore, the kinetic energy is conserved and the collisions are elastic, i.e. the relative momentum before and after the collision (\mathbf{k} and \mathbf{k}') have the same modulus $k = k'$, as illustrated by Figure 1.2. Thus, the elastic scattering of two atoms only leads to a phase shift in the wave function.

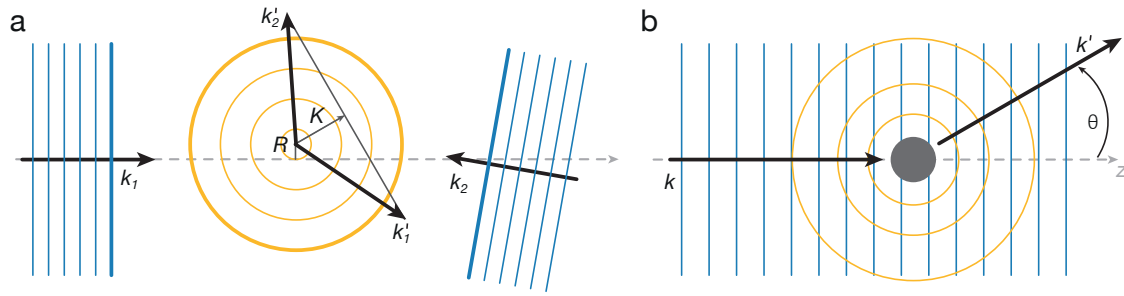


Figure 1.2 – (a) Schematic drawing of two-atom scattering. The two incoming atoms with mass m_i are represented by the blue plane waves \mathbf{k}_i and are scattered into the outgoing yellow spherical wave with the centre-of-mass coordinate $\mathbf{R} = (m_1\mathbf{r}_1 + m_2\mathbf{r}_2)/m_1m_2$ and the corresponding momentum \mathbf{K} , as well as the relative position $\mathbf{r} = \mathbf{r}_1 - \mathbf{r}_2$. (b) Representation of the scattering in the centre-of-mass reference frame. The incoming reduced mass M with the relative momentum \mathbf{k} (blue) is scattered on the central symmetric potential (gray circle) into the outgoing spherical wave $f(\theta)e^{ik'r}/r$ (yellow) under the angle θ .

Derivation of the scattering amplitude

As mentioned above, we can reduce the two-body problem into a one-body problem in the centre-of-mass frame. The relative wave function is determined by the time-independent Schrödinger equation [62]

$$\left[-\frac{\hbar^2 \nabla^2}{2M} + V(r) \right] \psi(\mathbf{r}) = E\psi(\mathbf{r}), \quad (1.3)$$

where E is the relative energy of the atoms. At large separation, the atoms are non-interacting $V(r \gg r_0) = 0$ and the energy is purely kinetic $E = \hbar^2 k^2 / 2M$. Here, the solution of the free Schrödinger equation is given by incoming and outgoing plane waves. Since the solution to the total Schrödinger equation has to asymptotically fulfil this boundary condition, we construct the scattering wave function from an incoming plane wave with wave vector \mathbf{k} and an outgoing spherical wave

$$\psi(\mathbf{r}) \propto e^{i\mathbf{k}\mathbf{r}} + f(\mathbf{k}', \mathbf{k}) \frac{e^{ik'r}}{r}. \quad (1.4)$$

We introduce the scattering amplitude $f(\mathbf{k}', \mathbf{k})$, i.e. the probability amplitude for scattering from \mathbf{k} into the new direction \mathbf{k}' . Due to the centrally symmetric potential, it is convenient to treat the problem in spherical coordinates $\mathbf{r} = (r, \theta, \phi)$. The general solution for a particle in a central potential is given by the product of angular and radial eigenfunctions $Y_l^m(\theta, \phi)$ and $R_l(k, r)$. Applying the partial-wave expansion to the scattering amplitude yields

$$f(\mathbf{k}', \mathbf{k}) = f(\theta) = \sum_{l=0}^{\infty} f_l(k) P_l(\cos \theta), \quad (1.5)$$

with P_l being the Legendre polynomial of order l , and f_l the corresponding partial wave amplitude. We subtract the incident plane wave from the general solution, both expanded

into plane waves. Imposing the regularity of the solution in the origin $r = 0$, we find that the partial wave amplitudes $f_l(k)$ are given by

$$f_l(k) = \frac{2l+1}{2ik} (e^{2i\eta_l(k)} - 1), \quad (1.6)$$

where $\eta_l(k)$ is the scattering phase shift of the l -th partial wave.

s-wave scattering length and effective range

In the limit of low energy scattering $k \rightarrow 0$, the only relevant term in the partial wave expansion is $l = 0$, the so-called s -wave. All higher partial waves are strongly suppressed for very low scattering energies due to the centrifugal barrier in the effective potential of the radial Schrödinger equation, as illustrated in Figure 1.4. Exploiting trigonometric identities, we can rewrite the s -wave scattering amplitude as

$$f_0(k) = \frac{1}{k \cot \eta_0(k) - ik}. \quad (1.7)$$

For arbitrary short-range potentials, we can apply the effective range expansion to the scattering phase shift [62]

$$k \cot \eta_0(k) \approx -\frac{1}{a} + \frac{1}{2} r_{\text{eff}} k^2, \quad (1.8)$$

where a is the s -wave scattering length and r_{eff} the effective range.

We can illustrate the physical meaning of the s -wave scattering length a by investigating the radial wave function in the far field. Here, the asymptotic wave function takes the form

$$\psi(\mathbf{r}) \propto_{k \rightarrow 0} \frac{r-a}{r}. \quad (1.9)$$

The, s -wave scattering length gives rise to a node in the radial wave function, which is real for $a > 0$ and virtual for $a < 0$. Thus we can interpret a as an effective hard sphere radius, leading to repulsive interaction for $a > 0$ and attractive for $a < 0$, as illustrated in Figure 1.3. The interpretation as effective hard sphere radius can also be seen from the scattering cross section σ that is fully determined by the s -wave scattering length, as we will derive in the next section.

The effective range cannot be interpreted in terms of an intuitive classical picture like for the scattering length. It is a measure for how the potential $V(r)$ influences the energy dependence of the cross section and it sets the upper bound for the low energy limit [62].

The scattering cross section

The differential cross section $d\sigma(\theta, \phi)/d\Omega = |f(\theta)|^2$ measures the probability that a particle is scattered into the solid angle $d\Omega$ around the angle θ . By integrating the differential cross section over all scattering angles we obtain the total scattering cross section, which determines the absolute likelihood of a scattering event. Since the contribution of higher

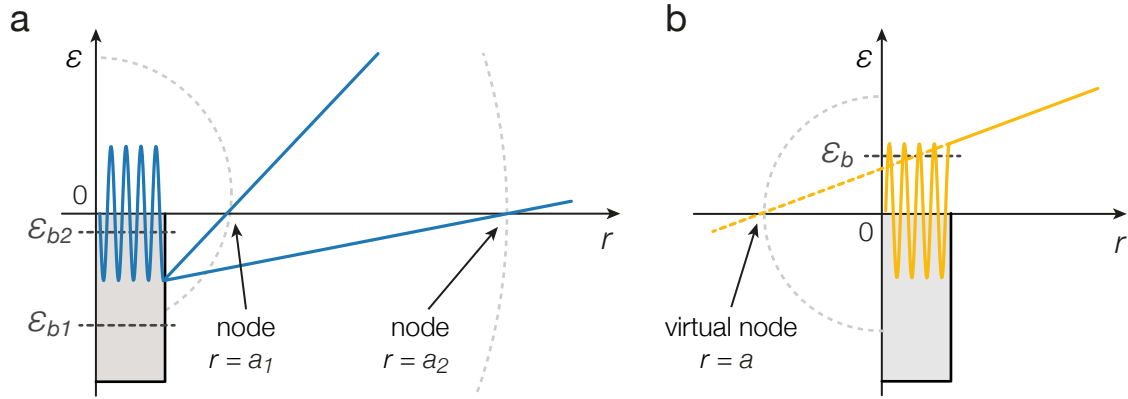


Figure 1.3 – Reduced radial wave function for continuum states ($\epsilon > 0$) in the limit $k \rightarrow 0$ on the example of a square well potential for (a) positive and (b) negative scattering length. A positive scattering length leads to a node in the wave function (1.9) at $r = a$, whereas a negative scattering length induces a virtual node at negative distances. The sign of the scattering length is determined by the position of the least-bound state in the potential. A real bound state ($\epsilon_B < 0$) causes a positive scattering length, whereas a virtual bound state ($\epsilon_B > 0$) leads to a negative scattering length. As the bound state energy approaches the continuum energy ($\epsilon_B \rightarrow 0$) the scattering length diverges. The dashed circles represent the effective size of the colliding atoms as hard spheres with radius a .

partial waves is negligible, we replace the total scattering cross section by the s -wave cross section

$$\sigma = 4\pi|f_0(k)|^2. \quad (1.10)$$

Applying the effective range expansion in $f_0(k)$ we arrive at

$$\sigma = 4\pi a^2 \left| \frac{1}{1 + k^2 a^2 (1 - r_{\text{eff}}/a)} \right|_{k \rightarrow 0} = 4\pi a^2. \quad (1.11)$$

The probability of a collision between two atoms is proportional to the area of a disc with radius a and thus increasing $|a|$ leads to a higher scattering probability. This result demonstrates once more the interpretation of a as an effective hard sphere radius.

So far, we have only discussed the case of elastic scattering. Yet, inelastic two-body processes are possible, e.g. part of the internal energy of the atoms is converted into kinetic energy. In the case of atoms in a trap, this process typically leads to a loss from the trap. We can account for such events by introducing an imaginary part into the scattering length $a = A + iB$ [63, 64]. In the limit of low energy scattering, this results in an elastic and inelastic s -wave cross section

$$\sigma_{\text{el}} = 4\pi(A^2 + B^2), \quad \sigma_{\text{inel}} = \frac{4\pi}{k}B. \quad (1.12)$$

1.1.2 The van der Waals potential

For an isotropic and short-range potential, we have seen that the interaction of two ultracold atoms can be reduced to a single parameter a , the s -wave scattering length. In

the following, we want to understand how the details of the actual molecular potential determine the value of a .

The molecular potential between two neutral atoms is governed at large distances by the van der Waals attraction, caused by induced dipole forces $\propto r^{-3}$. At short distances $r < r_c$, on the order of the of the atoms size, where the electron clouds are squeezed together, the repulsive exchange interaction dominates. We can model this type of interactions with an attractive r^{-6} tail at long distances and a repulsive hard core potential at short distances:

$$V(r) = \begin{cases} -C_6/r^6 & \text{for } r > r_c, \\ \infty & \text{for } r \leq r_c. \end{cases} \quad (1.13)$$

Here, $C_6 = V_0 r_c^6$ is the van der Waals coefficient with $V_0 = \hbar^2 k_c^2 / 2M$ the well depth at the boundary to the hard core. The potential can be neglected for distances $r \gg r_0$ where the zero point energy $\hbar^2 / 2M$ exceeds the potential energy $V(r_0)$ [62] (see Figure 1.4(a)). In this context, r_0 is conventionally called the van der Waals length

$$l_{\text{vdw}} = \frac{1}{2} \left(\frac{2MC_6}{\hbar} \right)^{1/4}. \quad (1.14)$$

As shown by Gribakin and Flambaum [65, 66], for any short range potential of the type C_n/r^n , there exists an analytic solution to the two-body problem (1.3). Based on the semi-classical WKB approximation, it is possible to relate the s -wave scattering length and effective range to the characteristic parameters of the potential. The WKB approximation assumes, that the solution of the Schrödinger equation is given by plane waves with a slowly varying complex phase Φ . In the lowest order of the WKB approximation, Φ is obtained by integration of the potential from the classical turning point r_c outwards [65]

$$\Phi = \frac{1}{\hbar} \int_{r_c}^{\infty} \sqrt{2M|V(r)|} dr = 2 \left(\frac{l_{\text{vdw}}}{r_c} \right)^2. \quad (1.15)$$

For the van der Waals potential, we find that the s -wave scattering length

$$a = \bar{a} [1 - \tan(\Phi - 3\pi/8)], \quad (1.16)$$

is given by two contributions: the background or mean scattering length $\bar{a} \simeq 0.956 l_{\text{vdw}}$, determined by asymptotic behaviour of the potential, and the resonant part influenced by the phase Φ and thus the short range behaviour of the potential. The small phase factor $3\pi/8$ is determined by the boundary condition at the turning point r_c . As illustrated in Figure 1.4(b), the mean scattering length shows a smooth behaviour as a function of the parameters of the potential, whereas the scattering length diverges and changes sign when the phase satisfies the condition $\Phi - 3\pi/8 = \pi/2 + \pi N_B$. These resonances in the scattering length are called shape resonances and they appear every time the potential can support a new bound state. The condition between the total number of bound states in the potential N_B and the occurrence of a new shape resonance is known as the Levinson's theorem [66].

The relation between the energy of the least-bound state and the scattering length can be derived by solving the radial Schrödinger equation for negative energies, i.e. inside the

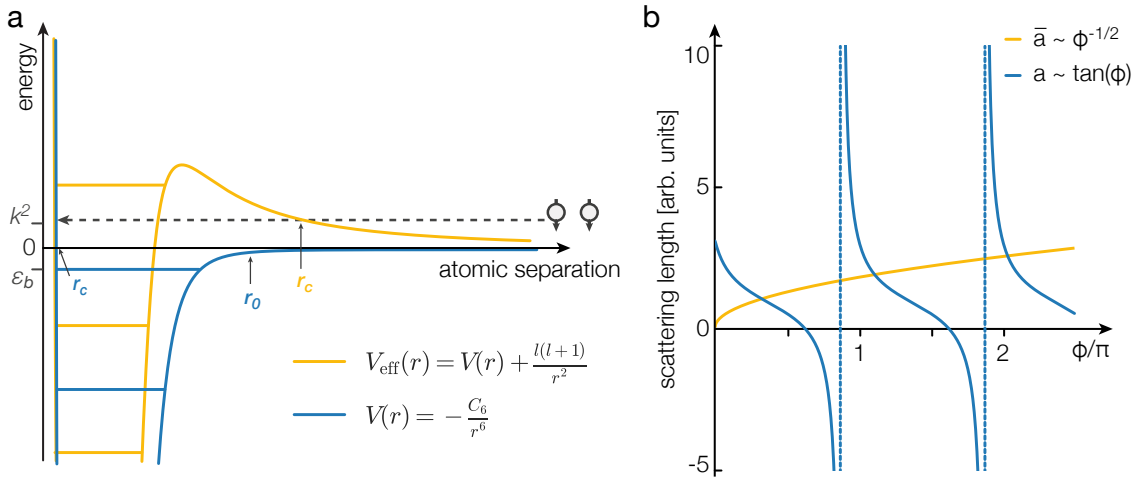


Figure 1.4 – (a) Molecular potentials with their bound state energies as a function of the interatomic separation. The blue line shows the van der Waals potential for zero angular momentum $l = 0$, the s -wave channel. The effective potential including the potential barrier for $l = 1$ (p -wave) is drawn in yellow. The classical turning point of each potential is marked by r_c . For low collision energies (black dashed line) the atoms are reflected on the centrifugal barrier at r_c and cannot enter the attractive part of the potential. In the s -wave channel the classical turning point r_c is given by the short-range part of the potential. (b) Dependence of the mean scattering length \bar{a} (yellow) and the scattering length a (blue) on the phase Φ . While the mean scattering length \bar{a} shows only a weak dependence on the parameters of the potential, the scattering length a diverges every time the potential can support a new bound state.

potential well. Taking into account the boundary conditions that the wave function inside and outside the well has to be smoothly connected, we find N_B bound states within the potential for $(N_B - 1/2)\pi < \Phi - 3/8 < (N_B + 1/2)\pi$. Close to the resonance, the energy of the least-bound state is given by

$$\sqrt{2M/\hbar^2 \epsilon_B} \approx \cot \Phi / \bar{a} \approx a^{-1}. \quad (1.17)$$

From this, we arrive at the famous relation that connects the scattering length to the energy of the least-bound state

$$\epsilon_B = -\frac{\hbar^2}{2Ma^2}. \quad (1.18)$$

A shallow bound state just below the continuum with $\epsilon_B < 0$ leads to a large and positive scattering length and thus a repulsive interaction. If the least-bound state is only virtually bound, i.e. possesses positive energy $\epsilon_B > 0$, the scattering length becomes negative, giving rise to attractive interactions.

The universal formula (1.18) is only valid in the vicinity of a resonance, where $a \gg \bar{a}$. Further away, higher order corrections due to the van der Waals potential have to be taken into account, leading to [67]

$$\epsilon_B = -\frac{\hbar^2}{2M(a - \bar{a}^2)} \left[1 + \frac{c_1 \bar{a}}{a - \bar{a}} + \frac{c_2 \bar{a}^2}{(a - \bar{a})^2} + \dots \right], \quad (1.19)$$

with $c_1 = \Gamma(1/4)^4 / 6\pi^2$ and $c_2 = (5/4)c_1^2 - 2$, where Γ denotes the Euler gamma function.

The effective range in the van der Waals can be expanded in orders of the mean scattering length

$$r_{\text{eff}} = 2.92\bar{a} \left(1 - 2\frac{\bar{a}}{a} + 2\left(\frac{\bar{a}}{a}\right)^2 \right), \quad (1.20)$$

By using the expression for the mean scattering length (1.16), we see that r_{eff} is constant with $\approx 2.97l_{\text{vdw}}$ in most cases and diverges as $a \rightarrow 0$. This result agrees with the exact quantum defect solution of Gao [68].

1.1.3 Interactions in a harmonic trap

In the previous section, we have treated binary collisions in free space. We have solved the scattering problem by investigating the asymptotic behaviour of the incident and outgoing plane waves. We showed that an elastic collision leads to a phase shift in the scattered wave, which is determined by the effective hard sphere radius of the atoms, the s -wave scattering length.

However, in experiments, atoms are usually confined to a finite volume by means of a trapping potential. The trap prohibits the construction of asymptotic scattering states and imposes a discrete energy spectrum on the atoms. The potential created by two crossed and focused Gaussian laser beams is well approximated by a 3D harmonic oscillator (see Section 2.3). The energy spectrum of an atom in this potential is simply given by the harmonic oscillator levels. In the following, we will investigate how the free-particle energy levels are modified for pairs of interacting atoms.

In order to simplify the mathematical treatment, we make two approximations. We assume, that the atoms are still further apart than the range of their interaction potential $nr_0^3 \ll 1$. Under this assumption, interactions can be modelled by a zero-range pseudopotential with a contact interaction strength proportional to the scattering length a , as introduced by Fermi [69]

$$V(r) = \frac{4\pi\hbar^2}{m} a \delta_{\text{reg}}(r). \quad (1.21)$$

Here, $\delta_{\text{reg}}(r) = \delta(r) \frac{\partial}{\partial r} r$ is the regularized delta function [70].

Furthermore, we restrict ourselves to the case of a three-dimensional isotropic harmonic oscillator ($\omega_x = \omega_y = \omega_z$). In the case of harmonic confinement, we can again separate the centre-of-mass motion and the relative motion of the atoms. We reduce the two-body problem to an effective one-body problem for the relative motion in the trap

$$\left(H_{\text{osc}} + \sqrt{2}\pi a_0 \delta(r) \frac{\partial}{\partial r} r \right) \psi(r) = E \psi(r), \quad (1.22)$$

where H_{osc} is the Hamiltonian of the harmonic oscillator of the relative motion. The interaction strength $a_0 = a/l_{\text{ho}}$ is parametrised in units of the harmonic oscillator length $l_{\text{ho}} = \sqrt{\hbar/(M\omega)}$ and the energy E in units of the harmonic oscillator energy $\hbar\omega$. This

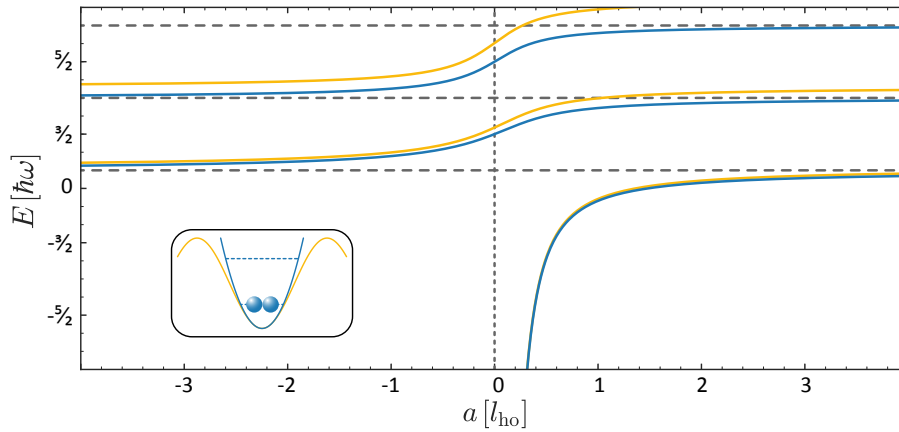


Figure 1.5 – Energy spectrum of two atoms in a three dimensional isotropic trap as a function of the interaction strength. The energy is parametrised by the harmonic oscillator spacing $\hbar\omega$, the scattering length by the harmonic oscillator length l_{ho} . The blue lines are the solutions for harmonic confinement (1.23) with the asymptotic behaviour $a \rightarrow \pm\infty$ marked by the gray dashed lines. The yellow lines are calculated for an anharmonic potential, here a lattice site around the minimum, expanded up to the 6th order. We use a lattice depth $V_0 = 30 E_r$, the value employed later in the clock-line spectroscopy experiments. The inset illustrates the difference between a harmonic potential and a lattice potential around one minimum.

model can be solved analytically, as shown by Busch et al. [71]. The energy E of two interacting atoms in a harmonic trap is given by [71]

$$\sqrt{2} \frac{\Gamma(-E/2 + 3/4)}{\Gamma(-E/2 + 1/4)} = \frac{1}{a_0}, \quad (1.23)$$

where Γ is the Euler gamma function.

The energy spectrum of the two-particle interacting states from (1.23) is represented in Figure 1.5. For $a = 0$, the two atoms are non-interacting and their energy is given by the unperturbed oscillator levels $E_n = (3/2 + 2n)\hbar\omega$ with n labelling the oscillator level. For repulsive interactions $a > 0$, the energy of the atom pair in the trap is raised compared to the non-interacting case. However, as $a \rightarrow \infty$ the energy is bounded from above by the next oscillator level. As the scattering length increases, the atoms repel each other as far as possible in order to minimize their interaction energy. This eventually leads to the appearance of a node in the relative wave function. Since the modulus of the wave function is identical to that of two identical fermions, this phenomenon is known as fermionization and happens for identical bosons [26, 72] as well as for distinguishable fermions [73]. The ground state of the system for both negative and positive scattering length is a bound state of the two atoms. Therefore, it has an energy lower than the non-interacting ground state, i.e. the lowest harmonic oscillator level. In free space the delta-like potential of Eq. (1.21) only supports a single bound state for positive scattering length. Here the bound state also exists for $a < 0$, where it is supported by the confining potential.

In section 2.3 we introduce optical lattices as a key ingredient for quantum simulation. In the following, we extend the model of two atoms in a harmonic trap to the case of

a sinusoidal lattice potential. A sinusoidal potential can be approximated by a harmonic potential around its minimum. We expand the potential in a Taylor series

$$V_{\text{lat}} = V_0 \sin^2(kx) \approx V_0(k^2x^2 + \frac{1}{3}k^4x^4 + \frac{2}{45}k^6x^6 + \dots). \quad (1.24)$$

The leading term is the harmonic one, whereas higher orders account for the anharmonicity of the actual sinusoidal potential. Owing to this anharmonicity, the centre-of-mass and relative motion are coupled. Therefore, we need to consider the Schrödinger equation for the full pair wave function $\psi(\mathbf{R}, \mathbf{r})$, where \mathbf{r} and \mathbf{R} are the relative and centre-of-mass coordinates of the atom pair, respectively. We can write:

$$\left(H_{\text{osc}}^{(\text{com})} + H_{\text{osc}}^{(\text{rel})} + \frac{4\pi\hbar}{M} \delta_{\text{reg}}(\mathbf{r}) + V_{\text{corr}}(\mathbf{R}, \mathbf{r}) \right) \psi(\mathbf{R}, \mathbf{r}) = E\psi(\mathbf{R}, \mathbf{r}), \quad (1.25)$$

where the harmonic term of the Taylor expansion is included in H_{osc} , whereas V_{corr} contains all higher orders. The Schrödinger equation is no longer separable; therefore, no analytic solution can be found. Deuretzbacher et al. have performed numerically exact diagonalization of the total Hamiltonian [74], in order to obtain the energy spectrum. We have calculated the corrections to the harmonic energy spectrum by including the effects of the anharmonicity by second order perturbation theory. Our results match very well the ones obtained by Deuretzbacher.

In Figure 1.5, the results obtained for a deep isotropic lattice are compared to the solution for a purely harmonic potential. The calculation is performed for a lattice depth of $V_0 = 30E_r$, the value employed for the interaction spectroscopy in chapter 4. As the pair energy increases, the anharmonic corrections become more substantial. This can be easily understood by considering the spatial extent of the corresponding state. With increasing scattering length, the atoms repel each other more strongly. Thus, they explore regions further away from the trap center and become more susceptible to the anharmonic character of the potential.

1.2 Feshbach resonances

In the previous section, we have seen that the actual value of the scattering length a is determined by the long-range behaviour of the underlying molecular potential. In particular, as the least-bound state approaches the free-particle continuum threshold, the scattering phase shift changes rapidly by π leading to a resonance in the scattering length. Therefore, it is highly desirable to gain control over the bound state energy and thus over the s-wave scattering length.

So far we have only discussed the scattering of atoms in a single channel, i.e. in the presence of one inter-atomic potential. However, the internal structure of the atoms can lead to the presence of several collision channels. For alkali atoms, these different channels are typically given by the spin singlet and triplet molecular potentials. A bound state in the energetically inaccessible potential can couple to the scattering continuum

and thus cause a scattering resonance. This phenomenon is called a Feshbach resonance in honor of Herman Feshbach, who developed a model to describe nuclear reactions based on this mechanism [75, 76]. Although the term Feshbach resonance is very common in the cold atom community, we owe the introduction of this concept in atomic physics to Ugo Fano [77].

In the following, we briefly introduce the molecular interaction potentials for alkali atoms with internal structure. We show that the hyperfine interaction couples the different potentials, and how their relative energies can be tuned by means of an external magnetic field. Based on this qualitative understanding, we present a coupled channel model, which allows to link the microscopic properties of the resonance to the scattering phase shift. Finally, we derive a simple expression for the magnetic field dependence of the scattering length. More details on the theory of resonant scattering in ultracold atoms can be found in [78–82], while a general review about the physics of Feshbach resonances is given in [9, 83].

1.2.1 Scattering of atoms with spin and hyperfine interaction

Let us consider a scattering process of two alkali atoms with electronic spin $S = 1/2$ in their ground state, which is typically a $^2S_{1/2}$ state with no orbital angular momentum $L = 0$. The combined molecular potential in its electronic ground state is a Σ potential with a rotational symmetry around the bond axis [84]. The total electronic spin $S = S_1 + S_2$ determines the symmetry of the molecular potential; whether the two spins are in a singlet $S = 0$ or triplet $S = 1$ configuration determines the bonding $^1\Sigma_g^+$ (denoted here by $V_s(r)$) and anti-bonding $^3\Sigma_u^+$ ($V_T(r)$) potentials, as depicted in Figure 1.6(a).

In the presence of a magnetic field, the two atoms experience a Zeeman energy shift dependent on total electron spin

$$V_{ZS} = 2\mu_B \mathbf{S} \cdot \mathbf{B}, \quad (1.26)$$

where μ_B is the Bohr magneton. Therefore, the triplet potential with $m_S = -1$ is shifted by a finite magnetic field to lower energies compared to the singlet potential with $m_S = 0$. This gives rise to a differential magnetic moment $\delta\mu \approx 2.8 \text{ MHz/G}$ between the two potentials for $S = 1/2$. The triplet potential is called *open channel*, since atoms can enter and leave in this channel. The singlet potential is referred to as *closed channel*, because its asymptote is shifted by $\delta\mu B$ and atoms in the low energy limit cannot enter it. Furthermore, a bound state in the closed channel can hence be brought into resonance with the continuum energy of the scattering atoms.

Alkali atoms also possess a nuclear spin \mathbf{I} , which in turn is coupled for each atom individually to the electronic spin via hyperfine interactions

$$V_{\text{HF}} = \alpha_{\text{HF}}/\hbar^2 \mathbf{S}_i \cdot \mathbf{I}_i \quad (1.27)$$

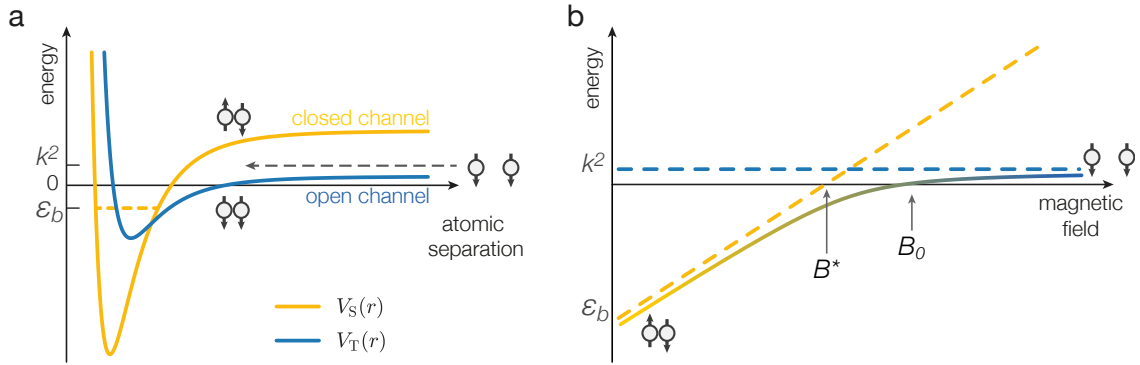


Figure 1.6 – (a) Schematic drawing of a simple two channel model for the occurrence of a Feshbach resonance in the presence of a finite magnetic field. Both potentials are caused by the same van der Waals interaction. They differ strongly at short distances, where the atoms are allowed on top of each other in the singlet potential, thus giving rise to a deeper attractive well and more bound states. The triplet potential is open for s -wave collisions, whereas the singlet is closed since its asymptote is shifted by $\delta\mu B$. The coupling of the molecular bound state ϵ_b in the closed channel to the free atoms is created by the hyperfine interaction. (b) Energies of the bare bound state (yellow dashed lines) and the free particle state (blue dashed line), as well as the dressed states (solid line) as a function of an external magnetic field. The bare bound state ϵ_b in the closed channel (yellow) crosses the dissociation threshold at B^* . The Feshbach resonance appears where the dressed state crosses the dissociation threshold and is shifted due to the coupling to B_0 .

with α_{HF} being the hyperfine structure constant and $i = 1, 2$ for the two atoms. For an atom pair, we can now write down the total hyperfine interaction in the following form $V_{\text{HF}} = V_{\text{HF}}^+ + V_{\text{HF}}^-$, with the two contributions [62]

$$V_{\text{HF}}^{\pm} = \frac{\alpha_{\text{HF}}}{2\hbar^2} (\mathbf{S}_1 \pm \mathbf{S}_2)(\mathbf{I}_1 \pm \mathbf{I}_2). \quad (1.28)$$

While V_{HF}^+ conserves the total electronic spin \mathbf{S} , the part V_{HF}^- converts a singlet state into a triplet and thus induces an off diagonal coupling between the two potentials. Due to this coupling, the bare triplet and singlet scattering states become dressed and the scattering phase in the open channel can be influenced by a resonant bound state in the closed channel.

In conclusion, we can identify three essential ingredients that are required for the appearance of a magnetic Feshbach resonance: (i) two possible collision channels, an open and a closed one, (ii) a coupling between the two channels and (iii) a differential magnetic moment allowing for a tuning of their relative energies.

1.2.2 Coupled channel approach

The physics of Feshbach resonances within the regime of dominant two-body collisions can be well described by a model of only two coupled scattering channels [78, 83, 85]. The two orthogonal scattering channels are labelled open $|o\rangle$ and closed $|c\rangle$, depending on whether their asymptotic values are energetically accessible for the free atoms. In the case of alkali atoms these channels are given by the spin singlet $|s\rangle$ (triplet $|t\rangle$) configuration of

the total angular momentum. Here we find $|o\rangle = |t\rangle|\psi_o\rangle$ and $|c\rangle = |s\rangle|\psi_c\rangle$, where $|\psi_{o,c}\rangle$ is the relative radial wave function in the corresponding channel. The coupling between the two channels leads to the emergence of dressed energy states composed of the initially uncoupled channels $|o\rangle$ and $|c\rangle$. The strength of the mixing between the two channels is determined by a set of coupled Schrödinger equations

$$\begin{aligned} H_o|o\rangle + W|c\rangle &= E|o\rangle, \\ W|o\rangle + H_c|c\rangle &= E|c\rangle. \end{aligned} \quad (1.29)$$

Here, the off-diagonal element W is composed of all interactions that induce a coupling of the two channels. The two single-channel Hamiltonians $H_{o,c}$ are given by the kinetic and potential energy in the respective uncoupled channels. We have set the energy scale such that the dissociation threshold in the open channel is zero.

The closed channel Hamiltonian incorporates the magnetic field dependence of the total system and experiences a shift of $\delta\mu B$ with respect to the open channel. Furthermore, it supports a bound state close to the dissociation threshold

$$H_c(B)|b\rangle = \epsilon_b(B)|b\rangle, \quad (1.30)$$

where $|b\rangle = |s\rangle|\psi_b\rangle$ is the bare Feshbach resonance state and $\epsilon_b(B) = \delta\mu(B - B^*)$ its energy, which crosses the dissociation threshold at the magnetic field B^* [85].

In order to solve the set of coupled Schrödinger equations, we introduce the dressed continuum states based to the relative momentum \mathbf{k} of the free atom pair with the spin configuration of the open channel. Their asymptotic behaviour is similar to the ansatz (1.4) for the single channel scattering. The open channel component $|\psi_{\mathbf{k}}^o\rangle$ is given for large separation by a superposition of an ingoing plane wave $|\psi_{\mathbf{k}}^+\rangle$ and an outgoing spherical wave $|\psi_{\mathbf{k}}^-\rangle$. The closed channel component $|\psi_{\mathbf{k}}^c\rangle$ decays exponentially outside of the potential well. Using the Green's function $G_{o,c}$, which solves the corresponding unperturbed Hamiltonian, we can rewrite the coupled Schrödinger equation as

$$\begin{aligned} |\psi_{\mathbf{k}}^o\rangle &= |\psi_{\mathbf{k}}^+\rangle + G_o(E + i0)W|\psi_{\mathbf{k}}^c\rangle, \\ |\psi_{\mathbf{k}}^c\rangle &= G_c(B, E)W|\psi_{\mathbf{k}}^o\rangle, \end{aligned} \quad (1.31)$$

where we have made the energy $E + i0$ imaginary by an infinitesimal amount. The detailed calculation of the scattering amplitude of the open channel scattering wave function is presented in [83]. In the low energy limit $k \rightarrow 0$, we derive the dependence of the s -wave scattering length in the open channel on the magnetic field [85]

$$a(B) = a_{bg} \left(1 - \frac{\Delta_B}{B - B_0} \right). \quad (1.32)$$

Here, a_{bg} is the so-called background scattering length, given by the scattering length in the unperturbed open channel. The width of the resonance Δ_B measures the distance from the singularity to the zero crossing of the scattering length

$$\Delta_B = \frac{m(2\pi\hbar^3)}{4\pi\hbar^2 a_{bg} \delta\mu} |\langle \psi_b | W | \psi_{k=0}^+ \rangle|^2 \quad (1.33)$$

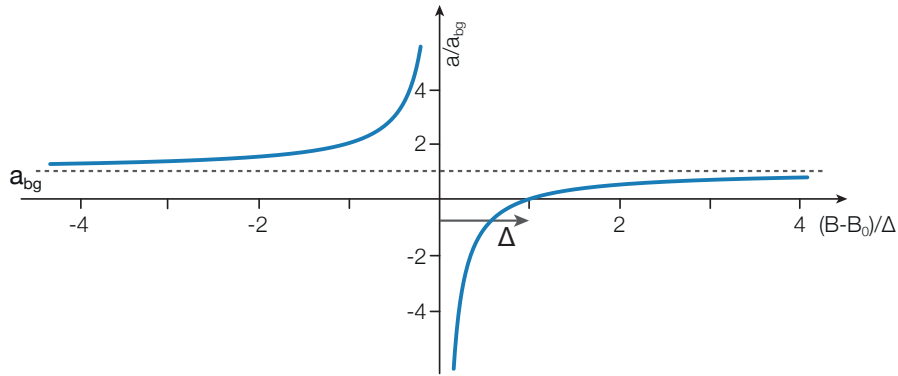


Figure 1.7 – Magnetic field dependence of the s -wave scattering length a around a Feshbach resonance. The magnetic field where the scattering length diverges $a \rightarrow \pm\infty$ is called the resonance position B_0 . The width of the resonance Δ measures the distance of the zero crossing of the scattering length to the singularity. Far away from the resonance, the s -wave scattering length approaches the background value a_{bg} which is determined by the asymptotic behaviour of the open channel potential.

and is determined by the coupling strength of the continuum state to the bound state in the closed channel. The position of the Feshbach resonance B_0 is shifted from the crossing of the bare bound state B^* by

$$B_0 - B^* = \langle \psi_b | W G_0(E=0) W | \psi_b \rangle / \delta\mu. \quad (1.34)$$

The resonance shift $B_0 - B^*$ is determined by the admixture of the closed-channel bound state to the scattering state. Including precise molecular potentials and van der Waals coefficients into the coupled-channel calculation allows for *ab initio* predictions for the position B_0 of Feshbach resonances. This proved very successful, leading to the experimental observation of many resonances after they were predicted theoretically [86–90].

In the unperturbed closed channel the bound state $|b\rangle$ is usually tightly bound and therefore stable. However due to the inter channel coupling it experiences a decay rate proportional to the coupling strength. In order to account for the decay of the bound state and thus the limited lifetime of the scattering state, we insert an additional imaginary part into Eq (1.32) [63, 64]:

$$\tilde{a} = a - ib = a_{\text{bg}} \left(1 + \frac{\Gamma_0}{-E_0 + i(\gamma/2)} \right), \quad (1.35)$$

with the decay rate γ/\hbar . Here, we have introduced the width in energy $\Gamma_0 = \delta\mu\Delta_B$ and the bound state energy $E_0 = \delta\mu(B - B_0)$ close to the resonance. For $\gamma = 0$, Eq. (1.35) takes again the form of Eq (1.32). However, the representation as an imaginary scattering length in Eq. (1.35) offers the advantage that it can also model the behaviour of an optical Feshbach resonance, as we will discuss in the next section.

1.2.3 Classification of Feshbach resonances

Feshbach resonances appear for all alkali atoms, for bosonic as well as for fermionic isotopes. In order to allow for a comparison among the different systems, Chin et al. have introduced the dimensionless resonance strength parameter s_{res} , as follows [9]

$$s_{\text{res}} = r_{\text{bg}} \frac{\Gamma_0}{\bar{E}} = \frac{a_{\text{bg}}}{\bar{a}} \frac{\delta\mu\Delta_B}{\bar{E}}, \quad (1.36)$$

with the dimensionless background scattering length $r_{\text{bg}} = a_{\text{bg}}/\bar{a}$.

This parameter classifies the resonances based to the resonance strength $a_{\text{bg}}\Gamma_0$ and compares it to the mean scattering length \bar{a} of the underlying van der Waals potential (1.16) and its corresponding energy $\bar{E} = \hbar^2(2M\bar{a}^2)$. As s_{res} is always positive, resonances are classified by the two limiting cases $s_{\text{res}} \gtrless 1$.

Resonances with a large strength parameter $s_{\text{res}} \gg 1$ are called entrance or *open-channel dominated*. As $s_{\text{res}} \gg 1$ usually stems from a large Δ_B (up to a few hundred Gauss [9]), they are also referred to as *broad resonances*. In this case, the bound state in the dressed scattering state preserves the initial spin character of the open channel over a wide range of Δ_B and its energy follows, in this regime, the universal formula (1.18). Due to the weak coupling of the metastable bound state in the closed channel to the scattering state, these resonances have shown a very low loss rate γ .

Resonances with a weak strength $s_{\text{res}} \ll 1$ and thus a narrow width Δ_B are called *closed-channel dominated* or *narrow resonances*. Here, the closed channel bound state dominates over a wide magnetic field range the character of the scattering state and only close to B_0 a universal bound state is found. Since the atoms effectively spend a long time in the closed channel they are strongly susceptible to the decay γ of the bound state and thus experience a strong decay into lower lying states. This leads to a gain in kinetic energy during the collision and hence atoms escaping from a trap.

1.2.4 Optical Feshbach resonances

Magnetic Feshbach resonances allow a global tuning of the scattering length via an external uniform magnetic field. The idea to control the value and the sign of the scattering length with a nearly resonant light field and thus gaining local, i.e. spatially resolved control, was first proposed by Fedichev et al. [91]. Here, the light couples a bound state in the excited molecular potential to the two colliding ground state atoms. Tuning the light frequency ν across the resonance, the free atoms become dressed with the bound state in the excited potential and thus the scattering length is modified. Owing to the strong radiative decay in the excited state, the bound state has a limited lifetime and the scattering length becomes complex [64]. Another limitation is the possibility of photoassociation, where the atoms absorb a photon, decay to deeply bound states and are subsequently lost. Although optical Feshbach resonances have been observed [92] and their ability to locally influence the scattering length has been demonstrated [93], they are always accompanied by strong atom loss restricting their experimental application.

Compared to alkali atoms, AEL atoms offer narrow transitions with long-lived excited states, which have been proposed to allow for large changes of the scattering length through the associated optical Feshbach resonances, while limiting atom losses [94]. For ytterbium [95] as well as strontium [96] the ground state scattering length has been modified by coupling the atoms on the intercombination line to the 3P_1 state. Even though beneficial ratios of coupling strength to decay rate Γ_0/γ compared to alkali atoms could be reached, the lifetimes were still limited to a few milliseconds [95, 96].

1.2.5 Experimental investigation of Feshbach resonances

The various experimental techniques to identify and characterize the magnetic field dependence of Feshbach resonances can be grouped according to three different approaches [9]: (i) inelastic loss spectroscopy, (ii) measurements of the elastic cross section and (iii) determination of the dimer binding energy.

The most frequently employed technique to determine the position of a Feshbach resonance is the observation of trap losses. The two major processes are inelastic two-body collisions and three-body recombination. In the vicinity of a resonance, both processes are enhanced. The two-body decay is caused by the divergent imaginary part (1.35) of the scattering length [97]. As the scattering length near a Feshbach resonance diverges, the gas leaves the regime of binary collisions. When three atoms interact, they can form a diatomic molecule and a free atom, where the binding energy is released as kinetic energy. For two atoms this process is forbidden due to momentum conservation. This process is known as three-body recombination. For typical molecular binding energies, all three atoms are lost from the trap. Since the three-body cross section scales with the scattering length as a^4 it is the dominant process near a Feshbach resonance. The first Feshbach resonance in ultracold atoms was identified in this way [98]. However, this technique is only suited to identify the position of the resonance and map out the imaginary part of the scattering length near the resonance. Furthermore, the three-body recombination is suppressed in a two-component Fermi gas.

The elastic scattering cross section is determined by the modulus of the s -wave scattering length. Therefore, it is suited to determine the position as well as the zero crossing of the resonance. It can be measured via the efficiency of evaporation [99, 100], the thermalisation of an out of equilibrium state [101–103] or the dephasing of trap oscillations [104]. By carefully calibrating densities and temperatures of the trapped atoms, these measurements even provide the exact value of the scattering length at a given magnetic field.

The most precise determination of the scattering properties near a Feshbach resonance can be achieved via radio-frequency spectroscopy [90, 105, 106]. Here, Feshbach molecules are prepared and afterwards dissociated on the bound-to-free transition. This allows a precise determination of the dimer binding energy and thereby the s -wave scattering length.

Ytterbium – an alkaline-earth-like atom

A large variety of elements with a common electronic structure is referred to as alkaline-earth-like (AEL). Additional to a set of completely filled inner shells, these atoms possess two outer s -shell electrons. In contrast, alkali atoms have only one valence electron. We find this electronic configuration for all alkaline earth elements, i.e. beryllium, magnesium, calcium, strontium, barium and radium. Further, this electronic configuration is displayed by some transition metals from the d -block and f -block of the periodic table, namely zinc, cadmium, mercury, ytterbium and nobelium.

The two s -shell electrons give rise to a helium-like electronic level structure, where orbitals are grouped depending on the alignment of the electronic spins. Two manifolds exist: the spin singlet with a total electronic spin $S = 0$ and the spin triplet manifold with a total electronic spin $S = 1$. Within the singlet manifold we find strong optical transitions, which are well-suited for laser cooling. Optical transitions connecting the two manifolds are forbidden since they involve a spin flip ($\Delta S = 1$). Therefore, they are generally more narrow with natural linewidths ranging from several kilohertz down to sub-millihertz. As a consequence, the corresponding excited states in the triplet manifold are metastable with lifetimes up to hundreds of seconds. The ground state of all AEL atoms possesses neither electronic spin $S = 0$ nor orbital angular momentum $L = 0$, giving rise to a total electronic angular momentum $J = 0$. In this state, the nuclear and electronic degrees of freedom are highly decoupled. In the fermionic isotopes, exhibiting a finite nuclear spin, an enhanced $SU(N)$ symmetry emerges.

In the following chapter, we will discuss the aforementioned distinctive properties of AEL on the example of ytterbium. First, we give a short introduction of the physical properties of ytterbium. Then, we emphasise the difference in how alkali and AEL atoms interact with each other and study the emergence of $SU(N)$ symmetric interactions for AEL atoms. Afterwards, we will review the electronic level structure. Here, we focus on the forbidden transitions between the singlet and triplet manifold and discuss why they are actually weakly allowed. Later, we present possibilities for creating state-dependent optical potentials and their application for quantum simulation. We discuss the feasibility of studying the $SU(N)$ Heisenberg model and the Kondo lattice model

Ytterbium

Ytterbium (Yb) is a lanthanide and thus a member of the rare-earth elements with an atomic number $Z = 70$. The configuration of the 70 electrons is based on the noble gas xenon with additionally the 4f- and 6s-shells completely filled $[\text{Xe}] 4f^{14} 6s^2$. The electronic properties are therefore determined by the two $6s^2$ valence electrons.

Like all rare-earth elements, ytterbium possesses a large number of isotopes, with a total number of seven stable isotopes. Among these are five bosonic isotope ^{168}Yb , ^{170}Yb , ^{172}Yb , ^{174}Yb and ^{176}Yb as well as two fermionic isotopes ^{171}Yb and ^{173}Yb . Due to the high natural abundance of bosonic and fermionic isotopes, no specially enriched samples are needed for the production of either quantum gases. This makes Ytterbium a unique candidate for the creation of Bose-Bose, Bose-Fermi and Fermi-Fermi mixtures composed of the same element.

For all AEL atoms, the nucleus of the bosonic isotopes is composed from an even number of protons and neutrons. In this so-called gg-nucleus, all the individual spins couple to a total nuclear spin of zero $I = 0$. Therefore, the total spin $F = J + I = 0$ of the 1S_0 ground state vanishes for all bosonic isotopes.

The fermionic isotopes possess a half integer nuclear spin of $I = 1/2$ and $I = 5/2$ for ^{171}Yb and ^{173}Yb , respectively. For the 1S_0 and 3P_0 state, interatomic interactions are $SU(N)$ -symmetric, owing to the decoupling between the nuclear and orbital degree of freedom. Here, $N \leq 2I + 1$ can be as large as $N = 6$ in the case of ^{173}Yb .

2.1 $SU(N)$ symmetric two-orbital interactions

For alkali atoms, we have studied the scattering process on the example of a pair of spin-1/2 atoms. There, we demonstrated how the hyperfine interaction couples different scattering channels and gives rise to Feshbach resonances.

However, for AEL atoms with large nuclear spin, we have to extend our scattering model beyond the spin-1/2 case. Furthermore, we find the nuclear and electronic degrees of freedom strongly decoupled for states with $J = 0$. In the following, we will demonstrate how this decoupling causes the emergence of $SU(N)$ symmetry and discuss the implications of this extended symmetry on the interactions of AEL atoms. We restrict our description to the interaction of fermions since the bosonic isotopes of AEL atoms possess neither electronic nor nuclear spin, resulting in a single uncoupled inter-atomic potential that determines the scattering length.

2.1.1 Interactions for high spin fermions

The Hamiltonian of a free fermion with total angular momentum $F = 1/2, 3/2, 5/2, \dots$ is symmetric under three-dimensional rotation and possesses therefore a $SU(2)$ symmetry. As we have seen previously, the singlet and triplet interaction potentials between two alkali atoms do not break this symmetry and the individual F and m_F of the atoms are still

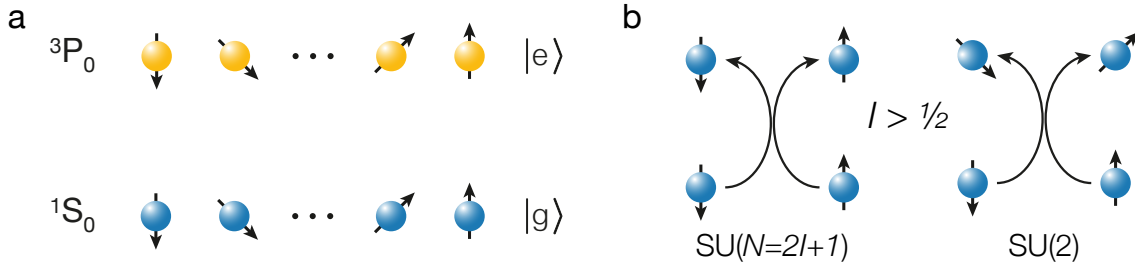


Figure 2.1 – (a) Illustration of fermionic AEL atoms with orbital and nuclear spin degree of freedom. The two orbitals exhibiting $SU(N)$ symmetric interactions are given by the two $J = 0$ states, the ground state $|g\rangle = {}^1S_0$ (blue) and the lowest energy triplet state $|e\rangle = {}^3P_0$ (yellow). A nuclear spin $I > 1/2$ and thus $SU(N > 2)$ symmetric interactions within each orbital are found in ${}^9\text{Be}$, ${}^{135,137}\text{Ba}$, ${}^{201}\text{Hg}$ with $I = 3/2$, ${}^{25}\text{Mg}$, ${}^{67}\text{Zn}$, ${}^{173}\text{Yb}$ with $I = 5/2$, ${}^{43}\text{Ca}$ with $I = 7/2$ and ${}^{87}\text{Sr}$ with $I = 9/2$. (b) Elastic scattering of high spin fermions $I > 1/2$. For AEL atoms with $SU(N = 2I + 1)$ symmetry (left) the individual projection of the spin is conserved. For alkali atoms with $SU(2)$ symmetry (right) only the pair projection is conserved.

good quantum numbers. However, at short distances, the hyperfine interaction leads to a mixing of the two interaction channels and breaks this symmetry. For collisions without relative angular momentum (s -wave scattering), only the total angular momentum of the pair F_{pair} and its projection $m_{F_{\text{pair}}}$ are conserved, creating a new $SU(2)$ symmetry. This implies for high-spin Fermions with $F > 1/2$, atoms can leave the collision with an angular momentum that differs from the initial one. Therefore the zero-range pseudo-potential (1.21) needs to be generalized in the following form [107]

$$V(r) = \frac{4\pi\hbar^2}{m} \sum_{F_{\text{pair}}=0,2,\dots}^{2F-1} a_{F_{\text{pair}}} \mathcal{P}_{F_{\text{pair}}} \delta(r), \quad (2.1)$$

where $\mathcal{P}_{F_{\text{pair}}}$ is the projector on states with even total spin. The condition of an even F_{pair} ensures an anti-symmetric spin wave function and thus an anti-symmetric total wave function, because the radial part is symmetric in the case of s -wave collisions. In order to account for all possible collision channels in (2.1), a single scattering length does not suffice. In total $(2F + 1)/2$ scattering lengths $a_{F_{\text{pair}}}$ are needed. These can vary drastically with the position of the last bound state in the corresponding molecular potential. The diverse scattering lengths among the atoms with same F but different m_F give rise to spin changing collisions [108, 109].

2.1.2 Emergence of $SU(N)$ symmetry in AEL atoms

For AEL atoms for states with vanishing electronic angular momentum $J = 0$ we find a starkly different situation. Here, the total angular momentum is exclusively determined by the nuclear spin $F = J + I = I$ and nuclear and electronic degrees of freedom are decoupled. Investigating the intraorbital collision between two atoms in either the 1S_0 ground or the 3P_0 metastable state, we find that both electronic orbitals give rise to only a single collision channel. The splitting into singlet and triplet collision channels for alkali atoms

is caused by the exchange interaction between the electron clouds. However, for $J = 0$ the only possible combination is a molecular potential with again vanishing total angular momentum. Due to the lack of hyperfine interactions the single collision channel remains independent of the nuclear spin for the fermionic isotopes. Therefore not only the pair momentum F_{pair} and its projection $m_{F_{\text{pair}}}$ are conserved but also the individual F and m_F of the colliding atoms are still good quantum numbers.

In this cases, we find all scattering lengths $a_{F_{\text{pair}}}$ to be equal. This reduces the interaction potential (2.1) back to the previously introduced form of Eq. (1.21), i.e. a single scattering length for all pairs, whereas the symmetry of the system is extended to $SU(N = 2F + 1)$. This means that the total Hamiltonian of the interacting system commutes with all spin-permutation operators [38, 39].

For the seven stable isotopes of ytterbium the entire set of intra- and inter-isotope ground state scattering length has been reported by the Kyoto group [110]. The intra-isotope scattering lengths have been obtained by two-color photoassociation spectroscopy on the $^1S_0 \rightarrow ^3P_1$ transition. In ^{173}Yb , the 1S_0 - 1S_0 scattering length, denoted a_{gg} has been determined to be $199.4 a_0$.

In order to estimate the residual variation of the scattering length with the different nuclear spin components $\delta a/a$, we recall the definition of the scattering length in the van der Waals potential (1.16). The scattering length is determined by the phase Φ (1.15) the atoms acquire in the molecular potential. Thus a variation in the scattering length δa is induced by a difference in the phase $\delta\Phi$. We can rewrite (1.15) as a time integral over a classical trajectory $r(t)$ in the molecular potential $V(r)$ [38]. The different nuclear spin projections can only influence the phase during the time Δt the atoms spend inside the short-range part of the potential. We estimate the relative variation by $\delta a/a \sim \delta\Phi \sim \Delta t \delta V/h$, where δV is the energy difference in the interaction potentials for the various spin projections. This difference is mainly caused by the lowest lying state with hyperfine splitting, the 3P_1 state. Since the 3P_0 state is the closest to the 3P_1 , we expect a stronger variation here. As the hyperfine splitting reduces towards the lighter AEL elements, ytterbium shows the largest variation of the scattering length. The residual variation $\delta a/a$ is predicted to be smaller than 10^{-8} for collisions in the 1S_0 state and 10^{-2} for the 3P_0 state [38].

We have obtained an experimental upper bound for the variation of the scattering length among the six different spin components for ^{173}Yb in both the 1S_0 and 3P_0 state. By measuring the absence of spin relaxation in a two component Fermi gas kept in an harmonic trap for up to 15 s, we can report an upper limit of $\delta a_{\text{gg}}/a_{\text{gg}} < 10^{-4}$ in the 1S_0 state [60]. The variation of the scattering length in the 3P_0 state was determined by clock-line spectroscopy. Here we can give an upper bound of $\delta a_{\text{ee}}/a_{\text{ee}} < 10^{-2}$ [60]. The strong suppression of spin changing collisions allows to prepare any mixture composed out of the six possible spin states without depolarisation.

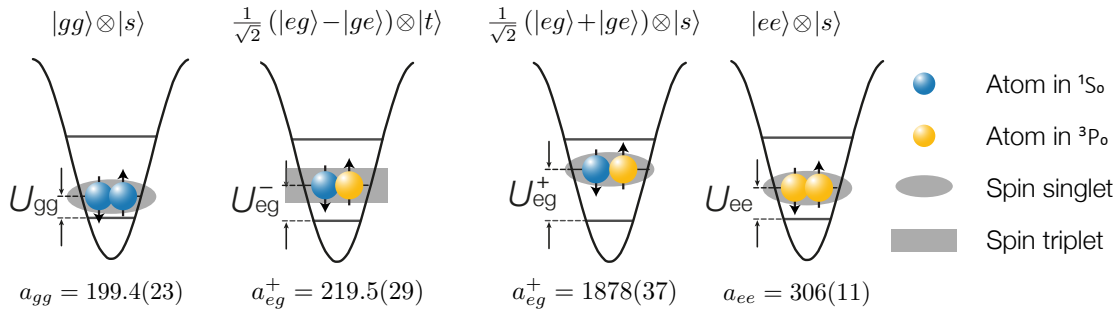


Figure 2.2 – Schematic drawing of the four possible interaction states and their corresponding energies of an AEL atom with orbital and nuclear spin degree of freedom in a harmonic trap or on a lattice site. The energy U_{XX} measures the energy of an interacting atom pair compared to two non-interacting atoms in a harmonic oscillator. Here, only repulsive interaction energies $U_{XX} > 0$ are drawn. In the bottom, the corresponding scattering lengths for ^{173}Yb are displayed. They are reported in Refs. [56, 59, 110].

2.1.3 Two-orbital $SU(N)$ -symmetric interactions

Let us now consider collision between fermionic AEL atoms with orbital and nuclear spin degree of freedom. We focus on collisions between the two $J = 0$ states, the ground 1S_0 (denoted $|g\rangle$) and the metastable state 3P_0 ($|e\rangle$). Both orbitals possess $SU(N)$ symmetry and their intraorbital interactions are fully characterised by a single scattering channel $|gg\rangle|s\rangle$ and $|ee\rangle|s\rangle$, respectively. For s -wave collisions, the radial and orbital part of the wave function are symmetric, enforcing an anti-symmetric combination (singlet) in the nuclear spin $|s\rangle = 1/\sqrt{2}(|\uparrow\downarrow\rangle - |\downarrow\uparrow\rangle)$.

For interorbital collisions both degrees of freedom can either be symmetric or anti-symmetric, while ensuring antisymmetry of the total wave function under particle exchange. Due to the $SU(N)$ symmetry only a total of four scattering channels is required to describe all possible combinations

$$\begin{aligned} |gg\rangle &= |gg\rangle \otimes |s\rangle, & |eg^+\rangle &= (|eg\rangle + |ge\rangle)/\sqrt{2} \otimes |s\rangle, \\ |ee\rangle &= |ee\rangle \otimes |s\rangle, & |eg^-\rangle &= (|eg\rangle - |ge\rangle)/\sqrt{2} \otimes |t\rangle, \end{aligned} \quad (2.2)$$

with the nuclear spin triplet state $|t\rangle = \{|\uparrow\uparrow\rangle, 1/\sqrt{2}(|\uparrow\downarrow\rangle + |\downarrow\uparrow\rangle), |\downarrow\downarrow\rangle\}$.

In analogy to (2.1), we generalise the pseudo-potential (1.21) to the case of two orbital interactions

$$V(r) = \frac{4\pi\hbar^2}{m} \delta(r) \sum_X a_X \mathcal{P}_X. \quad (2.3)$$

Here X denotes the four possible scattering channels $|gg\rangle$, $|eg^+\rangle$, $|eg^-\rangle$ and $|ee\rangle$ with their corresponding scattering lengths a_{gg} , a_{eg}^+ , a_{eg}^- and a_{ee} . \mathcal{P}_X is the projector onto these states.

As we have seen in section 1.1.3, the interaction energy of two atoms in a harmonic trap depends on the scattering length. Therefore, the four intra- and interorbital scattering lengths give rise to different interaction energies. Figure 2.2 illustrates the four possible interaction states in a harmonic trap with the corresponding interaction energies U_X , given

by (1.23). A difference in the scattering length a_{eg}^+ and a_{eg}^- causes an energy offset between the orbital singlet and triplet state. This energy difference is called exchange energy, in analogy to the energy splitting between the spin singlet and triplet scattering channel in alkali atoms with $SU(2)$ symmetry.

We have obtained the values of the interorbital scattering lengths a_{eg}^+ and a_{eg}^- via clock-line spectroscopy on a two component Fermi gas in a three-dimensional lattice [56, 59]. In order to demonstrate the $SU(N)$ symmetry of interorbital interaction, we repeated the measurements with various two component spin mixtures. Within our experimental precision we extracted the same interaction shift at zero magnetic field for the various spin mixtures. As an upper bound for the variation we extract $\delta a_{\text{eg}}/a_{\text{eg}} < 10^{-2}$. The values of the interorbital scattering lengths are presented at the bottom of Figure 2.2.

2.2 Electronic structure and optical transitions

After the investigation of the peculiar scattering properties of AEL atoms, we turn our attention to the second distinct feature of AEL atoms, metastable excited states. In the following, we explain the mechanism causing the long lifetimes of certain excited state as well as the narrow linewidth of the clock transition.

For all AEL atoms, ranging from Mg ($Z = 12$) up to Hg ($Z = 80$), the two valence electrons are in the intermediate coupling regime. Yet, the total angular momentum $\mathbf{J} = \mathbf{S} + \mathbf{L}$ is still a fairly good quantum number. Thus, we can label the states in the Russell-Saunders notation $^{2S+1}L_J$, where S is the total spin of the electrons and L the orbital angular momentum [111]. Here, the LS -coupling is able to produce an adequate description of the level structure. However, the corresponding selection rules for optical dipole transitions are violated with increasing Z .

2.2.1 Level structure of ytterbium

The ground state of the two $6s^2$ electrons in ytterbium is the spin singlet state 1S_0 . In this state the two electron spins align anti-parallel with $S = 0$ and possess no orbital angular momentum $L = 0$. This leads to a vanishing total angular momentum $J = 0$ and the complete absence of a hyperfine structure. The next higher-lying states have the structure $6s6p$ with one of the electrons excited to the p -orbital. For this configuration, we find one state in the spin singlet manifold 1P_1 and three states 3P_0 , 3P_1 , and 3P_2 in the spin triplet manifold, where the two electron spins align parallel $S = 1$. Here, the 3P_0 is the excited state with the lowest energy and again has no angular momentum $J = 0$. In the fermionic isotopes, the P states with $J \neq 0$ exhibit a hyperfine structure due to the coupling of J and I .

Within each of the two electronic manifolds we find strong dipole allowed transitions. In our experiment, we employ the broad $^1S_0 \rightarrow ^1P_1$ transition with a linewidth of 29 MHz

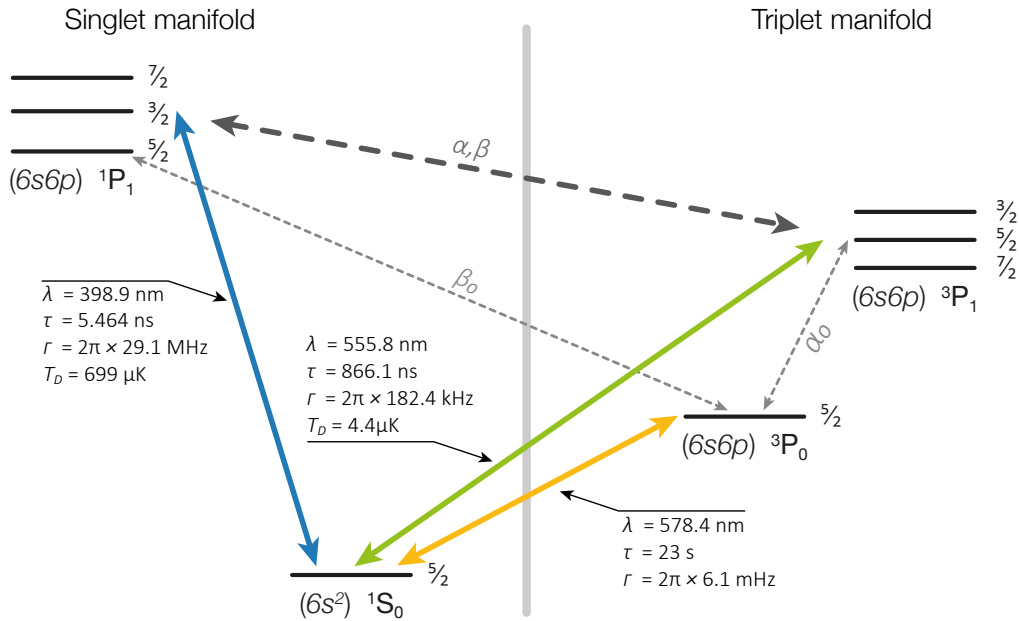


Figure 2.3 – Level diagram for the electronic and hyperfine structure of ^{173}Yb . The spacing between the electronic orbitals and the hyperfine levels is not to scale. The diagram is restricted to the relevant levels in the context of this work. The coloured arrows illustrate optical transitions between different orbitals. The characteristic properties of the optical transitions (wavelength λ , lifetime τ , natural linewidth $\Gamma = 1/\tau$ and Doppler temperature $T_D = \hbar\Gamma/(2k_B)$) are summarised next to them. The data for the excited state lifetimes are obtained from Refs. [112–114]. The thick dashed arrow represents the LS -coupling between the 1P_1 and 3P_1 orbitals (α, β). The thin arrows indicate the hyperfine induced (HFI) state mixing (α_0, β_0) of states with the same total angular momentum F .

at a wavelength of 398.9 nm for Zeeman-slowing and absorption imaging of ytterbium atoms in the ground state.

Although optical transitions between the two manifolds are forbidden by dipole selection rules (namely $\Delta S = 0$), they can still be addressed due to a small mixing between the singlet and triplet P states. The strongest transition from the ground state to the triplet manifold is the so-called intercombination line $^1S_0 \rightarrow ^3P_1$ at 555.8 nm with a natural linewidth of 182 kHz. Owing to its narrow and closed-transition character, it is frequently employed for magneto-optical trapping, as in our experiment.

The $^1S_0 \rightarrow ^3P_0$ transition is doubly forbidden by dipole selection rules, namely $\Delta S = 0$ and $J = 0 \rightarrow J' = 0$. Its natural linewidth is only on the order of a few milihertz and the corresponding states, both with $J = 0$, show the least sensitivity to an external magnetic field. Therefore, it is an ideal candidate for an optical frequency standard and referred to as clock transition or clock line.

In the following section, we study the mechanisms that lead to a violation of the dipole selection rules, enabling the transitions between singlet and triplet states. The structure of the lowest energy levels for ytterbium and the corresponding optical transitions are schematically represented in Figure 2.3.

2.2.2 Forbidden transitions are not forbidden

In this section, we show how the hyperfine interaction of fermionic ytterbium leads to a single-photon E1 coupling between the ground state and the triplet P states. In order to describe the LS -coupling and hyperfine quenching rates of the lowest energy states in ytterbium, we follow the relativistic many-body ansatz introduced by Breit and Wills [115] as well as Lurio [116]. We can decompose the wave functions of the P states in the bare LS eigenstates $|^iP_j^o\rangle$ as follows [117]

$$\begin{aligned} |^1P_1\rangle &= \alpha|^1P_1^o\rangle + \beta|^3P_1^o\rangle, \\ |^3P_0\rangle &= |^3P_0^o\rangle, \\ |^3P_1\rangle &= \alpha|^3P_1^o\rangle - \beta|^1P_1^o\rangle, \\ |^3P_2\rangle &= |^3P_2^o\rangle, \end{aligned} \tag{2.4}$$

with the mixing angles α, β that satisfy the relation $\alpha^2 + \beta^2 = 1$. Among all LS eigenstates, only the $|^1P_1^o\rangle$ state couples via an electric dipole moment to the ground state. The finite mixing β of the $|^1P_1^o\rangle$ into the $|^3P_1\rangle$ state induces an E1 decay channel to the ground state and thus a finite lifetime of the $|^3P_1\rangle$ state

$$\tau_{(^3P_1)} = \frac{|\alpha|^2}{|\beta|^2} \left(\frac{\nu_{(^1P_1)}}{\nu_{(^3P_1)}} \right)^3 \tau_{(^1P_1)}. \tag{2.5}$$

The strength of the mixing is experimentally determined by measuring the corresponding transition frequencies and state lifetimes. The ratio of the two lifetimes and transition frequencies (listed in Figure 2.3) together with the normalisation yields to $\alpha^2 = 0.9834$ and $\beta^2 = 0.0166$ for ytterbium.

For all bosonic AEL atoms with no nuclear spin, the $|^3P_1\rangle$ is the only state of the triplet manifold coupled to the singlet ground state via an electric dipole transition. Due to the lack of hyperfine interaction, the $|^3P_0\rangle$ state exhibits a lifetime of several years since it only decays to the ground state via a very weak two-photon E1-M1 transition [114]. However, an external magnetic field quenches the P-states and thus allows a direct optical excitation on the clock transition for the bosonic isotopes [118, 119].

In contrast, the fermionic isotopes possess a finite nuclear spin and thus a hyperfine structure for all state with $J \neq 0$, as illustrated in Figure 2.3. Here, the hyperfine interaction leads to an additional coupling of states with the same total angular momentum F . Following the ansatz for the lifetime of the $|^3P_1\rangle$ state, we decompose the $|^3P_0\rangle$ state in the LS eigentsates [117]

$$\begin{aligned} |^3P_0\rangle &= |^3P_0^o\rangle + \alpha_0|^3P_1^o\rangle + \beta_0|^1P_1^o\rangle + \gamma_0|^3P_2^o\rangle, \\ &= |^3P_0^o\rangle + (\alpha_0\alpha - \beta_0\beta)|^3P_1^o\rangle + (\alpha_0\beta + \beta_0\alpha)|^1P_1^o\rangle + \gamma_0|^3P_2^o\rangle, \end{aligned} \tag{2.6}$$

where $\alpha_0, \beta_0, \gamma_0$ are the hyperfine quenching rates. As shown by Lairo [120], the quenching rates can be obtained from the corresponding hyperfine structure constants. The mixing of the $|^1P_1^o\rangle$ induces a finite lifetime of the 3P_0 state [117]

$$\tau_{(^3P_0)} = \frac{\beta^2}{(\alpha_0\beta + \beta_0\alpha)^2} \left(\frac{\nu_{(^3P_1)}}{\nu_{(^3P_0)}} \right)^3 \tau_{(^3P_1)}. \quad (2.7)$$

The influence of the violation of the *LS* coupling and hyperfine quenching can be determined by *ab initio* relativistic many-body atomic structure calculations [114]. Porsev et al. obtained a hyperfine-coupling limited lifetime for the $|^3P_0\rangle$ state of 20 s (^{171}Yb) and 23 s (^{173}Yb), corresponding to a natural linewidth of $\Gamma = 2\pi \times 6.9$ mHz and $\Gamma = 2\pi \times 6.1$ mHz, respectively. Based on the high agreement between the *ab initio* calculated and experimentally measured hyperfine constants, Porsev et al. expect that the computed lifetimes of the 3P_0 state are accurate within at least a few per cent [114].

The most precise evaluation of the absolute clock transition frequency has been reported for the fermionic isotope $\nu(^{171}\text{Yb}) = 518\,295\,836\,590\,863.55(28)$ Hz, [121] with an isotope shift of $\delta\nu = -1\,259\,745\,597(10)$ Hz for ^{173}Yb [122]. For the fermionic isotopes, the maximum *Q*-factor for the interrogation of clock transition is $Q = \Gamma/2\pi\nu \simeq 1 \times 10^{-17}$.

In contrast, the $|^3P_2\rangle$ shows a drastically reduced lifetime even for the bosonic isotope. Here, a weak single photon M1 decay is allowed, limiting the lifetime to 15 s [114]. For the fermionic isotopes this lifetime is further reduced due to the additional E1 decay channel, resulting in a lifetime of 10 s and a natural linewidth of $\Gamma = 2\pi \times 15$ mHz [114].

2.2.3 Differential Zeeman shift of the clock transition

The fermionic isotope ^{173}Yb exhibits a finite nuclear spin of $F = 5/2$. Hence, the two clock states 1S_0 and 3P_0 both possess six m_F -states. An external magnetic field will lift the energy degeneracy of the Zeeman sub-levels. Because the total angular momentum of both states vanishes, the Zeeman energy shift is simply given by

$$\Delta_Z(B) = g_F m_F \mu_B B, \quad (2.8)$$

where μ_B is the Bohr magneton and m_F is the spin projection along the field axis. For $F = I$ and $J = 0$, the Landé *g*-factor g_F reduces to the nuclear *g*-factor $g_I = \mu_I/(\mu_B I)$, with the nuclear magnetic moment $\mu_I = -0.6776(25)\mu_N$ for ^{173}Yb [123]. Thus, both clock states experience a Zeeman splitting of $\Delta_Z(B) \approx h m_F B \cdot 1.3$ kHz/G. However, the transition frequency $^1S_0(5/2, m_F) \rightarrow ^3P_0(5/2, m_{F'})$ is only susceptible to this Zeeman shift for $m_F \neq m_{F'}$, i.e. if probed with σ^\pm -polarised light ($m_{F'} = m_F \pm 1$). The π -transition, i.e. $m_F = m_{F'}$, remains unaffected, as illustrated in Figure 2.4(a).

So far, we have neglected the hyperfine mixing higher lying states into the 3P_0 state. Here, the admixture of the 3P_1 state perturbs the 3P_0 wave function and gives rise to a slightly different nuclear *g*-factor for the excited state $\delta g = g_I^e - g_I^g = -8.1 \times 10^{-5}$ [124] for ^{173}Yb . The difference δg leads to a differential Zeeman shift for the π -polarised clock transition frequency

$$\Delta_{\delta Z}(B) = \delta g m_F \mu_B B, \quad (2.9)$$

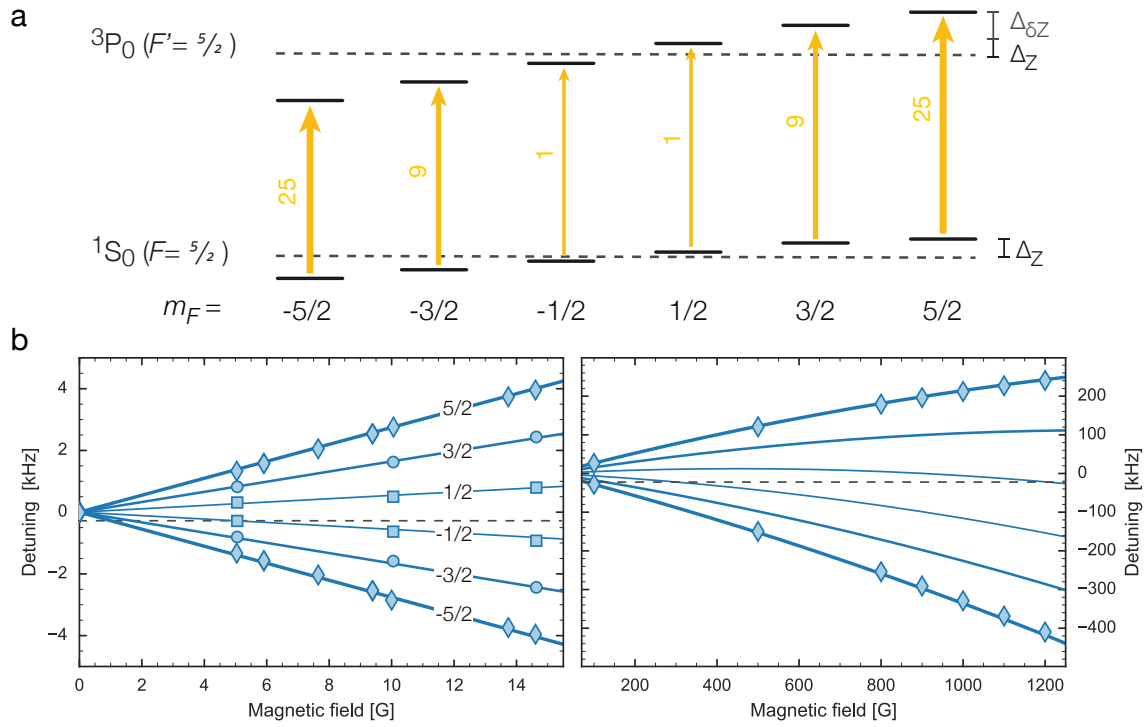


Figure 2.4 – (a) Schematic illustration of the differential Zeeman shift between 1S_0 and 3P_0 state for ^{173}Yb . The thickness of the yellow arrows indicates the transition strength of the corresponding π -transition. The Clebsch-Gordon coefficients (yellow numbers) are inherited from the $^1S_0 \rightarrow ^1P_1$ transition. (b) Breit-Rabi-like diagram of the clock-line Zeeman shift for the different m_F states. The lines are calculated from (2.10) with the theoretical values for the linear and the quadratic Zeeman shift. The symbols indicate measured resonances on the six π -transitions. The left figure shows a zoom into the low field region, where the quadratic Zeeman shift is negligible within our experimental precision. The right figure presents the entire experimentally accessible magnetic field range.

where the theoretically calculated value of $\Delta_B = h m_F B \cdot 113 \text{ Hz/G}$ [124] is in good agreement with the value reported by our experiment $\Delta_B = h m_F B \cdot 112(1) \text{ Hz/G}$ [56].

The quadratic Zeeman shift is induced by the mixing of the fine structure due to an external magnetic field and therefore present for all isotopes. For all ytterbium isotopes the differential quadratic Zeeman shift is given by $\Delta_{\delta Z}^{(2)} = B^2 \cdot 6.2 \times 10^{-2} \text{ Hz/G}^2$ [125]. The total shift of the π -polarised clock transition due to a magnetic field is given by

$$\delta\nu_{\pi}(B) = 112 \text{ Hz/G} \cdot m_F \cdot B - 0.062 \text{ Hz/G}^2 \cdot B^2. \quad (2.10)$$

Figure 2.4(b) displays $\delta\nu_{\pi}(B)$ for all m_F -states within the magnetic field range of our experimental setup. In the entire experimental field range, we verify the predicted magnetic field dependence of $\delta\nu_{\pi}(B)$.

Besides an external magnetic field, the black body radiation from the surrounding vacuum vessel leads to a shift of the clock transition frequency. At room temperature $T = 300 \text{ K}$, the black body radiation causes a -1.3 Hz shift of the clock transition [113]. This shift is well below the resolution of our laser system driving the clock transition and we will neglect it in the following.

2.3 Traps for alkaline-earth-like atoms

One of the building blocks of the success of ultracold neutral atoms for quantum simulations is the ability to trap and confine them in almost arbitrary potentials. These potentials are based on the electric dipole interaction of neutral atoms with far detuned light. Although the achievable trap depths are typically below milikelvin, optical traps offer vast advantages compared to magnetic traps relying on state-dependent forces in different Zeeman sub-levels. Especially for AEL atoms with no magnetic sub-levels in the ground state, optical dipole traps are an indispensable tool.

In the following we will briefly review the interaction of an atom with a classical light field. We show how harmonic and lattice potentials are tailored from Gaussian laser beams. Furthermore, we investigate the polarisability of the 1S_0 and 3P_0 states of ^{173}Yb . Here, the existence of the meta-stable state provides the possibility of engineering state-dependent potentials.

2.3.1 Optical potentials

A light beam incident on a neutral atoms induces an atomic dipole moment \mathbf{d} which oscillates with the driving frequency ω of the electric field \mathbf{E} . The strength of the induced dipole moment $\mathbf{d} = \alpha(\omega)\mathbf{E}$ is determined by the dynamic polarisability $\alpha(\omega)$ at the driving frequency and the amplitude of the electric field E_0 . The polarisability is in general complex, where the imaginary accounts for the dissipative part of the interaction. By time-averaging over many oscillations of the light field, one derives the dispersive interaction potential between the light field and the atom, also referred to as the AC-Stark shift [126]. The imaginary part of the polarisability results from out of phase oscillations of the dipole moment. In this dissipative processes, light is absorbed by the atom and spontaneously reemitted. This process can be described by scattering of photons on the atom [126]. In the vicinity of a strong transition ω_0 , we can approximate the atom as a two-level system. For small detunings between the driving field and the atomic transition $\Delta = \omega - \omega_0 \ll \omega_0$, the rotating wave approximation holds and the AC-Stark shift and the scattering rate are written as follows [126]

$$\begin{aligned} V(\mathbf{r}) &= \frac{3\pi c^2}{2\omega_0^3} \left(\frac{\Gamma}{\Delta} \right) I(\mathbf{r}), \\ \Gamma_{\text{sc}}(\mathbf{r}) &= \frac{3\pi c^2}{2\hbar\omega_0^3} \left(\frac{\Gamma}{\Delta} \right)^2 I(\mathbf{r}), \end{aligned} \tag{2.11}$$

with the intensity of the light field $I(\mathbf{r}) = 2\epsilon_0 c |E_0(\mathbf{r})|^2$. These two equations demonstrate nicely the fundamental working principles of optical potentials as they are utilized in experiments. As the scattering rate scales with I/Δ^2 , whereas the light shift only with I/Δ , high intensity light with large detuning is employed to create deep potentials, while keeping the scattering rate as low as possible. The force exerted by the light on the atoms is given by the gradient of the conservative potential $\mathbf{F}(\mathbf{r}) = -\nabla V(\mathbf{r})$. Thus, a so-called red-detuned light field with $\Delta < 0$ attracts atoms to the position of the maximum light

intensity, whereas atoms are repelled out of the beam for blue detuning $\Delta > 0$. In the following, we will introduce two configurations of optical traps, frequently employed in our experiment.

Crossed-beam dipole trap

Most experiments carried out within this thesis are performed in a harmonic trap. This kind of traps are typically formed by crossing two focused, red-detuned laser beams. The radial intensity distribution $I(r)$ is given by a two-dimensional Gaussian. Since the intensity gradient is usually much steeper in the radial direction than along the beam, two beams are crossed to create a step potential in all directions.

Typically, the spatial extension of the atomic ensemble is much smaller than the waist of the Gaussian laser beam ω_0 . Here, the potential around the intensity maximum can be well approximated by a harmonic oscillator [126]. By intersecting two identical beams at their foci, an isotropic three-dimensional harmonic oscillator is created

$$V_{\text{ho}} = -U_0 \frac{x^2 + y^2 + 2z^2}{\omega_0}, \quad (2.12)$$

where the absolute depth of the potential U_0 is determined by 2.11 for $I(r = 0)$. In section 1.1.3, we have already study the effect of the harmonic potential on the atomic interaction.

Optical lattices

Optical lattices confine the atoms in a periodic potential. This allows to simulate the properties of electrons in a solid, where the electrons move through the periodic potential created by a crystal of immobile ions [5, 19, 127]. Therefore, optical lattices have become an important and versatile tool for quantum simulation. Furthermore, they are also employed for optical lattice clocks. They allow for the recoil free excitation of atoms and thus have enable to build the most precise atomic clocks in the world [128, 129].

For ultracold atoms, we can create periodic potentials by interfering a single or multiple laser beams. A common experimental method is to retro-reflect a laser beam such that the forward and the backward-travelling beams are aligned and interfere with each other. This creates a standing wave with a periodicity of half of the laser wavelength λ . By orthogonally intercepting three retro-reflected laser beams, a three-dimensional square lattice potential is formed,

$$V_{\text{lat}} = \sum_{\xi=x,y,z} V_i \cos^2(k\xi) \quad (2.13)$$

where $k = 2\pi/\lambda$ is the wave vector of the laser light and V_ξ is the the lattice depth given by (2.11) of the ξ -axis . Conventionally, the lattice depth is expressed in units of the recoil energy $E_r = \hbar^2 k^2 / 2m$ of the laser creating the lattice. For red detuned lasers the atoms are trapped in the anti-nodes of the standing wave.

Here, we have approximated the laser beams with plane waves, neglecting the Gaussian intensity profile of the laser beams. This creates an additional harmonic confinement

and an energy between adjacent sites. However, as long as the spatial extension of the atomic cloud is small compared to the waist of the laser beam, we can assume a homogeneous lattice depth throughout the atomic ensemble.

2.3.2 State-dependent optical potentials

For alkali atoms, optical dipole potentials offer the possibility of trapping atoms independent of the Zeeman sub-level, since the difference in detuning of the individual states is very small. By choosing a wavelength between the D_1 and D_2 line one can furthermore tailor state-dependent potentials for the two hyperfine manifolds. However, such potentials are considered impractical for experimental purposes, since they are always closely tuned to the atomic transitions and therefore cause heating via substantial photon scattering.

In AEL we find a different situation. Here, the ground state 1S_0 and the metastable states 3P_0 and 3P_2 are separated by several eV and belong to different electronic manifolds. In the following discussion, we will focus on the two states 1S_0 (denoted $|g\rangle$) and 3P_0 ($|e\rangle$) employed in our experiment. Due to their opposite symmetry, they are coupled to different states. This results in a different frequency dependence in the polarisability for each state. Figure 2.5 displays the AC-Stark shift for the $|g\rangle$ and $|e\rangle$ states of ytterbium. It is based on the results obtained by Dzuba et al. by *ab initio* relativistic many-body calculations [130, 131].

As illustrated by Figure 2.5, the polarisabilities of the two states are in general not the same. Yet, we can identify special configurations, where the two states experience the same AC-Stark shift $V_g(\omega) = V_e(\omega)$. The corresponding wavelengths are called magic wavelengths.

Four magic wavelengths have been predicted $\lambda_m = 759.35, 551, 465$ and 413 nm for ytterbium [131]. So far, only the one at $\lambda_m = 759.35$ has been employed in experiments. Since the ultra narrow clock transition is highly sensitive to the residual AC-Stark shifts between the two clock states, magic wavelength lattices have become an indispensable tool for optical clocks. In such a potential, the clock transition can be probed in a pseudo Stark shift free environment, enabling longer interrogation times [129] which allowed to push the precision of optical lattice clocks to the 10^{-18} level [132, 133]. Exact evaluations of the magic wavelength are employed to improve the precision of the *ab initio* calculations of the polarisabilities [134].

At the so-called anti-magic wavelengths, the polarisabilities for both states are equal in magnitude, but opposite in sign. For ytterbium, this happens at $\lambda_{am} = 1117, 619, 436$ nm. Here, the atoms experience either a red or blue detuned potential of same magnitude $V_g(\omega) = -V_e(\omega)$. Therefore, $|e\rangle$ and $|g\rangle$ atoms are separated into two sub-lattices. Since each of this sub-lattices is given by the nodes or the anti-node of the standing wave, they are shifted by $\lambda/4$ with respect to each other. Applying a strong coupling between $|e\rangle$ and $|g\rangle$ on the clock line, allows to create adiabatic sub-wavelength lattices for the dressed states [135]. Furthermore, this setup has been proposed as a building block for the creation of strong artificial gauge fields [136, 137].

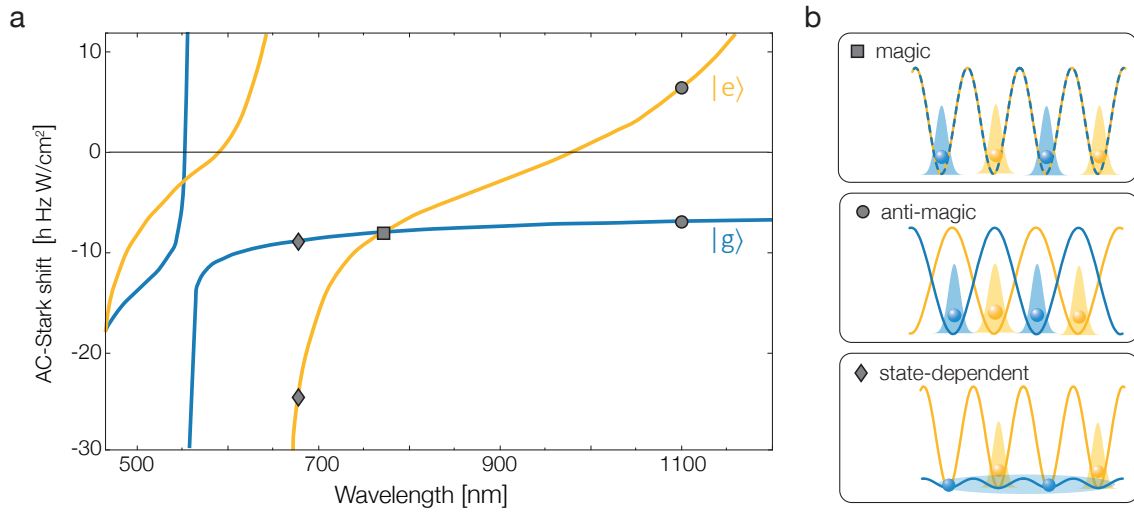


Figure 2.5 – (a) AC-Stark shift of the ground 1S_0 (blue) and metastable 3P_0 (yellow) state of ytterbium. The wavelength dependence of the dynamic polarisability was obtained from relativistic many-body calculations [131]. The two visible poles in displayed wavelength range result for the ground state from the $^1S_0 \rightarrow ^3P_1$ transition at 556 nm and for the excited state from the $^3P_0 \rightarrow ^3S_1$ transition at 649 nm. (b) Schematic representation of lattice potentials for ground and excited state atoms created by a monochromatic light field of a wavelength corresponding to the marks in figure (a). The shaded areas represent the magnitude of the Wannier functions on the lattice sites.

In general, the polarisabilities of $|e\rangle$ and $|g\rangle$ are not the same and lead to state-dependent optical potentials. The region between the magic wavelength at 759 nm and the resonance $^3P_0 \rightarrow ^3S_1$ at 649 nm offers a red detuning for both states. Close to the $^3P_0 \rightarrow ^3S_1$ resonance, the potential for the $|e\rangle$ atoms can be made substantially deeper than for the $|g\rangle$ atoms, as illustrated in 2.5(b). It is thus possible to achieve strong localization of atoms in the $|e\rangle$ state, while keeping atoms in the $|g\rangle$ state mobile. This configuration is particularly interesting because atoms in the $|e\rangle$ state have to be isolated in all experiments. While colliding, two $|e\rangle$ atoms can relax into the ground state and are lost from the trap due to the excess energy. Such state-dependent potentials are proposed for simulating condensed matter models with electrons in different orbitals [38, 51, 52].

2.4 Alkaline-earth-like atoms for quantum simulation

In the previous section, we have introduced the optical lattices allowing to create periodic potentials, as they are found in solid-state systems. Furthermore, we have investigated the polarisabilities of the two lowest electronic states (1S_0 and 3P_0) in ytterbium. We have seen how we can utilize the different polarisabilities to create state-dependent potentials. In the following, we give a brief overview of the physics that can be realized by AEL atoms.

First, we briefly review the properties of the $SU(N)$ Fermi liquid in a harmonic trap. Then, we turn the attention to optical lattices and introduce the Fermi Hubbard model.

This model developed for electrons in solids can be simulated by neutral atoms in optical lattices. In a second step, we extend the Hubbard model to the case of $SU(N)$ symmetry and two-orbital interactions. Finally, we present the scattering properties of ^{173}Yb and discuss the experimental feasibility of the proposed models.

2.4.1 $SU(N)$ Fermi liquid

In ^{173}Yb we find a $SU(6)$ symmetric configuration for the interactions in the ground state. Let us consider the implications of the enlarged symmetry on an interacting Fermi gas under typical experimental conditions. We confine the atoms in a harmonic trap and cool them down to temperatures about ten percent of the Fermi temperature T_F . In this regime, an interacting Fermi gas is well described by Landau's Fermi liquid theory [138]. Such a Fermi liquid exhibits a gapless Fermi surface with a radius k_F , the so-called Fermi wave vector. The elementary excitations are known as quasi-particles and have a fermionic character, they are long-lived and weakly interacting. In a uniform $SU(N)$ symmetric Fermi liquid, the Fermi surface reflects the full symmetry of the system. However, if the Fermi surface is unstable against deformation, the system's underlying symmetry can be spontaneously broken. The Fermi surface is deformed and has a lower symmetry than the initial state, a mechanism known as Pomeranchuk instability. Thus, the ground state of the interacting $SU(N)$ Fermi liquid, would not reflect the full $SU(N)$ symmetry.

It is relevant to ask whether, we can expect for an ^{173}Yb quantum gas a $SU(N)$ symmetric Fermi liquid or a ground state with lower symmetry. One famous example of a Pomeranchuk instability for repulsive interaction is Stoner magnetism. Here, the unpolarised Fermi gas becomes unstable against phase segregation and the formation of polarised, i.e. ferromagnetic domains. The Stoner criterion for ferromagnetism can be generalised to the $SU(N)$ case [36, 39]. The criterion for ferromagnetism is predicted to be nearly independent of N and has the same form as in the $SU(2)$ case [107]. For $k_F a < \pi/2$ the Fermi surface is stable against deformation. In ^{173}Yb with $a_{gg} = 199.4 a_0$, we find $k_F a \approx 0.1$ for typical experimental parameters. Hence, for ^{173}Yb the Fermi liquid phase is stable against ferromagnetic correlations.

For attractive interactions, the Fermi surface is unstable against pairing and the formation of Cooper pairs. This instability exists for any arbitrary weak interaction and leads to s -wave pairing. The $SU(N > 2)$ symmetric Fermi gas is proposed to show a rich phase diagram of paired states [53–55, 139]. In the case of $SU(3)$, a color superfluid state emerges. Here, in analogy to QCD, the formation of trimers can be understood as baryon production [54]. However, for ^{173}Yb as well as ^{87}Sr , the only $SU(N > 2)$ symmetric atoms cooled to quantum degeneracy, the interactions in the ground state are weak and repulsive. Kohn and Luttinger showed that also in the presence of repulsive interaction the Fermi gas is unstable against Cooper-pair formation, giving rise to triplet p -wave superfluidity [140]. Yet, in this regime, the demands on the temperature are even more challenging than for s -wave pairing. Due to the absence of magnetic Feshbach resonances and because optical Feshbach resonances break the $SU(N)$ symmetry, it is not possible to tune the scattering

length to large and negative values and promote the pairing instability. Therefore, unless one of the yet unexplored AEL atoms with $I > 1/2$ possesses such a scattering length in the ground state, these phases may remain unexplored.

2.4.2 The SU(N)-symmetric Fermi Hubbard model

In the following, we will study the implications of the enlarged spin rotation symmetry on the behaviour of fermionic AEL atoms in optical lattices. Therefore, we introduce the Fermi-Hubbard model. This model, originally designed to describe the properties of electrons in the ionic lattice structure of a solid, is exactly realised by ultracold neutral atoms in the lowest vibrational level of an optical lattice [19].

The wave function of a particle in a periodic potential can be expressed in the basis of so-called Bloch waves [6]. These waves are given by the product of a plane wave and a periodic function that reflects the periodicity of the underlying potential. The energy eigenstates of the Bloch waves can be grouped into continuous bands. Owing to their composition, Bloch waves are delocalised on the whole lattice. Therefore, they are not suited for the description of local effects on an individual lattice site.

However, by the appropriate superposition of Bloch waves, we can construct a new basis set of localised wave functions, which are called Wannier functions. These functions are maximally localised on the individual lattice sites and represent a good description of the system in the tight-binding limit. Here, we assume that all energy scales are small compared to the gap between the first two Bloch bands and we can restrict our self to the lowest energy Bloch band. This allows us to expand the field operators, creating an annihilating particles at an arbitrary point, in the basis of Wannier functions and we can reduce the Hamiltonian of fermions in an optical lattice to the Hubbard Hamiltonian [19],

$$\hat{H} = -J \sum_{\langle i,j \rangle, \sigma} \hat{c}_{i,\sigma}^\dagger \hat{c}_{j,\sigma} + \frac{U}{2} \sum_{i, \sigma \neq \sigma'} \hat{n}_{i,\sigma} \hat{n}_{i,\sigma'}. \quad (2.14)$$

Here, $\hat{c}_{i,\sigma}^{(\dagger)}$ are the creation and annihilation operators of a fermion with spin index σ on a lattice site i and $\hat{n}_{i,\sigma} = \hat{c}_{i,\sigma}^\dagger \hat{c}_{i,\sigma}$ the corresponding number operator. In the conventional case of spin one-half fermions, the spin index $\sigma = 1, \dots, N$ runs only upto 2. However, in the case of AEL atoms N can be as large as 10 and (2.14) represents in the given form directly the extended SU(N) symmetric FHM. This means that the Hamiltonian is invariant under a change of spin components.

The first term in the FHM describes the tunnelling of atoms from a lattice site i to a neighbouring one j . The tunnelling rate J is given by the tunnelling matrix element between adjacent sites

$$J = J_{i,j} = \int d^3x w^*(x - x_i) \left(-\frac{\hbar^2}{2m} \nabla^2 + V_{\text{lat}}(x) \right) w(x - x_j), \quad (2.15)$$

where $w(x - x_i)$ is the Wannier function on lattice site i and $V_{\text{lat}}(x)$ the potential of the optical lattice. The energy width of a Bloch band in a three dimensional lattice, can be expressed as $W = 12J$.

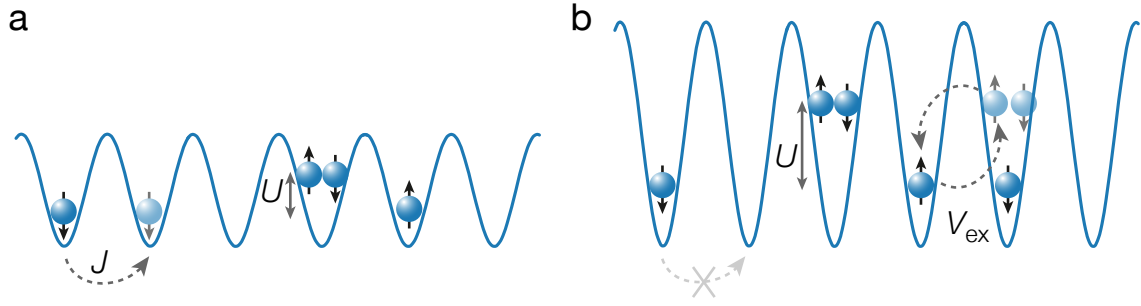


Figure 2.6 – A schematic of the Fermi Hubbard model and its characteristic parameters: the tunneling rate J , the interaction energy U and the super-exchange energy $V_{\text{ex}} = 4J^2/U$. (a) A shallow lattice, where the tunnelling rate is high and the atoms can hop around the lattice freely. (b) A deep lattice, where tunnelling is suppressed and the atoms interact only via virtual processes.

The second term of the FHM accounts for the interaction of different fermions $\sigma \neq \sigma'$ on a single lattice site. Assuming a zero-range pseudo potential for the interaction, the on-site interaction strength is given by the Wannier functions overlap

$$U = \frac{4\pi\hbar^2}{m} a \int d^3x |w(x)|^4. \quad (2.16)$$

Due to the $SU(N)$ symmetry, the interactions are the same for all possible spin combinations. Therefore, the Hamiltonian (2.14) commutes with all spin permutation operators $[S_n^m, H] = 0$, where $S_n^m = \sum_i \hat{c}_{i,m}^\dagger \hat{c}_{i,n}$.

The physics of the FHM are governed by the interplay between the tunnelling strength and interaction energy. Depending on the temperature and the magnitude and sign of U/J many different phases can be found. For the $SU(2)$ case, the phase diagram of the FHM has been extensively studied.

For attractive interaction $U < 0$, the ground state of the FHM is a superfluid. Depending on the strength of the attraction, the nature of the superfluid changes from BCS-like for small U to a BEC of composite bosons. Here, no spin order exists in the ground state. For repulsive interaction $U > 0$, the system undergoes a crossover from a conducting metal to a Mott insulating state with increasing U/J [22, 23]. In this regime, tunnelling is suppressed and we can map the $SU(N)$ FHM onto a $SU(N)$ Heisenberg spin model [141, 142]

$$\hat{H}_{\text{Heis}} = \frac{2J^2}{U} \sum_{m,n,\langle i,j \rangle} S_n^m(i) S_m^n(j). \quad (2.17)$$

Here, the atoms can only interact via a virtual tunnelling process. For temperatures below the super exchange energy $4J^2/U$, the ground state spontaneously breaks the spin symmetry and possesses anti-ferromagnetic spin ordering. The formation of anti-ferromagnetic ordering has been recently observed in the one- and two-dimensional FHM [44, 46].

In the following, we will study the implications of the enhanced $SU(N)$ symmetry on ground state in the lattice and the experimentally important procedure of adiabatically loading the lattice. In a typical experimental realization of the Hubbard model, the atoms

are first evaporatively cooled in a harmonic trap. Afterwards, the optical lattice is slowly turned on and the atoms are adiabatically transferred. Let us consider a non-interacting gas, in a harmonic trap, the entropy per particle scales as $S_i \sim N^{1/3}$. In the lattice the entropy per particle on a site grows as $S_i \sim \log N$, because it is equally likely for any of the N spins to occupy a site [143]. Thus, while adiabatically loading the lattice, more entropy can be stored in the spin degree of freedom. This effect is the so-called Pomeranchuk cooling and well known from ^3He . It has led to the production of $\text{SU}(N > 2)$ Mott insulators at temperatures, that would not support a Mott insulating state for $\text{SU}(2)$ [42, 43].

For fermionic AEL atoms, so far only positive scattering lengths have been reported. Therefore, we focus on the case of repulsive interactions. The ground state of a $\text{SU}(N)$ Fermi gas on a lattice depends strongly on N . For $\text{SU}(3)$ it is supposed to be a flavour density-wave [47], for $\text{SU}(4)$ a valence bond solid [48] and for $\text{SU}(N \geq 6)$ a staggered flux phase [36, 47]. Here, the staggered flux phase is of particular interest, since it breaks the translation symmetry of the lattice, while preserving the full $\text{SU}(N)$ symmetry. However, it is questionable if this phase can be created with ^{173}Yb . For $\text{SU}(N \leq 6)$ renormalization group studies show, that $\text{SU}(N)$ breaking phases like the flavour density-wave possess a lower energy [47]. Here, ^{87}Sr with $N = 10$ seems to be a more suitable candidate for the studies of $\text{SU}(N)$ magnetism. However, the exploration of $\text{SU}(N)$ magnetism requires as for the $\text{SU}(2)$ case temperatures on the super-exchange scale. Recent Quantum Monte-Carlo calculations hint, that even in this regime the final temperature decreases with increasing N [143, 144].

So far, the currently achievable temperatures have enabled us to experimental study the equation of state across the metal to Mott transition [43]. Especially in the regime, where the kinetic and interaction energy scales are comparable, the experimental findings go beyond current theoretical state-of-the-art models.

2.4.3 Two-orbital $\text{SU}(N)$ -symmetric models

For AEL atoms, we find $\text{SU}(N)$ symmetric interaction for the two $J = 0$ states. Therefore, we can generalise the $\text{SU}(N)$ FHM to the case of two electronic orbitals

$$\begin{aligned} \hat{H} = & - \sum_{\langle i,j \rangle, \sigma, \alpha} J_\alpha \hat{c}_{i,\sigma,\alpha}^\dagger \hat{c}_{j,\sigma,\alpha} + \sum_{i, \sigma \neq \sigma', \alpha} \frac{U_{\alpha,\alpha}}{2} \hat{n}_{i,\sigma,\alpha} \hat{n}_{i,\sigma',\alpha} \\ & + V_{\text{ex}} \sum_{i, \sigma, \sigma'} \hat{c}_{i,\sigma,g}^\dagger \hat{c}_{i,\sigma',e}^\dagger \hat{c}_{i,\sigma',g} \hat{c}_{i,\sigma,e} + V_{\text{d}} \sum_i \hat{n}_{i,g} \hat{n}_{i,e}, \end{aligned} \quad (2.18)$$

with the index $\alpha = \{|g\rangle, |e\rangle\}$ for the electronic states. The first line of 2.18 is similar to the single orbital FHM, with in intraorbital interaction $U_{\alpha,\alpha}$, calculated analogue to (2.16) for a_{gg} and a_{ee} . The interorbital interactions with the two scattering lengths a_{eg}^+ and a_{eg}^- give rise to the two additional terms in the second line. In analogy to the pseudo spin-1/2 language, these terms are called the direct energy $V_{\text{d}} = (U_{\text{eg}}^+ + U_{\text{eg}}^-)/2$ and exchange energy $V_{\text{ex}} = (U_{\text{eg}}^+ - U_{\text{eg}}^-)/2$, where U_{eg}^\pm are given by (2.16) for a_{eg}^+ and a_{eg}^- . Examining the

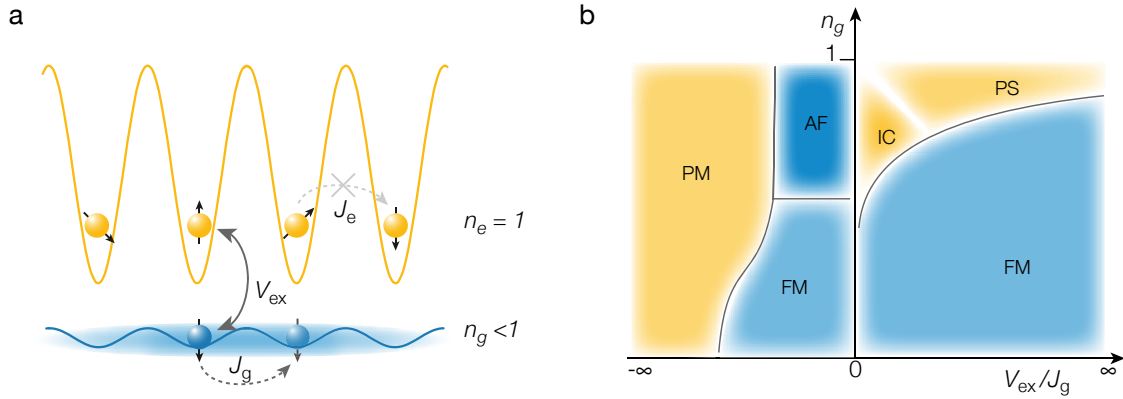


Figure 2.7 – (a) Realisation of the Kondo lattice model with AEL atoms in a state-dependent optical lattice. The $|e\rangle$ atoms are strongly localised and their tunneling is suppressed $J_e/J_g \approx 0$. The $|g\rangle$ atoms have a high mobility and interact with the localised $|e\rangle$ atoms via the on-site exchange interaction V_{ex} . (b) Schematic $T = 0$ phase diagram of the two dimensional KLM for ferromagnetic $V_{\text{ex}} < 0$ and anti-ferromagnetic $V_{\text{ex}} > 0$ exchange coupling. The different phases denote the magnetic order of the localised spins, i.e. the $|e\rangle$ atoms. Here, AF, FM, IC, PM, and PS denote regimes with anti- or ferromagnetic correlations, incommensurate correlations, paramagnetic correlations, and with phase separation between AF and FM regions, respectively. The phase diagram of the ferromagnetic side is based on [146, 148]. For the IC-PS crossover no phase boundary has been determined yet. The anti-ferromagnetic phase diagram was obtained by [51]. Both sides are based on dynamical mean-field calculations.

corresponding operators, we see that V_{ex} leads to an on-site orbital exchange process for atoms with different spin.

A prominent realization of a two orbital system is the Kondo lattice model (KLM). In solid state physics the KLM is applied to describes the interaction of mobile conduction electrons with strongly localized spins. These are usually given by unpaired electrons close to the nuclear core in the f -shells. AEL atoms are an ideal candidate for the simulation of the KLM. We can make use of the different polarisabilities of the $|g\rangle$ and $|e\rangle$ states and create state-dependent potentials. Choosing a suitable lattice wavelength, the $|e\rangle$ atoms become localised ($J_e = 0$), while keeping the $|g\rangle$ atoms mobile. Thus, the full two-orbital Hamiltonian 2.18 reduces to the KLM Hamiltonian [38]

$$\hat{H}_{\text{KLM}} = -J_g \sum_{\langle i,j \rangle, \sigma} \hat{c}_{i,\sigma,g}^\dagger \hat{c}_{j,\sigma,g} + V_{\text{ex}} \sum_{i,\sigma,\sigma'} \hat{c}_{i,\sigma,g}^\dagger \hat{c}_{i,\sigma',e}^\dagger \hat{c}_{i,\sigma',g} \hat{c}_{i,\sigma,e} \quad (2.19)$$

Here, the interplay between the strength of the ground state tunnelling rate J_g and the exchange energy V_{ex} gives rise to a rich phase diagram [38, 51, 145–147]. Depending on the sign of the exchange coupling, we can either realize the anti-ferromagnetic (AF) or ferromagnetic (FM) KLM with AEL atoms.

Let us first consider AF coupling $V_{\text{ex}} < 0$. This type of coupling is found in heavy fermion materials [34] and gives rise to the Kondo effect in the case on a single impurity [33]. Here, strong exchange coupling $|V_{\text{ex}}| > J_g$ leads to the formation of on-site spin singlets between the mobile $|g\rangle$ and localised $|e\rangle$ atoms, also referred to as Kondo singlets. Due to the screening of the localised spins, the formerly mobile $|g\rangle$ atoms acquire a large

effective mass and enter the heavy fermion phase. At weak exchange coupling $|V_{\text{ex}}| < J_g$, the mobile $|g\rangle$ atoms can mediate long-range Ruderman-Kittel-Kasuya-Yosida (RKKY) interactions between the localised spins. At half filling $n_g = 0.5$, the correlations in the $|e\rangle$ atoms change from FM to AF [51].

The FM KLM is associated with the appearance of the colossal magneto resistance in manganese oxides with perovskite structure [149, 150]. Here, the exchange coupling favours the formation of spin triplets. Thus, in the weak as well as in the strong coupling limit ferromagnetic order arises. Only for high $|g\rangle$ densities a paramagnetic phase, composed by phases of separated AF and FM regions, exists [148]. In the weak coupling limit, this phase extends down to half filling. Around half filling, a phase with incommensurate correlations can be found [146].

Let us now study the feasibility of the aforementioned with AEL atoms. Looking at Figure 2.5, we identify a region suited for a state-dependent lattice for the implementation of the KLM between 650 nm and 750 nm. In this region, the lattice light is red detuned for both states and creates a stronger confinement for the $|e\rangle$ atoms. Adopting a wavelength of 670 nm, we measure a ratio of approximately three in the polarisabilities and in the lattice depth. This wavelength is still far detuned from the $^3P_0 \rightarrow ^3S_1$ transition and offers an experimentally feasible lifetime of 1.7 s for the $|e\rangle$ atoms in a $30 E_r$ (measured for $|e\rangle$) deep lattice. For the KLM, the essential energy scale is the exchange coupling, caused by the difference between the two interorbital scattering lengths a_{eg}^+ and a_{eg}^- . In ^{173}Yb , we find a large difference $\Delta a \approx 1600a_0$ [59], making ^{173}Yb an ideal candidate for the implementation of the KLM. In comparison, for ^{87}Sr this difference is rather small $\Delta a \approx 100a_0$. Let us consider a state-dependent lattice depth of $3 E_r$ ($9 E_r$) for the $|g\rangle$ ($|e\rangle$) atoms in two dimensions and a strong magic lattice of $30 E_r$ in the third direction. In the two-dimensional plane, the $|g\rangle$ atoms are still mobile ($J_g \approx 290$ Hz), while the $|e\rangle$ atoms are sufficiently localised ($J_e \approx 50$ Hz) and the exchange energy is $V_{\text{ex}} \approx h \cdot 8$ kHz. Therefore, we expect ^{173}Yb to be in the strong coupling limit $V_{\text{ex}} > J_g$.

Experimental apparatus and sequence

Our experiments are based on the reproducible production of an ensemble of ultracold atoms. Repetitively, we create a degenerate Fermi gas, vary an external parameter and observe the influence on the atoms. In this chapter, we will give a brief overview of the experimental apparatus and sequence employed in this thesis for the investigation of the scattering properties of ^{173}Yb . First, the vacuum and laser system used for trapping, cooling and manipulating the atoms are introduced. Then, we explain the experimental cycle. Starting from the magneto-optical trap (MOT), we describe the all-optical production of a two-component degenerate Fermi gas of ^{173}Yb . Finally, we present the techniques for the coherent and incoherent manipulation of the orbital degree of freedom.

3.1 Experimental apparatus

The experimental apparatus consists of a vacuum system, surrounded by magnetic field coils and an extensive optical system steering the light onto the atoms. The main chamber of the vacuum system exhibits a background pressure below 10^{-11} mbar. Here, we obtain a background collision limited lifetime of the degenerate Fermi gas on the order of several tens of seconds [60]. These long lifetimes are essential for the experiments presented in this thesis, where we have observed the suppression of thermalisation up to five seconds. Another coupling to the environment is given by black-body radiation from the walls of the vacuum vessel. In order to ensure reproducible conditions, the entire optical table is boxed in and the air temperature around the apparatus is stabilised. A detailed discussion of the vacuum system, including the custom design of the ytterbium oven, can be found in Ref. [60]. We will restrict the overview of the experimental apparatus to the components of particular influence for the experiments presented in this thesis; the magnetic field setup and the so-called clock laser addressing the $^1\text{S}_0 \rightarrow ^3\text{P}_0$ transition.

3.1.1 Magnetic field coils

As we want to study the magnetic field dependence of the scattering length in ^{173}Yb , a good control over the magnetic field is needed. Around the main vacuum chamber various pairs of coils are placed, allowing to create magnetic fields along all three dimensions.

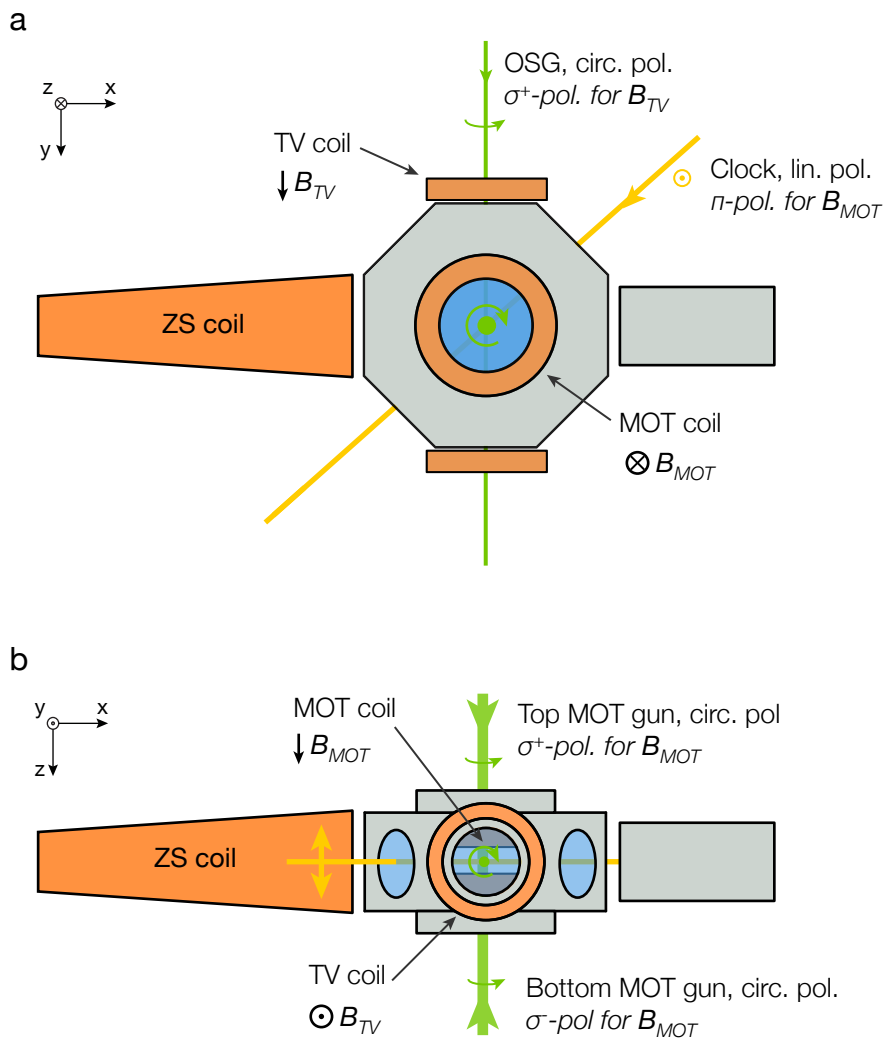


Figure 3.1 – Schematic drawing of the magnetic field coils (a) in the $x - y$ plane and (b) the $x - z$ plane. The steel parts of the vacuum chamber are drawn in gray, the copper parts of the magnetic field coils in orange. For clarity, we only present the high-field coils and omit the three sets of shim coils, used for the compensation of stray fields. In order to create the strongest possible fields, the MOT coils are immersed inside the bucket windows. The MOT coils are used in Helmholtz configuration to generate the bias fields for the optical pumping or excitation on the clock line. The TV coils in Helmholtz configuration create a field along the y -axis. They are employed to set the quantization axis during the optical Stern-Gerlach and ensure σ^+ polarised OSG light.

There are two water-cooled, high-current pairs of coils for the creation of strong magnetic fields, the so-called MOT coils and transverse (TV) coils. Furthermore, there are three pairs of small coils for the compensation of the earth magnetic field. The MOT and TV coils can be switched from Helmholtz to anti-Helmholtz configuration, by reversing the current in one of the coils via a MOSFET-based H-bridge. In Helmholtz configuration, the MOT coils create a uniform magnetic field along the z -axis. The field of the TV coils is

along the y -axis and thus transverse to the Zeeman slower and the propagation of the atomic beam (see Figure 3.1).

The central part of the magnetic field setup is the pair of MOT coils, creating a magnetic field of 1200 G for $I = 220\text{A}$ at the position of the atoms. This is the maximum current the connected power supply is capable of delivering. A detailed description of the coils can be found in Ref. [61]. In Helmholtz configuration, the MOT coils are used for the generation of the bias field during the optical pumping and the excitation on the clock transition. In the presence of the this field, the linearly polarised clock light is π -polarised.

The TV coils are connected to a power supply delivering up to 100 A and creating a maximum field of 25 G at the position of the atoms. In the presence of the TV field, the circular optical Stern-Gerlach light is σ^+ polarised. Furthermore, the TV field decomposes the linear clock light into σ^+ and σ^- polarised light. In anti-Helmholtz configuration, the combination of the MOT and TV coils creates the magnetic field gradient for the magneto-optical trap.

The three sets of small coils are not water cooled and can carry a current of up to 2 A. They create a field of ~ 1 G at the position of the atoms. We employ them to cancel the earth magnetic field (~ 400 mG) and stray fields from the ion pumps and other magnetic components.

3.1.2 Optical setup

In order to minimize thermal fluctuations on the main table, all laser sources are placed on individual tables. On the experimental table, all laser beams originate from polarisation maintaining, single-mode optical fibres. These fibres ensure a stable spatial position of the beams, a well-defined polarisation axis and a transverse Gaussian mode. As illustrated in Figure 3.2, the main chamber has an octagonal shape, where two sides are connected to the vacuum system. This grants optical access to the atoms via six viewports in the horizontal plane, as well as two viewports in the vertical direction. The entire optical setup consists of the MOT beams, two crossed optical dipole traps (ODT), a cubic three-dimensional lattice, one beam for optical Stern Gerlach (OSG), one for the clock light and two imaging beams.

The MOT is formed by six independent beams, two in the vertical and four in the horizontal direction. Since the vertical MOT beams can be intensity controlled individually, they are further used for the manipulation of the nuclear spin via optical pumping. In the presence of the MOT field, the vertical beams have opposite polarisation (σ^+ and σ^-) allowing to create any desired spin mixture.

The main ODT operates at 1064 nm and is employed for evaporative cooling of ytterbium in the 1S_0 state. The ODT is composed of two beams intersecting at their foci. The horizontal beam is strongly elliptical and has a waist of $w_h = 153\ \mu\text{m}$ and $w_v = 20\ \mu\text{m}$ in the focus. The vertical beam is circular with a waist of $w = 86\ \mu\text{m}$. At the maximum light power ($P_h = 10.5\ \text{W}$ and $P_v = 1\ \text{W}$) this creates an $82\ \mu\text{K}$ deep trap with frequencies

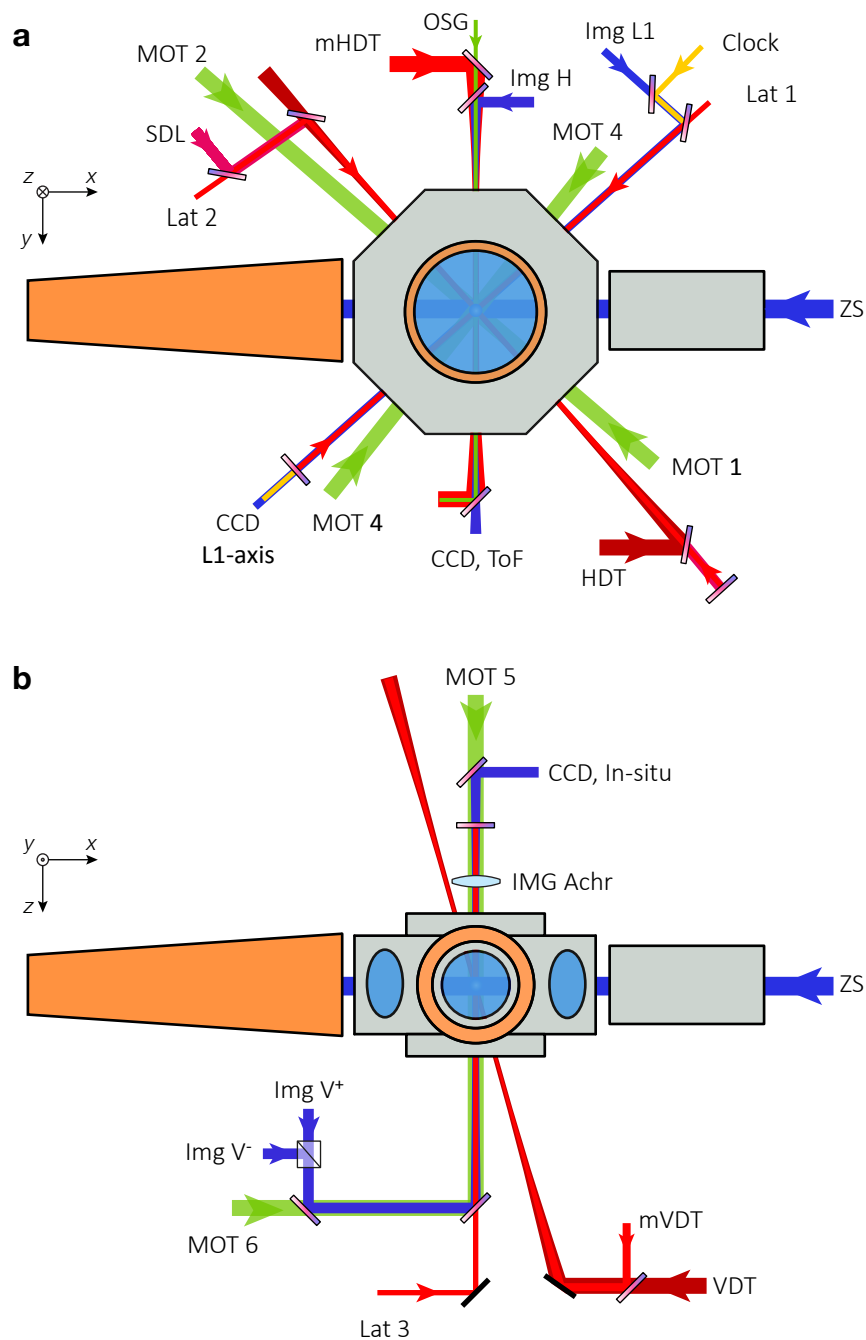


Figure 3.2 – Schematic drawing of the optical beam paths, delivering the light to the atoms in (a) the horizontal plane and (b) the vertical plane. Parts of the steel vacuum chamber are drawn in gray, the copper parts of the magnetic field coils in orange. The main octagon chamber offers six small viewports in the horizontal plane and two large viewports in the vertical plane. The various colours correspond to the following wavelengths: 399 nm (blue), 556 nm (green), 578 nm (yellow), 670 nm (magenta), 759 nm (red) and 1064 nm (dark red). This figure is an update of the optical setup presented in [60]. Compared to [60], we have removed the vertical path of the clock light and the imaging path on the lattice 2 axis. We have installed an additional magic dipole trap (mHDT and mVDT) and included a state-dependent lattice (SDL) coaligned to the L2 axis. Furthermore, we have split the vertical imaging into two paths (V^+ and V^-) allowing spin-resolved in-situ detection at high magnetic bias fields.

$\omega = 2\pi \times (20, 103, 1432)$ Hz. At the end of the evaporation, the typical trap frequencies are $\omega = 2\pi \times (22, 27, 215)$ Hz.

The cubic, 3D lattice is formed by three perpendicular retro-reflected beams. Two lattice beams (L1 and L2) propagate in the horizontal plane and a third one (L3) along the vertical direction. The lattice operates at the magic wavelength $\lambda = 759$ nm and creates a state-independent potential for the 1S_0 and 3P_0 state. With the available light power, we can create an isotropic lattice with a depth of $40 E_r$ in each arm.

The second ODT, the so-called magic ODT (mDT), also operates at the magic wavelength and allows simultaneous trapping of atoms in the 1S_0 and 3P_0 states. For the experiments reported in this thesis, it was formed by intersecting the horizontal mDT beam with the ingoing L2 beam. This configuration creates a cigar-shaped trap. For 0.7 W in the horizontal mDT and a power corresponding to $50 E_r$ in L2, we obtain a trap with frequencies $\omega = 2\pi \times (20, 120, 160)$ Hz.

The beam path of the $\lambda = 578$ nm clock light propagates along the L1 beam. The $\lambda = 556$ nm OSG beam is coaligned to the horizontal imaging $\lambda = 399$ nm beam employed for time-of-flight imaging. A second imaging beam along the vertical direction is used for high-resolution, in-situ absorption imaging. Here, an objective with a numerical aperture of $NA = 0.27$ allows for a resolution of $1.2 \mu\text{m}$ [61].

3.1.3 Laser sources

In the following, we will give a brief overview of the laser sources employed in the experiments presented in this thesis. The optical transitions connecting to the 1S_0 ground state are all in the visible part of the spectrum. In this regime, no commercial high-power laser sources are available. Therefore, we create the desired wavelengths by second harmonic generation (SHG). The light of high-power, near-infrared laser sources is frequency up-converted in custom designed doubling cavities. We employ the $^1S_0 \rightarrow ^1P_1$ and the $^1S_0 \rightarrow ^3P_1$ transition for laser cooling and trapping of ytterbium. Furthermore, we want to address the $^1S_0 \rightarrow ^3P_0$ transition and prepare atoms in the meta-stable state. In total, three custom designed laser systems are employed, operating at $\lambda = 399$ nm, $\lambda = 556$ nm and $\lambda = 578$ nm.

For the creation of a far-off-resonance optical dipole trap for ytterbium in the 1S_0 state, a laser operating $\lambda = 1064$ nm is employed. This wavelength is far detuned from the strong $^1S_0 \rightarrow ^1P_1$ transition at 399 nm and commercial high-power laser sources are available. The light for the magic-wavelength lattice as well as for the magic-wavelength dipole trap are both generated by a commercial Titanium-Sapphire ring laser. A detailed description of the laser sources can be found in Ref. [60].

In the following, we will briefly introduce the so-called clock laser. As we want to investigate the interaction properties between the two orbitals 1S_0 and 3P_0 , a laser system capable of addressing the 6.1 mHz [114] wide $^1S_0 \rightarrow ^3P_0$ transition is required. In order to achieve strong couplings to this ultra-narrow transition and to resolve interaction-induced shifts to the clock transition frequency with a precision on the level of a few hundred

Hertz, a significant reduction of the initial laser linewidth is necessary. We achieve the reduction of the laser linewidth by means of a high bandwidth locking scheme to a reference cavity [151, 152]. The clock laser is based on a high-power infrared laser diode with an elongated external cavity, which reduces the linewidth of the free-running laser well below 100 kHz. The laser is locked to a high-finesse reference cavity with the Pound-Drever-Hall (PDH) locking technique [153, 154]. The reference cavity is made from ultra-low expansion (ULE) glass and exhibits a finesse of $8.46(6) \times 10^4$ [155]. The PDH technique serves as a phase lock with the leakage of the intracavity field as phase reference, i.e. the instantaneous laser phase is compared to its historical average [151]. Thus, the laser linewidth can be reduced well below the cavity transmission linewidth. In order to reduce the laser linewidth, a control loop with a high bandwidth is required. We achieve a control-loop bandwidth of 800 kHz and reduce the laser linewidth down to ~ 30 Hz in the infrared, i.e. ~ 60 Hz after the SHG (see Figure 3.4). The initial construction of the clock laser is documented in Ref. [155]. A detailed discussion of the current setup, as well as an evaluation of the control loop can be found in Ref. [60].

During the course of this thesis, we have set out for the construction of a second-generation clock laser. With the new setup, we want to overcome several limitations of the current setup. In particular, we have introduced a second, so-called pre-stabilisation cavity. The clock light is first locked to the pre-stabilisation cavity in transmission before the lock to the high-finesse cavity is employed. This technique is expected to allow for a more efficient linewidth reduction. In Ref. [156], the construction and characterisation of the new clock laser is presented in detail.

3.2 Experimental sequence

In this section, we present the experimental sequence for the production of a two-component degenerate Fermi gas of ^{173}Yb . It consists of three stages. First, a magneto-optical trap (MOT) is loaded from a Zeeman slower (ZS), decelerating the ytterbium atoms leaving a hot oven. Secondly, the atoms are transferred from the MOT into an ODT and evaporatively cooled down to quantum degeneracy. Then, the actual experiments are performed. Finally, information about the state of the atoms is retrieved via absorption imaging. Since this destroys the atomic sample, we have to restart the experimental sequence. The entire experimental cycle and thus the acquisition of a single data point takes about 35 seconds.

3.2.1 Production of a degenerate Fermi gas

Ytterbium atoms, upon leaving the 400°C hot oven, enter the ZS with an average thermal velocity of 340 m/s. In the ZS, the atoms are longitudinally decelerated with resonant light on the $^1S_0 \rightarrow ^1P_1$ transition. Due to the high scattering rate, a reasonably short ZS is sufficient to slow the atoms below the capture velocity of the MOT (8 m/s), operating on the $^1S_0 \rightarrow ^3P_1$ transition [60].

In the MOT, the atoms are trapped and their velocity in all three dimensions is reduced. After 8 s of loading, the ZS is turned off and the MOT is compressed by increasing the magnetic field gradient and simultaneously decreasing the light power and detuning. This leads to an increase in the atomic density in the MOT, while reducing the temperature at the same time. Owing to the narrow linewidth of the $^1S_0 \rightarrow ^3P_1$ transition, temperatures down to the Doppler temperature of $4.4 \mu\text{K}$ can be reached. We aim for an efficient transfer of the atoms into the ODT, which is turned on during the MOT compression. The highest transfer efficiencies are achieved for hotter samples containing more atoms. Under optimal conditions for ^{173}Yb , we transfer 5×10^7 atoms at a temperature of $20 \mu\text{K}$ into the ODT.

Initially, the ODT has a trap depth of $80 \mu\text{K}$. The trap depth is lowered in an exponential ramp over 14 s to a final value of $0.3 \mu\text{K}$. During the evaporation process, atoms with the highest kinetic energy leave the trap. The change in the trapping potential is so slow that the atomic ensemble can largely rethermalise via elastic collisions. With our evaporation scheme, we routinely produce degenerate Fermi gases at $T \approx 0.14 T_F$, where T_F is the Fermi temperature. The temperatures are determined by fitting a Thomas-Fermi distribution to the momentum distribution of the atoms, obtained from time of flight absorption images.

The harmonically trapped, degenerate Fermi gas is the starting point for all experiments presented in this thesis. The atoms are either adiabatically transferred into the magic dipole trap or into a 3D isotropic lattice.

3.2.2 Manipulation and detection of the nuclear spin

After the MOT, all six nuclear-spin states of ^{173}Yb are equally populated. For the experiments presented in this thesis, we commonly work with a two-spin mixture. Therefore, we have to transfer atoms from one spin state into another. Unlike in alkali atoms, in AEL atoms, the total angular momentum F cannot be manipulated by microwave radiation, due to the absence of a hyperfine structure in the ground state. For this reason, we employ optical pumping on the $^1S_0 (F = 5/2) \rightarrow ^3P_1 (F' = 7/2)$ transition in the beginning of the evaporation. In the presence of an external magnetic field, the Zeeman sub-levels of the 3P_1 state split by $m_F \times 170 \text{ kHz/G}$. The optical pumping is performed at a bias field of $B_{\text{MOT}} = 50 \text{ G}$, which ensures a splitting of several linewidths. Using subsequent σ^\pm -polarised pulses, resonant to the various $^1S_0 (F = 5/2, m_F) \rightarrow ^3P_1 (F' = 7/2, m_F \pm 1)$ transitions, we can prepare any combination of spin states. Due to the $\text{SU}(N)$ symmetry, any prepared spin mixture is stable against depolarisation on experimentally relevant time scales [60].

The detection of the different nuclear spin states also requires an optical technique. In alkali atoms, different spin states can be separated in time of flight employing the Stern-Gerlach effect. Here, the magnetic moment in the ground state is so strong that for magnetic field gradients of a few Gauss per cm different, m_F states can be spatially separated. In AEL atoms, the magnetic moment in the ground state is about 2000 times weaker compared to alkali atoms. Thus, magnetic field gradients of Tesla per cm would be required for

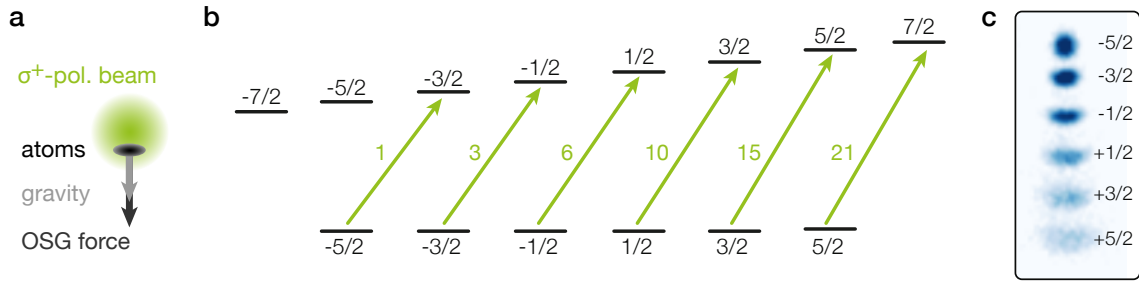


Figure 3.3 – Illustration of the working principle of the optical Stern-Gerlach technique on the 1S_0 ($F = 5/2$) \rightarrow 3P_1 ($F' = 7/2$) transition. (a) Alignment of the OSG beam. (b) The green arrows indicate the σ^+ transitions with the associated Clebsch-Gordon coefficients. (c) Absorption picture of a balanced SU(6) gas after OSG splitting of the m_F states.

a comparable splitting. Therefore, we have implemented a so-called optical Stern-Gerlach technique (OSG) [42, 157]. Here, a σ^+ -polarised, blue detuned laser beam is incident on the atoms. As the light is only 850 MHz detuned from the 1S_0 ($F = 5/2$) \rightarrow 3P_1 ($F' = 7/2$) transition, the optical dipole force is m_F dependent due to the different Clebsch-Gordon coefficients. For σ^+ -polarised light, the Clebsch-Gordon coefficients and thus the dipole force increase monotonically with m_F , as illustrated in Figure 3.3. The center of the Gaussian OSG beam is placed slightly above the atoms. Thus, the atoms are in the region of the steepest gradient, where the dipole force is strongest (see Section 2.3). The force of the OSG adds to the acceleration from gravity during the time of flight and leads to a splitting between the different m_F states.

3.2.3 Clock-line spectroscopy

The clock laser is locked to a high finesse ULE cavity. The cavity is thermally isolated from the environment and temperature stabilised to the zero-crossing of the ULE glass. At this temperature, the ULE glass shows the least susceptibility to thermal fluctuations, because the thermal expansion coefficient of the ULE vanishes to first order. Nevertheless, the reference frequency of the cavity is still susceptible to the ageing of the glass. As the ULE spacer is sagging between the suspension points, the optical length of the cavity shortens. This leads to an increase in the reference frequency. This process is slowing down over time and with it the drift rate of the reference frequency. Therefore, we have to carry out regular reference frequency measurements, in order to cancel this effect.

We perform the frequency reference measurements in an isotropic, 3D magic lattice. The value of the magic wavelength has been measured for ^{174}Yb [158] and ^{171}Yb [134]. By measuring the differential light shift of the clock transition for three different wavelengths, we obtain a magic wavelength of $\lambda_m = 759.30(4)\text{ nm}$ [60] for ^{173}Yb , which is in good agreement with the previously reported values.

For the reference frequency measurements, we employ a spin-polarised Fermi gas ($m_F = -5/2$). The spin-polarised sample is prepared by optical pumping, as discussed above. Here, we achieve temperatures of $T \approx 0.3T_F$. This temperature is sufficiently low

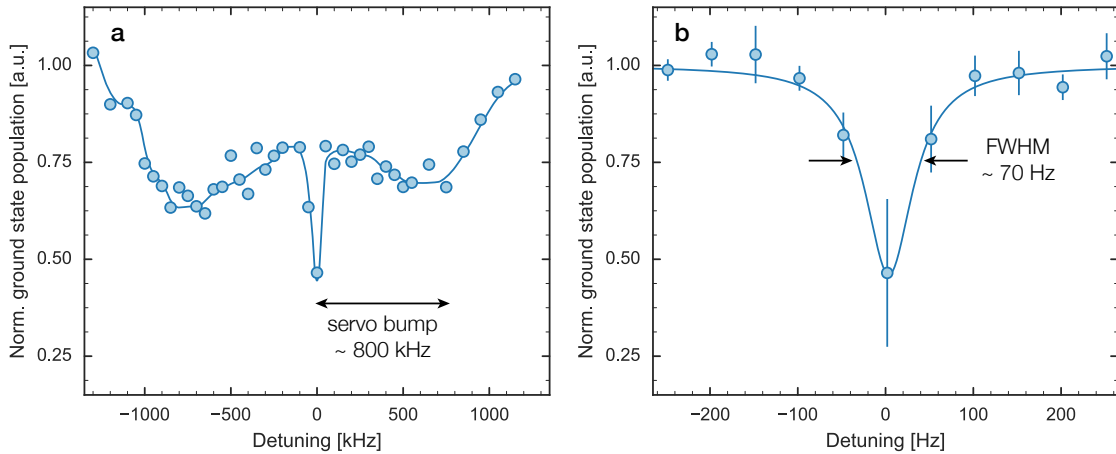


Figure 3.4 – Clock-line spectroscopy of a spin-polarised Fermi gas ($m_F = -5/2$) in a 3D magic lattice at a magnetic bias field of 10 G. (a) High power spectroscopy. A 1500 ms pulse with an intensity of 1.5 W/cm^2 is used. The bandwidth of the control loop can be estimated from the two servo bumps, 800 kHz apart from the carrier. The solid line is a guide to the eye. (b) High resolution spectroscopy. A 250 ms pulse with an intensity of 0.4 mW/cm^2 , corresponding to a Rabi frequency $\Omega = 2\pi \times 40 \text{ Hz}$, is employed. The errorbars represent the standard error around the mean value of six measurements. For our experimental cycle time of 35 s, it takes about 10 min to acquire a single resonance line. The six measurements were taken subsequently within 90 min. A minimum Lorentzian absorption linewidth of 60 Hz is observed. The averaged linewidth for the six measurements is 70 Hz. We can estimate the stability of the laser by comparing the measured linewidth to the absolute transition frequency. The averaged linewidth of 70 Hz corresponds to a fractional long-term stability of 1.4×10^{-13} at 90 min.

to avoid the transfer of atoms into excited bands of the lattice. Typically, we work at an isotropic lattice depth of $30 E_r$, corresponding to a band gap of 19.5 kHz and a bandwidth of 4 Hz in the ground band. In such a deep lattice, the atoms are strongly confined to a lattice site, and the corresponding harmonic oscillator length is shorter than the clock-light wavelength. Motional (band excitations in the lattice) and internal degrees of freedom ($|g\rangle$ and $|e\rangle$) are decoupled, thus satisfying the Lamb-Dicke conditions during the excitation. Furthermore, the deep lattice leads to a flattening of the dispersion relation of the Bloch bands. For bandwidths well below the Rabi frequency of the spectroscopy pulse, the coupling becomes independent of the quasimomentum. As our clock laser offers a linewidth below 100 Hz, we can resolve the band structure of the lattice. Scanning over the red sideband, we find no occupation of atoms in the first excited band [60].

During the excitation process, we apply a bias field of 10 G via the MOT coils. The MOT field sets a well-defined quantisation axis. In the presence of the MOT field, the linear polarised clock light is π -polarised. Therefore, we exclusively drive the transition $^1S_0(m_F = -5/2) \rightarrow ^3P_0(m_F = -5/2)$. The bare reference frequency is extracted by extrapolating the measured frequency to zero magnetic field.

We obtain the best evaluation of the clock transition frequency by incoherent spectroscopy. Here, long pulses with low light intensity are employed. The time of the clock excitation pulse is much longer than the coherence time of the laser, as well as the time

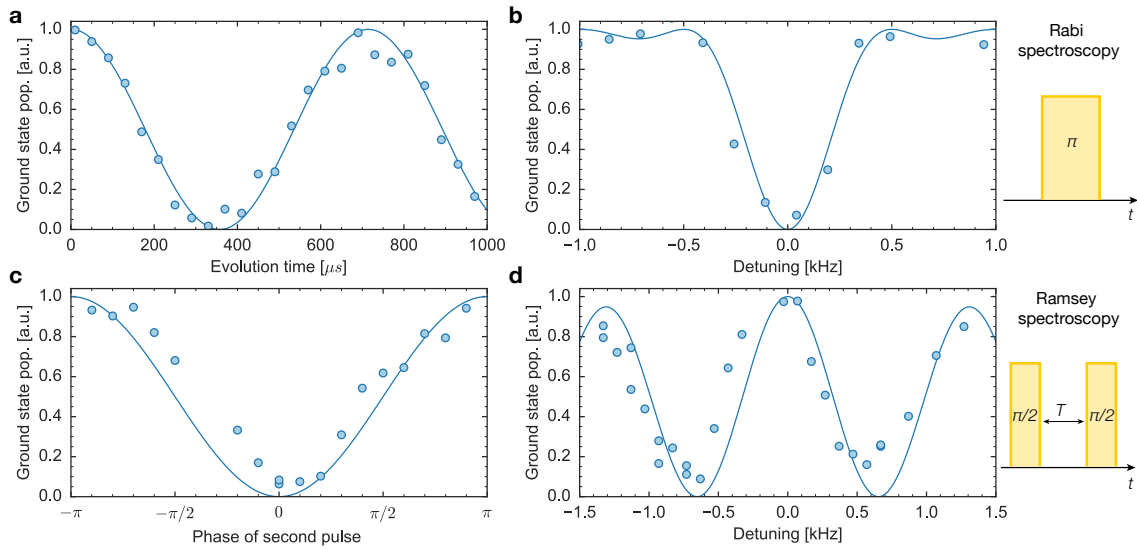


Figure 3.5 – Coherent manipulation of the $^3\text{P}_0$ population. All measurements are performed with a spin-polarised Fermi gas ($m_F = -5/2$) trapped in a magic-wavelength lattice with a depth of $30 E_r$ at a bias field of 10 G. (a) Rabi flopping: the transition is driven on resonance with a light intensity of 0.7 W/cm^2 , resulting in a Rabi frequency of $\Omega = 2\pi \times 1.5 \text{ kHz}$. (b) Fourier-limited Rabi spectroscopy: the transition is probed by a single π -pulse with intensity 40 mW/cm^2 corresponding to $\Omega = 2\pi \times 335 \text{ Hz}$. (c) Ramsey fringe: both $\pi/2$ -pulses are on resonance, after a dark time of $T = 100 \mu\text{s}$, the phase of the second $\pi/2$ -pulse with respect to the first one is varied. (d) Ramsey spectroscopy: the detuning of the two $\pi/2$ -pulses with a fixed dark time of $T = 500 \mu\text{s}$ is scanned. Since the second $\pi/2$ -pulse is phase delayed by π phase shift, all atoms are transferred back into the ground state on resonance.

corresponding to a π -pulse at the given intensity. In this regime, the measured resonance has a Lorentzian lineshape. A maximum excitation fraction of 0.5 can be obtained. The frequency resolution is limited by the linewidth of the clock laser (see Figure 3.4(b)).

By comparing two subsequent measurements of the absolute clock transition frequency under identical conditions, we determine the drift of the ULE cavity. We compensate this drift by applying the measured drift in a feed-forward scheme to the clock laser frequency. Thus, repeated measurements of the resonance result in the same transition frequency.

Figure 3.5 presents two possible coherent manipulation schemes on the clock line. The frequency of the clock light is controlled via an AOM. As the rf frequency for the AOM is generated by direct digital synthesis, we gain control over the frequency and phase of the clock light. Therefore, we can interrogate the clock transition by Rabi as well as Ramsey spectroscopy. The most robust state preparation is achieved by coupling both states via a rapid adiabatic passage.

Orbital Feshbach resonance

In this chapter, we report on the experimental observation of a novel interorbital Feshbach resonance. First, we will discuss the underlying mechanism, that leads to a coupling between the orbital and spin degree of freedom. Here, we will especially emphasise the differences and similarities of the orbital Feshbach resonance with respect to the common Feshbach resonances in alkali atoms, induced by hyperfine interactions. Afterwards, we present two types of experiments, where the resonance is observed at experimentally accessible magnetic field strengths and the universal occurrence for all hyperfine state combinations is demonstrated. We characterize the resonance in a degenerate Fermi gas via interorbital cross thermalisation as well as in a three-dimensional lattice using high-resolution clock-line spectroscopy. Our measurements are well described by a generalized two-channel model of the orbital-exchange interaction. The main result of this chapter have been published in [59].

4.1 An interorbital Feshbach resonance

The basic principles of resonant scattering have already been introduced in Section 1.2, using the example of alkali atoms. Here, we will briefly recall the three major ingredients that are required for the appearance of magnetic Feshbach resonance. Turning to AEL atoms, we show that these conditions are not fulfilled for intraorbital collisions in states with vanishing total angular momentum. However, for interorbital collisions, we demonstrate that these conditions can be matched also by $J = 0$ states. In the end, we derive a formula for the magnetic field dependence of the interorbital scattering length in analogy to the famous Feshbach formula (1.32).

4.1.1 Absence of intraorbital Feshbach resonances for AEL atoms

By studying the collisions between alkali atoms, we have worked out three major ingredients for the appearance of a Feshbach resonance. First, the existence of two coupled collision channels is required. Here, one channel is energetically accessible and connects to the continuum states of the free atoms and is therefore called open channel and a second energetically closed channel. Secondly, if the two channels possess a differential

magnetic moment, their relative energy can be tuned by means of an external magnetic field. And thirdly, a bound state in the closed channel can be brought into resonance with the energy of the incoming atoms due to the differential magnetic moment.

In alkali atoms, the two scattering potentials are caused by the symmetric or antisymmetric alignment of the electron spins during the collision. Since the resulting singlet and triplet potential possess either a total electronic spin of zero or one, their relative energy can be tuned by typically $2\mu_B \approx 2.8 \text{ MHz/G}$. The hyperfine interaction does not conserve the total electronic angular momentum during the collisions and therefore gives rise to a coupling of the two collision channels.

In contrast to alkali atoms, AEL atoms possess no unpaired electron and thus have vanishing electronic angular momentum $J = 0$ in the atomic ground state for the electronic spin singlet 1S_0 as well as for the triplet 3P_0 . Hence, the only contribution to the magnetic moment stems from the nucleus and we expect a very limited tunability of relative energies by a magnetic field. Furthermore, for ^{173}Yb , the reasonably small intraorbital scattering lengths $a_{gg} = 199.4 a_0$ [110] and $a_{ee} = 300 a_0$ [56], suggest that the last bound states of the associated molecular potentials are very deeply bound, on the order of a few MHz.

As already introduced in Section 2.1, for states with $J = 0$, we find a strong decoupling of nuclear and electronic degrees of freedom, the total angular momentum being given by $F = |\mathbf{J} + \mathbf{I}| = I$. Due to this decoupling and the associated suppression of hyperfine coupling, all scattering processes are independent of the nuclear spin projection m_F . Thus, only a single scattering channel exists for all intraorbital collisions. For these reasons, no magnetic Feshbach resonances are expected for collisions within each of the two orbitals

So far, Feshbach resonances in AEL atoms have been observed exclusively in the collisions involving at least one state with a strong magnetic moment. The only long-lived state with a large magnetic moment is the 3P_2 state. Here, Feshbach resonances in the collision between 1S_0 and 3P_2 atoms have been observed for two bosonic isotopes of ytterbium, ^{170}Yb and ^{174}Yb [159]. For the mixtures between alkali atoms in the ground and AEL earth atoms in one of the 3P_J state, various Feshbach resonances have been predicted [160]. The ^6Li - ^{174}Yb (3P_2) mixture is of special interest due to the strong anisotropy of the interaction [161].

Also, optical Feshbach resonances have been proposed [94] and observed [95, 96] for collisions between 1S_0 and 3P_1 atoms. Owing to their limited tunability and lifetime, they have been difficult to exploit in experiments (see Section 1.2.4).

Now, we want to focus on the states 1S_0 and 3P_0 in ^{173}Yb , where we find an $\text{SU}(N = 6)$ -symmetric configuration for the intra- and interorbital interactions. As we have shown in Section 2.1.3, two scattering channels exist for interorbital collisions between atoms in different nuclear spin states. The first experiments concerning the interorbital interaction properties obtained two vastly different scattering lengths for the orbital singlet $a_{eg}^- = 220 a_0$ [56] and orbital triplet channel $a_{eg}^+ > 2000 a_0$ [56, 57]. Recalling the results from Section 1.1.2, we know that such an extremely large scattering length is related to the existence of a shallow bound state. For ^{173}Yb , we estimate a binding energy of the least-bound state $\epsilon_B = -\hbar^2/(ma^2)$ of less than 10 kHz below the continuum energy for the

aforementioned values. This has motivated the prediction of a magnetically tuneable scattering resonance for ^{173}Yb [58]. Note the models applied for the evaluation of the experiments [56, 57] neglected finite range effects. In particular, the value of a_{eg}^+ was strongly overestimated. The following calculations are already based on the value $a_{eg}^+ = 1878 a_0$ [59], determined in the course of these thesis.

4.1.2 Orbital interaction-induced Feshbach resonance

In the following section, we will first give an illustrative picture of the orbital Feshbach resonance. Afterwards, we will construct the Hamiltonian describing the scattering process and solve the two-body problem in free space in order to derive the magnetic field dependence of the scattering amplitude for an interorbital collision.

Let us consider a scattering event between two atoms in the orbital $^1\text{S}_0$ (denoted $|g\rangle$) and $^3\text{P}_0$ ($|e\rangle$) states. For ^{173}Yb with $I = 5/2$, both atoms possess orbital and nuclear spin degrees of freedom. We focus on the case, where the two atoms are in different nuclear spin states ($|\downarrow\rangle, |\uparrow\rangle$) with $m_F^\downarrow, m_F^\uparrow \in -\frac{5}{2} \dots \frac{5}{2}$. The focus on atom pairs with $m_F^\downarrow \neq m_F^\uparrow$ will become apparent in the next paragraph.

While constructing the relative wave function of the two colliding fermionic atoms, we have to ensure anti-symmetrisation under particle exchange. At ultracold temperatures, where all higher partial waves are frozen out, only the s -wave scattering channel is available. Hence, the spatial part of the relative wave function is symmetric and thus enforces an anti-symmetric distribution of the combined orbital and nuclear spin degree of freedom. This results for s -wave collisions in two possible scattering channels: the orbital triplet channel

$$|+\rangle = (|eg\rangle + |ge\rangle) / \sqrt{2} \otimes (|\downarrow\uparrow\rangle - |\uparrow\downarrow\rangle) / \sqrt{2} \quad (4.1)$$

and the orbital singlet channel

$$|-\rangle = (|eg\rangle - |ge\rangle) / \sqrt{2} \otimes (|\downarrow\uparrow\rangle + |\uparrow\downarrow\rangle) / \sqrt{2}. \quad (4.2)$$

The corresponding s -wave scattering lengths are $a_{eg}^+ > 2000 a_0$ and $a_{eg}^- = 220 a_0$, where the superscript $+, -$ denotes the orbital configuration. Since we have assumed $m_F^\downarrow \neq m_F^\uparrow$ the aligned nuclear spin triplet states $|\uparrow\uparrow\rangle$ and $|\downarrow\downarrow\rangle$ are not possible. Thus, the interorbital scattering for atoms in different m_F -states fulfils the first requirement for a Feshbach resonance, two different scattering channels. For atoms with $m_F^\downarrow = m_F^\uparrow$ only the orbital singlet exists, because the nuclear spin is forced into the aligned triplet configuration.

Let us now introduce a finite magnetic field B and study the effect on a pair of separated, non-interacting atoms. We are interested in the pair energies for the Zeeman Hamiltonian magnetic field eigenstates $|e\downarrow\rangle|g\uparrow\rangle$ and $|e\uparrow\rangle|g\downarrow\rangle$, as shown in Figure 4.2. In both states $|g\rangle$ and $|e\rangle$, the degeneracy of the Zeeman sub-levels is lifted in the presence of an external magnetic field due to the finite nuclear Landé g -factors. In the case of an isolated two level system of $^1\text{S}_0$ and $^3\text{P}_0$, both states would share the same g -factors. Thus, spin up-down symmetry would be conserved at finite fields and there would be no

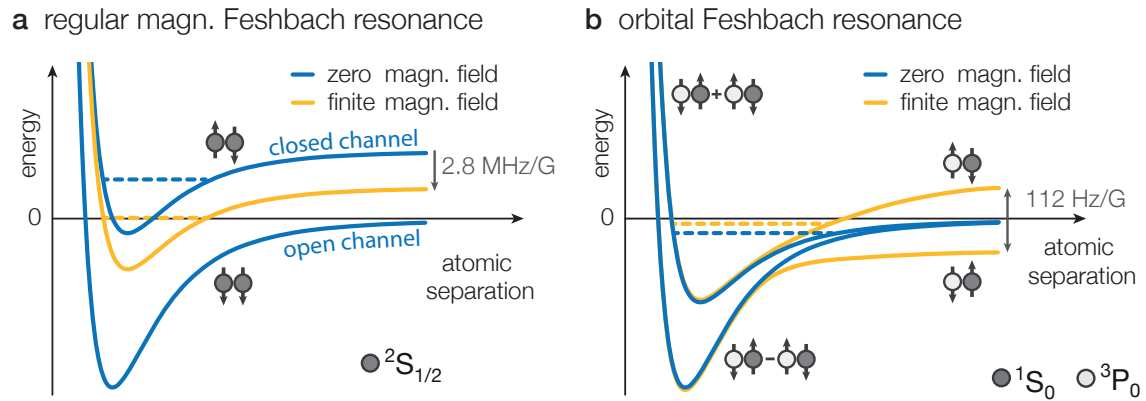


Figure 4.1 – Illustration of the magnetic field dependence of the scattering potential for (a) a regular magnetic Feshbach resonance and (b) an orbital Feshbach resonance in AEL atoms. Blue solid lines represent the scattering potentials at zero magnetic field, whereas the yellow solid lines show the influence of a finite magnetic field. (a) For alkali atoms, the two scattering potentials are given by the spin singlet and triplet channels. Here, open (triplet) and closed (singlet) channel are split by the hyperfine interaction at zero magnetic field. At finite field, the closed channel energy relative to the energy of two far-apart atoms typically scales with twice the Bohr magneton ≈ 2.8 MHz/G. (b) For AEL atoms, the interaction potential at short distances is given by the orbital singlet and triplet scattering channel. Here, the open and closed channel are given by the nuclear spin product states. These are degenerate at zero magnetic field and atoms can enter and leave in both of them, leading to an orbital-exchange interaction. For finite magnetic field, open and closed channel are split by ≈ 112 Hz/G due to different Landé g-factors.

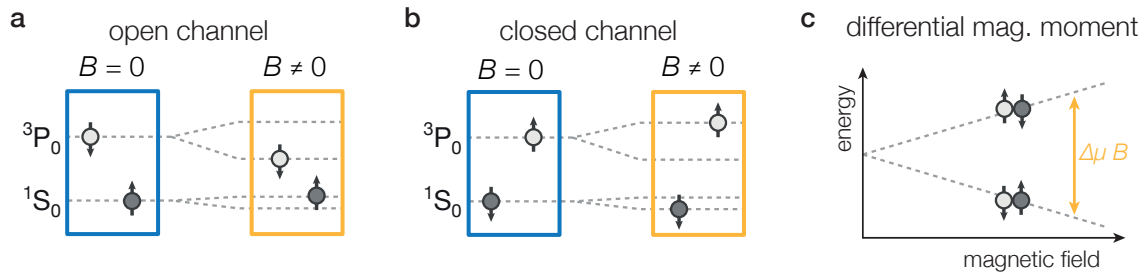


Figure 4.2 – Illustration of the origin of the differential magnetic moment $\delta\mu$ due to different Landé g-factors for the 1S_0 (dark symbols) and 3P_0 (light symbols) states. As drawn, the 3P_0 state experiences a larger energy splitting between $|\downarrow\rangle$ and $|\uparrow\rangle$ compared to the 1S_0 state. Therefore, the atom pair in (a) $|e\downarrow\rangle|g\uparrow\rangle$ has a lower energy compared to the pair in (b) $|e\uparrow\rangle|g\downarrow\rangle$, giving rise to the labelling of open- and closed channel. (c) Magnetic field dependence of the energy splitting $\delta\mu B = \delta m_F B \cdot 112(1) \text{ Hz/G}$ between open and closed channel. Due to the nuclear spin independence of the quadratic Zeeman shift, the linear energy splitting persists for all magnetic fields.

energy difference between the two atom pairs. Therefore, we would not be able to tune the energy of one channel with respect to the other.

However, as discussed in Section 2.2.2, a small admixture of the 3P_1 state into the 3P_0 state, caused by hyperfine interaction, leads to a difference in the nuclear Landé g-factors of $\delta g = g_g - g_e = -8.1 \times 10^{-5}$ [124] for ^{173}Yb . Consequently, the symmetry

between singlet and triplet states is broken under finite magnetic fields and the energy of the depicted atom pairs experiences a shift

$$\begin{aligned}\delta\mu B &= \delta g \delta m_F \mu_B B \\ &= h \delta m_F B \cdot 112(1) \text{ Hz/G.}\end{aligned}\quad (4.3)$$

Because the interaction eigenstates $|\pm\rangle$ are composed of the nuclear singlet and triplet combinations, they cannot be eigenstates of the Zeeman Hamiltonian at the same time. The eigenbasis of the non-interacting system, i.e. two separated atoms, in a magnetic field, is given by the nuclear product states

$$\begin{aligned}|o\rangle &= (|g \uparrow\rangle|e \downarrow\rangle - |e \downarrow\rangle|g \uparrow\rangle) / \sqrt{2} \equiv |e \downarrow\rangle|g \uparrow\rangle, \\ |c\rangle &= (|e \uparrow\rangle|g \downarrow\rangle - |g \downarrow\rangle|e \uparrow\rangle) / \sqrt{2} \equiv |e \uparrow\rangle|g \downarrow\rangle.\end{aligned}\quad (4.4)$$

Since we are effectively dealing with distinguishable fermions, we can omit the anti-symmetrisation of the wave function. Due to the larger Landé g -factor g_e , the energy of $|e \downarrow\rangle|g \uparrow\rangle$ is lower than the one of $|e \uparrow\rangle|g \downarrow\rangle$ in a finite magnetic field, as illustrated in Figure 4.2. Therefore, we introduced the two labels $|o\rangle$ and $|c\rangle$ for the open and closed channel.

With the two sets of eigenstates, we can write down the total Hamiltonian $\hat{H} = \hat{H}_0 + \hat{V}$. The non-interacting part is given by the Zeeman and kinetic part

$$\hat{H}_0 = \sum_{\mathbf{k}} 2\epsilon_{\mathbf{k}} |o, \mathbf{k}\rangle \langle o, \mathbf{k}| + \sum_{\mathbf{k}} (2\epsilon_{\mathbf{k}} + \delta\mu B) |c, \mathbf{k}\rangle \langle c, \mathbf{k}| \quad (4.5)$$

with the differential Zeeman energy $\delta\mu B$ and the kinetic energy $\epsilon_{\mathbf{k}} = \hbar^2 \mathbf{k}^2 / 2m$. Here, \mathbf{k} is the relative momentum of two colliding atoms.

The interaction part is given by

$$\hat{V} = U_+ \sum_{\mathbf{k}, \mathbf{k}'} |+, \mathbf{k}'\rangle \langle +, \mathbf{k}| + U_- \sum_{\mathbf{k}, \mathbf{k}'} |-, \mathbf{k}'\rangle \langle -, \mathbf{k}| \quad (4.6)$$

where U_{\pm} is the corresponding interaction strength in the singlet and triplet channel. Here, we employ a zero-range pseudo potential for the interaction. In this notation, we see that the non-interacting part of the Hamiltonian is diagonal in the basis of the open and closed channel, whereas the eigenbasis of the interaction part are the orbital singlet and triplet states, which we rewrite as

$$\begin{aligned}|+\rangle &= (|o\rangle + |c\rangle) / \sqrt{2}, \\ |-\rangle &= (|o\rangle - |c\rangle) / \sqrt{2}.\end{aligned}\quad (4.7)$$

From this we deduce that the interaction part of the Hamiltonian is not conserving the orbital configuration and leads to an exchange of the orbital degree of freedom. Two separated atoms, approaching each other in the open channel are not in the eigenstate of the interaction Hamiltonian and thus become coupled to the closed channel.

Thus, we finally realise, that all three requirements for a Feshbach resonance are fulfilled. For interorbital collisions in ^{173}Yb there are two scattering channels, where one is supporting a shallow bound state. The energies of a free atom pair in the open channel can be tuned into resonance with the bound state. There is a coupling between open and closed channel based on the orbital exchange interactions.

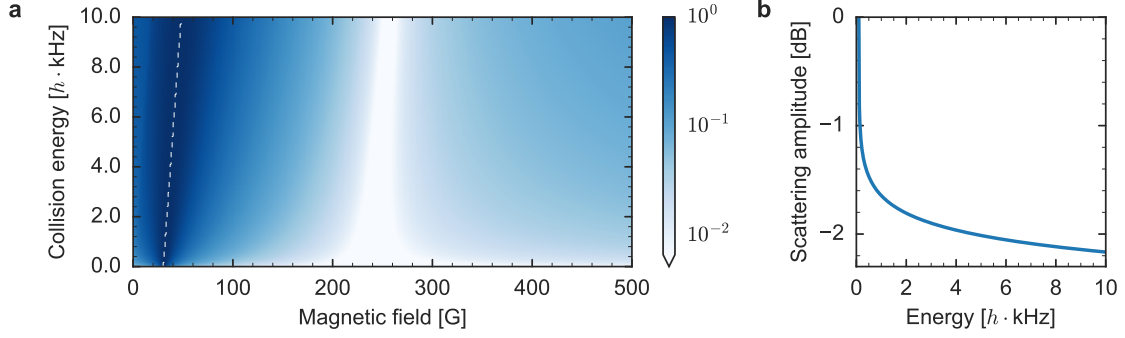


Figure 4.3 – Magnetic field and energy dependence of the open-channel scattering amplitude $f(E) \sim \langle o|T(E)|o\rangle$. For each collision energy, the scattering amplitude is normalised to the maximum value along the dashed line. As $f(E)$ changes over several orders of magnitude, $\log\{f(E)\}$ is plotted. The color scale is limited to two orders of magnitude. (b) Reduction of the maximum in $f(E)$ along the dashed line in (a) with increasing collision energy.

4.1.3 A two-channel model for the interorbital interaction

In order to obtain the magnetic field dependence of the s -wave scattering length in the open channel, we have to solve the two-body problem

$$[\hat{H}_0 + \hat{V}]|\psi\rangle = E|\psi\rangle, \quad (4.8)$$

as shown in Section 1.1.1, where we have studied the elastic scattering of two atoms. We have to calculate the scattering amplitude, i.e. how much of the incident plane wave $|\mathbf{k}\rangle$ is scattered into the outgoing spherical wave $|\mathbf{k}'\rangle$.

Here, we will apply the transition matrix (T-matrix) approach, as another formal treatment of the scattering process. The two-body T-matrix is determined by the Lippmann–Schwinger equation $\hat{T}(E) = \hat{V} - \hat{V}/(E - \hat{H}_0)\hat{T}(E)$ [79]. A detailed derivation of the T-matrix can be found in the Appendix A. The two-body T-matrix fully determines the scattering amplitude. By projecting the T-matrix onto the open channel, we obtain the scattering amplitude in the open channel (see App. A)

$$f(E) = -\frac{m}{4\pi\hbar^2} \langle o|T(E)|o\rangle. \quad (4.9)$$

For s -wave scattering, the T-matrix and thus the scattering amplitude, is independent of the angle between $|\mathbf{k}\rangle$ and $|\mathbf{k}'\rangle$ and only depends on the collision energy $E \sim k^2$. Here, the T-matrix is determined by the matrix equation

$$T(E) = \frac{4\pi\hbar^2}{m} \left[\begin{pmatrix} 1/a_{\text{eg}}^- & 0 \\ 0 & 1/a_{\text{eg}}^+ \end{pmatrix} + \frac{\sqrt{-mE}}{2\hbar} \begin{pmatrix} 1 & 1 \\ 1 & 1 \end{pmatrix} + \frac{\sqrt{m(\delta\mu B - E)}}{2\hbar} \begin{pmatrix} 1 & -1 \\ -1 & 1 \end{pmatrix} \right]^{-1}. \quad (4.10)$$

As usual in scattering theory we use the convention that $\sqrt{-E} = -i\sqrt{|E|}$ if $E > 0$.

The energy and magnetic field dependence of the scattering amplitude (4.9) as determined by the T-matrix is illustrated in Figure 4.3. We clearly see that the scattering

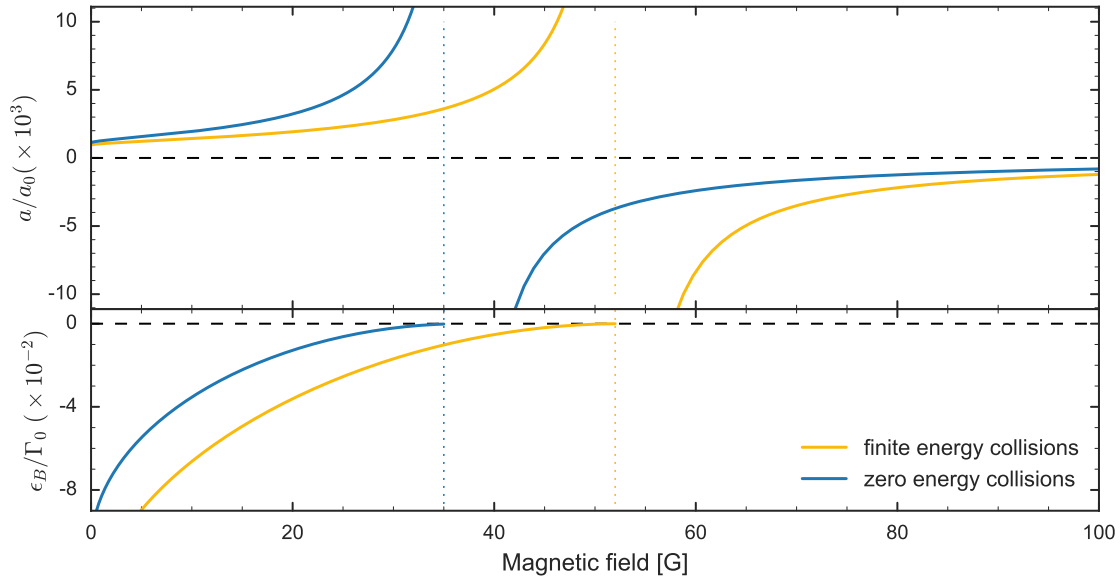


Figure 4.4 – Magnetic field dependence of (a) the s -wave scattering length in the open channel as described by Equation 4.11 and (b) the energy of the bound state, given by the poles of the T-matrix. The blue line is calculated for collisions at zero energy, whereas the yellow line is calculated for a collision energy of 5 kHz, demonstrating the high sensitivity of the resonance position on the collision energy. The molecular state energy is normalized to the resonance strength $\Gamma_0 = \delta\mu \cdot \Delta$, given by product of the differential magnetic moment and the resonance width.

amplitude exhibits a well-defined maximum and minimum, both strongly dependent on the collision energy. With increasing energy, i.e. temperature of the gas, both values shift to higher magnetic fields. In order to retrieve the scattering length, we apply the effective range expansion to the scattering amplitude, as demonstrated in Section 1.1.1. In the limit of low energy scattering $k \rightarrow 0$, we can write $f(E)^{-1} + ik \approx -a^{-1} + \frac{1}{2}r_{\text{eff}}k^2$. Thus, we obtain the open-channel s -wave scattering length

$$a = \frac{1}{2} \frac{1/a_{\text{eg}}^- + 1/a_{\text{eg}}^+ - 2\sqrt{m\delta\mu B/\hbar^2}}{\left(1/a_{\text{eg}}^- - \sqrt{m\delta\mu B/\hbar^2}/2\right)\left(1/a_{\text{eg}}^+ - \sqrt{m\delta\mu B/\hbar^2}/2\right) - \left(\sqrt{m\delta\mu B/\hbar^2}/2\right)^2} \quad (4.11)$$

and the corresponding effective range

$$r_{\text{eff}} = -\frac{\hbar}{\sqrt{m\delta\mu B}} \left(\frac{1/a_{\text{eg}}^- - 1/a_{\text{eg}}^+}{1/a_{\text{eg}}^- + 1/a_{\text{eg}}^+ - 2\sqrt{m\delta\mu B/\hbar^2}} \right)^2. \quad (4.12)$$

The magnetic field dependence of (4.11) is displayed in 4.4. There, we can identify the divergence of the scattering length typical for a Feshbach resonance. The denominator of (4.11) becomes zero and the open channel scattering length diverges when the differential Zeeman shift matches the energy of the bound state in the closed channel. We find the resonance position to be

$$B_0 = \frac{1}{\delta\mu} \frac{\hbar^2}{ma_c^2}, \quad (4.13)$$

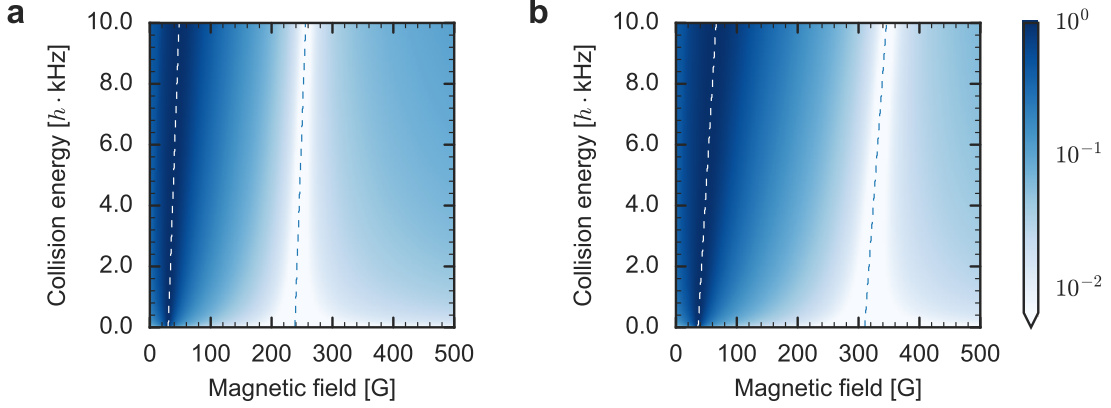


Figure 4.5 – Finite-range effects on the magnetic field and energy dependence of the open-channel scattering amplitude. Here, the scattering amplitude is drawn in a logarithmic scale and normalised to the maximum for each temperature. (a) displays $f(E)$, as it is shown in Figure 4.3. (b) includes finite-range effects in the orbital singlet and triplet channel via the effective range expansion $a^{-1} \rightarrow a^{-1} - \frac{1}{2}r_{\text{eff}}k^2$. The maximum (minimum) of $f(E)$ is indicated by the white (blue) dashed line.

where $a_c = (a_{\text{eg}}^- + a_{\text{eg}}^+)/2$ is the closed-channel scattering length. Inserting the known values for scattering lengths yields a resonance position of $B_0 \approx 33$ G for zero temperature and $\delta m_F = 5$. A smaller differential magnetic moment shifts the resonance to higher magnetic fields. As for regular Feshbach resonances, the orbital Feshbach resonance appears when the bound state in the closed channel crosses the continuum energy. We find the zero crossing of the scattering length by setting the nominator of (4.11) to zero:

$$B_{\Delta} = \frac{1}{\delta\mu} \frac{\hbar}{4m} \left(\frac{1}{a_{\text{eg}}^+} + \frac{1}{a_{\text{eg}}^-} \right)^2. \quad (4.14)$$

We calculate $B_{\Delta} \approx 238$ G, leading to a resonance width of $\Delta_B = B_{\Delta} - B_0 \approx 200$ G.

We have used a zero-range pseudo potential for the interaction and thereby we disregard the finite range of the actual van-der-Waals potential. However, at short distances, we have to consider finite-range effects. These are particularly important for the singlet channel, where the s -wave scattering length a_{eg}^- is only slightly larger than the van-der-Waals length $r_0 = 80 a_0$. Hence, we underestimate the strength and the magnetic field at which the resonance occurs. Applying the effective range expansion to the singlet and triplet channel, we can account for finite-range effects. This is accomplished by the substitution $a_i^{-1} \rightarrow a_i^{-1} - \frac{1}{2}r_{\text{eff},i}k^2$ in (4.11). The effective ranges for the two channels $r_{\text{eff}}^+ = 216 a_0$ and $r_{\text{eff}}^- = 122 a_0$ are calculated as in (1.20), assuming a long-range van-der-Waals potential with $C_6 = 2561$ a.u. [162].

By including the effective range, the position of the orbital Feshbach resonance becomes energy dependent and shifts to higher fields for finite collision energy, as shown in Figure 4.4 and 4.5. In particular, the minimum of the scattering amplitude is very sensitive to finite-range effects. For zero collision energy, the minimum shifts 71 G towards higher fields. The effective range in the open channel (4.12) is large and negative close

to the orbital Feshbach resonance $r_{\text{eff}} = -960 a_0$. For Feshbach resonances in alkali atoms, such large effective ranges are usually found for narrow or closed-channel dominated resonances.

As introduced in (1.2.3), a Feshbach resonance is called narrow for resonance strength $s_{\text{res}} \ll 1$. Here, we find it to be in this regime, with $s_{\text{res}} = 0.15$. This implies a strong atom loss near the Feshbach resonance, due to the strong coupling to the bound state. Owing to the small differential magnetic moment $\delta\mu$, the width of the resonance is several hundred Gauss (see Figure 4.4). This is in contrast to alkali atoms, where $s_{\text{res}} \ll 1$ typically is accompanied by a narrow width in the magnetic field.

By solving the two-body problem, we showed that the scattering length in the open channel can be tuned via an external magnetic field and possesses a resonance at an experimentally accessible field. Furthermore, we find a resonance width of several hundred Gauss, although the resonance shows the characteristics of a narrow resonance with $s_{\text{res}} < 1$. Since the effective range is large, the resonance position is highly dependent on the collision energy. Therefore, in an experiment, we expect to measure a resonance position shifted to higher magnetic fields.

4.2 Determination of the scattering amplitude

In the following, we will determine the elastic and inelastic part of the scattering amplitude and map out the magnetic field dependence of the s -wave scattering length.

In Section 1.2, we have presented various experimental techniques for this. The most precise determination of the position of a Feshbach resonance has been obtained by spectroscopy of the associated bound state [90, 105, 106]. However, this technique cannot be employed for measuring the dimer energy in the bulk in our setup. Instead of an rf transition, we have to excite the bound-to-free transition with an optical photon. Without confining the atoms in an optical lattice and thus ensuring the Lamb-Dicke condition, this is not possible. Therefore, we directly measure the elastic scattering cross section and perform inelastic loss spectroscopy.

4.2.1 Measurement of the elastic cross section

First, we will present our measurements of the interorbital scattering amplitude in the bulk, i.e. in a 3D harmonic trap. We determine the magnetic field dependence of the elastic scattering length by cross dimensional thermalisation (CDT) measurements. Afterwards, we compare our experimental findings to the two-body scattering theory.

Cross dimensional thermalisation

A thermalisation measurement is based on the observation of the relaxation of an out of equilibrium state back into the equilibrium. For the CDT measurement, an anisotropic thermal energy distribution $\eta = E_x - E_y$ along two major axes of the trap is created, where

E_i is the mean energy per particle in the axis i . This anisotropic out-of-equilibrium state decays back into an isotropic thermal distribution by elastic collisions. Due to the elastic collisions, the relative momentum of two scattering atoms is changed, but the total energy is conserved. Chapman and Enskog derived from Boltzmann's transport equation, that in a gas governed by binary collisions, the thermalisation rate is proportional to the mean rate of collision [163]

$$\Gamma_{\text{th}} = \frac{1}{\alpha} \langle n \rangle \sigma_{\text{el}} \langle v_{\text{rel}} \rangle. \quad (4.15)$$

Here, $\sigma_{\text{el}} = 4\pi|f(E)|^2$ is the elastic scattering cross section $\langle n \rangle$ is the atomic density and $\langle v_{\text{rel}} \rangle$ is the relative collision speed, both averaged over the thermal distribution. The dimensionless proportionality factor α is given by the mean number of collisions per particle required for rethermalisation. Numerical simulations have shown that α has a value between 2.5 and 2.7 [164] for s -wave collisions and diverges to 10.5 in the unitary limit [165]. In the limit of low energy scattering $k \rightarrow 0$, the elastic scattering cross section $\sigma_{\text{el}} = 4\pi a^2$ is proportional to the square of the s -wave scattering length. Thus, a divergence in a leads to an enhanced thermalisation rate, whereas thermalisation becomes strongly suppressed for $a \rightarrow 0$.

The relaxation of the energy anisotropy is, in very good approximation, described by a single exponential decay [166]

$$\eta(t) = 1 + \eta_0 e^{-\Gamma_{\text{th}} t}, \quad (4.16)$$

where the amplitude η_0 is fixed by the initial condition $\eta(0) = 1 + \eta_0$. The in-trap energy distribution is measured by releasing the atoms from the trap and imaging them after a sufficiently long time of flight. This maps out the in-trap momentum distribution. The anisotropic energy distribution is therefore mapped onto an anisotropic aspect ratio of the cloud: $\eta(t) \propto \chi(t)$.

The method of CDT is suited to measure minima and maxima in the elastic scattering cross section. However, it is limited in the case of strong interactions where the gas enters the hydrodynamic regime. In this regime, the collision rate exceeds the trap frequency and the assumption of binary collisions breaks down. Instead collective modes govern the relaxation process [167]. The thermalisation rate is then limited by the trap frequency and becomes independent of temperature and density.

Experimental procedure

In order to measure the elastic scattering cross section of in the open channel, we need a mixture of $|e \downarrow\rangle|g \uparrow\rangle$ atoms. Therefore, we create a degenerate two-component Fermi gas $|g \downarrow\rangle|g \uparrow\rangle$, as described in chapter 3. If not mentioned otherwise, we employ the two nuclear spin states $m_F = \pm 5/2$. The $|g \downarrow\rangle|g \uparrow\rangle$ mixture is prepared in an optical dipole trap operating at 1064 nm. This wavelength is anti-trapping for the atoms in $|e\rangle$. Therefore, we transfer the $|g \downarrow\rangle|g \uparrow\rangle$ mixture into a magic-wavelength, i.e. state-independent dipole trap operating at $\lambda_m = 754$ nm. Here, atoms in both states feel the same potential and the CDT is not influenced by differences in the trap frequencies.

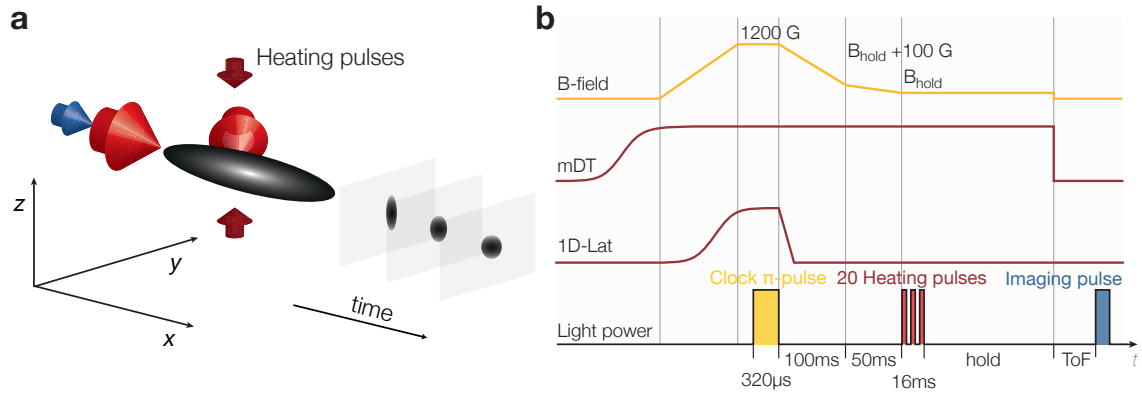


Figure 4.6 – a) Experimental configuration for the observation of cross-dimensional thermalisation of a two-orbital mixture in a harmonic trap. A two-component Fermi gas $|e\downarrow\rangle|g\uparrow\rangle$ in the magic dipole trap is heated along the vertical direction by repeated Bragg pulses. Imaging perpendicular to the heating direction allows to observe the redistribution of the energy. b) Experimental sequence: after preparation of the two-orbital mixture, the 1D lattice is ramped down and the atoms are released into the magic dipole trap. 20 heating pulses with 1,2 kHz repetition rate and 7% duty cycle are applied to heat up the mixture along the vertical direction. The subsequent thermalisation into the perpendicular direction is observed after a variable hold time and 12 ms of time of flight.

In a second step, a one-dimensional (1D), magic-wavelength lattice is adiabatically turned on before the clock-line excitation to the $|e\rangle$ state. Without the lattice, the atoms would be Doppler shifted after the excitation and gain one recoil energy $E_r = h \cdot 2.7$ kHz per photon. This would lead to substantial heating. Therefore, the 1D lattice is coaligned with the 579 nm clock excitation beam which ensures Lamb-Dicke conditions. The π -polarized clock light is resonant with the single atom $|g\downarrow\rangle \rightarrow |e\downarrow\rangle$ transition at the applied magnetic field of $B = 1200$ G. In order to compensate for mean field interaction shifts in the two-dimensional planes and to achieve a high transfer efficiency, we apply a large $\Omega = 2\pi \cdot 1.5$ kHz π -pulse with a corresponding pulse duration of $320 \mu\text{s}$. After the preparation, the $|e\downarrow\rangle|g\uparrow\rangle$ mixture is again released from the 1D lattice into the magic dipole trap. This trap has a cigar shape with trap frequencies $\omega_{x,y,z} = 2\pi \times (20, 120, 160)$ Hz. Simultaneously, the magnetic field is lowered within 100 ms from the preparation value to a value of 100 G above the desired final field strength. In a second ramp, the magnetic field is ramped to the final value with a fixed speed of 2 G/ms. In particular for magnetic fields below the resonance, a fixed ramp speed is required. This ensures, that always the same number of molecules is potentially created during the sweep. The directional heating is applied at the final magnetic field value by pulsing of the vertical lattice beam with an intensity corresponding to a lattice depth of $1 E_r$, and a repetition rate of 1.2 kHz. In total, twenty square pulses with a duty cycle of 7% are applied over a time of three trap oscillation periods. This ensures thermalisation of the cloud along the excitation direction. After the preparation of the energy anisotropy, we allow for thermalisation of the atoms for a variable hold time in the harmonic trap. At the end of the experiment, the traps and magnetic fields are simultaneously switched off. The atoms cloud is expanded for 12 ms

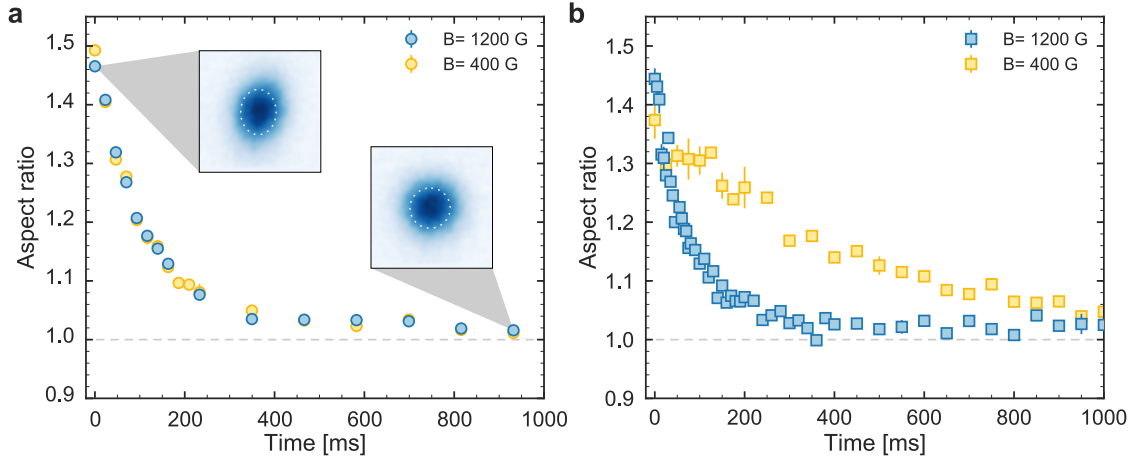


Figure 4.7 – Time evolution of the cloud aspect ratio at different magnetic fields for (a) a $|g \downarrow\rangle|g \uparrow\rangle$ mixture and (b) a $|e \downarrow\rangle|g \uparrow\rangle$ mixture. The insets in (a) display absorption pictures of the atoms after 12 ms ToF for two different evolution times. The white dashed line indicates the fit results from a 2D Gaussian fit to the cloud. The relaxation from a strongly anisotropic cloud back to a cloud in thermal equilibrium is clearly visible for both mixtures. Only the thermalisation rate of the $|e \downarrow\rangle|g \uparrow\rangle$ mixture depends on the magnetic field.

time of flight and the fraction of the atoms in the $|g \uparrow\rangle$ state is imaged via absorption imaging. By fitting a 2D Gaussian function to the spatial distribution of the atoms, we extract the width along the two trap axes y and z . Sample images at the beginning and the end of the thermalisation are shown in the inset of Figure 4.7. We define the cloud aspect ratio as

$$\chi(t) = w_z(t)/w_y(t), \quad (4.17)$$

with $w_i(t)$ being the width along the axis i after a certain evolution time t . Thermalisation measurements are carried out at various magnetic fields from 10 G up to 1200 G, typical data sets of $\chi(t)$ are shown in Figure 4.7. At every magnetic field value, we determine the thermalisation rate $\Gamma_{eg}(B)$ by fitting (4.16) to the time dependence of $\chi(t)$. Furthermore, we perform additional thermalisation measurements with a $|g \downarrow\rangle|g \uparrow\rangle$ mixture, where the clock π -pulse in the preparation sequence is omitted. Thus, the thermalisation rate Γ_{gg} under the same experimental conditions is observed. As we expect the Γ_{gg} to be independent on the magnetic field, we use this measurements together with the known value of a_{gg} as a reference.

Magnetic field dependence of the scattering cross section

The magnetic field dependence of the thermalisation rate for both a $|e \downarrow\rangle|g \uparrow\rangle$ and a $|g \downarrow\rangle|g \uparrow\rangle$ mixture with $\delta m_F = 5$ is presented in Figure 4.8. While Γ_{gg} shows no dependence on the magnetic field, as expected for an $SU(N)$ symmetric situation, we observe a change over two orders of magnitude for the thermalisation rate Γ_{eg} . The magnetic field dependence of Γ_{eg} resembles the characteristic shape of a Feshbach resonance, with a peak position $B_0 = 55(8)$ G and a zero crossing at $B_\Delta = 417(7)$ G. Both values are determined by

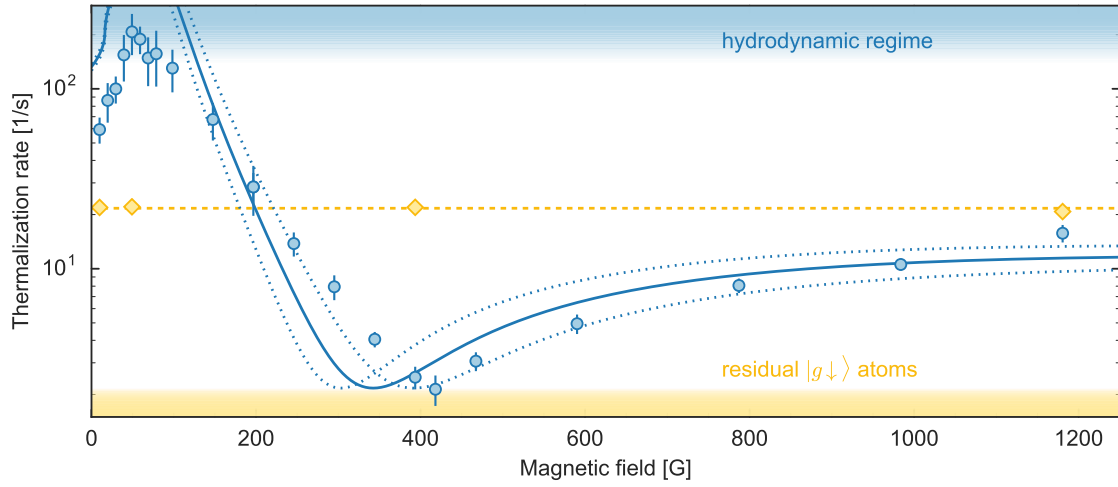


Figure 4.8 – Cross dimensional thermalisation rate as a function of the magnetic field for one orbital (yellow) and two orbital (blue) mixtures, with $\delta m_F = 5(m_F = -5/2; +5/2)$. Error bars denote the 1σ uncertainty of the fit to the cloud aspect ratio. The blue shaded area at the top indicates the hydrodynamic regime, where the color gradient area accounts for the error due to the uncertainty in the trap frequencies. The yellow shaded area is a lower bound due to the thermalisation with residual $|g\downarrow\rangle$ atoms. The blue solid line is the expected thermalisation rate (4.15) based on the magnetic field dependence of the scattering amplitude (4.9) for an $|e\downarrow\rangle|g\uparrow\rangle$ mixture at a temperature of 290 nK. The calculation is based on the values of a_{eg}^{\pm} obtained by clock-line spectroscopy in the 3D lattice. The dashed lines indicate the change in Γ_{eg} due to $\pm 5\%$ variation in a_{eg}^{\pm} .

quadratic fits within ± 15 G (± 40 G) regions around the resonance (zero-crossing) position, respectively.

We make use of the linear dependence of the thermalisation rate on the atomic density (4.15), in order to influence the time scales of the CDT. We carry out CDT measurements with two different atomic densities. At high magnetic fields, where we expect a low scattering cross section, we employ a high atomic density to counteract the diverging time scales. For magnetic fields below 200 G, close to the Feshbach resonance, the thermalisation rate of the high density sample is faster than the excitation process. After the excitation, no anisotropy can be measured. Therefore, we compensate for the large scattering cross section by lowering the atomic density. The two data sets are merged using the reference CDT measurements performed with the $|g\downarrow\rangle|g\uparrow\rangle$ mixture for the two densities at the same magnetic field.

Since intraorbital collisions within the $|e\downarrow\rangle$ or $|g\uparrow\rangle$ atoms are blocked by the Pauli-exclusion principle, thermalisation can only happen through interorbital collisions. Therefore, observing the thermalisation of the $|g\uparrow\rangle$ atoms is sufficient and yields all required information. We verify that the thermalisation is prohibited with a spin polarized $|g\uparrow\rangle$ sample, where no change in $\chi(t)$ is observed over several seconds of thermalisation.

As discussed above, close to the resonance, where the scattering amplitude diverges, the gas enters the hydrodynamic limit. The thermalisation rate is bounded from above by the mean trap frequency of the two observed axes $\omega_r = \sqrt{\omega_y \omega_z}$. Thus, the maximum

possible thermalisation rate is $\Gamma_{\max} = 139(5) \text{ 1/s}$. The error stems from the uncertainty in the determination of the trap frequencies. The hydrodynamic regime is marked in Figure 4.8 by the blue shaded area and nicely bounds the experimental data from above. The fastest measured thermalisation rates are all within the color gradient area, which indicates the error on Γ_{\max} caused by the uncertainty in the trap frequency evaluation.

Due to the finite bandwidth of the clock π -pulse, not all of the $|g \downarrow\rangle$ atoms are transferred into $|e \downarrow\rangle$. A residual fraction of $\approx 10\%$ $|g \downarrow\rangle$ atoms remains. These atoms open up an additional thermalisation channel for the $|g \uparrow\rangle$ atoms. The total thermalisation rate is thus given by $\Gamma_{\text{th}} = \Gamma_{eg} + \Gamma_{\text{res}}$. Since the thermalisation rate is linear in density (4.15), we approximate the contribution of the residual $|g \downarrow\rangle$ atoms to be $\Gamma_{\text{res}} = 0.1 \cdot \Gamma_{gg} = 2.17 \text{ 1/s}$. In our experiment, the thermalisation rate $\Gamma_{\text{th}} = \Gamma_{eg} + \Gamma_{\text{res}}$ is then bounded from below by the magnetic field independent rate Γ_{res} , as indicated by the yellow shaded area in Figure 4.8.

In the regime of moderate scattering amplitudes, the measured thermalisation rates are in good agreement with the theoretical prediction given by Equation (4.15). Away from the hydrodynamic regime, the thermalisation rate is determined by three free parameters, the temperature T and the orbital singlet and triplet scattering length a_{eg}^{\pm} . The temperature determines the mean density $\langle n \rangle = N_0 \cdot \bar{\omega}^3 (4\pi k_B T/m)^{-3/2}$ for the total atom number N_0 and the averaged velocity $\langle v_{\text{rel}} \rangle = \sqrt{16k_B T/(\pi m)}$. Furthermore, the temperature enters in the scattering cross section σ_{eg} via the effective range. Therefore, the three parameters are highly entangled and a fit to all three parameters simultaneously does not converge. In order to make the fit more robust, we have to eliminate one of the parameters. Thus, we use values for a_{eg}^{\pm} , obtained independently by clock-line spectroscopy in a 3D lattice (see section 4.3). With the scattering length fixed, the temperature remains as a single free parameter in our model. We find the best agreement of Γ_{eg} with our experimental data for a temperature of 290 nK. In Figure 4.8, the dashed lines indicate a change in Γ_{eg} due to $\pm 5\%$ variation in a_{eg}^{\pm} .

Universal appearance of the orbital Feshbach resonance

A unique property of this new type of orbital Feshbach resonance is, that it exhibits a universal coupling between open and closed channel with respect to the involved m_F states. Since the interaction channels are fully $SU(N)$ symmetric in the absence of a magnetic field, the choice of the m_F states scales the strength of the coupling only via the varying differential magnetic moment $\delta\mu \sim \delta m_F$. Thus, the orbital Feshbach resonance exists for all m_F combinations with $\delta m_F \neq 0$. The position B_0 and width B_{Δ} are scaled by $1/\delta m_F$, as shown by Equation (4.13) and (4.14). The strength of the resonance s_{res} , proportional to the product of $\delta\mu \Delta_B$, is therefore independent of δm_F . The orbital Feshbach resonance shows the same character for any possible m_F combination. This is in stark contrast to all other Feshbach resonances in alkali atoms, where the choice of the hyperfine levels is crucial for the appearance of a resonance and its character.

In order to demonstrate this unique property, we perform thermalisation measurements with different δm_F . In Figure 4.9 we compare the thermalisation rates for the two

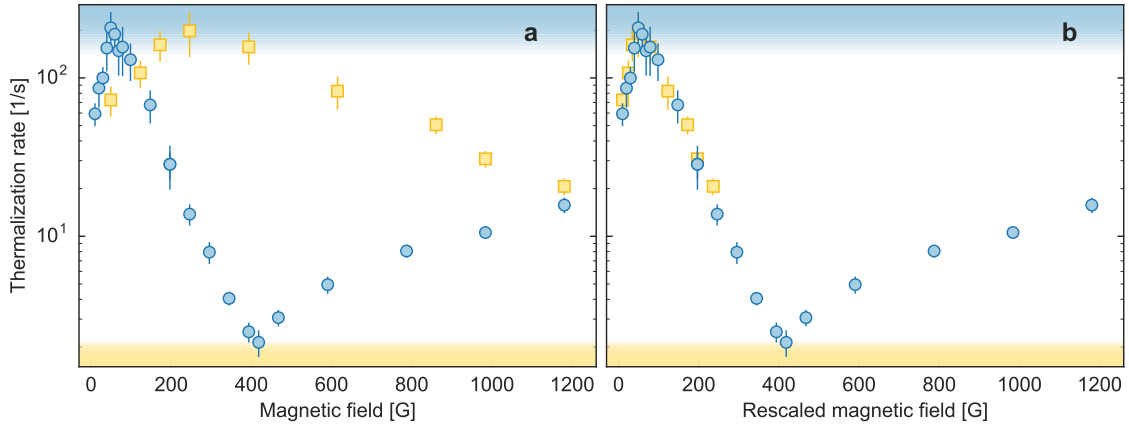


Figure 4.9 – Cross dimensional thermalisation rate as a function of the magnetic field for two-orbital mixtures, with $\delta m_F = 5$, i.e. $m_F = -5/2; +5/2$ (blue dots) and $\delta m_F = 1$, i.e. $m_F = -5/2; -3/2$ (yellow squares). Error bars denote the 1σ uncertainty of the fit to the cloud aspect ratio. The blue shaded area at the top indicates the hydrodynamic regime. The yellow shaded area at the bottom is excluded due to thermalisation with residual $|g, \downarrow\rangle$ atoms. The thermalisation rate is drawn as a function of the absolute magnetic field (a) and for an effective magnetic field $B \rightarrow 1/\delta m_F B$, rescaled with respect to the δm_F . The coincidence of the two data sets demonstrates the universal appearance of the orbital Feshbach resonance for the different m_F combinations.

extreme cases with $\delta m_F = 5$ and $\delta m_F = 1$. As predicted, the resonance exists independent on the involved m_F states. For $\delta m_F = 1$ we identify a resonance position of $B_0 = 275(16)$ G. This corresponds to $B_0(\delta m_F = 1) = 5 \cdot B_0(\delta m_F = 5)$ and thus demonstrates the universal behaviour with respect to different m_F combinations. The expected zero crossing $B_\Delta(\delta m_F = 1) \approx 2100$ G is outside of our experimental magnetic field range. When δm_F is taken into account by rescaling the magnetic field axis correspondingly $B \rightarrow 1/5\delta m_F B$, the data sets collapse onto a single curve without further adjustments (see Figure 4.9(b)).

4.2.2 Determination of the inelastic scattering cross section

In order to gain a complete understanding of the behaviour of the scattering amplitude $f(E)$, we further have to investigate the inelastic part of the scattering cross section σ_{inel} , which is given by $\text{Im}\{f(E)\}$. The most common way of mapping out the magnetic field dependence of σ_{inel} is by observing atom loss from the trap.

Spin resolved losses

We perform two types of loss measurements, where the experimental procedure is the same as for the CDT but without the heating pulses. In a first experiment, we keep the atoms the magnetic field of interest for a fixed time of 150 ms and apply the optical Stern-Gerlach technique to resolve the different nuclear spin states after a short time of flight.

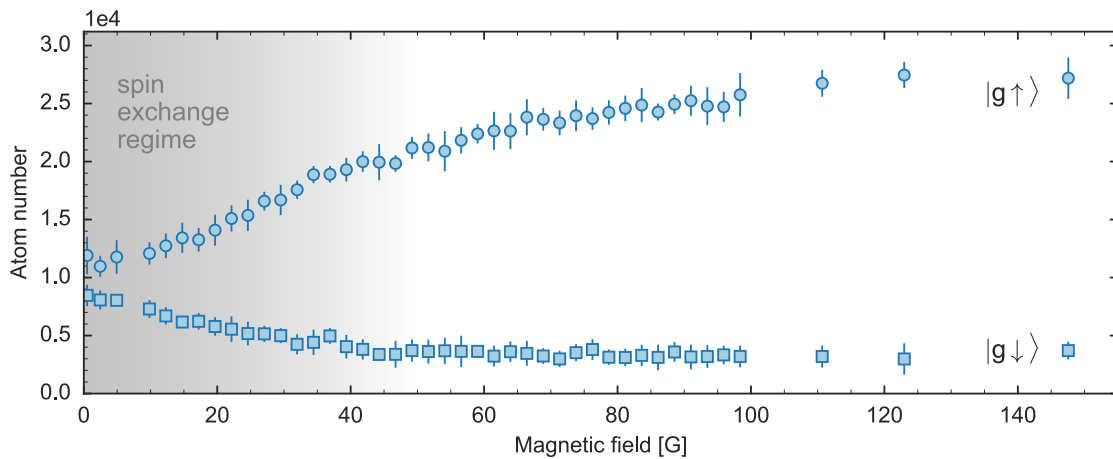


Figure 4.10 – Atom loss in a $|e \downarrow\rangle|g \uparrow\rangle$ mixture after a fixed evolution time of 150 ms as a function of the magnetic field B close to the orbital Feshbach resonance. Number of atoms in the state $|g \uparrow\rangle$ with $m_F = +5/2$ (circles) and the residual $|g \downarrow\rangle$ fraction with $m_F = -5/2$ (diamonds), resolved by spin sensitive measurement using an optical Stern-Gerlach technique. All data points represent averages of at least eight individual measurements.

As shown in Figure 4.10, we observe a magnetic field dependent loss in the $|g \uparrow\rangle$ population close to the orbital Feshbach resonance. However, we cannot identify a maximum in the loss around the orbital Feshbach resonance, but observe increasing losses towards lower fields. As the magnetic field approaches zero, the energy splitting between the open and closed channel vanishes ($\delta\mu B \rightarrow 0$). Thus, the closed channel can no longer be considered energetically closed. Due to the orbital exchange interaction, atoms can leave via this channel after a scattering event. This leads to a depletion of the $|g \uparrow\rangle$ fraction and suggests a stronger loss than actually caused by the inelastic cross section of the open channel. The process is monitored by the repopulation of $|g \downarrow\rangle$ atoms for low magnetic fields.

We account for the exchange process by normalizing the $|g \uparrow\rangle$ population with respect to the one of $|g \downarrow\rangle$, as presented in Figure 4.11. Even after this normalization the maximum of the atom loss is still at zero magnetic field, whereas the maximum in the elastic scattering is at $B_0 = 50$ G. This strong shift between the maximum of the elastic and inelastic part has already been reported for other two-component Fermi mixtures [168, 169]. There, the maximum in the decay rate is shifted by half the width of the Feshbach resonance towards the repulsive side [169]. The shift is caused by the decay of the halo Feshbach molecules.

Since we prepare our $|e \downarrow\rangle|g \uparrow\rangle$ mixture at high magnetic fields and slowly ramp through the Feshbach resonance, we will transfer a fraction of the $|e \downarrow\rangle|g \uparrow\rangle$ pairs into the molecular branch. As these molecules are highly vibrationally excited, one expects these molecules to collide inelastically. During a collision, they can decay into deeper bound states and in consequence are lost from the trap as the binding energy is released as kinetic energy. However, close to the resonance, where the molecules are very weakly bound, their size

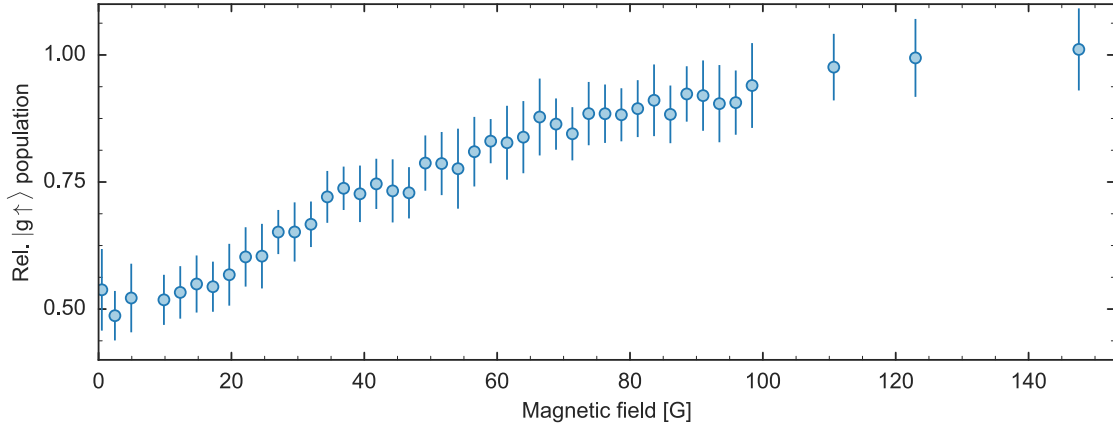


Figure 4.11 – Atom loss in a $|e \downarrow\rangle|g \uparrow\rangle$ mixture after a fixed evolution time of 150 ms as a function of the magnetic field B close to the orbital Feshbach resonance. Relative population of $|g \uparrow\rangle$, i.e. number of atoms in $|g \uparrow\rangle$ normalized to $\tilde{N}_{g\uparrow}(B) = \bar{N}_g - N_{g\downarrow}(B)$, where \bar{N}_g is the ground-state atom number without losses, averaged for fields $B > 120$ G, and $N_{g\downarrow}(B)$ is the residual atom number in $|g \downarrow\rangle$. All data points represent averages of at least eight individual measurements.

diverges and their wave function is more similar to two free atoms. Hence, the Frank-Condon overlap to deeper bound and thus smaller molecules is drastically reduced. This leads to an enhanced lifetime of the molecules close to the resonance. At lower magnetic fields, where the molecules are more tightly bound, the loss increases. Therefore, the maximum of the inelastic scattering is shifted to the left.

Time resolved losses

In a second experiment, we measure the lifetime of an $|e \downarrow\rangle|g \uparrow\rangle$ mixture on the attractive side of the resonance. Here, no bound state is present and the only possible collisions are pure two-body collisions. We use the same preparation scheme as in the previous experiments. After a variable hold time at the magnetic field of interest, we switch off all traps and count the remaining $|g\rangle$ atoms after a short time of flight. A typical time trace of such an experiment is shown in Figure 4.12. We assume that all inelastic collisions are only due to two-body collisions and that thermalisation by elastic collisions is much faster. Therefore, the time evolution of the atomic density is given by

$$\dot{\bar{n}}(t) = -\beta \bar{n}^2(t), \quad (4.18)$$

where β is the two-body decay rate and $\bar{n} = N \bar{\omega}^3 (4\pi k_B T / m)^{-3/2}$ is the mean density for the given temperature T and $\bar{\omega}$ is the geometric mean of the trap frequencies. Since this is an ordinary differential equation, we can directly give the solution

$$\bar{n}(t) = \frac{1}{\alpha + \beta t}. \quad (4.19)$$

Here, α is determined by the initial density $\bar{n}(0) = 1/\alpha$. The $1/e$ lifetime equivalent of the two-body decay (4.19), can be calculated via $\alpha/\beta(e^1 - 1)$. The solid line in 4.12 is a fit

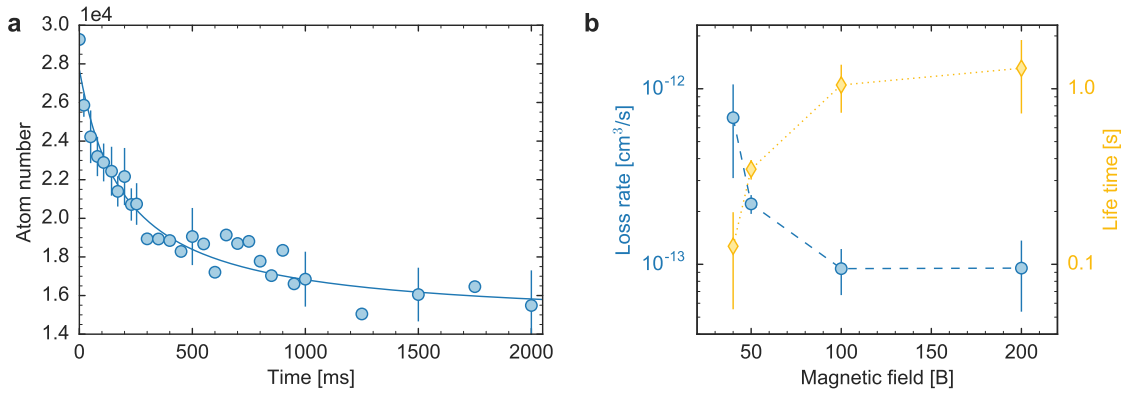


Figure 4.12 – (a) Time trace of the total atom number decay of a $|e \downarrow\rangle|g \uparrow\rangle$ mixture held at a magnetic field of 50 G, close to the Feshbach resonance. The line shows the best fit of the solution of the two-body decay rate equation. (b) The two-body decay rate as a function of the magnetic field (blue circles) and in addition a conversion into the $1/e$ -lifetime is given (yellow diamonds).

of the two-body decay (4.19) to the data. On resonance at 50 G, we extract a two-body loss rate of $\beta = 2.2(3) \times 10^{-13} \text{ cm}^3/\text{s}$. The initial density $\bar{n}(0) \approx 5 \times 10^{13} \text{ atoms}/\text{cm}^3$ is calculated for a temperature of $T \approx 0.3T_F$, which was independently determined. The corresponding $1/e$ -lifetime on resonance is $\tau_{1/e} = 348(4) \text{ ms}$. A simple exponential decay yields a lifetime of $\tau_{1/e} = 386(9) \text{ ms}$. The magnetic field-dependence of β close to the Feshbach resonance is shown in the inset of Figure 4.12. We measure very low loss rates and long lifetimes on the order of seconds on the attractive side of the resonance. They compare well to the ones reported for other fermionic Feshbach resonances [168, 169].

It is important to point out, that these long lifetimes have so far only been observed for broad, i.e. open-channel dominated resonances with $s_{\text{res}} \gg 1$. For the first time, we report long lifetimes for a narrow Feshbach resonance. The long lifetimes exceed the trap oscillation times by far. Therefore, the atoms can undergo multiple elastic collisions before they are lost from the trap. This opens up the possibility of producing strongly interacting and even superfluid Fermi gases close to a narrow Feshbach resonance [58, 170, 171]. Furthermore, it allows to study the interplay of two large length scales, the scattering length and the effective range. It is still unclear, if the unitary regime can be reached under such conditions.

4.2.3 The s -wave scattering length

As a final result, we present the magnetic field dependence of the s -wave scattering length. We extract the elastic, i.e. real part of the scattering length from the CDT measurement and the inelastic, i.e. imaginary part, from the decay rates.

The CDT rate only depends on the scattering length via the scattering amplitude. In the limit of low energy scattering, the scattering amplitude is proportional to $|a|^2$. Since the different CDT experiments have been performed under the same conditions, all further

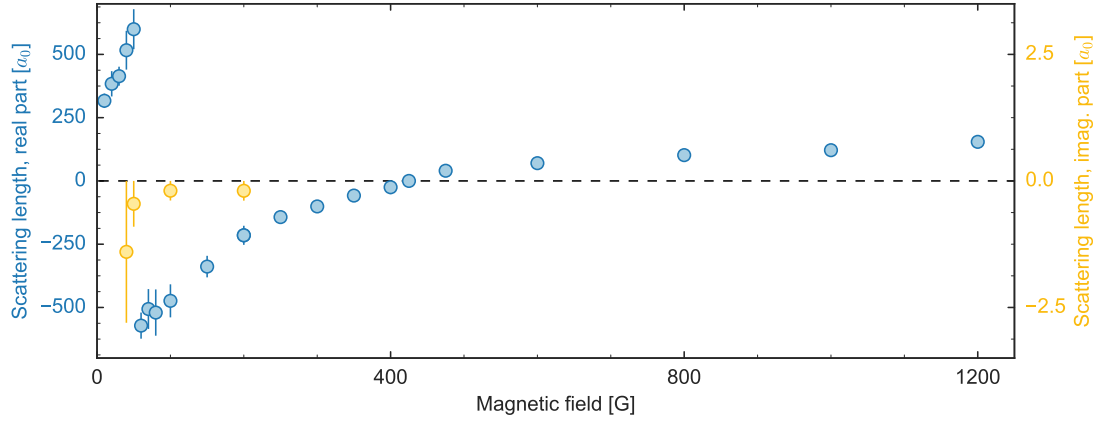


Figure 4.13 – Open channel s -wave scattering length $a_{e\downarrow g\uparrow}$ as a function of the magnetic field. The elastic, respectively real part of the scattering length is based on the cross-thermalisation measurement, where the conversion from the thermalisation rate to the scattering length is based on the reference provided by the background scattering length a_{gg} . The inelastic, respectively imaginary part of the scattering length is based on the loss measurements and converted from the two-body decay rate.

parameters are constant. Thus, we rewrite the thermalisation rate as $\Gamma_{\text{th}} = \kappa|a|^2$, where $\kappa = 4\pi/\alpha\langle n\rangle\langle v_{\text{rel}}\rangle$ is a proportionality factor combining all constants. In order to determine this factor, we make use of the known ground state intraorbital scattering length $a_{gg} = 199.9a_0$ [110]. Thus, we can extract the proportionality factor by $\kappa = \Gamma_{gg}/|a_{gg}|^2$. The modulus of open-channel scattering length is therefore given by

$$|a_{\text{eg}}| = \sqrt{\Gamma_{\text{eg}}/\kappa}. \quad (4.20)$$

The sign of the scattering length is fixed by the knowledge about the resonance position and width, i.e. between B_0 and $B_0 + \Delta_B$ the scattering length has to be negative.

The two-body loss rate coefficient can be related to the thermal average over the inelastic scattering cross section $\beta = 2\hbar/m\langle k\sigma_{\text{in}}\rangle$ [64]. Employing Equation (1.12), we can obtain a scattering length from the two-body loss rate [64]

$$b_{\text{eg}} = -\frac{m}{8\pi\hbar}\beta_{\text{eg}}, \quad (4.21)$$

where $b_{\text{eg}} = \text{Im}\{a_{\text{eg}}\}$.

The results from this conversion are presented in Figure 4.13. As predicted by our model (4.11), we gain the classic resonance shape for the s -wave scattering length across the orbital Feshbach resonance. The ratio between elastic and inelastic collisions is favourable and will in future allow for further investigations of the strongly interacting two orbital quantum gas.

However, Figure 4.13 should be recognised as an illustrative demonstration. Note that the maximum measured scattering length is limited to $\approx 500a_0$. Above, the gas enters the hydrodynamic regime and the thermalisation rate is limited by the trap frequency. Hence, we expect the real value of the scattering length to be much larger. Due to the directional

heating for the CDT, we heat up the atoms to $T \approx 290$ nK. Therefore, the assumption $\sigma_{el} = 4\pi a^2$ in the limit of low energy scattering is violated. Instead we measure $\sigma_{el} = 4\pi |f(E)|^2$, with $f(E) + ik = a^{-1} + 1/2r_{\text{eff}}k^2$. Owing to the large effective range, the collisions are highly energy dependent. Different collision energies will thus result in other resonance positions. As we work with a harmonic trap, we can only measure values averaged over the thermal distribution. This smears out the position of the resonance and the zero crossing.

4.3 Interaction spectroscopy in the isotropic magic lattice

In the previous section, we introduced the new concept of an orbital Feshbach resonance and presented the first experimental observation on such a resonance in an ultracold gas of AEL atoms. We have determined the position and the zero crossing of the resonance in the bulk and have shown that this new kind of resonance appears universally throughout the different m_F -components.

Nevertheless, the quantitative results still exhibit large uncertainties intrinsic to the bulk measurements, because it is hard to disentangle the possible many-body effects from the pure two-body physics. The scattering amplitude is calculated on the basis of the two-body T-matrix, neglecting the effects of the surrounding Fermi sea. Furthermore, due to the narrow character of this Feshbach resonance, i.e. the large effective range, the scattering amplitude is strongly energy dependent. As we keep our atoms in a shallow harmonic trap, we will always perform a measurement averaged over the thermal distribution.

In order to overcome these difficulties, we perform clock-line spectroscopy of a two-component Fermi gas in a three-dimensional (3D) magic-wavelength lattice. In contrast to the measurements in the bulk, we can now probe the two-particle interaction energy of an atom pair on an isolated lattice site. Here, we achieve a high spectral resolution, only limited by the linewidth of our clock laser. We confine the atoms in a deep isotropic lattice with a depth of $\tilde{V} = 29.8E_r$, where E_r is the recoil energy of the lattice light. This corresponds to a band gap of $h \cdot 19$ kHz to the first excited band and a bandwidth of $h \cdot 4$ Hz in the ground band. In this regime, the lattice sites are decoupled and can be approximated as isolated harmonic oscillators (see Section 1.1.3). We employ large atom numbers, leading to singly and doubly occupied lattice sites. Hence, we limit the interaction to two atoms at most and suppress all many-body effects.

Figure 4.14 presents the spectral response of the two-component Fermi gas for varying magnetic field. Since the differential Zeeman shift and the lattice band structure are well characterised, we can easily identify the resonances, stemming from singly occupied sites (dashed black lines). Further resonances are associated to doubly occupied sites. By scanning the clock laser frequency, we probe the interaction energy of an $|e\rangle|g\rangle$ atom pair compared to the initial energy of the $|g\rangle|g\rangle$ pair. Therefore, at zero detuning both pairs have the same interaction energy. The contrast of a resonance, i.e. the number of atoms transferred into the $|e\rangle$ state, depends on the overlap of the final and initial state. We

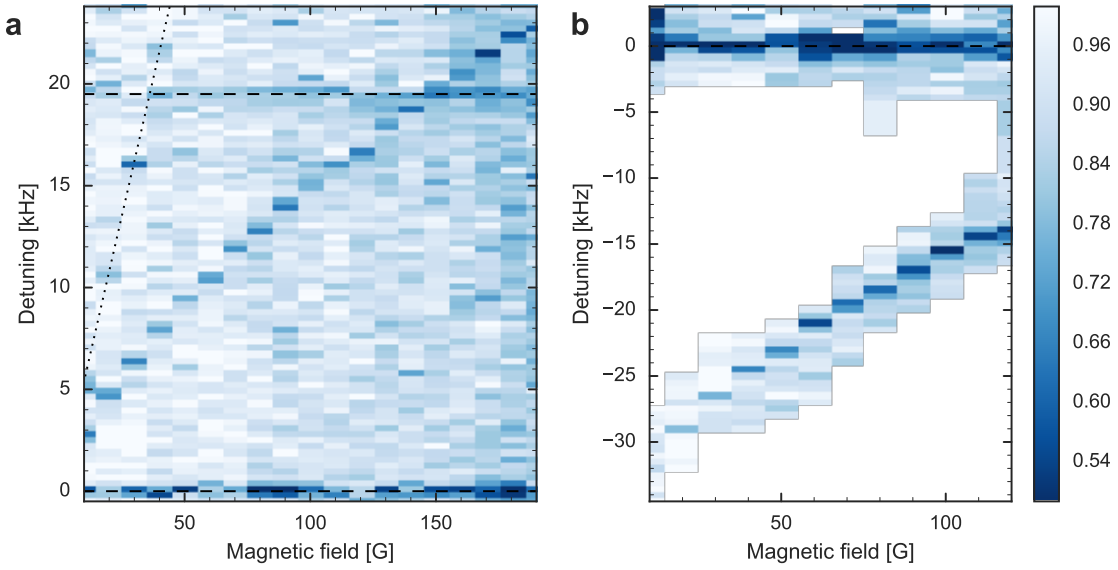


Figure 4.14 – Clock-line spectroscopy spectra of a two-spin Fermi gas ($m_F = -5/2; +5/2$) in a $\tilde{V} = 29.8 E_r$ deep 3D isotropic magic lattice. (a) Low-intensity spectroscopy for determining the $|e\rangle|g\rangle$ atom pair interaction energy with high fidelity. The black lines indicate the position of the single atom transitions. Since the detuning axis is given relative to the transition $|g\downarrow\rangle \rightarrow |e\downarrow\rangle$ (dashed line), the transition $|g\uparrow\rangle \rightarrow |e\uparrow\rangle$ (dotted line) shows twice the differential Zeeman shift. The dashed line at 19 kHz marks the position of the first excited band. (b) High intensity spectroscopy to reveal the binding energy of the molecular branch in the 3D lattice.

use the measured contrast for the assignment of different resonances to the respective the final state. Furthermore, as shown in Figure 4.14 (a) and (b), we perform spectroscopy with high and low intensity at the same magnetic field. Thereby, we can also detect states like the confinement-induced bound state, which possesses a very weak coupling to the initial state.

4.3.1 Two atoms on an isotropic lattice site

In this section, we want to extend our free space scattering model to deep lattices, in order to describe the measured $|e\rangle|g\rangle$ interaction shifts from the clock-line spectroscopy. Therefore, we have to calculate the magnetic-field dependence of the interaction energy on a lattice site. In Section 1.1.3, we have already introduced a model, derived by Busch et al., for the interaction of two particles in a harmonic trap. As we work in a deep and isotropic 3D lattice, we can approximate a lattice site by a harmonic oscillator.

Let us now extend the above formalism of the two-channel scattering process to the case of isotropic confinement with $V(r) = \frac{1}{2}m\omega^2r^2$. As shown in Section 1.1.3, the centre-of-mass and relative motion can be decoupled for harmonic confinement. In the centre-

of-mass frame, the Hamiltonian of the relative motion is given by $\hat{H} = \hat{H}_0 + \hat{V}$, with the non-interacting part

$$\hat{H}_0 = \sum_n \epsilon_n |o, n\rangle \langle o, n| + \sum_n (\epsilon_n + \delta\mu B) |c, n\rangle \langle c, n|. \quad (4.22)$$

Here, n labels the relative harmonic oscillator states with angular momentum $l = 0$, which are the only ones involved in short-range interactions [71]. The non-interacting energy in the harmonic oscillator is given by $\epsilon_n = (2n + 3/2)\hbar\omega$, where ω is the radial harmonic oscillator frequency. The magnetic field dependent energy shift $\delta\mu B$ is caused by the differential magnetic moment $\delta\mu$. For the non-interacting system, the eigenbasis is composed of the open $|o\rangle$ and closed channel $|c\rangle$. The interaction part is diagonal in the basis of the orbital singlet and triplet states $|\pm\rangle$

$$\hat{V} = \sum_{n, n'} \varphi_n(0) \varphi_{n'}(0) \{U^+ |+, n\rangle \langle +, n'| + U^- |-, n\rangle \langle -, n'|\}, \quad (4.23)$$

where U^\pm are corresponding on-site interaction strengths. Here, $\varphi_n(0)$ is the real-space harmonic oscillator wave function at $r = 0$. In order to investigate the scattering properties of this potential, we will use again the T-matrix formalism. A detailed derivation of the T-matrix from the interaction Hamiltonian is presented in the Appendix A. The general shape of the T-matrix is the same as in free space

$$\mathcal{T}(E) = [\tau^{-1} + \mathbf{\Pi}(E)]^{-1}. \quad (4.24)$$

However, here $\mathbf{\Pi}(E)$ is the equivalent of the one-loop polarization bubble on the lattice site

$$\mathbf{\Pi}(E) = \mathbf{\Pi}(E) |o\rangle \langle o| + \mathbf{\Pi}(E - \delta\mu B) |c\rangle \langle c| \quad (4.25)$$

with $\mathbf{\Pi}(E)$ being the renormalized pair propagator in the lattice site, as it was introduced in Eq. 1.23. As we incorporate finite-range corrections, the interaction matrix τ^{-1} becomes dependent on the collision energy

$$\tau^{-1}(E_c) = \sqrt{E} \left(\cot \eta_{eg}^-(E_c) |-\rangle \langle -| + \cot \eta_{eg}^+(E_c) |+\rangle \langle +| \right) \quad (4.26)$$

where η_{eg}^\pm is the s -wave phase shift and the collision energy is $E_c = E - \delta\mu B/2 + 3/2\hbar\omega$. We apply a low-energy expansion up to and including the effective range of both channels. Thus, we can rewrite the scattering phase shift as

$$\frac{\sqrt{mE_c}}{\hbar} \cot \eta_{eg}^\pm(E_c) \simeq -(a_{eg}^\pm)^{-1} + \frac{1}{2} r_{\text{eff}}^\pm \frac{mE_c}{\hbar^2} \quad (4.27)$$

Finally, we arrive at an expression for the interaction energies of the two-particle states in the harmonic trap, given by the poles of the T-matrix

$$\det(\mathcal{T}(E))^{-1} = \det[\tau^{-1}(E_c) + \mathbf{\Pi}(E)] \stackrel{!}{=} 0. \quad (4.28)$$

So far, we have assumed harmonic confinement. As we have already shown in Section 1.1.3, this approximation is only valid for low interaction energies compared to the

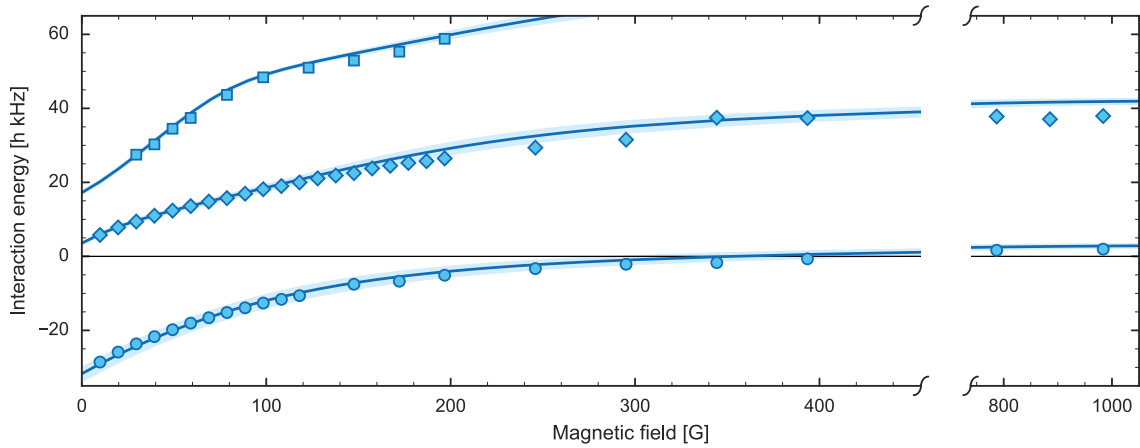


Figure 4.15 – Magnetic field dependence of the $|e\rangle|g\rangle$ atom-pair interaction energy on a lattice site. The values are given relative to the energy of two non-interacting atoms. The assignment of the spectroscopy resonances (circles, squares and diamonds) is based on the observed transition strengths. Solid lines are solutions of the two-particle problem (4.28). Light blue bands indicate a range of variation of the theoretical model spanned by varying a_{eg}^{\pm} by $\pm 10\%$. This figure has been adapted from Ref. [59]

band gap. However, in Figure 4.14, we see that the $|e\rangle|g\rangle$ interaction energy exceeds for high magnetic fields the energy of the first excited band. For such high energies, the pair wave function becomes strongly modified by the anharmonic character of the potential. In analogy to section 1.1.3, we expand the lattice potential in a Taylor series up to the 6th order and correct the harmonic energy spectrum using second-order perturbation theory.

We solve (4.28) numerically by using Newton's root finding algorithm. The effective ranges for the two channels $r_{\text{eff}}^+ = 216 a_0$ and $r_{\text{eff}}^- = 122 a_0$ are calculated analytically, based on the C_6 coefficient [66, 68]. Therefore, the only free parameters in our model are the singlet and triplet scattering lengths a_{eg}^{\pm} .

The new model, incorporating the effective range, is first applied to the zero magnetic field data in [56]. Here, the unperturbed state $|-\rangle$ is probed. A best fit of (4.28) yields $a_{eg}^- = 219.7 \pm 2.2 a_0$. The deviation from the previously published value $a_{eg}^- = 219.5(29)$ stems from the incorporation of the effective range.

In a second step, we fit (4.28) with a_{eg}^+ as the only free parameter to the magnetic field dependence of the interaction energy. We obtain a best fit value $a_{eg}^+ = 1878 a_0$ with a fit uncertainty of $37 a_0$. However, we expect that the uncertainty due to simplifications in our model such as the expansion of the lattice potential in a Taylor series and the first order expansion of the scattering phase shift are comparable or large than this error.

Figure 4.15 demonstrates the good agreement of the best fit of our model 4.28 (solid lines) to the measured interaction shifts. The shaded areas result from a 10% variation of both scattering length in order to illustrate how the model is affected by a variation of these parameters. The model reproduces very well the observed resonances. We have assigned the resonances based on the transition strength to different interaction states

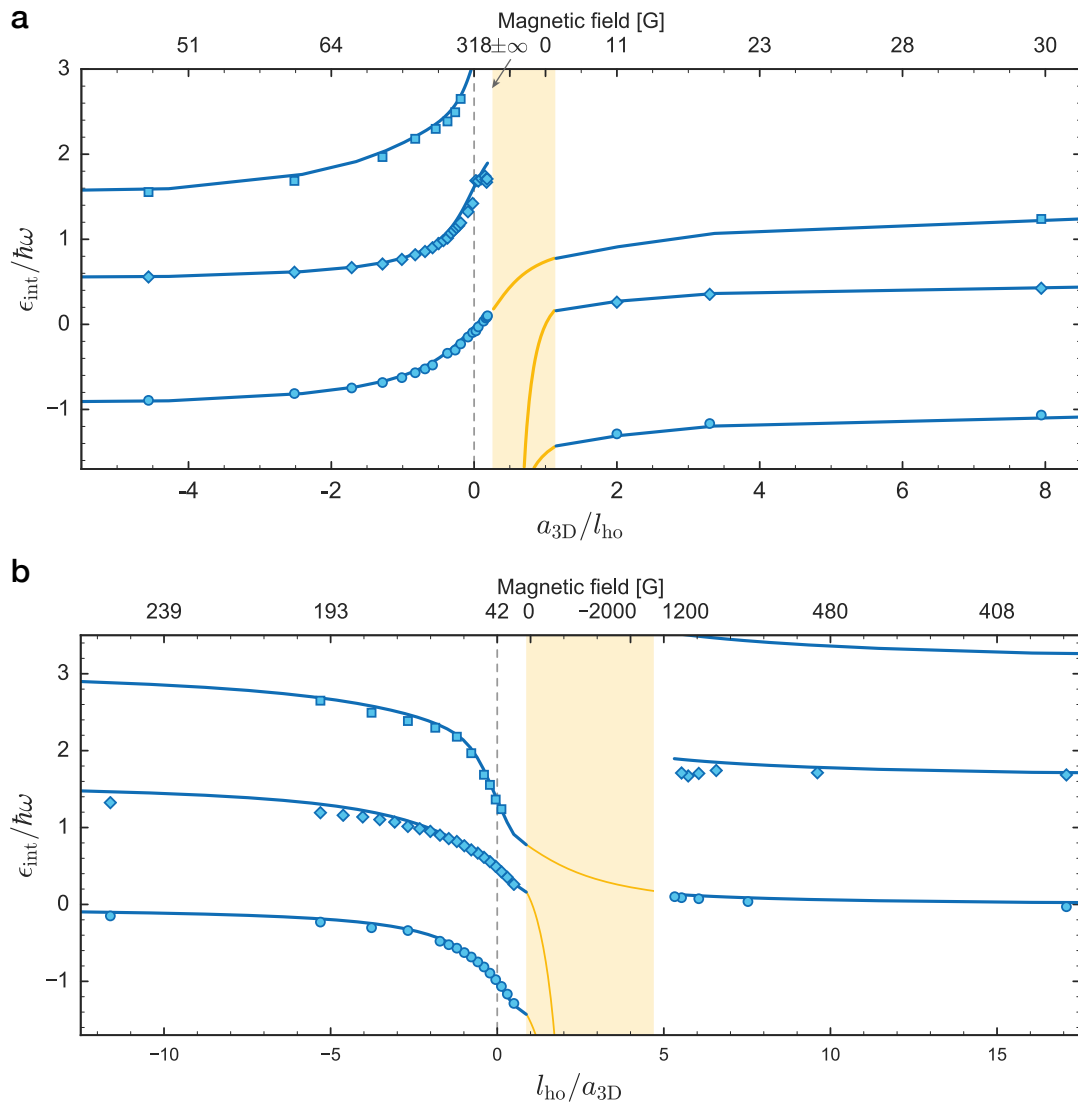


Figure 4.16 – On-site $|e\rangle|g\rangle$ pair energies as a function of (a) the ratio 3D scattering length to the harmonic oscillator length and (b) the inverted ratio. The interaction energies are normalized to the harmonic oscillator spacing $\hbar\omega$. The symbols (circles, squares and diamonds) correspond to the data presented in Figure 4.15. The 3D scattering length is calculated from (4.11) for zero collision energy. The yellow shaded area is experimentally not accessible, since the corresponding 3D scattering length could only be obtained for negative magnetic fields. On the top, the corresponding magnetic fields are indicated. In (a) zero corresponds to the zero crossing of the scattering length, whereas in (b) it marks the positions on the resonance.

(indicated by the three different symbols). As the same symbols correspond to the same branch in the interaction model, this assignment is confirmed.

By calculating the 3D scattering length for each magnetic field, we can parametrise the interaction energies by a_{3D}/l_{ho} . The transformation of the x -axis in Figure 4.16 results in a similar structure of the interaction states, as known from single-channel model (1.23) derived by Busch et al. [71]. Comparing Figure 4.15 to Figure 4.16, we can easily identify the molecular branch. For low magnetic fields we identify the branch with neg-

ative interaction energy as the molecular branch of $|+\rangle$. Extrapolating with our model to zero magnetic field, we extract an on-site bound state energy of $\epsilon_B^+/h = -32(2)$ kHz. For the bound state of the $|-\rangle$ state, we predict an energy of $\epsilon_B^-/h \approx -1$ MHz. This demonstrates once more the sensitivity of the bound state energy on the scattering length and the importance of this shallow bound state ϵ_B^+ for the orbital Feshbach resonance.

4.3.2 Spectroscopic determination of the interaction states symmetry

Our two-channel interaction model reproduces nicely the observed magnetic field dependence of the interaction shift. Now, we want to further verify the proposed coupling mechanism of the orbital Feshbach resonance, i.e. the evolution of the orbital singlet and triplet states at zero field into the open and closed channels at high fields.

First, we will investigate the symmetry of the low field interaction states. So far, we have performed spectroscopy with π -polarised light on a two-component Fermi gas with opposite m_F states. For these states, the Clebsch-Gordan coefficients of the corresponding single-atom π -transitions have the same magnitude but opposite sign. Owing to this change in sign, the π -light changes the sign of the nuclear spin state, $|s\rangle \xrightarrow{\pi} |t\rangle$ and vice versa. Since the initial state is $|gg\rangle \otimes |s\rangle$, the π -light can only couple to the state $|-\rangle = 1/\sqrt{2}(|eg\rangle - |ge\rangle) \otimes |t\rangle$. The excitation into the state $|+\rangle = 1/\sqrt{2}(|eg\rangle + |ge\rangle) \otimes |s\rangle$ is forbidden. A detailed derivation of the two-particle spectroscopy Hamiltonian can be found in [60].

Accordingly, we see in Figure 4.15, that only the $|-\rangle$ is experimentally observed at low fields. However, in order to verify that the low-field state is indeed the state $|-\rangle$, we carry out spectroscopy with σ -polarised clock light in the same lattice configuration. We now employ a spin mixture composed of two adjacent spins $m_F = -5/2; -3/2$, denoted by $|{-5/2}\rangle = |\downarrow\rangle$ and $|{-3/2}\rangle = |\uparrow\rangle$. We detect, by means of an OSG measurement, the loss in each of the two ground-state spin components. The initial spectroscopy state is $|gg\rangle \otimes |s\rangle$. Let us consider the influence of σ^- light on this state. Since we are addressing the $^1S_0(5/2, m_F) \rightarrow ^3P_0(5/2, m_F - 1)$ transition, the σ^- -light exclusively drives atoms from the state $|g, -3/2\rangle$ into $|e, -5/2\rangle$. After the excitation, both atoms have the nuclear spin $m_F = -5/2$. As both nuclear spins are aligned, the final state must be $1/\sqrt{2}(|eg\rangle - |ge\rangle) \otimes |\downarrow\downarrow\rangle$. Associated to this state is the interaction energy $U_{eg}^{\downarrow\downarrow}$. Following the same argument for σ^+ -light, we derive that the final state has the structure $1/\sqrt{2}(|eg\rangle - |ge\rangle) \otimes |\uparrow\uparrow\rangle$ with the corresponding interaction energy $U_{eg}^{\uparrow\uparrow}$.

Figure 4.17 presents the spin-resolved clock-line spectra. The main graph displays the splitting between the π and σ^\pm transitions in a spin-polarised gas in a weak magnetic bias field of 10 G. The inset of Figure 4.17 shows the spectra obtained from the $m_F = -5/2; -3/2$ mixture. Using σ^- light, we detect a resonance in the $|g\uparrow\rangle$ atoms shifted by 0.4 kHz from the single particle transition. This corresponds to the transition into the $|\downarrow\downarrow\rangle$ state. In the $|g\downarrow\rangle$ atoms, we observe using σ^+ light, the transition into the $|\uparrow\uparrow\rangle$ state with the same interaction shift. Therefore, the final states have the same interaction energy $U_{eg}^{\downarrow\downarrow} = U_{eg}^{\uparrow\uparrow}$. This interaction energy matches the energy of the central spin-triplet

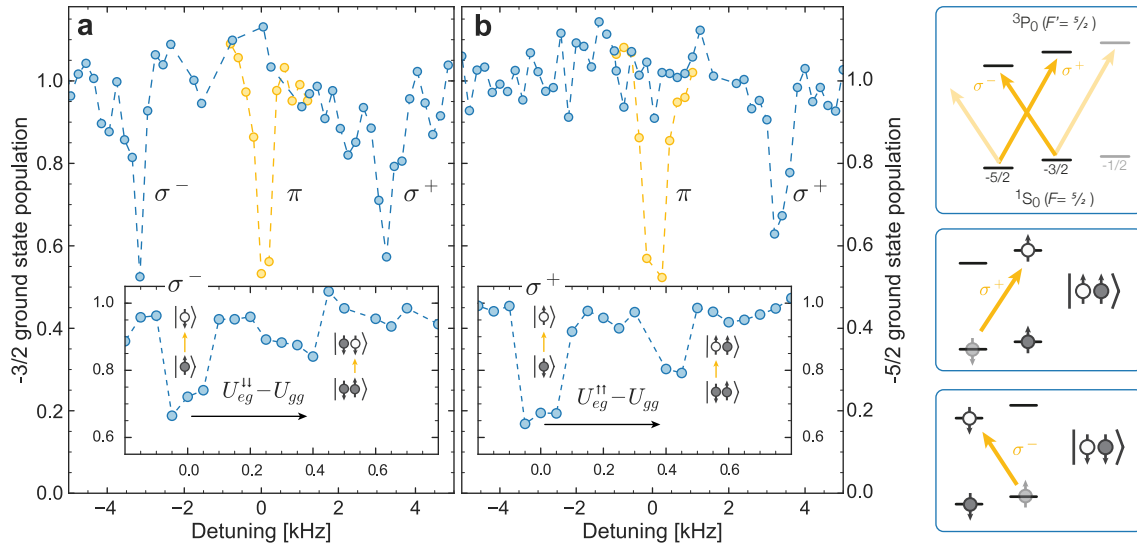


Figure 4.17 – Spin resolved clock-line spectroscopy with π as well as σ^\pm light in a 3D isotropic magic lattice at a bias field of 10 G on a spin polarized Fermi gas. The data shows the normalized ground state population of (a) $m_F = -3/2$ and (b) $m_F = -5/2$, where the frequency axes are referenced to the corresponding π -transition. The insets show a detailed scan of the interaction peak in a two spin mixture ($m_F = -3/2; -5/2$). The detection is spin resolved and the data shows the normalized ground state population of (a) $m_F = -3/2$ and (b) $m_F = -5/2$. As illustrated in the schematic drawing, the σ -light couples the initial spin singlet state to a spin triplet state. In (a) the σ^- -light drives the atoms into the $|\downarrow\downarrow\rangle$ state, whereas the σ^+ -light in (b) drives into the state $|\uparrow\uparrow\rangle$

branch in Figure 4.15, which was measured with π light in the $m_F = -5/2; +5/2$ mixture. This result verifies that this state is indeed the orbital singlet state $|-\rangle$. The actual configuration of the spins ($|\downarrow\downarrow\rangle, |\downarrow\uparrow\rangle + |\uparrow\downarrow\rangle, |\uparrow\uparrow\rangle$) is unimportant for the interaction energy. Only the orbital singlet structure determines the interaction strength.

In a second experiment, we turn back to π -polarised light and $m_F = -5/2; +5/2$ mixture. Now, we will verify by spin-sensitive measurements that the state $|-\rangle$ at low fields evolves into the open channel state $|o\rangle$ at high fields. The high field regime is determined by the differential magnetic moment. The atom pair enters this regime for $\delta\mu B \geq V_{\text{ex}}$. At low fields, the π -polarised light drives the atoms into the state $|-\rangle = 1/\sqrt{2}(|eg\rangle - |ge\rangle) \otimes |t\rangle$. Because this state possesses a symmetric spin configuration $|t\rangle = 1/\sqrt{2}(|\downarrow\uparrow\rangle + |\uparrow\downarrow\rangle)$, we expect to observe a loss in both ground state spin components. In contrast, at high fields, the final state is the nuclear spin product state $|o\rangle = |e\downarrow\rangle|g\uparrow\rangle$. Thus, we expect to see only a loss feature in the $|g\downarrow\rangle$ atoms.

We perform clock spectroscopy at two different magnetic fields. An equal loss in both spin components at low fields indicates that the final state is indeed a superposition of both spin states, as depicted in Figure 4.18. At high fields, the clock light addresses atoms from the state $|g\downarrow\rangle$ exclusively, indicating that the final state is the nuclear spin product state $|o\rangle$.

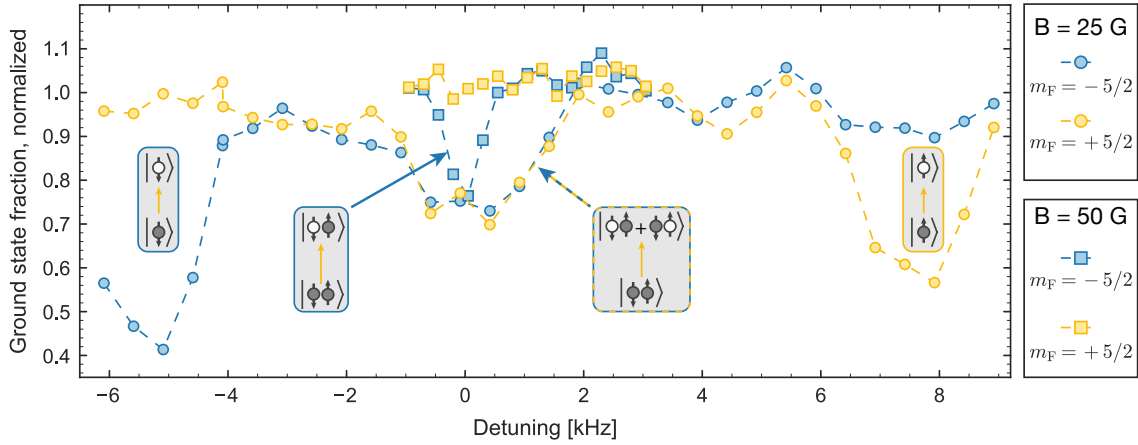


Figure 4.18 – Spin resolved clock-line spectra of a two-spin Fermi gas ($m_F = -5/2; +5/2$) in a 3D isotropic magic lattice at two different magnetic fields. The blue (yellow) dots show the normalized ground state population for 25 G (50 G). The $|e\rangle|g\rangle$ atom pair resonance is chosen as reference for the detuning axis in order to illustrate that the state $|-\rangle$ evolves with increasing magnetic field into $|o\rangle$, i.e. the nuclear spin product state $|o\rangle = |e \downarrow\rangle|g \uparrow\rangle$.

The results from the high-resolution clock-line spectroscopy provide a clear verification of the orbital interaction induced Feshbach resonance. We verified the coupling mechanism between the orbital singlet and triplet states in the presence of a magnetic field through spin-selective imaging. We have shown that the zero-field orbital singlet and triplet state evolve into the open and closed channel states at high magnetic fields. We have developed a new scattering model (4.28) which goes beyond the usual solution of the two-body problem in a harmonic trap, since it incorporates the effect of confinement on both open and closed channel. This model is in very good agreement with the measured magnetic field-dependent interaction energies.

4.3.3 Position of the Feshbach resonance in the bulk

As a final remark, we want to turn back to the Feshbach resonance in the bulk. By removing the many-body effects via the deep 3D lattice, we probe the pure two-body interactions. We employ the values of the singlet and triplet scattering length from the best fit of (4.28) in our scattering theory for the bulk. This enables us to derive a better estimate of the resonance position and zero crossing compared to the cross-thermalisation measurement. For a gas at zero temperature, we calculate a resonance position in the bulk of $\tilde{B}_0 = 42_8^{11}$ G and a zero crossing at $\tilde{B}_\Delta = 319_{62}^{87}$ G. Since the scattering is strongly dependent on the collision energy of the particles due to the narrow character of the Feshbach resonance, the values \tilde{B}_0 and \tilde{B}_Δ are not observed directly in the bulk experiment. For a finite temperature of $T = 290$ nK, we calculate a resonance position $B_0 = 50_8^{11}$ G and the zero crossing $B_\Delta = 327_{62}^{89}$ G. Both values are in good agreement with the results obtained from the independent cross-thermalisation measurement.

A strongly interacting Fermi gas in two dimensions

In this chapter, we study the strongly interacting Fermi gas in two dimensions (2D). The reduction of the dimensionality has dramatic consequences on interacting many-body systems [172]. Already at the level of the bare two-body interaction, the 2D system exhibits completely different scattering properties compared to the three-dimensional (3D) system. Due to the influence of the confinement, a bound state exists for repulsive as well as attractive interactions. This gives rise to an effective 2D scattering length, which is always positive [173]. For Feshbach resonances, we find the pole shifted by the confinement to lower magnetic fields compared to the 3D situation [174]. Also, the many-body physics are strongly altered. Owing to the increased role of fluctuations, the ground state of the 2D system possesses no true long-range order [24]. In solid state systems, we can find strongly interacting 2D Fermi gases for example in the layered structure of cuprate high temperature superconductors [20]. Therefore, studying the attractive 2D Fermi gas may provide a deeper understanding of unconventional superconductivity.

In our experiment, the 2D geometry is realized by means of a one-dimensional (1D) optical lattice. This enables us, to perform spectroscopy of the strongly interacting Fermi gas near the orbital Feshbach resonance. We verify the existence of the confinement-induced dimer at all magnetic fields. Furthermore, we demonstrate the universal scaling of the dimer binding energy at the position of the orbital Feshbach resonance with the confinement depth [173]. By driving the system from the weakly interacting state $|g \downarrow\rangle|g \uparrow\rangle$ into the strongly interacting state $|e \downarrow\rangle|g \uparrow\rangle$, we reveal the existence of a repulsive and attractive polaronic branch.

5.1 Interactions in a quasi-2D geometry

Before we discuss the experimental findings in detail, we will first review the scattering process in 2D. In the first chapter, we have discussed the scattering problem in free space as well as in the presence of an isotropic confinement. Following [175], we will now study how the scattering properties are changed due to the reduced dimensionality. We

directly apply the 2D scattering formalism to our two-channel model for the interorbital interaction.

In our experiment, we confine the atoms in two dimensions by superimposing a deep 1D optical lattice on top of the 3D harmonic trap. The initial 3D Fermi gas is distributed in a set of separated 2D ensembles along the axis of the 1D optical lattice. Each ensemble experiences a transverse harmonic potential $V_z = 1/2m\omega_z^2 z^2$, where we choose the coordinate system such that the 2D system extends in the xy -plane. In the Gaussian vibrational ground state of the potential, the gas has a finite extension along the transverse direction, the so-called harmonic oscillator length

$$l_z = \sqrt{\hbar/2m\omega_z}. \quad (5.1)$$

As long as l_z is much smaller than the inter-particle spacing and the thermal wavelength, all transverse degrees of freedom are frozen out. In our experiment, the inter-particle spacing and thermal wavelength are on the order of 500 nm, whereas the harmonic oscillator length is typically 50 nm or shorter. Under these conditions, the gas is considered to be in a quasi two-dimensional (quasi-2D) regime [176, 177].

Due to the harmonic character of the confining potential, we can separate the centre-of-mass motion from the relative motion. The relative motion along the z -axis, i.e. perpendicular to the 2D plane is simply given by a harmonic oscillator. Therefore, the non-interacting part of the quasi-2D Hamiltonian can be written as

$$H_0 = \sum_{\mathbf{k},n} 2\epsilon_{\mathbf{k},n} |o, \mathbf{k}n\rangle \langle o, \mathbf{k}n| + \sum_{\mathbf{k},n} (2\epsilon_{\mathbf{k},n} + \delta\mu B) |c, \mathbf{k}n\rangle \langle c, \mathbf{k}n|, \quad (5.2)$$

where $\epsilon_{\mathbf{k},n} = \hbar^2 \mathbf{k}^2 / 2m + (n+1/2)\hbar\omega_z$ with n being the harmonic oscillator quantum number for the z -direction and \mathbf{k} the in-plane momentum. Once again, $|o\rangle$ and $|c\rangle$ denote the open and closed channel.

We can derive the two-body interaction strength in the quasi-2D geometry from the bare interaction in 3D by the following consideration. Since the harmonic oscillator length ($l_z \gtrsim 1000 a_0$) is much larger than the range of the van der Waals interaction potential ($r_0 \sim 100 a_0$), the bare two-body interaction remains unaffected by the confinement. We assume that the 3D interaction strength can be separated into a component in the 2D-plane and a perpendicular component. The scattering event $\mathbf{k}_{3D} \rightarrow \mathbf{k}'_{3D}$ gives rise to a change of the in plane momentum $\mathbf{k} \rightarrow \mathbf{k}'$, whereas the relative motion in the transverse harmonic potential changes by $n \rightarrow n'$ [175]. A detailed derivation, of the quasi-2D interaction is presented in the Appendix C. In the quasi-2D basis, the interaction part of the Hamiltonian is given by

$$\hat{V}_{\text{q2D}} = \sum_{\mathbf{k}, \mathbf{k}', n, n'} f_n f_{n'} \{ U^+ |+, \mathbf{k}n\rangle \langle +, \mathbf{k}'n'| + U^- |-, \mathbf{k}n\rangle \langle -, \mathbf{k}'n'| \}, \quad (5.3)$$

with the f -coefficient determined by $f_{2n} = (-1)^n / (2\pi l_z^2)^{1/4} \sqrt{(2n)! / (2^n n!)}$ and $f_{2n+1} = 0$. The states $|\pm\rangle$ label the orbital singlet and triplet state. In analogy to the treatment presented in the previous chapter, we construct the T-matrix

$$\hat{T}_{n,n'}(E) = \sqrt{2\pi} l_z f_n f_{n'} \left[V_{\text{q2D}}^{-1} - \Pi_{\text{q2D}}(E) \right]^{-1} \quad (5.4)$$

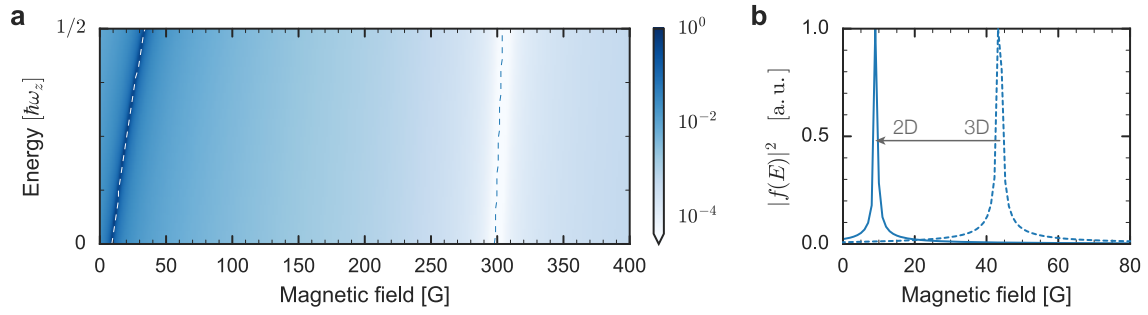


Figure 5.1 – (a) Magnetic field and energy dependence of the quasi-2D open-channel scattering amplitude $f(E)$, calculated for a transverse confinement depth of $25 E_r$. For each energy, the scattering amplitude is normalised to the maximum value along the dashed line. As $f(E)$ changes over several orders of magnitude, we choose a logarithmic color scale. The white and blue dashed line highlight the energy-dependent shift of the maximum and minimum respectively. (b) Confinement-induced shift of the maximum in $f(E)$. In quasi-2D, the pole of \mathcal{T} is shifted towards lower magnetic fields compared to the situation in 3D.

with $\Pi_{\text{q2D}}(E)$ the quasi-2D polarization bubble. In the limit of low-energy scattering and strong confinement $|E| < \omega_z$, we only have to consider scattering in the lowest level $n = n' = 0$. In order to obtain the scattering amplitude, we project the T-matrix onto the open channel. Hence, the scattering amplitude in the quasi-2D geometry in the lowest harmonic oscillator level for low collision energies is given by

$$f_{\text{q2D}}(E) = 2\sqrt{\pi}l_z f_0 f_0 \mathcal{T}_{00}, \quad (5.5)$$

with the matrix element $\langle \mathbf{k}', 0 | \hat{T}_{00}(E + i0) | \mathbf{k}, 0 \rangle$ evaluating to

$$\mathcal{T}_{00} = \sqrt{2\pi} \frac{\frac{l_z}{a_{\text{eg}}} + \frac{l_z}{a_{\text{eg}}^+} + 2\mathcal{F}(\epsilon')}{\left(\frac{l_z}{a_{\text{eg}}} - [\mathcal{F}(\epsilon) + \mathcal{F}(\epsilon')]\right) \left(\frac{l_z}{a_{\text{eg}}^+} - [\mathcal{F}(\epsilon) + \mathcal{F}(\epsilon')]\right) - [\mathcal{F}(\epsilon) + \mathcal{F}(\epsilon')]^2 / 4}. \quad (5.6)$$

Here, we have used the substitution $\epsilon = -E/(\hbar\omega_z)$ and $\epsilon' = -(E + \delta\mu B)/(\hbar\omega_z)$. Analogous to the treatment in free space and isotropic confinement, we incorporate finite range effects by the effective range expansion: $a^{-1} \rightarrow a^{-1} - \frac{1}{2}r_0(mE_c)/\hbar^2$, where the collision energy is given by $E_c = E - \frac{\delta\mu B}{2} + 1/2\hbar\omega_z$. The \mathcal{F} function is determined by the transcendental equation [175]

$$F(\epsilon) = \int_0^\infty du \frac{1}{\sqrt{4\pi u^3}} \left[1 - \frac{e^{-\epsilon u}}{\sqrt{(1 - e^{-2u})/2u}} \right]. \quad (5.7)$$

Figure 5.1(a) present the magnetic field dependence of the quasi-2D scattering amplitude 5.4 for collision energies up to $1/2\hbar\omega_z$. The confinement-induced shift of the pole of the T-matrix towards lower magnetic fields [174] is illustrated in Figure 5.1(b). For low collision energies close to the scattering threshold, i.e. $\epsilon, \epsilon' \ll 1$ we can expand the \mathcal{F} -function into [175]

$$\mathcal{F}_0(x) = \frac{1}{\sqrt{2\pi}} \ln(\pi x / \chi) + \frac{\ln 2}{\sqrt{2\pi}} x + \frac{\pi^2 - 12 \ln^2 2}{48\sqrt{2\pi}} x^2 + \mathcal{O}(x^3), \quad (5.8)$$

where $\chi = 0.905$ is a numerically determined value [173]. Based on the first term of this expansion, we define the effective 2D scattering length [173]

$$a_{2D} = l_z \sqrt{\pi/\chi} \exp\left(-\sqrt{\pi/2} l_z/a_{3D}\right), \quad (5.9)$$

where a_{3D} is the bare 3D s -wave scattering length in the open channel, defined by (4.11). In the limit, where the harmonic oscillator length is larger than the 3D scattering length $|l_z/a_{3D}| \gg 1$, the scattering amplitude can be approximated by [176]

$$f(\mathbf{k}) \approx 2\sqrt{2\pi} a_{3D}/l_z. \quad (5.10)$$

In this regime, the two-body scattering amplitude becomes independent of the collision energy.

5.2 Clock-line spectroscopy of the quasi-2D dimer

Before we start to investigate possible many-body effects of the strongly interacting quasi-2D gas, we want to probe its two-body properties. Therefore, we perform spectroscopy of the two-body bound state, the quasi-2D dimer. In a 3D geometry this technique has been employed by many experiments for a precise determination of the scattering properties near a Feshbach resonance [90, 105, 106]. We perform so-called inverse spectroscopy, where the system is driven from the free states into the bound state. Probing the bound-to-free transition is conventionally called direct spectroscopy. We have the atoms confined in a tight 1D optical lattice, in order to create the quasi-2D quantum gas. The optical lattice is coaligned with the propagation axis of the yellow clock excitation light, as illustrated in Figure 5.2. This geometry ensures Lamb-Dicke conditions during the excitation. Therefore, we can directly probe the quasi-2D gas spectroscopically.

For all experiments presented in the following, the experimental procedure is the same. First, a degenerate two-component Fermi gas $|g \downarrow\rangle|g \uparrow\rangle$ with a temperature of $T = 0.2T_F$ is produced by evaporative cooling in the 1064 nm dipole trap (see Section 3.2). Here, we employ the two nuclear spin states $m_F = \pm 5/2$. We transfer the $|g \downarrow\rangle|g \uparrow\rangle$ mixture into a magic-wavelength, i.e. state-independent dipole trap operating at $\lambda_m = 759$ nm. In a second step, the 1D magic-wavelength lattice is adiabatically turned on. The 2D planes are formed perpendicular to the long axis of the cigar shaped dipole trap. Depending on the atom number, we typically distribute the Fermi gas over 140 to 220 planes. If not mentioned otherwise, we ramp the lattice to a final depth of $V_{\text{lat}} = 25 E_r$, which corresponds to a transverse trapping frequency of $\omega_z = 2\sqrt{V_{\text{lat}} E_r} \approx 2\pi \times 20$ kHz and a harmonic oscillator length of $l_z = 1013 a_0$. An uncertainty of $\pm 1 E_r$ in the calibration of the lattice depth corresponds to $2\pi \times 0.8$ kHz in the trap frequency and $10 a_0$ in the harmonic oscillator length. The radial frequency in the 2D plane is $\omega_r = 2\pi \times 140$ Hz. Finally, the magnetic field is ramped to the desired value. We apply a spectroscopy pulse with varying frequency in order to measure the spectral response of the Fermi gas at the given magnetic field. The overlap of the bound state with the initial state of two free atoms is very weak. In order

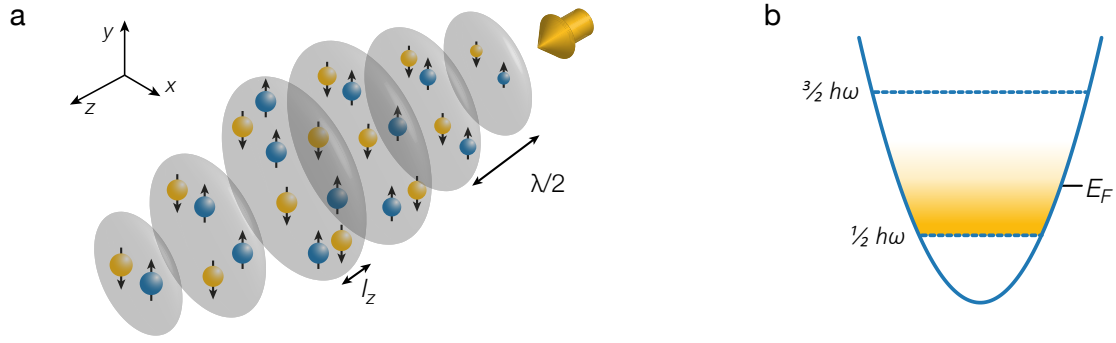


Figure 5.2 – (a) A schematic of the experimental setup. The quasi-2D planes are stacked along the L1 axis. The planes are spaced by half the lattice wavelength and have a finite width of $l_z = 1013 a_0$ for a lattice depth of $25 E_r$. The clock light is coaligned with L1, ensuring the Lamb-Dicke condition during the excitation. The interparticle distance and the harmonic oscillator length are not to scale. (b) Illustration of the transverse harmonic oscillator levels. As long as the Fermi energy in the planes and the temperature are smaller than the harmonic oscillator spacing, the transverse degrees of freedom are frozen out.

to achieve a good spectral resolution, we employ long pulses of duration $\tau = 1$ s with low intensities $I_1 \sim 3$ mW/cm² and $I_2 \sim 0.03$ mW/cm², corresponding to single-particle Rabi frequencies of 100 Hz and 10 Hz respectively. As we drive the system into the bound state, we perform inverse spectroscopy. Directly after the excitation, all traps are switched off and the atoms are released. After a time of flight of 12 ms, the remaining ground-state atoms are imaged.

5.2.1 Magnetic field dependence of the binding energy

Figure 5.3 displays the magnetic field dependence of the quasi-2D dimer across the orbital Feshbach resonance. The data in Figure 5.3(a) is obtained with the higher intensity I_1 . Here, the detuning of the clock light is given relative to the unperturbed single atom transition $|g \downarrow\rangle \rightarrow |e \downarrow\rangle$. Towards lower magnetic fields, where the dimer is more tightly bound, the contrast of the resonance is strongly reduced. For magnetic fields above 60 G, the power broadened resonance of the free transition $|g \downarrow\rangle \rightarrow |e \downarrow\rangle$ overlaps with the dimer resonance. Thus, we employ pulses with the lower intensity I_2 and reduce the power broadening. For this intensity, we can resolve the dimer up to 140 G, i.e. far beyond the resonance position in 3D and thus into the attractive side.

In Figure 5.3(b), the energy of the dimer ϵ_B is plotted relative to the continuum energy E_{th}^{3D} in 3D. In quasi-2D, the dissociation threshold is the energy of the zero-point motion of the harmonic oscillator $\hbar\omega_z/2$. The binding energy ϵ_B is determined by the poles of the two-body T-matrix. The blue lines in Figure 5.3(b) are obtained from solving the equation $\det[\mathcal{T}(\epsilon_B)]^{-1} = 0$ numerically by using Newton's root finding algorithm. The solid line, shows the result for the solution of the quasi-2D T-matrix (5.6), whereas the dashed line represents the free-space T-matrix (4.10). For a_{eg}^- and a_{eg}^+ , we employ the values obtained from the high-resolution clock-line spectroscopy in the previous chapter. Thus, there are

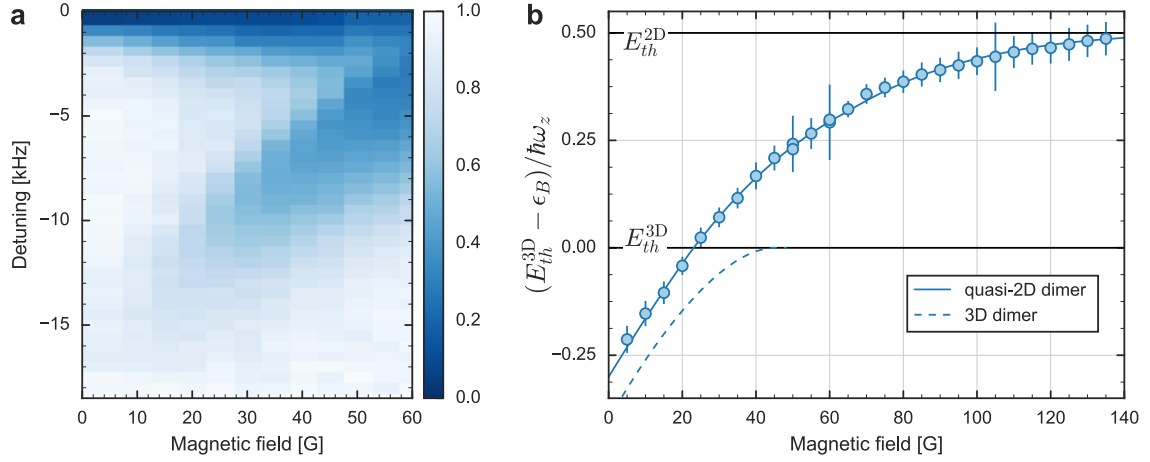


Figure 5.3 – Binding energy of the quasi-2D dimer across the orbital Feshbach resonance. (a) Spectral response of a two-spin Fermi gas ($m_F = -5/2; +5/2$) in a quasi-2D geometry with $\omega_z \approx 2\pi \times 20$ kHz. The normalized ground-state population is shown as a function of the magnetic field and the detuning relative to the single particle transition $|g \downarrow\rangle \rightarrow |e \downarrow\rangle$. (b) Binding energy of the quasi-2D (solid line) and 3D (dashed line) dimer relative to the corresponding threshold energy E_{th} . The solid black lines display the threshold energies $\hbar\omega_z/2$ for quasi-2D and 0 for 3D. The errorbars indicate the 1σ uncertainty of the Lorentzian fit, used to determine the position of the resonance.

no free parameters in this model. The measured resonances are very well reproduced by the two-channel model adapted to the quasi-2D geometry.

In Figure 5.3(b), we can identify two regions, corresponding to the repulsive and attractive side of the Feshbach resonance in 3D. For magnetic fields $B \gtrsim 50$ G, where the 3D scattering length is negative, the 3D dimer vanishes. However, in quasi-2D, the continuum energy is raised by $\hbar\omega_z/2$ because of the harmonic confinement. Therefore, for all magnetic fields a dimer with binding energy $\epsilon_B < \hbar\omega_z/2$ is found. In this regime, the dimer is induced by the confinement. The existence of a bound state for all magnetic fields implies that the effective scattering length in 2D is always positive.

Far away from the resonance, the 3D scattering length (4.11) is smaller than the harmonic oscillator length $l_z/|a_{3D}| \gg 1$. For the given confinement ($V_{\text{lat}} = 25 E_r$), we reach this regime for magnetic fields beyond 100 G. Here, the 3D scattering length is small and negative ($l_z/a_{3D} < -1$) and the dimer spreads out in the 2D plane. Thus, the system approaches the pure 2D regime, where the binding energy takes the form $\epsilon_B = \hbar^2/(2ma_{2D}^2)$ [175]. Based on the expression for the 2D scattering length (5.9), we can write the dimer energy as

$$\epsilon_B \approx \hbar\omega_z \frac{\chi}{\pi} \exp\left\{\sqrt{2\pi} l_z/a_{3D}(B)\right\}. \quad (5.11)$$

In the region of small and positive scattering length ($l_z/a_{3D} > 1$), the dimer is tightly bound. Here, the dimer is so small that it is not influenced by the confinement. The system becomes effectively 3D and the binding energies of the quasi-2D and 3D dimers

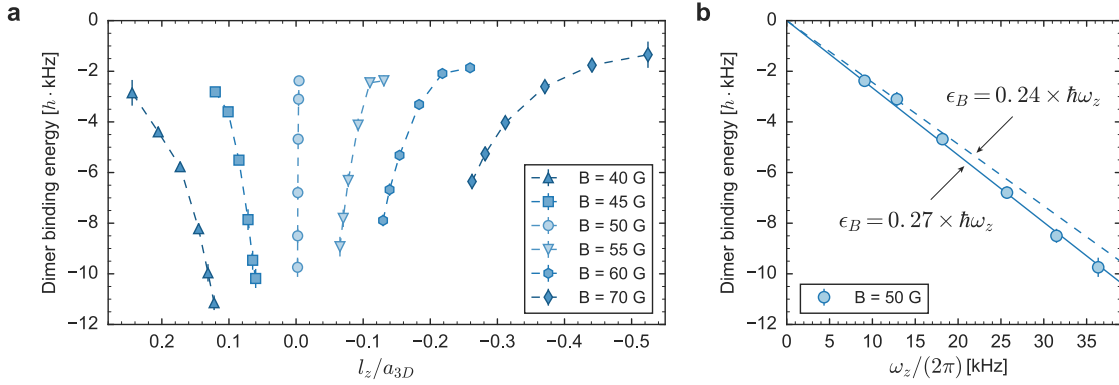


Figure 5.4 – Binding energy of the quasi-2D dimer as a function of the 2D confinement near the orbital Feshbach resonance. (a) Binding energies measured at different magnetic fields as a function of the confinement frequency ω_z . The x-axis is parametrised by the ratio l_z/a_{3D} , where $l_z = \sqrt{\hbar/2m\omega_z}$ and $a_{3D}(B)$ is given by (4.10). The dashed lines are guides to the eye. (b) Binding energy as a function of the harmonic confinement frequency at the position of the resonance in 3D. The dashed line indicates the predicted scaling [173], whereas the solid line is a fit to the data.

are the same. This regime can not be reached in our experiment. For zero magnetic field, the 3D scattering length is still as large as the harmonic oscillator length.

Close to the Feshbach resonance, where the scattering length is large, the dimer is strongly modified by the confinement. At the position of the resonance, the dimer becomes a universal function of the 2D confinement [6]

$$\epsilon_B \approx 0.244 \times \hbar\omega_z. \quad (5.12)$$

As shown in Figure 5.3(b), the binding energy of the quasi-2D dimer acquires this energy at $B \approx 50$ G, the position of the Feshbach resonance in 3D.

5.2.2 Confinement dependence of the binding energy

In a second experiment, we want to investigate the influence of the transverse confinement on the binding energy of the quasi-2D dimer. In order to reveal the universal scaling (5.12), we measure the binding energy as a function of the confinement at different magnetic fields near the orbital Feshbach resonance. Again, the binding energy is determined via inverse spectroscopy, i.e. by associating two free $|g \downarrow\rangle|g \uparrow\rangle$ atoms in to the dimer. The experimental sequence is the same as for the previous measurements with the exception that we vary the final depth of the 1D optical lattice as follows:

$V_{\text{lat}} [E_r]$	5	10	20	40	60	80
$\omega_z/(2\pi)$ [kHz]	9	13	18	26	32	36
$l_z [a_0]$	1515	1274	1072	901	814	758

For the strongest confinement achievable in our experiment, the harmonic oscillator length is much larger than the range of the van der Waals interaction. Hence, the short-range

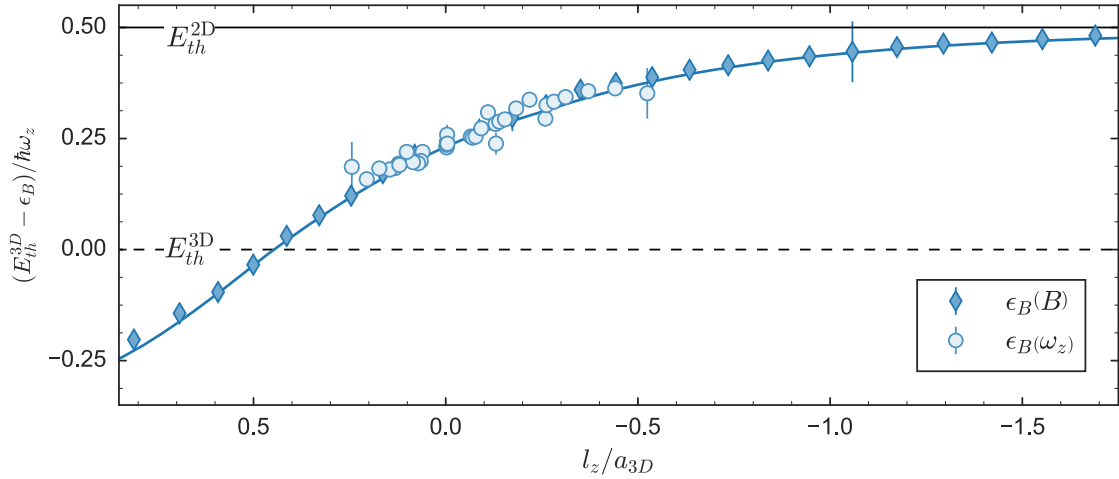


Figure 5.5 – Binding energy of the quasi-2D dimer relative to the dissociation threshold energy as a function of the ratio l_z/a_{3D} . The diamonds correspond to the data already presented in Figure 5.3, whereas the circles are the data points from (a). The data has been obtained as a function of the magnetic field at a fixed confinement depth (diamonds) and as a function of the confinement at a fixed magnetic field (circles) respectively.

physics are unaffected and the assumptions made for the derivation of the two-body T-matrix are valid for all confinements.

Figure 5.4 presents the binding energy of the quasi-2D dimer as a function of the confinement depth. In the previous discussion, we have already used the ratio of the harmonic oscillator length to the 3D scattering length l_z/a_{3D} for characterising the quasi-2D system. Here, in order to pronounce the effect of the confinement, we parametrise the binding energy by the ratio l_z/a_{3D} . In Figure 5.4 (a), data points connected by a dashed line show the confinement dependence of the binding energy at a fixed magnetic field. On both sides of the resonance a stronger confinement causes a deeper bound state. The exponential behaviour of the binding energy (5.11) is not observed, because $l_z/a_{3D} > -1$. As the resonance is approached ($a_{3D} \rightarrow \pm\infty$), the parameter l_z/a_{3D} becomes independent of l_z . On resonance, this gives rise to the linear dependence of the binding energy on the confinement strength, as illustrated in Figure 5.4(b). Here, a best fit of the linear dependence (5.12) results in $\epsilon_B = 0.27(1)\hbar\omega_z$. This is in good agreement with the theoretical value and similar to other experimentally reported values [178, 179]. Figure 5.5 demonstrates that the binding energy relative to the confinement frequency $\epsilon_B/\hbar\omega_z$ is a universal function of the parameter l_z/a_{3D} [173]. When the binding energy is rescaled by the corresponding confinement frequency, all data points collapse and are well reproduced by the solution of the two-body T-matrix.

5.2.3 Many-body effects on the dimer

In a third experiment, we want to study possible many-body effects on the quasi-2D dimer. In the previous chapter, we have performed spectroscopy in a deep 3D lattice. There, we

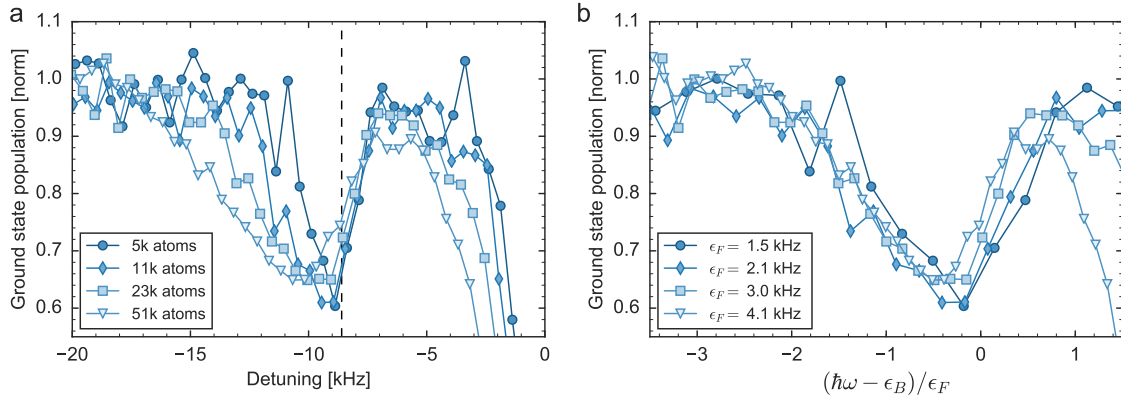


Figure 5.6 – Binding energy of the quasi-2D dimer at a fixed magnetic field for different total atom numbers. (a) Spectral response of the two-component Fermi gas around the transition into the dimer. The detuning is given relative to the single particle transition $|g \downarrow\rangle \rightarrow |e \downarrow\rangle$. The ground state population is normalised to the total atom number. The legend gives the atom number per spin state. Here, the binding energy corresponds to $\epsilon_B = 0.45\hbar\omega_z$. (b) The energy axis is given relative to the binding vacuum two-body energy ϵ_B . Each spectrum is normalised to the Fermi energy in the central plane.

could selectively probe the interaction properties of an isolated atom pair on a single lattice site and found very good agreement with our two-body scattering model. Here, we have also treated the bound state as a pure two-body problem. However, as we typically employ atom numbers up to several ten thousand, the dimer is actually surrounded by a Fermi sea of ground state atoms. Yet, the binding energy, calculated from the two-body T-matrix, reproduces very well the measured binding energies (see Figure 5.3 and 5.4). Based on the assumption that we are probing the transition of two free atoms into a bound state, the transition linewidth is limited by the lifetime of the dimer. Therefore, we would expect to resolve the same linewidth, independent on the total atom number.

Figure 5.6 displays the observed transition spectra for different total atom numbers. Each spectrum is normalised to the corresponding total atom number. For each atom number, we observe the same maximum depletion, about 40 percent. Yet, the width of the resonance depends on the total atom number. With increasing atom number the resonance widens.

We can understand the broadening by considering the effect of the Fermi sea on the dimer. As the associated atoms are initially immersed in a Fermi sea, they originate from different energy levels. Thus, atoms from different initial energies are paired into the dimer. With increasing atom number, the Fermi energy ϵ_F grows and thus the spread in energy. Therefore, we expect all transitions to show the same spectral broadening with respect to the Fermi energy. Figure 5.6(b) shows that after rescaling each resonance with the corresponding Fermi energy, the data sets overlap. The width (FWHM) of the resonance is roughly ϵ_F .

In direct spectroscopy, the high frequency tail of the spectrum is proportional to the contact [180] and exhibits a $\omega^{-3/2}$ decay [181]. The contact can be interpreted as a mea-

surement of the local pair density. The contact is of particular interest in the strongly interacting regime, where strong correlations defy a perturbative treatment. Still, a system in this regime can be described by universal relations based on the contact [12]. To measure the contact, the strongly interacting system has to be prepared in an equilibrium state and probed by direct spectroscopy, i.e. transferred into a non-interacting final state [182]. However, as we have performed inverse spectroscopy, our measurements would only reveal the contact of the weakly interacting initial state. Further, due to the strong final-state interaction an interpretation along these lines is challenging. A possible protocol for future experiments would be to first prepare an $|e \downarrow\rangle|g \uparrow\rangle$ mixture at high magnetic field, where the interorbital interaction is weak. Afterwards the system would be slowly ramped into the strongly interacting regime. There, the contact can be measured via direct spectroscopy back into the weakly interacting state $|g \downarrow\rangle|g \uparrow\rangle$.

In this section, we have presented the results of inverse clock-line spectroscopy of the quasi-2D dimer. The existence of the quasi-2D dimer was observed on both sides of the orbital Feshbach resonance. The demonstration of the magnetic field dependence of the binding energy is a further verification of the existence of the orbital Feshbach resonance. The measured binding energies of the quasi-2D dimer are well reproduced by the two-channel model based on the orbital scattering length obtained in the previous experiments. On resonance, we have showed the universal scaling of the binding energy with the 2D confinement frequency.

5.3 Spectroscopy of the quasi-2D many-body system

After the detailed spectroscopic study of the dimer properties, we want to probe possible many-body interaction effects of the quasi-2D Fermi gas. For alkali atoms, the technique of inverse spectroscopy has already been applied to measure the mean-field interaction shift in a strongly interacting Fermi gas [183]. Furthermore, recent studies of strongly interacting Fermi gases have revealed the existence of metastable polarons in 3D [184, 185] and 2D [186, 187].

So far, we have employed long and low-intensity pulses, in order to achieve a good resolution of the dimer binding energy. We have ensured a good contrast of the dimer resonance, by adapting the pulse intensities to suite the decreasing overlap with the tightly bound dimer. Now, we will employ short pulses with a fixed intensity for the entire magnetic field range. Thus, by measuring the spectral response of the Fermi gas via inverse spectroscopy we are susceptible to possible short time dynamics in the strongly interacting Fermi gas, e.g. metastable quasiparticles such as polarons. Further, using a constant pulse intensity in the various interaction regimes allows us to observe how the overlap into the final state changes.

The experiment starts, with the preparation of a weakly interacting two-component Fermi gas $|g \downarrow\rangle|g \uparrow\rangle$ at a temperature of $0.2T_F$ in the dipole trap. In order to promote density dependent interaction shifts, we employ a large atom number. Both spin states are

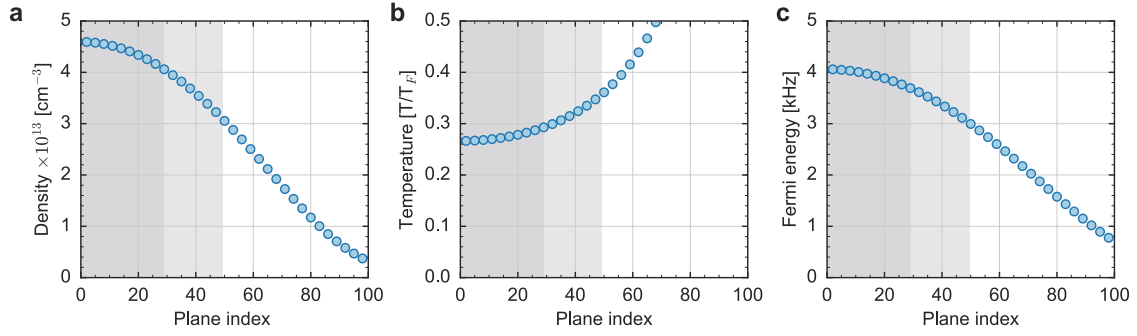


Figure 5.7 – Characteristic properties of the two-component quasi-2D Fermi gas. 50×10^3 atoms per spin state are adiabatically transferred from the dipole trap into the 1D lattice. In total 220 planes are occupied by the atoms. As the distribution along the lattice is symmetric, only one half of the planes are shown. In order to further reduce visual clutter, only every third plane is drawn. The planes are counted from the center outwards. Each point corresponds to the (a) peak density, (b) temperature and (c) Fermi energy in a plane. The values are calculated for an initial temperature of $0.2 T_F$ in the dipole trap. The gray shaded areas indicate the regions containing 50% (75%) of the atoms.

equally populated with a total of 50×10^3 atoms per nuclear spin state ($m_F = \pm 5/2$). For the transfer into the 1D lattice, we assume that the gas is always in thermal equilibrium and that the total entropy is largely conserved. We model the density profile inside the 2D planes by a 2D Thomas-Fermi density distribution. Transverse to the planes the gas is assumed to be in the Gaussian vibrational ground state. The lattice is aligned along the long axis of the cigar shaped trap and we find around 220 planes occupied. The peak in-plane density in the central plane is $n_{g\downarrow} = n_{g\uparrow} = 4.7 \times 10^{13}$ atoms per cm^3 . This results, with a transverse trapping frequency of 20 kHz and a mean radial frequency of 140 Hz, in a Fermi energy of $\epsilon_F = h \cdot 4$ kHz. The distribution of the atomic density and the corresponding Fermi energies across the 220 planes are displayed in Figure 5.7. Since the scattering length a_{gg} is small and $l_z/a_{gg} = 5.1 \gg 1$, the initial spectroscopy state $|g\downarrow\rangle|g\uparrow\rangle$ is weakly interacting. In this regime, we use the energy-independent mean-field approximation (5.10) for the scattering amplitude. We calculate the interaction energy of one $|g\downarrow\rangle$ atom in the initial state with the $|g\uparrow\rangle$ atoms through

$$E_{gg} = \frac{2\sqrt{2}\pi\hbar^2}{ml_z} a_{gg} n_{g\uparrow}. \quad (5.13)$$

For the central planes, we obtain an interaction energy of $h \cdot 0.7$ kHz. All interaction energies of the final state are measured relative to this energy.

5.3.1 Mean-field interaction shift

For the spectroscopy, we employ short and intense pulses with $\tau = 1.4$ ms and $I \sim 19$ mW/ cm^2 . These pulses correspond to π -pulses with a Rabi frequency of 250 Hz on the unperturbed single particle $|g\downarrow\rangle \rightarrow |e\downarrow\rangle$ transition. The detuning $\delta\nu$ is measured relative to this transition. We convert the detuning into the dimensionless ratio $(h\delta\nu + E_{gg})/\epsilon_F$, where we

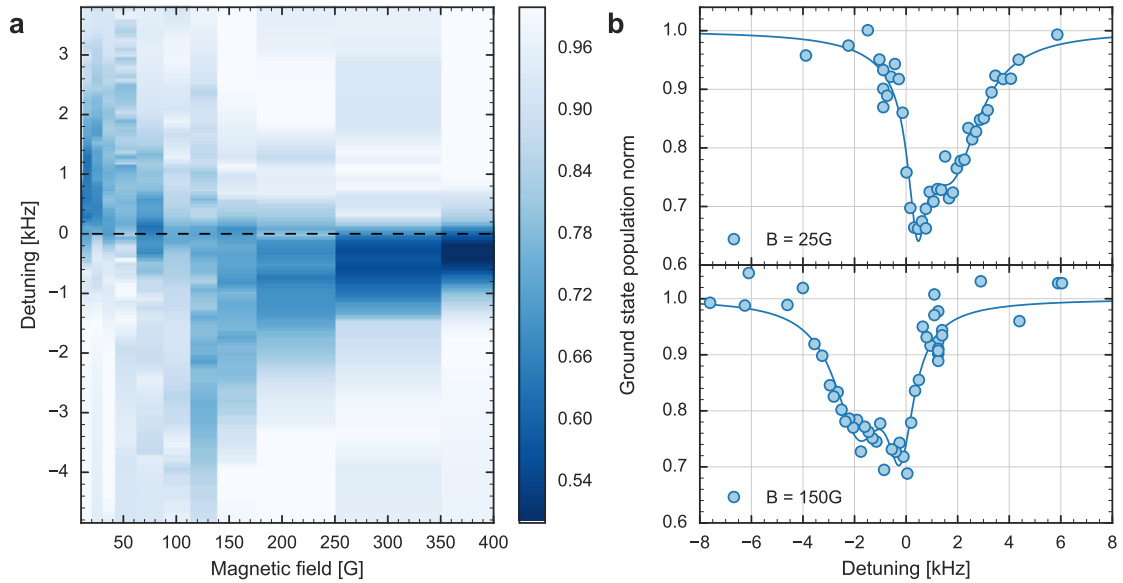


Figure 5.8 – Trap averaged measurements of the spectral response of the quasi-2D Fermi gas near the orbital Feshbach resonance. (a) Normalized population of atoms remaining in the $|g \downarrow\rangle$ as a function of the magnetic field and for different values of the clock laser detuning relative to the single particle transition $|g \downarrow\rangle \rightarrow |e \downarrow\rangle$. (b) Cuts through the data from (a) at two magnetic fields, below and above the Feshbach resonance. The data clearly illustrates the non-trivial lineshape of the resonance, that cannot be described by a single Lorentzian. The solid lines are fits of a double Lorentzian used to determine the position of the polaronic branches.

compare the measured interaction energy to the Fermi energy of the initial system. By adding the initial state interaction energy to the measured detuning, zero energy corresponds to the energy of non-interacting atoms.

The measured spectral response of the quasi-2D Fermi gas around the orbital Feshbach resonance is presented in Figure 5.8. We see that the obtained spectral response does not resemble a simple Rabi or Lorentzian lineshape. The lineshape suggests the existence of two overlapping resonances. Indeed, by fitting a double Lorentzian profile to the data, we obtain a smaller sum of squared errors compared to a single Lorentzian. From this heuristic model, we obtain two resonance positions. One of the resonances shows only a relatively small detuning compared to the single particle transition as well as a narrow width. We attribute this signal to atoms from the edges of the cloud. There, the densities are very low and thus the corresponding interaction shift. This assumption is supported by the low and magnetic field-independent depletion, as illustrated in Figure 5.9. The second resonance is found for magnetic fields below the Feshbach resonance at large positive and above the Feshbach resonance at large negative detunings, as illustrated in 5.8 (b). As the resonance is approached, the detuning, i.e. interaction energy increases monotonically on the repulsive as well as on the attractive side. Furthermore, the resonance is significantly broader than the first one and the depletion shows a strong magnetic field dependence. Based on these criteria (the magnetic field dependence of the detuning and depletion) we

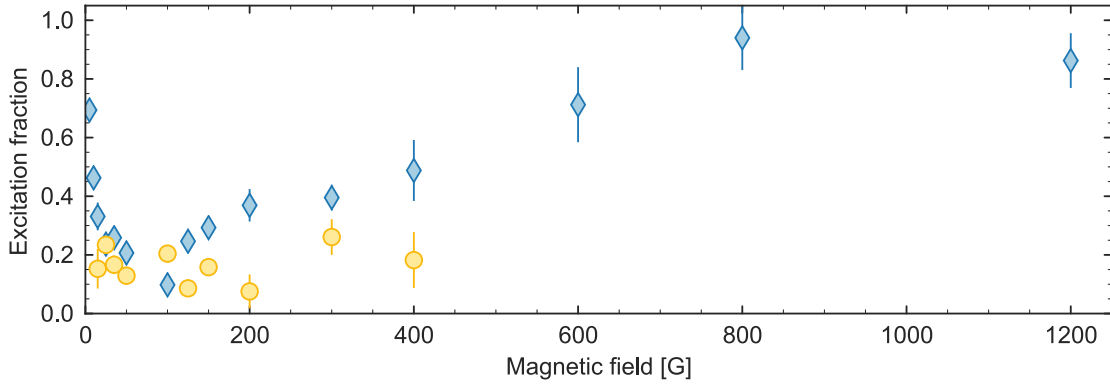


Figure 5.9 – Magnetic field dependence of the excitation fraction in the two resonances of the heuristic line-shape model. The excitation fraction is normalised to the population of the $|g \downarrow\rangle$ state, i.e. 1 corresponds to 100% transfer efficiency of the pulse. The circles (diamonds) correspond to the resonance with small (large) detuning respectively. Errorbars correspond to the 1σ uncertainty of the fits. Below 25 G and above 400 G, only a single resonance can be resolved.

attribute the second resonance to the strongly interacting gas in the central planes. The interaction shift, obtained from this resonance is shown in Figure 5.10.

For magnetic fields above 400 G, where the interorbital scattering length is small and repulsive, the final state $|e \downarrow\rangle|g \uparrow\rangle$ is weakly interacting. Here, only a single resonance is resolved by the spectroscopy. We transfer nearly all $|g \downarrow\rangle$ atoms into the $|e \downarrow\rangle$ state (see Figure 5.9) and we produce an equal mixture of $|e \downarrow\rangle$ and $|g \uparrow\rangle$ atoms. In this regime, the measured interaction shift is proportional to the scattering length and the density. Thus, we approximate the interaction shift in the final state by a simple mean-field treatment, where an $|e \downarrow\rangle$ atom is interacting with all the $|g \uparrow\rangle$ atoms. Since the scattering length diverges at the resonance, we cannot employ the energy independent mean-field approximation as for the initial state interaction. In order to take the energy dependence of the 2D interaction into account, we calculate the interaction shift based on the two-body T-matrix averaged over the whole Fermi sea in the central plane

$$\delta E = \int \frac{d^2k}{(2\pi)^2} \mathcal{T}_{00}(E). \quad (5.14)$$

The solid line in Figure 5.10 presents the resulting mean-field interaction shift of the clock line. Far away from the resonance, i.e. for small scattering lengths, Equation 5.14 reproduces very well the measured interaction shifts. However, close to the resonance, where the final state is strongly interacting, this approach fails to capture the experimentally observed behaviour. In particular, on the repulsive side of the resonance, the measured interaction energies exceed the mean-field prediction. So far, the two-channel model was capable of describing all measured interaction energies correctly. Therefore, we attribute the discrepancy between the experimental data and the theory to the mean-field approach. In particular, the mean-field approach does not take into account Pauli blocking of intermediate states in the interactions. Furthermore, in Figure 5.9, we see that the excitation

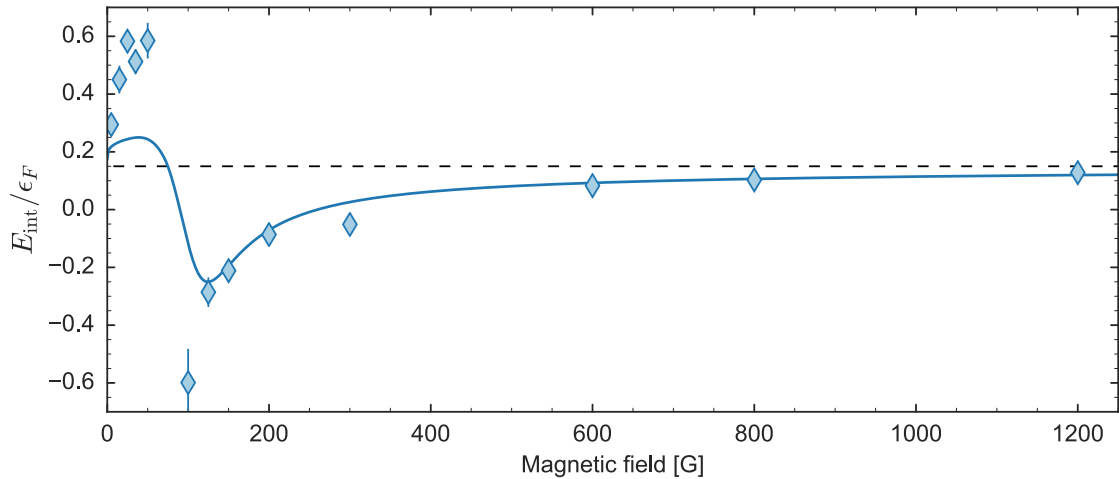


Figure 5.10 – Magnetic field dependence of the interaction energy of the attractive and repulsively interacting quasi-2D gas. The interaction energies corresponding to the diamond symbols are obtained from the resonances corresponding with larger detunings, as illustrated in Figure 5.8. Errorbars correspond to the 1σ uncertainty of the fit determining the resonance position. The solid blue line is the mean field shift, calculated from Equation (5.14). The black dashed line indicates the initial state interaction energy.

fraction close to the orbital Feshbach resonance is strongly reduced. The final state is not an equal mixture of $|e\downarrow\rangle$ and $|g\uparrow\rangle$ atoms but rather a few $|e\downarrow\rangle$ atoms immersed in a Fermi sea of $|g\downarrow\rangle|g\uparrow\rangle$ atoms. This scenario is known as the Fermi polaron problem.

5.3.2 Repulsive and attractive polarons

The idea of the polaron was first introduced to describe electrons moving through an ionic crystal [188]. Owing to the coulomb attraction, the electron distorts the ionic crystal and becomes dressed by virtual phonons. In ultracold, neutral atom experiments, typically a single $|\downarrow\rangle$ impurity in a polarised $|\uparrow\rangle$ Fermi sea is considered [189]. Following Landau's theory, we can describe the impurity interacting with the medium by a quasiparticle. Here, the quasiparticle is formed by the bare impurity dressed with particle-hole excitations of the surrounding Fermi sea. The surrounding $|\uparrow\rangle$ atoms tend to screen the impurity spin. Therefore, while moving through the medium, the impurity acquires a large effective mass. Depending on the underlying two-body scattering length, the polaron either attracts or repels the surrounding medium. Recently, Feshbach resonances in alkali atoms have allowed to study the polaron problem in both regimes [184–187].

The interaction energy of the impurity in the medium can be obtained via two approaches: a many-body variational wave function, the so-called Chevy ansatz [190] and the T-matrix approximation [181, 191]. Both methods lead to the same results [192]. So far, we have based our scattering model on the T-matrix approximation and will also apply it to the polaron problem. In the following, we present a many-body T-matrix based treatment of the polaron problem, tailored by M. Parish and J. Levinsen [193] for the peculiar

situation of the orbital Feshbach resonance, i.e. an $|e\downarrow\rangle$ impurity immersed in a $|g\downarrow\rangle|g\uparrow\rangle$ Fermi sea. The energy shift of the impurity is determined by the equation [193]

$$E = \text{Re}\{\Sigma(E)\}, \quad (5.15)$$

where $\Sigma(E)$ is the impurity self energy [193]

$$\Sigma(E) = \sum_{\mathbf{q}} T_{\text{med}}(\mathbf{q}, E + \epsilon_{\mathbf{q}}). \quad (5.16)$$

Here, T_{med} is the many-body T-matrix of the medium and \mathbf{q} the wave vector of the quasi-particle. Using the many-body T-matrix, we also take into account Pauli blocking of intermediate states in the interaction, which we have neglected in the mean-field approach. Owing to the constant density of states in 2D, the many-body T-matrix can be written as the two-body T-matrix, energetically shifted due to the Pauli blocking [191]. In our experimental configuration, Pauli blocking can happen in two different channels. Translating the typical polaron problem to the orbital Feshbach resonance, we have a single $|e\downarrow\rangle$ impurity immersed in a $|g\uparrow\rangle$ Fermi sea. In this scenario, the closed channel is unoccupied and is available as an intermediate state during a scattering event (see Figure 5.11(a)). Here, we only have to take Pauli blocking in the open channel into account. However, via the inverse spectroscopy, we have prepared a scenario, where we find a few $|e\downarrow\rangle$ impurities immersed in a $|g\downarrow\rangle|g\uparrow\rangle$ Fermi sea. Here, the open and closed channel are occupied (see Figure 5.11(b)). Therefore, the intermediate scattering states in the closed channel are Pauli blocked. The medium T-matrix can be related to the vacuum two-body matrix \mathcal{T} via [193]

$$T_{\text{med}}^{-1}(\mathbf{q}, x) = \mathcal{R} \mathcal{T}^{-1}(x - \epsilon_{\mathbf{q}}/2) \mathcal{R} - \begin{pmatrix} \Pi(\mathbf{q}, x) - \tilde{\Pi}(x - \epsilon_{\mathbf{q}}/2) & 0 \\ 0 & \Pi(\mathbf{q}, y) - \tilde{\Pi}(y - \epsilon_{\mathbf{q}}/2) \end{pmatrix} \quad (5.17)$$

with $x = E + \epsilon_{\mathbf{q}}$ and $y = E - \delta\mu B + \epsilon_{\mathbf{q}}$. The two terms on the diagonal of the second matrix account for the Pauli blocking. The first term is related to Pauli blocking in the open channel, whereas the second term is only included if the closed channel is also occupied. The rotation matrix \mathcal{R} between the orbital singlet-triplet and open-closed channel basis is defined in the Appendix A. The difference between the medium Π and vacuum polarization bubbles $\tilde{\Pi}$ is given by [193]

$$\Pi(\mathbf{q}, E + \epsilon_{\mathbf{q}}) - \tilde{\Pi}(E - \epsilon_{\mathbf{q}}/2) = - \sum_{|\mathbf{k}| < k_{\text{F}}} \frac{1}{E + \epsilon_{\mathbf{q}} - \epsilon_{\mathbf{k}} - \epsilon_{\mathbf{q}-\mathbf{k}} + i0}. \quad (5.18)$$

The blue and yellow lines in Figure 5.11(c) present the solution of (5.16) for the two depicted scenarios, i.e. Pauli blocking in the open (blue) and in both channels (yellow). We call the second scenario a *frustrated* polaron. Here, the pairing channel, i.e. the bound state in the closed channel is blocked, decreasing the energy of the attractive polaron. At the same time, the frustration enhances the energy of the repulsive polaron. This may be understood by considering the picture of the avoided crossing between the coupled scattering channels, which was introduced in the first chapter. The shift of the attractive,

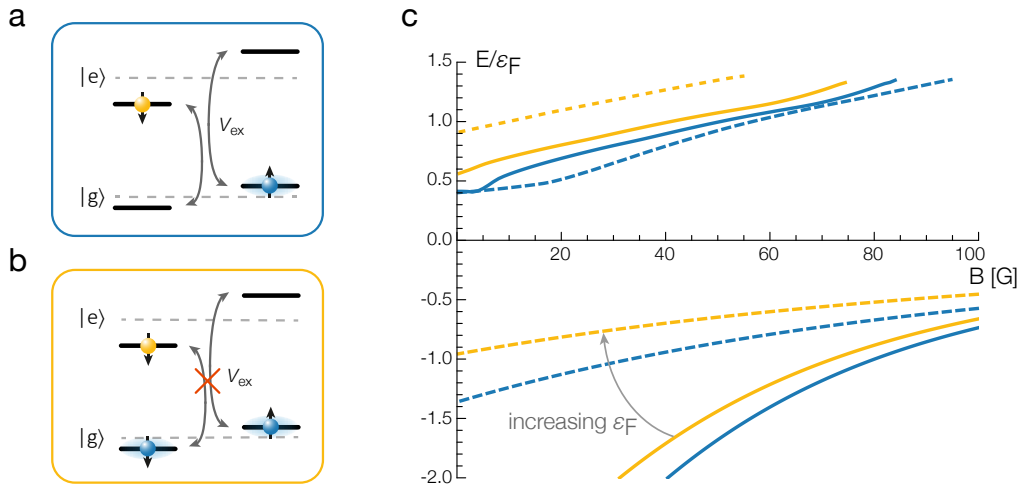


Figure 5.11 – Schematic of the two possible polaron scenarios around the orbital Feshbach resonance. (a) Regular Fermi polaron: an $|e\downarrow\rangle$ impurity immersed in a $|g\uparrow\rangle$ Fermi sea. Here, Pauli blocking occurs only in the open channel. (b) *Frustrated* polaron: an $|e\downarrow\rangle$ impurity immersed in a $|g\downarrow\rangle|g\uparrow\rangle$ Fermi sea. Here, intermediate interaction states in both open and closed channel are Pauli blocked. (c) Polaron energies as a function of the magnetic field: The blue (yellow) lines show the energy of the regular (frustrated) polaron, respectively. The solid lines are obtained for $\epsilon_F = h \cdot 4 \text{ kHz}$ in both channels. For the dashed lines, the Fermi energy matches the differential Zeeman energy at the resonance ($\epsilon_F = h \cdot 20 \text{ kHz}$), causing maximum frustration. The calculation of the polaron energies was kindly provided by M. Parish and J. Levinsen [193].

i.e. lower branch to smaller interaction energy and thus higher total energy also causes a shift of the upper, i.e. repulsive branch to higher energies. The effect of frustration becomes more pronounced as the Fermi energy approaches the energy splitting between open and closed channel at the resonance. For $\epsilon_F = h \cdot \delta\mu B_0$, the shift between the regular and the frustrated polaron is as large as $\epsilon_F/2$.

In Figure 5.12, the thick blue lines are the solutions of the polaron energy (5.16) for $\epsilon_F = h \cdot 4 \text{ kHz}$ in both open and closed channel. On the attractive side of the resonance, the frustrated polaron theory agrees well with the measured interaction energies. On the repulsive side, the measured energies are significantly lower than the calculated ones. Yet, the polaron theory agrees qualitatively better with the data than the mean-field approximation. The remaining discrepancy is potentially caused by two reasons. The polaron energies are calculated based on the Fermi energy of the central planes. In our experiment, we measure the polaron energy averaged over all 220 planes. This trap average leads to a shift towards lower energies. Furthermore, the high final state population ($\sim 20\%$) breaks the assumption of a single impurity.

The repulsive polaron is of particular interest. Close to a Feshbach resonance, where the scattering length is large and positive, the energy of the polaron can exceed the Fermi energy of the surrounding medium. In this regime, the polaron is believed to give rise to itinerant ferromagnetism [194, 195]. However, as we have shown in Chapter 1, strong repulsive interaction is caused by a shallow two-body bound state below the continuum. Thus, the repulsive polaron is only metastable and the gas is unstable towards the forma-

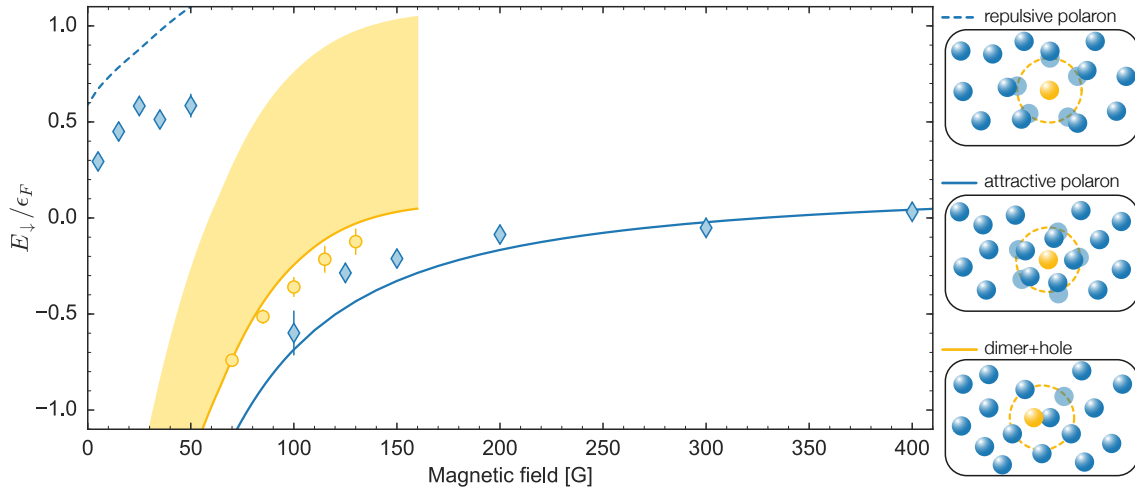


Figure 5.12 – Energy spectrum of the attractively and repulsively interacting quasi-2D gas as a function of the magnetic field. Diamonds represent the measured interaction energies, as displayed in Figure 5.10. The solid blue lines are the repulsive and attractive polaron energies $\Sigma(E)$ Ep.(5.16). Yellow circles indicate the binding energies of the quasi-2D dimer, as shown in Figure 5.3. The quasi-2D dimer energy, determined by the poles of the vacuum T-matrix (5.6), is given by the yellow line with the dimer-hole continuum ranging from ϵ_B to $\epsilon_B + \epsilon_F$ on top, marked by the yellow shaded area. Errorbars correspond to the 1σ uncertainty of the fit determining the resonance position. The insets are schematic drawings on the corresponding interaction regimes.

tion of bound pairs [196]. In order to comment on the feasibility of observing the phase separation of the paramagnetic Fermi liquid into spatially-separated polarised domains, further experiments are necessary. In particular, the lifetime of the repulsive polaron has to be determined. Employing coherent excitation, i.e. driving Rabi flopping, the quasiparticle properties of the polaron such as the residue and lifetime can be probed [185, 187].

The results from the inverse spectroscopy demonstrate that we have created a strongly interacting two-orbital Fermi gas in a quasi-2D geometry. The quasi-2D geometry enables us to directly probe spectroscopically the many-body effects on the two-body interaction. In particular, the measurements of the confinement-induced dimer present a strong validation of our two-channel scattering model, incorporating effective ranges and confinement. In the limit of weak final state interaction, we find the measured interaction energies to be well reproduced by a quasi-2D mean-field approach. For magnetic fields, where the 3D scattering length diverges, the strongly interacting many-body system can no longer be described in terms of a mean field. In this regime, we notice the emergence of two distinct branches in the spectral response of the quasi-2D Fermi gas. We attribute these to attractive and repulsive polarons. A many-body T-matrix based treatment of the interaction is in qualitative agreement with the experimental data.

Conclusion and Outlook

In this thesis, we have presented the experimental observation of a new type of Feshbach resonance between different atomic orbitals of ^{173}Yb arising from strong interorbital spin-exchange interactions. For collisions between fermionic AEL atoms in different orbitals as well as nuclear spin states, two interaction channels exist. The extremely large scattering length in one of the interorbital interaction channels and the corresponding shallow bound state lead to the appearance of the orbital Feshbach resonance at experimentally accessible magnetic fields for. Owing to the $\text{SU}(N)$ -symmetric nature of the exchange interaction, the resonance occurs universally for any combination of two different nuclear spins.

We have revealed the existence of the orbital Feshbach resonance via cross-dimensional thermalisation measurements in the bulk. Here, a resonance at a magnetic field of 55 G and a zero crossing at 417 G have been found for a mixture of atoms in the nuclear spin states $m_F = \pm 5/2$. The universal coupling with respect to the choice of the m_F states has been demonstrated by repeating the thermalisation measurements with another m_F combination. Both experiments have led to the same results when rescaling the magnetic field according to the change in the differential magnetic moment. Furthermore, we have performed inelastic loss spectroscopy. Spin resolved measurements have allowed to identify the two main loss processes. Towards lower magnetic fields, the repopulation of the initially unoccupied closed channel due to the orbital exchange interaction has been observed. For magnetic fields close to the resonance, we have characterised the inelastic two-body decay rate in the open channel. Although the orbital Feshbach resonance is a narrow resonance, a long lifetime for the degenerate Fermi gas on resonance has been discovered. So far, long lifetimes on resonance have been reported only for alkali Fermi gases exhibiting broad Feshbach resonances.

We have generalised the coupled two-channel model to the case of isotropic confinement and energy-dependent collisions. The model was benchmarked against the results obtained by high-resolution clock-line spectroscopy in an isotropic three-dimensional magic lattice. Here, a remarkable agreement between the measured and calculated atom pair interaction energy across the entire experimentally accessible magnetic field range was found. Furthermore, the initially introduced illustrative model of the orbital Feshbach resonance has been verified. Using spin resolved detection in combination with the high-resolution clock line spectroscopy, we demonstrated the evolution of anti-symmetric superposition states into the open-channel state with increasing magnetic field.

In a third experiment, we have created a strongly interacting Fermi gas in quasi two dimensions. In the quasi-2D geometry, the threshold energy of two atoms is raised by the energy of the transversal harmonic oscillator. The existence of the confinement in-

duced quasi-2D dimer is proven by inverse spectroscopy. On resonance, we demonstrate the universal scaling of the dimer energy with the confinement. The observed scaling factor is in good agreement with the theoretical prediction. The technique of inverse spectroscopy quenches the system from the weakly into to the strongly interacting regime. Employing low excitation fractions, we study the regime of strongly interacting impurities immersed in a Fermi sea. The measured interaction energies are in qualitative agreement with a many-body T-matrix based treatment of the interaction. The interpretation of the experimental data along this line allows us to identify an attractive as well as a repulsive polaronic branch.

Outlook

Our findings are a first step towards the investigation of new two-orbital few- and many-body phenomena with AEL atoms. They pave the way for the experimental realisation of a strongly interacting Fermi superfluid around a narrow resonance and have already stimulated many theoretical proposals [170, 171, 197, 198]. Furthermore, the tunability of the interorbital interaction strength suggests novel avenues for the realisation of two-orbital many-body lattice models [199–201]. In the following, we will discuss based on three different examples how this new experimental tool allows the implementation of hitherto inaccessible models with ultracold quantum gases.

First, let us consider the BEC-BCS crossover, the most prominent example of interaction tuning via a Feshbach resonance. Strongly interacting Fermi gases close to a narrow Feshbach resonance have been experimentally realised [202–204]. However, the superfluid state as well as the BEC-BCS crossover have so far only been observed with Fermi gases offering a broad resonance [13–15]. In experiments, narrow Feshbach resonances typically suffer from strong limitations. In order to stay in the strongly interacting regime, the narrow width of the resonance requires precise control of the magnetic field. The universal bound state exists only close to the resonance, and over a wide magnetic field range, the molecular branch has a strong closed channel admixture. Therefore, narrow Feshbach resonances typically suffer from limited lifetimes.

For the orbital Feshbach resonance, we have demonstrated a long lifetime on resonance, making the superfluid state accessible. The narrow character of the resonance is caused by the small differential magnetic moment between open and closed channel. Hence, the requirements on the magnetic field control in the experiment can be relaxed. Additionally, the small energy gap between open and closed channel is predicted to increase the critical temperature for reaching superfluidity away from unitarity [171]. The BEC-BCS crossover is conventionally studied using a single-channel, or a two-channel model, where only the bound state in the closed channel is considered [8, 12]. However, when the energy gap to the closed channel becomes smaller than the Fermi energy, the continuum scattering states in the closed channel have to be taken into account. This leads to the appearance of pairing not only in the open but also in the closed channel and thus

two independent order parameters, i.e. pairing gaps [58]. NSR calculations yield a higher critical temperature on the BCS side for the two-gapped superfluid [171] compared to the single channel superfluid [11]. This opens the door for the investigation of two-band superconductors with anomalously high critical temperatures [205]. Furthermore, the orbital Feshbach resonance offers a more accurate realisation of the much quoted analogue between a strongly interacting atomic Fermi gas and the low-density matter in the crust of neutron stars [18]. In contrast to the interactions around broad Feshbach resonances, the neutron-neutron interaction is dominated by a large effective range. This is similar to the situation for the orbital Feshbach resonance, where our two-channel model predicts an effective range of $960 a_0$ around the resonance.

Our experimental setup offers all necessary ingredients for the study of the BEC-BCS crossover. With our magnetic field setup, we can cover the whole interaction range from non-interacting to strongly attractive and repulsive interactions. Furthermore, our high-resolution objective grants us direct access to local thermodynamic properties and allows to measure the equation of state [16, 17].

In a second example, let us consider the implications of the orbital Feshbach resonance for the study of two-orbital magnetism. With the implementation of a state-dependent lattice in our experimental setup, we are en route towards the realisation of the Kondo lattice model. In a one-dimensional system, the tunability of the interorbital scattering length leads to the appearance of confinement induced resonances. Such confinement induced resonances are envisioned to enhance the spin-exchange scattering and hence dramatically increase the Kondo temperature [199]. Here, an increase of the Kondo temperature to ten percent of the Fermi temperature has been predicted [199]. So far, within our experiment, we have realised temperatures of $0.07 T_F$ for a single-orbital mixture and $0.14 T_F$ for a two-orbital mixture, respectively. Thus, the enhanced Kondo temperature is in the range of experimentally accessible temperatures. Furthermore, the orbital Feshbach resonance should enable us to produce even colder two-orbital mixtures. With this new tool, we can maintain a strong thermalisation rate and thus perform more efficient evaporation towards lower temperatures.

In the last example, we turn to the regime of few-body physics and our studies of the polaron problem in quasi-2D. Once again, the small energy gap as well as the orbital exchange coupling between the open and closed channel create a peculiar situation. Populating the spin state of the impurity with ground state atoms leads to a blocking of interaction states in the closed channel and thus causes a frustration of the polaron energy. This frustration should promote the repulsive polaron energy beyond the Fermi energy [193] and thus may give rise to itinerant ferromagnetism [194, 206]. Although, it has been shown that the growth rate of the pairing instability (formation of tightly bound dimers) is dominant over the Stoner instability (formation of spatially separated, polarised domains) [196], the orbital Feshbach resonance may provide a new route towards this regime. For Feshbach resonances with a large effective range, such as the orbital Feshbach resonance, the pairing instability is expected to be weaker [207]. Furthermore, in the case of the frustrated polaron, it is likely that some of the decay channels are effectively

blocked [193]. Here, a detailed study of the repulsive polaron lifetime is necessary in order to judge the feasibility of these models. In addition, as the impurity and majority atoms originate from different orbitals, a state-dependent lattice enables us to tune the effective mass of the polaron. Depending on the impurity to majority atom mass ratio, a rich phase diagram for the strongly interacting Fermi gas is predicted [208]. Changing the wavelength of the state-dependent lattice allows us to continuously tune from a mobile to a static impurity. The two extremes, where impurities are much lighter than majority atoms or very heavy, i.e. static impurities, are of particular interest. Depending on the mass ratio, the ground state of the light impurities is expected to consist of trimers or to have non-zero momentum, an FFLO-like phase [208]. The case of a static impurity immersed in a Fermi sea is also known as Anderson orthogonality catastrophe. In this regime, the quasi-particle picture of the impurity breaks down because the static impurity can excite multiple low-energy particle-hole pairs [209]. These excitations give rise to a characteristic power-law singularity in the spectral response of the impurity. As the orthogonality catastrophe belongs to the small group of solvable nonequilibrium many-body problems, a comparison between theory and experiment is particularly interesting.

Based on these three examples, we see that our experimental setup indeed presents a versatile platform for the investigation of diverse problems originating from condensed matter, few- and many-body physics. In this spirit, the orbital Feshbach resonance is an exquisite tool, enhancing the flexibility of ^{173}Yb for the purpose of quantum simulation.

Two-body problem in free space

Here we present the detailed solution of the two-body problem as it was introduced in Chapter 4. We will employ the T-matrix formalism to solve the two-body problem and obtain the scattering amplitude. We start again from the time-independent Schrödinger equation

$$[\hat{H}_0 + \hat{V}]|\psi\rangle = E|\psi\rangle. \quad (\text{A.1})$$

The solution for the free particle states is given by plane waves \mathbf{k} . The non-interacting part of the Hamiltonian, given by the Zeeman and kinetic part is diagonal in the basis of the open channel $|o\rangle$,

$$\hat{H}_0 = \sum_{\mathbf{k}} 2\epsilon_{\mathbf{k}} |o, \mathbf{k}\rangle \langle o, \mathbf{k}| + \sum_{\mathbf{k}} (2\epsilon_{\mathbf{k}} + \delta\mu B) |c, \mathbf{k}\rangle \langle c, \mathbf{k}| \quad (\text{A.2})$$

with the differential Zeeman energy $\delta\mu B$ and the kinetic energy $\epsilon_{\mathbf{k}} = \hbar^2 \mathbf{k}^2 / 2m$. The interaction part is given in the basis of the orbital single and triple state $|\pm\rangle$.

$$\hat{V} = U_+ \sum_{\mathbf{k}, \mathbf{k}'} |+, \mathbf{k}'\rangle \langle +, \mathbf{k}| + U_- \sum_{\mathbf{k}, \mathbf{k}'} |-, \mathbf{k}'\rangle \langle -, \mathbf{k}| \quad (\text{A.3})$$

where $g_{\pm} = 4\pi\hbar^2 / ma_{eg}^{\pm}$ is the corresponding interaction strength in the singlet and triplet channel. Here, we employ a zero-range pseudo potential $V = g\delta(\mathbf{r})$ for the interaction.

The total Hamiltonian is a 2-by-2 matrix. We choose the basis such, that the interaction potentials are on the diagonal. In this basis, the orbital singlet and triplet states have the eigenvectors $(1, 0)$ and $(0, 1)$. The open and closed channel live on the equator of the corresponding Bloch sphere $1/\sqrt{2}(1, 1)$ and $1/\sqrt{2}(1, -1)$. The two sets of states are linked via the rotation matrix

$$\mathcal{R} = \frac{1}{\sqrt{2}} \begin{pmatrix} 1 & 1 \\ 1 & -1 \end{pmatrix}. \quad (\text{A.4})$$

Let us now calculate the scattering amplitude. The scattering amplitude is fully determined by the two-body T-matrix

$$f(\mathbf{k}', \mathbf{k}) = -\frac{m}{4\pi\hbar^2} \langle \mathbf{k}' | \hat{T} | \mathbf{k} \rangle, \quad (\text{A.5})$$

where the T-matrix is given by the Lippmann-Schwinger equation

$$\hat{T}(E) = \hat{V} + \hat{V} \hat{G}_0 \hat{T}(E). \quad (\text{A.6})$$



Figure A.1 – Schematic representation of the T-matrix (yellow square) as the sum of all possible scattering processes of two atoms. Solving the Lippmann-Schwinger equation for the two-body T-matrix lead to the so-called Born series $\hat{T} = \hat{V} + \hat{V}\hat{G}_0\hat{V} + \hat{V}\hat{G}_0\hat{V}\hat{G}_0\hat{V} + \dots$. Here, \hat{G}_0 is the non-interacting propagator, i.e. the Greens function solving the free Hamiltonian \hat{H}_0 . The yellow circles represent the interaction \hat{V} of a possible scattering process and the blue lines the free propagation \hat{G}_0 .

Here, $\hat{G}_0 = [E^+ - \hat{H}_0]^{-1}$ is the free Green's function, i.e. the noninteracting propagator of the atoms. In order to avoid the singularity at $E - \hat{H}_0$, we have made the energy slightly complex $E^+ = E + i0$. Therefore, we can rewrite the matrix element in the scattering amplitude as

$$\langle \mathbf{k}' | \hat{T}(E) | \mathbf{k} \rangle = \langle \mathbf{k}' | \hat{V} | \mathbf{k} \rangle + \sum_{\mathbf{k}''} \langle \mathbf{k}' | \hat{V} | \mathbf{k}'' \rangle \langle \mathbf{k}'' | \hat{G}_0 | \mathbf{k}'' \rangle \langle \mathbf{k}'' | \hat{T}(E) | \mathbf{k} \rangle. \quad (\text{A.7})$$

We will evaluate this sum in the basis of the orbital interaction states. The interaction is given in this basis by

$$\langle \mathbf{k}' | \hat{V} | \mathbf{k} \rangle = \begin{pmatrix} U_- & 0 \\ 0 & U_+ \end{pmatrix} \equiv V. \quad (\text{A.8})$$

Since the interaction is independent on the change in momentum, we can rewrite the T-matrix as

$$T(E) = V + V \sum_{\mathbf{k}} \langle \mathbf{k} | \hat{G}_0 | \mathbf{k} \rangle T(E). \quad (\text{A.9})$$

In the next step, we write the free propagation in the same basis and get rid of the summation of the momentum. Here, we use that $|\mathbf{k}\rangle$ is the solution for of the non-interacting Hamiltonian $\hat{H}_0 |\mathbf{k}\rangle = 2\epsilon_{\mathbf{k}} |\mathbf{k}\rangle$,

$$\sum_{\mathbf{k}} \langle \mathbf{k} | \hat{G}_0 | \mathbf{k} \rangle = \mathcal{R} \begin{pmatrix} \sum_{\mathbf{k}} \frac{1}{E^+ - 2\epsilon_{\mathbf{k}}} & 0 \\ 0 & \sum_{\mathbf{k}} \frac{1}{E^+ - 2\epsilon_{\mathbf{k}} + \delta\mu B} \end{pmatrix} \mathcal{R} = \mathcal{R} \begin{pmatrix} \Pi(E) & 0 \\ 0 & \Pi(E - \delta\mu B) \end{pmatrix} \mathcal{R} = \mathbf{\Pi}(E), \quad (\text{A.10})$$

where we have introduced the one-loop polarisation bubble $\Pi(E) = \sum_{\mathbf{k}} 1/(E^+ - 2\epsilon_{\mathbf{k}})$. Thus, we can finally write the T-matrix as

$$T(E) = [1 - V\mathbf{\Pi}(E)]^{-1} V = [V^{-1} - \mathbf{\Pi}(E)]^{-1}. \quad (\text{A.11})$$

We want to rewrite everything in terms of the orbital singlet and triplet scattering length,. The bare coupling constant U_{\pm} is related to the s -wave scattering length via the Lippmann-Schwinger equation

$$U_{\pm}^{-1} = \frac{m}{4\pi\hbar^2 a_{eg}^{\pm}} - \sum_{\mathbf{k}} \frac{1}{2\epsilon_{\mathbf{k}}}. \quad (\text{A.12})$$

Hence, we obtain

$$\mathcal{T}(E) = [\tau_0^{-1} - \tilde{\mathbf{\Pi}}(E)]^{-1}, \quad (\text{A.13})$$

where τ_0 contains the interaction strengths

$$\tau_0 = \frac{4\pi\hbar^2}{m} \begin{pmatrix} a_- & 0 \\ 0 & a_+ \end{pmatrix} \quad (\text{A.14})$$

and $\tilde{\Pi}(E)$ has the same form as in (A.10), but the one-loop polarisation bubble $\Pi(E)$ replaced by

$$\Pi(E) = \sum_{\mathbf{k}} \left(\frac{1}{E^+ - 2\epsilon_{\mathbf{k}}} + \frac{1}{2\epsilon_{\mathbf{k}}} \right) = \frac{m}{4\pi\hbar^2} \sqrt{-mE}. \quad (\text{A.15})$$

Now, by projecting the T-matrix on the open channel $|o\rangle$, we retrieve the scattering amplitude in the open channel

$$f(E) = -\frac{m}{4\pi\hbar^2} \langle o | [\tau_0^{-1} - \tilde{\Pi}(E)]^{-1} | o \rangle. \quad (\text{A.16})$$

Substituting the definitions of τ_0 and $\tilde{\Pi}(E)$ we arrive at

$$f(E) = -\frac{1}{2} \begin{pmatrix} 1 & 1 \end{pmatrix} \left[\begin{pmatrix} a_-^{-1} & 0 \\ 0 & a_+^{-1} \end{pmatrix} + \frac{\sqrt{-mE}}{2\hbar} \begin{pmatrix} 1 & 1 \\ 1 & 1 \end{pmatrix} + \frac{\sqrt{m(\delta\mu B - E)}}{2\hbar} \begin{pmatrix} 1 & -1 \\ -1 & 1 \end{pmatrix} \right]^{-1} \begin{pmatrix} 1 \\ 1 \end{pmatrix} \quad (\text{A.17})$$

which leads to

$$f(E) = -\frac{1}{2} \frac{a_-^{-1} + a_+^{-1} - 2\sqrt{\frac{m(\delta\mu B - E)}{\hbar}}}{\left(a_-^{-1} - \left(\sqrt{\frac{-mE}{\hbar}} + \sqrt{\frac{m(\delta\mu B - E)}{\hbar}} \right) / 2 \right) \left(a_+^{-1} - \left(\sqrt{\frac{-mE}{\hbar}} + \sqrt{\frac{m(\delta\mu B - E)}{\hbar}} \right) / 2 \right) - \left(\sqrt{\frac{-mE}{\hbar}} - \sqrt{\frac{m(\delta\mu B - E)}{\hbar}} \right)^2 / 4}. \quad (\text{A.18})$$

In the limit of low energy scattering $k \rightarrow 0$, we can write $f(E)^{-1} + ik \approx -a^{-1} + 1/2r_{\text{eff}}k^2$. Thus, we obtain the open channel s -wave scattering length

$$a = \frac{1}{2} \frac{1/a_{\text{eg}}^- + 1/a_{\text{eg}}^+ - 2\sqrt{m\delta\mu B/\hbar^2}}{\left(1/a_{\text{eg}}^- - \sqrt{m\delta\mu B/\hbar^2}/2 \right) \left(1/a_{\text{eg}}^+ - \sqrt{m\delta\mu B/\hbar^2}/2 \right) - \left(\sqrt{m\delta\mu B/\hbar^2}/2 \right)^2} \quad (\text{A.19})$$

and the corresponding effective range

$$r_{\text{eff}} = -\frac{\hbar}{\sqrt{m\delta\mu B}} \left(\frac{1/a_{\text{eg}}^- - 1/a_{\text{eg}}^+}{1/a_{\text{eg}}^- + 1/a_{\text{eg}}^+ - 2\sqrt{m\delta\mu B/\hbar^2}} \right)^2. \quad (\text{A.20})$$

Two-body problem in a harmonic trap

To model two ^{173}Yb atoms of mass m on a single site, we first consider the two-body problem in a 3D harmonic trap, $V(r) = \frac{1}{2}m\omega^2 r^2$. In this case, the center-of-mass and relative coordinates decouple, and in the relative basis, we have Hamiltonian $\hat{\mathcal{H}} = \hat{H}_0 + \hat{V}$, with

$$\hat{H}_0 = \sum_n \epsilon_n |o, n\rangle \langle o, n| + \sum_n (\epsilon_n + \Delta\mu B) |c, n\rangle \langle c, n| \quad (\text{B.1})$$

and interaction part

$$\hat{V} = \sum_{n, n'} \varphi_n(0) \varphi_{n'}(0) \{U^+ |+, n\rangle \langle +, n'| + U^- |-, n\rangle \langle -, n'|\} \quad (\text{B.2})$$

Here, n labels the relative harmonic oscillator states with angular momentum $l = 0$ (these are the only ones that are affected by the short-range interactions), $\varphi_n(0)$ is the real-space harmonic oscillator wavefunction at $r = 0$, and the non-interacting energy $\epsilon_n = 2n\hbar\omega_r$. The triplet and singlet configurations are defined as $|\pm\rangle = \frac{1}{\sqrt{2}}(|o\rangle \pm |c\rangle)$, with corresponding interaction strengths U^\pm , which do not depend directly on the nuclear spin. For simplicity, we focus on a zero-range interaction here, but finite-range corrections are easily incorporated into the formalism provided the range of the interactions is much smaller than the harmonic oscillator length $l_r \equiv \sqrt{\hbar/m\omega}$.

To determine the two-body eigenstates, we consider the general wavefunction in the singlet-triplet basis

$$|\psi\rangle = \sum_n (b_n^+ |+, n\rangle + b_n^- |-, n\rangle) \quad (\text{B.3})$$

and then insert this into the Schrödinger equation as follows:

$$\frac{1}{2} \begin{pmatrix} 1 & 1 \\ 1 & -1 \end{pmatrix} \begin{pmatrix} \epsilon_n - E & 0 \\ 0 & \epsilon_n + \Delta\mu B - E \end{pmatrix} \begin{pmatrix} 1 & 1 \\ 1 & -1 \end{pmatrix} \begin{pmatrix} b_n^+ \\ b_n^- \end{pmatrix} + \varphi_n(0) \begin{pmatrix} U^+ & 0 \\ 0 & U^- \end{pmatrix} \sum_{n'} \varphi_{n'}(0) \begin{pmatrix} b_{n'}^+ \\ b_{n'}^- \end{pmatrix} = 0 \quad (\text{B.4})$$

By summing over n and replacing the bare interactions U^\pm with the scattering lengths a_{eg}^\pm , we arrive at the matrix equation for the regular part of the two-channel wave function Ψ :

$$[\tau_0^{-1} + \mathbf{\Pi}(E)] \Psi_{\text{reg}} = 0 \quad (\text{B.5})$$

where

$$\boldsymbol{\tau}_0 = -\frac{\sqrt{m}}{\hbar} \begin{pmatrix} a_{eg}^+ & 0 \\ 0 & a_{eg}^- \end{pmatrix} \quad (\text{B.6})$$

and the quantity

$$\boldsymbol{\Pi}(E) = \frac{\Pi(E)}{2} \begin{pmatrix} 1 & 1 \\ 1 & 1 \end{pmatrix} + \frac{\Pi(E - \Delta\mu B)}{2} \begin{pmatrix} 1 & -1 \\ -1 & 1 \end{pmatrix}. \quad (\text{B.7})$$

contains the pair propagator in a harmonic potential

$$\Pi(E) = \frac{\sqrt{2\hbar}}{\sqrt{m}l_r} \frac{\Gamma(-E/2\hbar\omega)}{\Gamma(-E/2\hbar\omega - 1/2)} \quad (\text{B.8})$$

The interaction energies are thus obtained from the condition $\det(\boldsymbol{\tau}_0^{-1} + \boldsymbol{\Pi}(E)) = 0$, leading to:

$$\left[\frac{2l_r}{a_{eg}^-} - F_0\left(\frac{-E}{\omega}\right) - F_0\left(\frac{-E + \delta}{\omega}\right) \right] \left[\frac{2l_r}{a_{eg}^+} - F_0\left(\frac{-E}{\omega}\right) - F_0\left(\frac{-E + \delta}{\omega}\right) \right] - \left[F_0\left(\frac{-E}{\omega}\right) - F_0\left(\frac{-E + \delta}{\omega}\right) \right]^2 = 0 \quad (\text{B.9})$$

For finite-range corrections, we need to replace $\boldsymbol{\tau}_0^{-1}$ by an energy-dependent matrix that depends on the scattering phase shifts, as in Eq. (4.28) of the main text:

$$\boldsymbol{\tau}^{-1}(E_c) = \sqrt{E_c} \begin{pmatrix} \cot \delta_{eg}^+(E_c) & 0 \\ 0 & \cot \delta_{eg}^-(E_c) \end{pmatrix} \quad (\text{B.10})$$

where the collision energy is $E_c = E - \frac{\Delta\mu B}{2} + \frac{3}{2}\hbar\omega$. We are interested in the leading order terms of the low-energy expansion:

$$\frac{\sqrt{mE_c}}{\hbar} \cot \delta_{eg}^\pm(E_c) \simeq -(a_{eg}^\pm)^{-1} + \frac{1}{2} r_{\text{eff}}^\pm \frac{mE_c}{\hbar^2} \quad (\text{B.11})$$

where r_{eff}^\pm denotes the effective range. Formally, such an effective range may be included by using a two-channel model for each of the singlet and triplet interactions. For the trapped two-body problem, the low-energy expansion of $\boldsymbol{\tau}$ is thus equivalent to making the replacement $1/a_{eg}^\pm \mapsto 1/a_{eg}^\pm - \frac{1}{2} m r_{\text{eff}}^\pm \left(E - \frac{\Delta\mu B}{2} + \frac{3}{2}\hbar\omega \right)$.

Two-body problem in quasi-2D

We will now investigate the scattering properties of a two-orbital mixture in a quasi-2D geometry. The transverse confinement is given by the harmonic potential $V(z) = \frac{1}{2}m\omega_z^2 z^2$. In such a confinement the quantum gas has a finite extension along the z -axis $l_z = \sqrt{\hbar/(m\omega_z)}$. Again, the harmonic confinement allows us to separate the relative and centre-of-mass motion. In relative coordinates, the transverse motion reduces to the harmonic oscillator equation [175]

$$\left(-\frac{1}{2M}\frac{d^2}{dz^2} + \frac{1}{2}M\omega^2 z^2\right)\phi_n(z) = \left(n + \frac{1}{2}\right)\omega_z\phi_n(z). \quad (\text{C.1})$$

Here, M is the reduced mass, $\phi_n(z)$ is the harmonic oscillator wave function and n labels the harmonic oscillator quantum number for relative motion. The non-interacting part of the two-channel quasi-2D Hamiltonian becomes

$$H_0 = \sum_{\mathbf{k}, n} 2\epsilon_{\mathbf{k}, n} |o, \mathbf{k} n\rangle \langle o, \mathbf{k} n| + \sum_{\mathbf{k}, n} (2\epsilon_{\mathbf{k}, n} + \delta\mu B) |c, \mathbf{k} n\rangle \langle c, \mathbf{k} n|, \quad (\text{C.2})$$

with $\epsilon_{\mathbf{k}, n} = \hbar^2 \mathbf{k}^2 / 2M + (n + 1/2)\omega_z$ and \mathbf{k} the in plane momentum. If the harmonic oscillator spacing is larger than all other energy scales in the system, we can restrict the description to the lowest oscillator level $n = 0$. In this regime, the gas is considered to be kinematically two dimensional.

We can derive the two-body interaction strength in the quasi-2D geometry from the bare interaction in 3D by the following consideration. Under typical experimental conditions, the confinement length l_z is much larger than the range of the van-der-Waals interaction potential and the bare two-body interaction remains unaffected by the confinement. We assume, that the 3D interaction strength can be separated into a component in the 2D-plane and a perpendicular component [175]

$$V(\mathbf{k}'_{3D}, \mathbf{k}_{3D}) = \langle \mathbf{k}'_{3D} | \hat{V} | \mathbf{k}_{3D} \rangle = V e^{-(k^2 + k'^2 + k_z^2 + k'_z{}^2) / \Lambda^2}, \quad (\text{C.3})$$

where Λ is a large ultraviolet cut-off, up to which the interaction V is taken constant and is the magnitude of the in plane momentum $k = \sqrt{k_x^2 + k_y^2}$. The scattering event $\mathbf{k}_{3D} \rightarrow \mathbf{k}'_{3D}$ gives rise to a change of the in plane momentum $\mathbf{k} \rightarrow \mathbf{k}'$, whereas the relative motion

in the transverse harmonic potential changes by $n \rightarrow n'$. The matrix element of the 3D interaction in the quasi-2D basis is therefore given by [175]

$$\begin{aligned} \langle \mathbf{k}, n | \hat{V} | \mathbf{k}', n' \rangle &= \sum_{\mathbf{k}_{3D}, \mathbf{k}'_{3D}} \langle \mathbf{k}' n' | \mathbf{k}'_{3D} \rangle \langle \mathbf{k}'_{3D} | \hat{V} | \mathbf{k}_{3D} \rangle \langle \mathbf{k}_{3D} | \mathbf{k} n \rangle \\ &= V f_n f_{n'} e^{-(k^2 + k'^2)/\Lambda^2} \end{aligned} \quad (\text{C.4})$$

where $f_n = \sum_{q_z} \phi(q_z) e^{-q_z^2/\Lambda}$ and $\phi(q_z)$ is the Fourier transform of the harmonic oscillator wave function. The f coefficients are given by [175]

$$\begin{aligned} f_{2n} &= (-1)^n \frac{1}{(2\pi l_z^2)^{1/4}} \frac{\sqrt{(2n)!}}{2^n n!} \frac{1}{\sqrt{1+\lambda}} \left(\frac{1-\lambda}{1+\lambda} \right)^n, \\ f_{2n+1} &= 0. \end{aligned} \quad (\text{C.5})$$

Under typical experimental conditions, the ratio $\lambda = 1/(\Lambda l_z)^2$ between the length scale of the short distance physics and the harmonic oscillator length is very small. In the limit $\lambda \rightarrow 0$, we can finally write down the interaction part of the quasi-2D Hamiltonian

$$\hat{V}_{2D} = \sum_{\mathbf{k}, \mathbf{k}', n, n'} f_n f_{n'} \{ U^+ |+, \mathbf{k} n \rangle \langle +, \mathbf{k}' n' | + U^- |-, \mathbf{k} n \rangle \langle -, \mathbf{k}' n' | \}, \quad (\text{C.6})$$

with U^\pm being the interaction strength of the orbital triplet and singlet channel. From here, we construct the T-matrix via the Lipmann-Schwinger equation

$$\hat{T}_{n, n'}(E) = f_n f_{n'} [V^{-1} - \Pi_{q2D}(E)]^{-1} \quad (\text{C.7})$$

with the quasi-2D polarization bubble given by [175]

$$\Pi_{q2D}(E) = \sum_{\mathbf{q}, n} \frac{|f_n|^2}{E - (n + 1/2)\omega_z - q^2/2M + 0i}. \quad (\text{C.8})$$

In the limit of low energy scattering and strong confinement $|E| < \omega_z$, we only have to consider scattering in the lowest level $n = n' = 0$. In order to obtain the scattering amplitude, we project the T-matrix on to the open channel. The scattering amplitude in the quasi-2D geometry in the lowest harmonic oscillator level for low collision energies, is hence given by

$$f_{q2D}(E) = 2M f_0 f_0 \langle \mathbf{k}', 0 | \hat{T}_{00}(E + i0) | \mathbf{k}, 0 \rangle \quad (\text{C.9})$$

with the matrix element evaluation to

$$\mathcal{T}_{00} = \frac{\sqrt{2\pi}}{M} \frac{\frac{l_z}{a_{eg}^-} + \frac{l_z}{a_{eg}^+} + 2\mathcal{F}(\epsilon')}{\left(\frac{l_z}{a_{eg}^-} - [\mathcal{F}(\epsilon) + \mathcal{F}(\epsilon')] \right) \left(\frac{l_z}{a_{eg}^+} - [\mathcal{F}(\epsilon) + \mathcal{F}(\epsilon')] \right) - [\mathcal{F}(\epsilon) + \mathcal{F}(\epsilon')]^2 / 4}. \quad (\text{C.10})$$

Here, we have used the substitution $\epsilon = -E/\omega_z$ and $\epsilon' = -(E + \delta\mu B)/\omega_z$. The \mathcal{F} function is given in the limit $\lambda \rightarrow 0$ by [175]

$$F_0(\epsilon) = \int_0^\infty du \frac{1}{\sqrt{4\pi u^3}} \left[1 - \frac{e^{-\epsilon u}}{\sqrt{(1 - e^{-2u})/2u}} \right]. \quad (\text{C.11})$$

Once again, finite range effects can be incorporated by the effective range expansion: $a^{-1} \rightarrow a^{-1} - \frac{1}{2} M r_0 (E - \frac{\delta\mu B}{2} + 1/2\omega_z)$.

Bibliography

- [1] R. P. Feynman. *Simulating Physics with Computers*. International Journal of Theoretical Physics **21**, 467–488 (1982). See page: 1
- [2] I. Buluta and F. Nori. *Quantum Simulators*. Science **326**, 108 (2009). See page: 1
- [3] A. Aspuru-Guzik and P. Walther. *Photonic Quantum Simulators*. Nat. Phys. **8**, 285–291 (2012).
- [4] R. Blatt and C. F. Roos. *Quantum Simulations with Trapped Ions*. Nat. Phys. **8**, 277–284 (2012).
- [5] I. Bloch, J. Dalibard, and S. Nascimbene. *Quantum Simulations with Ultracold Quantum Gases*. Nat. Phys. **8**, 267–276 (2012). See pages: 1, 34
- [6] I. Bloch, J. Dalibard, and W. Zwerger. *Many-Body Physics with Ultracold Gases*. Rev. Mod. Phys. **80**, 885–964 (2008). See pages: 1, 38, 87
- [7] F. Dalfovo, S. Giorgini, L. P. Pitaevskii, and S. Stringari. *Theory of Bose-Einstein Condensation in Trapped Gases*. Rev. Mod. Phys. **71**, 463–512 (1999). See page: 1
- [8] S. Giorgini, L. P. Pitaevskii, and S. Stringari. *Theory of Ultracold Atomic Fermi Gases*. Rev. Mod. Phys. **80**, 1215–1274 (2008). See pages: 1, 100
- [9] C. Chin, R. Grimm, P. Julienne, and E. Tiesinga. *Feshbach Resonances in Ultracold Gases*. Rev. Mod. Phys. **82**, 1225–1286 (2010). See pages: 1, 17, 21, 22
- [10] J. Bardeen, L. N. Cooper, and J. R. Schrieffer. *Theory of Superconductivity*. Phys. Rev. **108**, 1175–1204 (1957). See page: 1
- [11] P. Nozières and S. Schmitt-Rink. *Bose Condensation in an Attractive Fermion Gas: From Weak to Strong Coupling Superconductivity*. Journal of Low Temperature Physics **59**, 195–211 (1985). See pages: 1, 101
- [12] W. Zwerger. *The BCS-BEC Crossover and the Unitary Fermi Gas*. Number 836 in Lecture Notes in Physics. Springer-Verlag Berlin Heidelberg (2012). See pages: 1, 90, 100
- [13] C. Chin, M. B. A. Altmeyer, S. Riedl, S. Jochim, J. H. Denschlag, and R. Grimm. *Observation of the Pairing Gap in a Strongly Interacting Fermi Gas*. Science **305**, 1128–1130 (2004). See pages: 1, 100

- [14] M. W. Zwierlein, C. A. Stan, C. H. Schunck, S. M. F. Raupach, A. J. Kerman, and W. Ketterle. *Condensation of Pairs of Fermionic Atoms Near a Feshbach Resonance*. Phys. Rev. Lett. **92** (2004).
- [15] C. A. Regal, M. Greiner, and D. S. Jin. *Observation of Resonance Condensation of Fermionic Atom Pairs*. Phys. Rev. Lett. **92** (2004). See pages: 1, 100
- [16] S. Nascimbène, N. Navon, K. Jiang, F. Chevy, and C. Salomon. *Exploring the Thermodynamics of a Universal Fermi Gas*. Nature **463**, 1057–1060 (2010). See pages: 2, 101
- [17] M. J. H. Ku, A. T. Sommer, L. W. Cheuk, and M. W. Zwierlein. *Revealing the Superfluid Lambda Transition in the Universal Thermodynamics of a Unitary Fermi Gas*. Science **335**, 563–567 (2012). See pages: 2, 101
- [18] A. Gezerlis and J. Carlson. *Strongly Paired Fermions: Cold Atoms and Neutron Matter*. Phys. Rev. C **77**, 032801 (2008). See pages: 2, 101
- [19] D. Jaksch, C. Bruder, J. I. Cirac, C. W. Gardiner, and P. Zoller. *Cold Bosonic Atoms in Optical Lattices*. Phys. Rev. Lett. **81**, 3108–3111 (1998). See pages: 2, 34, 38
- [20] P. A. Lee, N. Nagaosa, and X.-G. Wen. *Doping a Mott Insulator: Physics of High Temperature Superconductivity*. arXiv:cond-mat/0410445 (2004). See pages: 2, 81
- [21] M. Greiner, O. Mandel, T. Esslinger, T. W. Hansch, and I. Bloch. *Quantum Phase Transition from a Superfluid to a Mott Insulator in a Gas of Ultracold Atoms*. Nature **415**, 39–44 (2002). See page: 2
- [22] R. Jordens, N. Strohmaier, K. Gunter, H. Moritz, and T. Esslinger. *A Mott Insulator of Fermionic Atoms in an Optical Lattice*. Nature **455**, 204–207 (2008). See pages: 2, 39
- [23] U. Schneider, L. Hackermüller, S. Will, T. Best, I. Bloch, T. A. Costi, R. W. Helmes, D. Rasch, and A. Rosch. *Metallic and Insulating Phases of Repulsively Interacting Fermions in a 3D Optical Lattice*. Science **322**, 1520–1525 (2008). See pages: 2, 39
- [24] J. M. Kosterlitz and D. J. Thouless. *Ordering, Metastability and Phase Transitions in Two-Dimensional Systems*. J. Phys. C: Solid State Phys. **6**, 1181 (1973). See pages: 2, 81
- [25] Z. Hadzibabic, P. Krüger, M. Cheneau, B. Battelier, and J. Dalibard. *Berezinskii-Kosterlitz-Thouless Crossover in a Trapped Atomic Gas*. Nature **441**, 1118–1121 (2006). See page: 2
- [26] B. Paredes, A. Widera, V. Murg, O. Mandel, S. Fölling, I. Cirac, G. V. Shlyapnikov, T. W. Hansch, and I. Bloch. *Tonks-Girardeau Gas of Ultracold Atoms in an Optical Lattice*. Nature **429**, 277–281 (2004). See pages: 2, 15

- [27] K. M. O'Hara, S. L. Hemmer, M. E. Gehm, S. R. Granade, and J. E. Thomas. *Observation of a Strongly-Interacting Degenerate Fermi Gas of Atoms*. *Science* **298**, 2179–2182 (2002). See page: 2
- [28] M. Greiner, I. Bloch, O. Mandel, T. W. Hänsch, and T. Esslinger. *Exploring Phase Coherence in a 2D Lattice of Bose-Einstein Condensates*. *Phys. Rev. Lett.* **87**, 160405 (2001). See page: 2
- [29] S. Fölling, F. Gerbier, A. Widera, O. Mandel, T. Gericke, and I. Bloch. *Spatial Quantum Noise Interferometry in Expanding Ultracold Atom Clouds*. *Nature* **434**, 481–484 (2005). See page: 2
- [30] N. Gemelke, X. Zhang, C.-L. Hung, and C. Chin. *In Situ Observation of Incompressible Mott-Insulating Domains in Ultracold Atomic Gases*. *Nature* **460**, 995–998 (2009). See page: 2
- [31] J. F. Sherson, C. Weitenberg, M. Endres, M. Cheneau, I. Bloch, and S. Kuhr. *Single-Atom-Resolved Fluorescence Imaging of an Atomic Mott Insulator*. *Nature* **467**, 68–72 (2010). See page: 2
- [32] W. S. Bakr, A. Peng, M. E. Tai, R. Ma, J. Simon, J. I. Gillen, S. Fölling, L. Pollet, and M. Greiner. *Probing the Superfluid-to-Mott Insulator Transition at the Single-Atom Level*. *Science* **329**, 547 (2010). See page: 2
- [33] L. Kouwenhoven and L. Glazman. *Revival of the Kondo Effect*. *Phys. World* **14**, 33 (2001). See pages: 2, 41
- [34] P. Coleman. *Heavy Fermions: Electrons at the Edge of Magnetism*. arXiv:cond-mat/0612006 (2006). See pages: 2, 41
- [35] Y. Tokura and N. Nagaosa. *Orbital Physics in Transition-Metal Oxides*. *Science* **288**, 462 (2000). See pages: 2, 3
- [36] M. A. Cazalilla, A. F. Ho, and M. Ueda. *Ultracold Gases of Ytterbium: Ferromagnetism and Mott States in an $SU(6)$ Fermi System*. *New J. Phys.* **11**, 103033 (2009). See pages: 3, 37, 40
- [37] M. Hermele, V. Gurarie, and A. M. Rey. *Mott Insulators of Ultracold Fermionic Alkaline Earth Atoms: Underconstrained Magnetism and Chiral Spin Liquid*. *Phys. Rev. Lett.* **103**, 135301 (2009).
- [38] A. V. Gorshkov, M. Hermele, V. Gurarie, C. Xu, P. S. Julienne, J. Ye, P. Zoller, E. Demler, M. D. Lukin, and A. M. Rey. *Two-Orbital $SU(N)$ Magnetism with Ultracold Alkaline-Earth Atoms*. *Nat. Phys.* **6**, 289–295 (2010). See pages: 3, 26, 36, 41
- [39] M. A. Cazalilla and A. M. Rey. *Ultracold Fermi Gases with Emergent $SU(N)$ Symmetry*. *Reports on Progress in Physics* **77**, 124401 (2014). See pages: 3, 26, 37

- [40] T. Fukuhara, Y. Takasu, M. Kumakura, and Y. Takahashi. *Degenerate Fermi Gases of Ytterbium*. Phys. Rev. Lett. **98**, 030401 (2007). See page: 3
- [41] B. J. DeSalvo, M. Yan, P. G. Mickelson, Y. N. Martinez de Escobar, and T. C. Killian. *Degenerate Fermi Gas of ^{87}Sr* . Phys. Rev. Lett. **105**, 030402 (2010). See page: 3
- [42] S. Taie, Y. Takasu, S. Sugawa, R. Yamazaki, T. Tsujimoto, R. Murakami, and Y. Takahashi. *Realization of a $SU(2) \times SU(6)$ System of Fermions in a Cold Atomic Gas*. Phys. Rev. Lett. **105**, 190401 (2010). See pages: 3, 40, 50
- [43] C. Hofrichter, L. Riegger, F. Scazza, M. Höfer, D. R. Fernandes, I. Bloch, and S. Fölling. *Direct Probing of the Mott Crossover in the $SU(N)$ Fermi-Hubbard Model*. Phys. Rev. X **6**, 021030 (2016). See pages: 3, 40
- [44] M. Boll, T. A. Hilker, G. Salomon, A. Omran, I. Bloch, and C. Gross. *Spin and Charge Resolved Quantum Gas Microscopy of Antiferromagnetic Order in Hubbard Chains*. Science **353**, 1257–1260 (2016). See pages: 3, 39
- [45] L. W. Cheuk, M. A. Nichols, K. R. Lawrence, M. Okan, H. Zhang, E. Khatami, N. Trivedi, T. Paiva, M. Rigol, and M. W. Zwierlein. *Observation of Spatial Charge and Spin Correlations in the 2D Fermi-Hubbard Model*. Science **353**, 1260–1264 (2016).
- [46] M. F. Parsons, A. Mazurenko, C. S. Chiu, G. Ji, D. Greif, and M. Greiner. *Site-Resolved Measurement of the Spin-Correlation Function in the Fermi-Hubbard Model*. Science **353**, 1253 (2016). See pages: 3, 39
- [47] C. Honerkamp and W. Hofstetter. *Ultracold Fermions and the $SU(N)$ Hubbard Model*. Phys. Rev. Lett. **92**, 170403 (2004). See pages: 3, 40
- [48] F. F. Assaad. *Phase Diagram of the Half-Filled Two-Dimensional $SU(N)$ Hubbard-Heisenberg Model: A Quantum Monte Carlo Study*. Phys. Rev. B **71**, 075103 (2005). See page: 40
- [49] P. Sinkovicz, A. Zamora, E. Szirmai, M. Lewenstein, and G. Szirmai. *Spin Liquid Phases of Alkaline-Earth-Metal Atoms at Finite Temperature*. Phys. Rev. A **88**, 043619 (2013). See page: 3
- [50] J. van den Brink, G. Khaliullin, and D. Khomskii. *Orbital Effects in Manganites*. arXiv:cond-mat/0206053 (2002). See page: 3
- [51] M. Foss-Feig, M. Hermele, V. Gurarie, and A. M. Rey. *Heavy Fermions in an Optical Lattice*. Phys. Rev. A **82**, 053624 (2010). See pages: 3, 36, 41, 42
- [52] M. Foss-Feig, M. Hermele, and A. M. Rey. *Probing the Kondo Lattice Model with Alkaline-Earth-Metal Atoms*. Phys. Rev. A **81**, 051603 (2010). See pages: 3, 36

- [53] L. He, M. Jin, and P. Zhuang. *Superfluidity in a Three-Flavor Fermi Gas with SU(3) Symmetry*. Phys. Rev. A **74**, 033604 (2006). See pages: 3, 37
- [54] A. Rapp, G. Zarand, C. Honerkamp, and W. Hofstetter. *Color Superfluidity and Baryon Fomeration in Ultracold Fermions*. Phys. Rev. Lett. **98**, 160405 (2007). See page: 37
- [55] T. Ozawa and G. Baym. *Population Imbalance and Pairing in the BCS-BEC Crossover of Three-Component Ultracold Fermions*. Phys. Rev. A **82**, 063615 (2010). See pages: 3, 37
- [56] F. Scazza, C. Hofrichter, M. Höfer, P. C. De Groot, I. Bloch, and S. Fölling. *Observation of Two-Orbital Spin-Exchange Interactions with Ultracold SU(N)-Symmetric Fermions*. Nat. Phys. **10**, 779–784 (2014). See pages: 3, 27, 28, 32, 54, 55, 75
- [57] G. Cappellini, M. Mancini, G. Pagano, P. Lombardi, L. Livi, M. Siciliani de Cumis, P. Cancio, M. Pizzocaro, D. Calonico, F. Levi, C. Sias, J. Catani, M. Inguscio, and L. Fallani. *Direct Observation of Coherent Interorbital Spin-Exchange Dynamics*. Phys. Rev. Lett. **113**, 120402 (2014). See pages: 3, 54, 55
- [58] R. Zhang, Y. Cheng, H. Zhai, and P. Zhang. *Orbital Feshbach Resonance in Alkali-Earth Atoms*. Phys. Rev. Let. **115** (2015). See pages: 3, 55, 70, 101
- [59] M. Höfer, L. Riegger, F. Scazza, C. Hofrichter, D. R. Fernandes, M. M. Parish, J. Levinsen, I. Bloch, and S. Fölling. *Observation of an Orbital Interaction-Induced Feshbach Resonance in 173-Yb*. Phys. Rev. Let. **115** (2015). See pages: 4, 27, 28, 42, 53, 55, 75
- [60] F. Scazza. *Probing SU(N)-Symmetric Orbital Interactions with Ytterbium Fermi Gases in Optical Lattices*. PhD thesis, Ludwig-Maximilians-Universität (2015). See pages: 5, 26, 43, 46, 47, 48, 49, 50, 51, 77
- [61] C. Hofrichter. *Probing the SU(N) Fermi-Hubbard Model with Ytterbium Atoms in an Optical Lattice*. PhD thesis, Ludwig-Maximilians-Universität, München (2016). See pages: 5, 45, 47
- [62] J. T. M. Walraven. *Quantum Gases - Statistics and Interactions* (2014). See pages: 9, 10, 12, 18
- [63] N. Mott and H. Massey. *The Theory of Atomic Collisions*. International series of monographs on physics. Clarendon Press (1965). See pages: 11, 20
- [64] J. L. Bohn and P. S. Julienne. *Prospects for Influencing Scattering Lengths with Far-off-Resonant Light*. Phys. Rev. A **56**, 1486–1491 (1997). See pages: 11, 20, 21, 71

- [65] G. F. Gribakin and V. V. Flambaum. *Calculation of the Scattering Length in Atomic Collisions Using the Semiclassical Approximation*. Phys. Rev. A **48**, 546–553 (1993). See page: 12
- [66] V. V. Flambaum, G. F. Gribakin, and C. Harabati. *Analytical Calculation of Cold-Atom Scattering*. Phys. Rev. A **59**, 1998–2005 (1999). See pages: 12, 75
- [67] B. Gao. *Binding Energy and Scattering Length for Diatomic Systems*. J. Phys. B: At. Mol. Opt. Phys. **37**, 4273 (2004). See page: 13
- [68] B. Gao. *Quantum-Defect Theory of Atomic Collisions and Molecular Vibration Spectra*. Phys. Rev. A **58**, 4222–4225 (1998). See pages: 14, 75
- [69] E. Fermi. *Sul Moto Dei Neutroni Nelle Sostanze Idrogena- Te*. La Ricerca Scientifica **VII**, 13–52 (1936). See page: 14
- [70] K. Huang and C. N. Yang. *Quantum-Mechanical Many-Body Problem with Hard-Sphere Interaction*. Phys. Rev. **105**, 767–775 (1957). See page: 14
- [71] T. Busch, B.-G. Englert, K. Rzazewski, and M. Wilkens. *Two Cold Atoms in a Harmonic Trap*. Foundations of Physics **28**, 549–559 (1998). See pages: 15, 74, 76
- [72] D. S. Petrov, G. V. Shlyapnikov, and J. T. M. Walraven. *Regimes of Quantum Degeneracy in Trapped 1D Gases*. Phys. Rev. Lett. **85**, 3745–3749 (2000). See page: 15
- [73] G. Zürn, F. Serwane, T. Lompe, A. N. Wenz, M. G. Ries, J. E. Bohn, and S. Jochim. *Fermionization of Two Distinguishable Fermions*. Phys. Rev. Lett. **108** (2012). See page: 15
- [74] F. Deuretzbacher, K. Plassmeier, D. Pfannkuche, F. Werner, C. Ospelkaus, S. Ospelkaus, K. Sengstock, and K. Bongs. *Heteronuclear Molecules in an Optical Lattice: Theory and Experiment*. Phys. Rev. A **77**, 032726 (2008). See page: 16
- [75] H. Feshbach. *Unified Theory of Nuclear Reactions*. Annals of Physics **5**, 357–390 (1958). See page: 17
- [76] H. Feshbach. *A Unified Theory of Nuclear Reactions. II*. Annals of Physics **19**, 287–313 (1962). See page: 17
- [77] U. Fano. *Effects of Configuration Interaction on Intensities and Phase Shifts*. Phys. Rev. **124**, 1866–1878 (1961). See page: 17
- [78] E. Timmermans, P. Tommasini, M. Hussein, and A. Kerman. *Feshbach Resonances in Atomic Bose–Einstein Condensates*. Physics Reports **315**, 199–230 (1999). See pages: 17, 18

- [79] R. Duine and H. T. C. Stoof. *Atom–molecule Coherence in Bose Gases*. *Physics Reports* **396**, 115 – 195 (2004). See page: 58
- [80] K. Góral, T. Köhler, S. A. Gardiner, E. Tiesinga, and P. S. Julienne. *Adiabatic Association of Ultracold Molecules via Magnetic-Field Tunable Interactions*. *J. Phys. B: At. Mol. Opt. Phys.* **37**, 3457 (2004).
- [81] B. Marcelis, E. G. M. van Kempen, B. J. Verhaar, and S. J. J. M. F. Kokkelmans. *Feshbach Resonances with Large Background Scattering Length: Interplay with Open-Channel Resonances*. *Phys. Rev. A* **70**, 012701 (2004).
- [82] M. Raoult and F. H. Mies. *Feshbach Resonance in Atomic Binary Collisions in the Wigner Threshold Law Regime*. *Phys. Rev. A* **70**, 012710 (2004). See page: 17
- [83] T. Köhler, K. Góral, and P. S. Julienne. *Production of Cold Molecules via Magnetically Tunable Feshbach Resonances*. *Rev. Mod. Phys.* **78**, 1311–1361 (2006). See pages: 17, 18, 19
- [84] H. Haken and H. Wolf. *Molekülphysik Und Quantenchemie*. Springer-Verlag Berlin Heidelberg, Berlin, Heidelberg (2006). See page: 17
- [85] A. J. Moerdijk, B. J. Verhaar, and A. Axelsson. *Resonances in Ultracold Collisions of ${}^6\text{Li}$, ${}^7\text{Li}$, and ${}^{23}\text{Na}$* . *Phys. Rev. A* **51**, 4852–4861 (1995). See pages: 18, 19
- [86] E. R. I. Abraham, W. I. McAlexander, J. M. Gerton, R. G. Hulet, R. Côté, and A. Dalgarno. *Triplet S-Wave Resonance in ${}^6\text{Li}$ collisions and scattering lengths of ${}^6\text{Li}$ and ${}^7\text{Li}$* . *Phys. Rev. A* **55**, 3299–3302 (1997). See page: 20
- [87] A. Marte, T. Volz, J. Schuster, S. Dürr, G. Rempe, E. G. M. van Kempen, and B. J. Verhaar. *Feshbach Resonances in Rubidium 87: Precision Measurement and Analysis*. *Phys. Rev. Lett.* **89**, 283202 (2002).
- [88] E. G. M. van Kempen, S. J. J. M. F. Kokkelmans, D. J. Heinzen, and B. J. Verhaar. *Interisotope Determination of Ultracold Rubidium Interactions from Three High-Precision Experiments*. *Phys. Rev. Lett.* **88**, 093201 (2002).
- [89] T. Loftus, C. A. Regal, C. Ticknor, J. L. Bohn, and D. S. Jin. *Resonant Control of Elastic Collisions in an Optically Trapped Fermi Gas of Atoms*. *Phys. Rev. Lett.* **88**, 173201 (2002).
- [90] M. Bartenstein, A. Altmeyer, S. Riedl, R. Geursen, S. Jochim, C. Chin, J. H. Denschlag, R. Grimm, A. Simoni, E. Tiesinga, C. J. Williams, and P. S. Julienne. *Precise Determination of ${}^6\text{Li}$ Cold Collision Parameters by Radio-Frequency Spectroscopy on Weakly Bound Molecules*. *Phys. Rev. Lett.* **94**, 103201 (2005). See pages: 20, 22, 61, 84

- [91] P. O. Fedichev, Y. Kagan, G. V. Shlyapnikov, and J. T. M. Walraven. *Influence of Nearly Resonant Light on the Scattering Length in Low-Temperature Atomic Gases*. Phys. Rev. Lett. **77**, 2913–2916 (1996). See page: 21
- [92] F. K. Fatemi, K. M. Jones, and P. D. Lett. *Observation of Optically Induced Feshbach Resonances in Collisions of Cold Atoms*. Phys. Rev. Lett. **85**, 4462–4465 (2000). See page: 21
- [93] L. W. Clark, L.-C. Ha, C.-Y. Xu, and C. Chin. *Quantum Dynamics with Spatiotemporal Control of Interactions in a Stable Bose-Einstein Condensate*. Phys. Rev. Lett. **115**, 155301 (2015). See page: 21
- [94] R. Ciuryło, E. Tiesinga, and P. S. Julienne. *Optical Tuning of the Scattering Length of Cold Alkaline-Earth-Metal Atoms*. Phys. Rev. A **71**, 030701 (2005). See pages: 22, 54
- [95] K. Enomoto, K. Kasa, M. Kitagawa, and Y. Takahashi. *Optical Feshbach Resonance Using the Intercombination Transition*. Phys. Rev. Lett. **101**, 203201 (2008). See pages: 22, 54
- [96] M. Yan, B. J. DeSalvo, B. Ramachandhran, H. Pu, and T. C. Killian. *Controlling Condensate Collapse and Expansion with an Optical Feshbach Resonance*. Phys. Rev. Lett. **110**, 123201 (2013). See pages: 22, 54
- [97] C. Chin, V. Vuletić, A. J. Kerman, S. Chu, E. Tiesinga, P. J. Leo, and C. J. Williams. *Precision Feshbach Spectroscopy of Ultracold Cs₂*. Phys. Rev. A **70**, 032701 (2004). See page: 22
- [98] S. Inouye, M. R. Andrews, J. Stenger, H.-J. Miesner, D. M. Stamper-Kurn, and W. Ketterle. *Observation of Feshbach Resonances in a Bose-Einstein Condensate*. Nature **392**, 151–154 (1998). See page: 22
- [99] S. Jochim, M. Bartenstein, G. Hendl, J. H. Denschlag, R. Grimm, A. Mosk, and M. Weidemüller. *Magnetic Field Control of Elastic Scattering in a Cold Gas of Fermionic Lithium Atoms*. Phys. Rev. Lett. **89**, 273202 (2002). See page: 22
- [100] K. M. O’Hara, S. L. Hemmer, S. R. Granade, M. E. Gehm, J. E. Thomas, V. Venturi, E. Tiesinga, and C. J. Williams. *Measurement of the Zero Crossing in a Feshbach Resonance of Fermionic ⁶Li*. Phys. Rev. A **66**, 041401 (2002). See page: 22
- [101] C. R. Monroe, E. A. Cornell, C. A. Sackett, C. J. Myatt, and C. E. Wieman. *Measurement of Cs-Cs Elastic Scattering at T = 30 μK*. Phys. Rev. Lett. **70**, 414–417 (1993). See page: 22
- [102] B. DeMarco, J. L. Bohn, J. Burke, M. Holland, and D. S. Jin. *Observation of P-Wave Threshold Law Using Evaporatively Cooled Fermionic Atoms*. Phys. Rev. Lett. **82**, 4208–4211 (1999).

- [103] T. Loftus, C. A. Regal, C. Ticknor, J. L. Bohn, and D. S. Jin. *Resonant Control of Elastic Collisions in an Optically Trapped Fermi Gas of Atoms*. Phys. Rev. Lett. **88**, 173201 (2002). See page: 22
- [104] D. Naik, A. Trenkwalder, C. Kohstall, F. M. Spiegelhalder, M. Zaccanti, G. Hendl, F. Schreck, R. Grimm, T. M. Hanna, and P. S. Julienne. *Feshbach Resonances in the ${}^6\text{Li}$ - ${}^{40}\text{K}$ Fermi-Fermi Mixture: Elastic versus Inelastic Interactions*. The European Physical Journal D **65**, 55–65 (2011). See page: 22
- [105] C. A. Regal, C. Ticknor, J. L. Bohn, and D. S. Jin. *Creation of Ultracold Molecules from a Fermi Gas of Atoms*. Nature **424**, 47–50 (2003). See pages: 22, 61, 84
- [106] G. Zürn, T. Lompe, A. N. Wenz, S. Jochim, P. S. Julienne, and J. M. Hutson. *Precise Characterization of ${}^6\text{Li}$ Feshbach Resonances Using Trap-Sideband-Resolved RF Spectroscopy of Weakly Bound Molecules*. Phys. Rev. Lett. **110**, 135301 (2013). See pages: 22, 61, 84
- [107] S.-K. Yip and T.-L. Ho. *Zero Sound Modes of Dilute Fermi Gases with Arbitrary Spin*. Phys. Rev. A **59**, 4653–4656 (1999). See pages: 25, 37
- [108] N. Bornemann, P. Hyllus, and L. Santos. *Resonant Spin-Changing Collisions in Spinor Fermi Gases*. Phys. Rev. Lett. **100** (2008). See page: 25
- [109] J. S. Krauser, J. Heinze, N. Fläschner, S. Götzke, C. Becker, and K. Sengstock. *Coherent Multi-Flavour Spin Dynamics in a Fermionic Quantum Gas*. Nat. Phys. **8**, 813–818 (2012). See page: 25
- [110] M. Kitagawa, K. Enomoto, K. Kasa, Y. Takahashi, R. Ciuryło, P. Naidon, and P. S. Julienne. *Two-Color Photoassociation Spectroscopy of Ytterbium Atoms and the Precise Determinations of s-Wave Scattering Lengths*. Phys. Rev. A **77**, 012719 (2008). See pages: 26, 27, 54, 71
- [111] C. Foot. *Atomic Physics*. Oxford University Press, Oxford (2004). See page: 28
- [112] Y. Takasu, K. Komori, K. Honda, M. Kumakura, T. Yabuzaki, and Y. Takahashi. *Photoassociation Spectroscopy of Laser-Cooled Ytterbium Atoms*. Phys. Rev. Lett. **93**, 123202 (2004). See page: 29
- [113] K. Beloy, J. A. Sherman, N. D. Lemke, N. Hinkley, C. W. Oates, and A. D. Ludlow. *Determination of the $5d6s\ {}^3D_1$ state lifetime and blackbody-radiation clock shift in Yb*. Phys. Rev. A **86**, 051404 (2012). See page: 32
- [114] S. Porsev and A. Derevianko. *Hyperfine Quenching of the Metastable ${}^3P_{0,2}$ States in Divalent Atoms*. Phys. Rev. A **69** (2004). See pages: 29, 30, 31, 47
- [115] G. Breit and L. A. Wills. *Hyperfine Structure in Intermediate Coupling*. Phys. Rev. **44**, 470–490 (1933). See page: 30

- [116] A. Lurio, M. Mandel, and R. Novick. *Second-Order Hyperfine and Zeeman Corrections for an (sl) Configuration*. Phys. Rev. **126**, 1758–1767 (1962). See page: 30
- [117] M. M. Boyd, T. Zelevinsky, A. D. Ludlow, S. Blatt, T. Zanon-Willette, S. M. Foreman, and J. Ye. *Nuclear Spin Effects in Optical Lattice Clocks*. Phys. Rev. A **76**, 022510 (2007). See pages: 30, 31
- [118] A. V. Taichenachev, V. I. Yudin, C. W. Oates, C. W. Hoyt, Z. W. Barber, and L. Hollberg. *Magnetic Field-Induced Spectroscopy of Forbidden Optical Transitions with Application to Lattice-Based Optical Atomic Clocks*. Phys. Rev. Lett. **96**, 083001 (2006). See page: 30
- [119] N. Poli, Z. W. Barber, N. D. Lemke, C. W. Oates, L. S. Ma, J. E. Stalnaker, T. M. Fortier, S. A. Diddams, L. Hollberg, J. C. Bergquist, A. Brusch, S. Jefferts, T. Heavner, and T. Parker. *Frequency Evaluation of the Doubly Forbidden $^1S_0 \rightarrow ^3P_0$ transition in bosonic ^{174}Yb* . Phys. Rev. A **77**, 050501 (2008). See page: 30
- [120] A. Lurio. *Configuration Interaction and the Hfs of the sl Configuration*. Phys. Rev. **142**, 46–50 (1966). See page: 31
- [121] M. Pizzocaro, P. Thoumany, B. Rauf, F. Bregolin, G. Milani, C. Clivati, G. A. Costanzo, F. Levi, and D. Calonico. *Absolute Frequency Measurement of the $1S_0 - 3P_0$ Transition of ^{171}Yb* . Metrologia **54**, 102–112 (2017). See page: 31
- [122] C. Clivati, G. Cappellini, L. F. Livi, F. Poggiali, M. S. de Cumis, M. Mancini, G. Pagano, M. Frittelli, A. Mura, G. A. Costanzo, F. Levi, D. Calonico, L. Fallani, J. Catani, and M. Inguscio. *Measuring Absolute Frequencies beyond the GPS Limit via Long-Haul Optical Frequency Dissemination*. Opt. Express **24**, 11865–11875 (2016). See page: 31
- [123] A. C. Gossard, V. Jaccarino, and J. H. Wernick. *Ytterbium NMR: Yb^{171} Nuclear Moment and Yb Metal Knight Shift*. Phys. Rev. **133**, A881–A884 (1964). See page: 31
- [124] S. G. Porsev, A. Derevianko, and E. N. Fortson. *Possibility of an Optical Clock Using the $6^1S_0 \rightarrow 6^3P_0^o$ transition in $^{171,173}\text{Yb}$ atoms held in an optical lattice*. Phys. Rev. A **69**, 021403 (2004). See pages: 31, 32, 56
- [125] Z. W. Barber, C. W. Hoyt, C. W. Oates, L. Hollberg, A. V. Taichenachev, and V. I. Yudin. *Direct Excitation of the Forbidden Clock Transition in Neutral ^{174}Yb Atoms Confined to an Optical Lattice*. Phys. Rev. Lett. **96**, 083002 (2006). See page: 32
- [126] R. Grimm, M. Weidemüller, and Y. B. Ovchinnikov. *Optical Dipole Traps for Neutral Atoms*. arXiv:physics/9902072 (1999). See pages: 33, 34
- [127] M. Greiner and S. Fölling. *Condensed-Matter Physics: Optical Lattices*. Nature **453**, 736–738 (2008). See page: 34

- [128] M. Takamoto, F.-L. Hong, R. Higashi, and H. Katori. *An Optical Lattice Clock*. *Nature* **435**, 321–324 (2005). See page: 34
- [129] A. D. Ludlow, M. M. Boyd, J. Ye, E. Peik, and P. O. Schmidt. *Optical Atomic Clocks*. *Rev. Mod. Phys.* **87**, 637–701 (2015). See pages: 34, 35
- [130] S. G. Porsev, Y. G. Rakhlina, and M. G. Kozlov. *Electric-Dipole Amplitudes, Lifetimes, and Polarizabilities of the Low-Lying Levels of Atomic Ytterbium*. *Phys. Rev. A* **60**, 2781–2785 (1999). See page: 35
- [131] V. Dzuba and A. Derevianko. *Dynamic Polarizabilities and Related Properties of Clock States of the Ytterbium Atom*. *Journal of Physics B: Atomic, Molecular and Optical Physics* **43**, 074011 (2010). See pages: 35, 36
- [132] N. Hinkley, J. A. Sherman, N. B. Phillips, M. Schioppo, N. D. Lemke, K. Beloy, M. Pizzocaro, C. W. Oates, and A. D. Ludlow. *An Atomic Clock with 10^{-18} Instability*. *Science* **341**, 1215–1218 (2013). See page: 35
- [133] B. J. Bloom, T. L. Nicholson, J. R. Williams, S. L. Campbell, M. Bishof, X. Zhang, W. Zhang, S. L. Bromley, and J. Ye. *An Optical Lattice Clock with Accuracy and Stability at the 10^{-18} Level*. *Nature* **506**, 71–75 (2014). See page: 35
- [134] N. D. Lemke, A. D. Ludlow, Z. W. Barber, T. M. Fortier, S. A. Diddams, Y. Jiang, S. R. Jefferts, T. P. Heavner, T. E. Parker, and C. W. Oates. *Spin-1/2 Optical Lattice Clock*. *Phys. Rev. Lett.* **103**, 063001 (2009). See pages: 35, 50
- [135] W. Yi, A. J. Daley, G. Pupillo, and P. Zoller. *State-Dependent, Addressable Subwavelength Lattices with Cold Atoms*. *New J. Phys.* **10**, 073015 (2008). See page: 35
- [136] F. Gerbier and J. Dalibard. *Gauge Fields for Ultracold Atoms in Optical Superlattices*. *New J. Phys.* **12**, 033007 (2010). See page: 35
- [137] J. Dalibard, F. Gerbier, G. Juzeliūnas, and P. Öhberg. *Colloquium : Artificial Gauge Potentials for Neutral Atoms*. *Rev. Mod. Phys.* **83**, 1523–1543 (2011). See page: 35
- [138] G. Baym and C. Pethick. *Landau Fermi-Liquid Theory*. Wiley, New York (1991). See page: 37
- [139] R. W. Cherng, G. Refael, and E. Demler. *Superfluidity and Magnetism in Multicomponent Ultracold Fermions*. *Phys. Rev. Lett.* **99**, 130406 (2007). See page: 37
- [140] W. Kohn and J. M. Luttinger. *New Mechanism for Superconductivity*. *Phys. Rev. Lett.* **15**, 524–526 (1965). See page: 37
- [141] S. R. Manmana, K. R. A. Hazzard, G. Chen, A. E. Feiguin, and A. M. Rey. *$SU(N)$ Magnetism in Chains of Ultracold Alkaline-Earth-Metal Atoms: Mott Transitions and Quantum Correlations*. *Phys. Rev. A* **84**, 043601 (2011). See page: 39

- [142] H. Song and M. Hermele. *Mott Insulators of Ultracold Fermionic Alkaline Earth Atoms in Three Dimensions*. Phys. Rev. B **87**, 144423 (2013). See page: 39
- [143] L. Bonnes, K. R. A. Hazzard, S. R. Manmana, A. M. Rey, and S. Wessel. *Adiabatic Loading of One-Dimensional $SU(N)$ Alkaline-Earth-Atom Fermions in Optical Lattices*. Phys. Rev. Lett. **109**, 205305 (2012). See page: 40
- [144] L. Messio and F. Mila. *Entropy Dependence of Correlations in One-Dimensional $SU(N)$ Antiferromagnets*. Phys. Rev. Lett. **109**, 205306 (2012). See page: 40
- [145] A. Cichy and A. Sotnikov. *Orbital Magnetism of Ultracold Fermionic Gases in a Lattice: Dynamical Mean-Field Approach*. Phys. Rev. A **93**, 053624 (2016). See page: 41
- [146] S. Yunoki, J. Hu, A. L. Malvezzi, A. Moreo, N. Furukawa, and E. Dagotto. *Phase Separation in Electronic Models for Manganites*. Phys. Rev. Lett. **80**, 845–848 (1998). See pages: 41, 42
- [147] E. Dagotto, S. Yunoki, A. L. Malvezzi, A. Moreo, J. Hu, S. Capponi, D. Poilblanc, and N. Furukawa. *Ferromagnetic Kondo Model for Manganites: Phase Diagram, Charge Segregation, and Influence of Quantum Localized Spins*. Phys. Rev. B **58**, 6414–6427 (1998). See page: 41
- [148] J. Kienert and W. Nolting. *Magnetic Phase Diagram of the Kondo Lattice Model with Quantum Localized Spins*. Phys. Rev. B **73**, 224405 (2006). See pages: 41, 42
- [149] H. Röder, R. R. P. Singh, and J. Zang. *High-Temperature Thermodynamics of the Ferromagnetic Kondo-Lattice Model*. Phys. Rev. B **56**, 5084–5087 (1997). See page: 42
- [150] Y.-D. Chuang, A. D. Gromko, D. S. Dessau, T. Kimura, and Y. Tokura. *Fermi Surface Nesting and Nanoscale Fluctuating Charge/Orbital Ordering in Colossal Magnetoresistive Oxides*. Science **292**, 1509–1513 (2001). See page: 42
- [151] C. Salomon, D. Hils, and J. L. Hall. *Laser Stabilization at the Millihertz Level*. Journal of the Optical Society of America B **5**, 1576 (1988). See page: 48
- [152] J. Alnis, A. Matveev, N. Kolachevsky, T. Udem, and T. W. Hänsch. *Subhertz Linewidth Diode Lasers by Stabilization to Vibrationally and Thermally Compensated Ultralow-Expansion Glass Fabry-Pérot Cavities*. Phys. Rev. A **77**, 053809 (2008). See page: 48
- [153] R. W. P. Drever, J. L. Hall, F. V. Kowalski, J. Hough, G. M. Ford, A. J. Munley, and H. Ward. *Laser Phase and Frequency Stabilization Using an Optical Resonator*. Appl. Phys. B **31**, 97–105 (1983). See page: 48
- [154] E. D. Black. *An Introduction to Pound–Drever–Hall Laser Frequency Stabilization*. American Journal of Physics **69**, 79–87 (2001). See page: 48

- [155] P. Ketterer. *A Stable Laser Setup for the 578 nm Clock Transition of Ytterbium*. Master's thesis, Ludwig-Maximilians-Universität, München (2012). See page: 48
- [156] T. Bähr. *Construction and Characterization of a Narrow-Line Laser Source for the Clock Transition of Ytterbium-173*. Master's thesis, Ludwig-Maximilians-Universität, München (2016). See page: 48
- [157] T. Sleator, T. Pfau, V. Balykin, O. Carnal, and J. Mlynek. *Experimental Demonstration of the Optical Stern-Gerlach Effect*. *Phys. Rev. Lett.* **68**, 1996–1999 (1992). See page: 50
- [158] Z. W. Barber, J. E. Stalnaker, N. D. Lemke, N. Poli, C. W. Oates, T. M. Fortier, S. A. Diddams, L. Hollberg, C. W. Hoyt, A. V. Taichenachev, and V. I. Yudin. *Optical Lattice Induced Light Shifts in an Yb Atomic Clock*. *Phys. Rev. Lett.* **100**, 103002 (2008). See page: 50
- [159] S. Kato, S. Sugawa, K. Shibata, R. Yamamoto, and Y. Takahashi. *Control of Resonant Interaction between Electronic Ground and Excited States*. *Phys. Rev. Lett.* **110**, 173201 (2013). See page: 54
- [160] M. L. González-Martínez and J. M. Hutson. *Magnetically Tunable Feshbach Resonances in $Li + Yb(^3P_J)$* . *Phys. Rev. A* **88**, 020701 (2013). See page: 54
- [161] A. Petrov, C. Makrides, and S. Kotochigova. *Magnetic Control of Ultra-Cold 6Li and $^{174}Yb(^3P_2)$ Atom Mixtures with Feshbach Resonances*. *New J. Phys.* **17**, 045010 (2015). See page: 54
- [162] S. G. Porsev, M. S. Safronova, A. Derevianko, and C. W. Clark. *Long-Range Interaction Coefficients for Ytterbium Dimers*. *Phys. Rev. A* **89**, 012711 (2014). See page: 60
- [163] F. Reif. *Fundamentals of Statistical and Thermal Physics*. McGraw-Hill, New York (1965). See page: 62
- [164] J. Goldwin, S. Inouye, M. L. Olsen, and D. S. Jin. *Cross-Dimensional Relaxation in Bose-Fermi Mixtures*. *Phys. Rev. A* **71**, 043408 (2005). See page: 62
- [165] M. Arndt, M. Ben Dahan, D. Guéry-Odelin, M. W. Reynolds, and J. Dalibard. *Observation of a Zero-Energy Resonance in Cs-Cs Collisions*. *Phys. Rev. Lett.* **79**, 625–628 (1997). See page: 62
- [166] L. Costa, J. Brachmann, A.-C. Voigt, C. Hahn, M. Taglieber, T. W. Hänsch, and K. Dieckmann. *S-Wave Interaction in a Two-Species Fermi-Fermi Mixture at a Narrow Feshbach Resonance*. *Phys. Rev. Lett.* **105**, 123201 (2010). See page: 62
- [167] V. Vuletić, A. J. Kerman, C. Chin, and S. Chu. *Observation of Low-Field Feshbach Resonances in Collisions of Cesium Atoms*. *Phys. Rev. Lett.* **82**, 1406–1409 (1999). See page: 62

- [168] S. Jochim, M. Bartenstein, A. Altmeyer, G. Hendl, C. Chin, J. H. Denschlag, and R. Grimm. *Pure Gas of Optically Trapped Molecules Created from Fermionic Atoms*. Phys. Rev. Lett. **91**, 240402 (2003). See pages: 68, 70
- [169] C. A. Regal, M. Greiner, and D. S. Jin. *Lifetime of Molecule-Atom Mixtures near a Feshbach Resonance in ^{40}K* . Phys. Rev. Lett. **92**, 083201 (2004). See pages: 68, 70
- [170] Y. Cheng, R. Zhang, and P. Zhang. *Orbital Feshbach Resonance with Small Energy Gap between Open and Closed Channels*. Phys. Rev. A **93** (2016). See pages: 70, 100
- [171] J. Xu, R. Zhang, Y. Cheng, P. Zhang, R. Qi, and H. Zhai. *Reaching a Fermi-Superfluid State near an Orbital Feshbach Resonance*. Phys. Rev. A **94**, 033609 (2016). See pages: 70, 100, 101
- [172] M. Randeria, J.-M. Duan, and L.-Y. Shieh. *Bound States, Cooper Pairing, and Bose Condensation in Two Dimensions*. Phys. Rev. Lett. **62**, 981–984 (1989). See page: 81
- [173] D. S. Petrov and G. V. Shlyapnikov. *Interatomic Collisions in a Tightly Confined Bose Gas*. Phys. Rev. A **64**, 012706 (2001). See pages: 81, 84, 87, 88
- [174] M. Wouters, J. Tempere, and J. T. Devreese. *Feshbach Resonances in a Quasi-Two-Dimensional Atomic Gas*. Phys. Rev. A **68**, 053603 (2003). See pages: 81, 83
- [175] J. Levinsen and M. M. Parish. *Strongly Interacting Two-Dimensional Fermi Gases*. Annual Review of Cold Atoms and Molecules **3**, 1–75 (2015). See pages: 81, 82, 83, 86, 109, 110
- [176] D. S. Petrov, M. Holzmann, and G. V. Shlyapnikov. *Bose-Einstein Condensation in Quasi-2D Trapped Gases*. Phys. Rev. Lett. **84**, 2551–2555 (2000). See pages: 82, 84
- [177] D. S. Petrov, M. A. Baranov, and G. V. Shlyapnikov. *Superfluid Transition in Quasi-Two-Dimensional Fermi Gases*. Phys. Rev. A **67**, 031601 (2003). See page: 82
- [178] B. Fröhlich, M. Feld, E. Vogt, M. Koschorreck, W. Zwerger, and M. Köhl. *Radio-Frequency Spectroscopy of a Strongly Interacting Two-Dimensional Fermi Gas*. Phys. Rev. Lett. **106**, 105301 (2011). See page: 88
- [179] A. T. Sommer, L. W. Cheuk, M. J. H. Ku, W. S. Bakr, and M. W. Zwierlein. *Evolution of Fermion Pairing from Three to Two Dimensions*. Phys. Rev. Lett. **108**, 045302 (2012). See page: 88
- [180] S. Tan. *Energetics of a Strongly Correlated Fermi Gas*. Annals of Physics **323**, 2952–2970 (2008). See page: 89
- [181] M. Punk and W. Zwerger. *Theory of Rf-Spectroscopy of Strongly Interacting Fermions*. Phys. Rev. Lett. **99**, 170404 (2007). See pages: 89, 94

- [182] S. K. Baur, B. Fröhlich, M. Feld, E. Vogt, D. Pertot, M. Koschorreck, and M. Köhl. *Radio-Frequency Spectra of Feshbach Molecules in Quasi-Two-Dimensional Geometries*. Phys. Rev. A **85**, 061604 (2012). See page: 90
- [183] C. A. Regal and D. S. Jin. *Measurement of Positive and Negative Scattering Lengths in a Fermi Gas of Atoms*. Phys. Rev. Lett. **90**, 230404 (2003). See page: 90
- [184] A. Schirotzek, C.-H. Wu, A. Sommer, and M. W. Zwierlein. *Observation of Fermi Polarons in a Tunable Fermi Liquid of Ultracold Atoms*. Phys. Rev. Lett. **102** (2009). See pages: 90, 94
- [185] C. Kohstall, M. Zaccanti, M. Jag, A. Trenkwalder, P. Massignan, G. M. Bruun, F. Schreck, and R. Grimm. *Metastability and Coherence of Repulsive Polarons in a Strongly Interacting Fermi Mixture*. Nature **485**, 615–618 (2012). See pages: 90, 97
- [186] M. Koschorreck, D. Pertot, E. Vogt, B. Fröhlich, M. Feld, and M. Köhl. *Attractive and Repulsive Fermi Polarons in Two Dimensions*. Nature **485**, 619–622 (2012). See page: 90
- [187] F. Scazza, G. Valtolina, P. Massignan, A. Recati, A. Amico, A. Burchianti, C. Fort, M. Inguscio, M. Zaccanti, and G. Roati. *Observation of Repulsive Fermi Polarons in a Resonant Mixture of Ultracold ${}^6\text{Li}$ Atoms*. arXiv:1609.09817 (2016). See pages: 90, 94, 97
- [188] L. Landau and S. Pekar. *Effective Mass of a Polaron*. Zh. Eksp. Teor. Fiz. **18**, 419–423 (1933). See page: 94
- [189] F. Chevy and C. Mora. *Ultra-Cold Polarized Fermi Gases*. Rep. Prog. Phys. **73**, 112401 (2010). See page: 94
- [190] F. Chevy. *Universal Phase Diagram of a Strongly Interacting Fermi Gas with Unbalanced Spin Populations*. Phys. Rev. A **74**, 063628 (2006). See page: 94
- [191] R. Schmidt, T. Enss, V. Pietilä, and E. Demler. *Fermi Polarons in Two Dimensions*. Phys. Rev. A **85** (2012). See pages: 94, 95
- [192] R. Combescot, A. Recati, C. Lobo, and F. Chevy. *Normal State of Highly Polarized Fermi Gases: Simple Many-Body Approaches*. Phys. Rev. Lett. **98**, 180402 (2007). See page: 94
- [193] M. M. Parish and J. Levinsen. *Orbital Feshbach Notes*. Privat Communication (2015). See pages: 94, 95, 96, 101, 102
- [194] X. Cui and H. Zhai. *Stability of a Fully Magnetized Ferromagnetic State in Repulsively Interacting Ultracold Fermi Gases*. Phys. Rev. A **81**, 041602 (2010). See pages: 96, 101

- [195] P. Massignan and G. M. Bruun. *Repulsive Polarons and Itinerant Ferromagnetism in Strongly Polarized Fermi Gases*. The European Physical Journal D **65**, 83–89 (2011). See page: 96
- [196] D. Pekker, M. Babadi, R. Sensarma, N. Zinner, L. Pollet, M. W. Zwierlein, and E. Demler. *Competition between Pairing and Ferromagnetic Instabilities in Ultracold Fermi Gases near Feshbach Resonances*. Phys. Rev. Lett. **106**, 050402 (2011). See pages: 97, 101
- [197] L. He, J. Wang, S.-G. Peng, X.-J. Liu, and H. Hu. *A Strongly Correlated Fermi Superfluid near an Orbital Feshbach Resonance: The Stability, Universal Equation of State and Leggett Mode*. arXiv:1606.00188 [cond-mat] (2016). See page: 100
- [198] M. Iskin. *Two-Band Superfluidity and Intrinsic Josephson Effect in Alkaline-Earth Fermi Gases across an Orbital Feshbach Resonance*. arXiv:1605.00470 [cond-mat] (2016). See page: 100
- [199] R. Zhang, D. Zhang, Y. Cheng, W. Chen, P. Zhang, and H. Zhai. *Kondo Effect in Alkaline-Earth-Metal Atomic Gases with Confinement-Induced Resonances*. Phys. Rev. A **93**, 043601 (2016). See pages: 100, 101
- [200] L. Isaev, J. Schachenmayer, and A. M. Rey. *Spin-Orbit-Coupled Correlated Metal Phase in Kondo Lattices: An Implementation with Alkaline-Earth Atoms*. Phys. Rev. Lett. **117**, 135302 (2016).
- [201] I. Kuzmenko, T. Kuzmenko, Y. Avishai, and G.-B. Jo. *Coqblin-Schrieffer Model for an Ultracold Gas of Ytterbium Atoms with Metastable State*. Phys. Rev. B **93**, 115143 (2016). See page: 100
- [202] K. E. Strecker, G. B. Partridge, and R. G. Hulet. *Conversion of an Atomic Fermi Gas to a Long-Lived Molecular Bose Gas*. Phys. Rev. Lett. **91** (2003). See page: 100
- [203] A. Trenkwalder, C. Kohstall, M. Zaccanti, D. Naik, A. I. Sidorov, F. Schreck, and R. Grimm. *Hydrodynamic Expansion of a Strongly Interacting Fermi-Fermi Mixture*. Phys. Rev. Lett. **106** (2011).
- [204] E. L. Hazlett, Y. Zhang, R. W. Stites, and K. M. O'Hara. *Realization of a Resonant Fermi Gas with a Large Effective Range*. Phys. Rev. Lett. **108** (2012). See page: 100
- [205] S. Souma, Y. Machida, T. Sato, T. Takahashi, H. Matsui, S.-C. Wang, H. Ding, A. Kaminski, J. C. Campuzano, S. Sasaki, and K. Kadowaki. *The Origin of Multiple Superconducting Gaps in MgB₂*. Nature **423**, 65–67 (2003). See page: 101
- [206] P. Massignan, M. Zaccanti, and G. M. Bruun. *Polarons, Dressed Molecules and Itinerant Ferromagnetism in Ultracold Fermi Gases*. Rep. Prog. Phys. **77**, 034401 (2014). See page: 101

- [207] D. Pekker and E. Demler. *Competing Instabilities in Quench Experiments with Ultracold Fermi Gases near a Feshbach Resonance*. arXiv:1107.3930 (2011). See page: 101
- [208] J. Levinsen and S. K. Baur. *High-Polarization Limit of the Quasi-Two-Dimensional Fermi Gas*. Phys. Rev. A **86**, 041602 (2012). See page: 102
- [209] M. Knap, A. Shashi, Y. Nishida, A. Imambekov, D. A. Abanin, and E. Demler. *Time-Dependent Impurity in Ultracold Fermions: Orthogonality Catastrophe and Beyond*. Phys. Rev. X **2**, 041020 (2012). See page: 102

Danksagung

Zum Gelingen meiner Doktorarbeit haben in den letzten viereinhalb Jahren viele Personen beigetragen. An dieser Stelle möchte ich mich hiermit recht herzlich bedanken.

An erster Stelle sei mein Doktorvater Prof. Immanuel Bloch erwähnt. Durch sein unermüdliches Engagement und Enthusiasmus hat er ein großartiges Umfeld für das wissenschaftliche Arbeiten geschaffen und es einem ermöglicht in der ersten Liga der Forschung mitzuspielen. Genauso danke ich meinem Gruppenleiter Simon Fölling. Von seinem schier endlosen Wissen über unterschiedlichsten Details, sowohl in der Physik als auch bei technischen Fragen, konnte ich viel lernen und es hat uns oft vor manchen zu schnellen Handlungen bewahrt. Auch Meera Parish und Jesper Levinsen möchte ich für die gute Zusammenarbeit und die vielen inspirierenden Diskussionen danken.

Der Erfolg dieser Doktorarbeit wäre so nicht möglich gewesen ohne meine Mitdoktoranden. Sowohl Francesco Scazza und Chrisitan Hofrichter die den Grundstein für unser Experiment gelegt haben als auch Luis Riegger und Nelson Darkwah Oppong, die jetzt das Ruder übernehmen. Wir alle sind über die vielen Stunden gemeinsamer Arbeit Freunde geworden und ich bin froh, dass sie ein jeweils ein Stück dieser Promotion mitgegangen sind.

Allen Mitgliedern der gesamten Gruppe danke ich für das gute Klima, den regen Austausch von Ideen und die schönen gemeinsamen Abende auf den vielen Konferenzen und Gruppenretreats. Einige sind dabei gute Freunde geworden mit denen ich großartige Erlebnisse beim Rennradfahren, Bergsteigen und auf Skitouren geteilt habe.

Unseren Teamassistentinnen Ildiko Kecskesi und Kristina Schuldt vielen Dank für die super Unterstützung bei jeglichem Papierkram und dass alles immer reibungslos geklappt hat, auch wenn man mal wieder eine Frist vergessen hatte.

Meinen Eltern danke ich für ihre fortwährende und bedingungslose Unterstützung zu allen Zeiten. Zuletzt möchte ich meiner Freundin Stefanie danken. Danke für Alles.